

## Equilibrium pressure limits in stellarators

Présentée le 16 juin 2023

Faculté des sciences de base  
SPC - Théorie  
Programme doctoral en physique

pour l'obtention du grade de Docteur ès Sciences

par

**Antoine BAILLOD**

Acceptée sur proposition du jury

Prof. A. Pasquarello, président du jury  
Prof. J. Graves, Dr J. Loizu Cisquella, directeurs de thèse  
Dr S. R. Hudson, rapporteur  
Dr S. A. Henneberg, rapporteuse  
Dr H. Reimerdes, rapporteur





"I have not failed.  
I've just found 10,000 ways that won't work."  
— Thomas Edison

To Mélanie



# Abstract

This thesis delves into the potential of magnetic fusion energy, and in particular focuses on the stellarator concept. Stellarators use external coils to produce 3-dimensional (3D) magnetic fields that confine a thermonuclear plasma in a topologically toroidal volume, and thus do not, in general, require an externally driven plasma current. This is one of the main advantages of the stellarator, as the absence of strong currents in the plasma makes it intrinsically more stable than his cousin, the tokamak. It also comes at a price, since the stellarator needs to break axisymmetry to provide confinement, which is a major engineering challenge.

The fusion performance in stellarators increases with  $\beta$ , *i.e.* the plasma pressure normalized by the magnetic pressure. At finite pressure however, the plasma generates additional currents, and therefore its own magnetic field, that adds up to the vacuum magnetic field generated by the external coils. The computation of the vacuum field produced by the external coils is thus not sufficient to design, optimize, operate, and interpret experimental results. Instead, it is crucial to compute the magnetohydrodynamical (MHD) equilibrium, which takes into account the non-linear contributions from the plasma.

Of particular interest is the magnetic field line topology of 3D magnetic equilibria. These equilibria are in general composed of nested magnetic surfaces, magnetic islands and chaotic field lines, where the latter two topologies are, in general, detrimental to core confinement. Configurations with large regions filled with nested magnetic surfaces are thus usually sought. While it is possible to design stellarators with nested magnetic surfaces in vacuum, the plasma contribution to the total magnetic field can destroy the carefully designed magnetic surfaces at finite plasma  $\beta$ , thereby setting the maximum achievable  $\beta$  in stellarators, and ultimately limiting their performance.

This thesis investigates the effect of pressure and currents generated by the plasma on the topology of magnetic field lines in MHD equilibria. Tools to compute free-boundary 3D MHD equilibria with magnetic islands and chaotic field lines are presented and extended. In particular, the *Stepped Pressure Equilibrium Code* (SPEC) is expanded to allow the prescription of the net toroidal current profile, and is used to perform large parameter scans to identify the equilibrium  $\beta$ -limits in different stellarator geometries, taking into account the effect of the bootstrap current. New measures are developed to

## Abstract

---

evaluate the amount of chaotic field lines in an equilibrium, and to calculate their impact on particle transport. An analytical model is then proposed to explain the numerical results and expose the underlying scaling laws. Finally, this thesis explores the use of SIMSOPT, a python optimization framework, to optimize a configuration equilibrium  $\beta$ -limit.

Broadly, this thesis contributes to the ongoing research on magnetic fusion reactors and the potential of nuclear fusion as a clean, safe, and abundant energy source. Specifically, it provides a better understanding of the effect of pressure on the topology of magnetic field lines in MHD equilibria, and how it impacts the performance of the stellarator. Additionally, this thesis gives insight into how optimizations can improve the performance of the stellarator and increase the equilibrium  $\beta$ -limit.

**Keywords:** nuclear fusion, plasma, stellarator, magnetohydrodynamic, equilibrium, chaos, optimization

# Résumé

Cette thèse s'intéresse au potentiel des réacteurs à fusion magnétique, en se concentrant en particulier sur le concept de stellarator. Les stellarators utilisent des bobines externes pour produire un champ magnétique tridimensionnel (3D) qui confine un plasma thermonucléaire dans un tore, et ne nécessite donc pas, en général, de conduire un courant dans le plasma. C'est l'un des principaux avantages du stellarator, car l'absence de courants dans le plasma le rend plus stable que son cousin le tokamak. Cela a également un prix, car le stellarator doit briser l'axisymétrie pour permettre le confinement, ce qui complexifie l'ingénierie des machines.

L'efficacité des stellarators augmente avec  $\beta$ , *i.e.* la pression du plasma normalisée par la pression magnétique. Cependant, à une pression finie, le plasma génère des courants supplémentaires, et donc son propre champ magnétique, qui s'ajoute au champ magnétique du vide généré par les bobines externes. Le calcul du champ produit par les bobines externes n'est donc pas suffisant pour concevoir, optimiser, exploiter et interpréter les résultats expérimentaux. Au contraire, il est crucial de calculer l'équilibre magnétohydrodynamique (MHD), qui prend en compte les contributions non linéaires du plasma.

La topologie des lignes de champ magnétique des équilibres 3D présente un intérêt particulier. Ces équilibres sont en général composés de surfaces magnétiques imbriquées, d'îlots magnétiques et de lignes de champ chaotiques, ces deux dernières topologies étant, en général, préjudiciables au confinement du plasma. Des configurations avec de grandes régions remplies de surfaces magnétiques imbriquées sont donc préférables. Bien qu'il soit possible de concevoir des stellarators avec des surfaces magnétiques imbriquées dans le vide, la contribution du plasma au champ magnétique total finit par détruire les surfaces magnétiques soigneusement conçues à une valeur finie de  $\beta$ , fixant ainsi la valeur maximale réalisable de  $\beta$  dans les stellarators, et limitant leur performance.

Cette thèse étudie l'effet de la pression et des courants générés par le plasma sur la topologie des lignes de champ magnétique dans les équilibres MHD. Des outils pour calculer les équilibres MHD 3D avec des îlots magnétiques et des lignes de champ chaotiques sont présentés et étendus. En particulier, le *Stepped Pressure Equilibrium Code* (SPEC) est étendu pour permettre la prescription du profil de courant toroïdal, et est utilisé pour effectuer de large balayages de paramètres afin d'identifier la limite

## Résumé

---

$\beta$  d'équilibre dans différentes géométries de stellarator, en prenant en compte l'effet du courant de bootstrap. De nouvelles mesures sont développées pour évaluer la quantité de lignes de champ chaotiques dans un équilibre, et pour calculer leur impact sur le transport des particules. Un modèle analytique est ensuite proposé pour expliquer les résultats numériques et exposer les lois d'échelle sous-jacentes. Enfin, cette thèse explore l'utilisation de SIMSOPT pour optimiser la limite  $\beta$  d'équilibre d'un stellarator.

De manière générale, cette thèse contribue à mieux comprendre l'effet de la pression sur la topologie des lignes de champ magnétique dans les équilibres MHD, et son impact sur les performances du stellarator. En outre, cette thèse donne un aperçu des possibles optimisations pour améliorer les performances du stellarator et augmenter la limite  $\beta$  d'équilibre.

**Mots clefs :** fusion nucléaire, plasma, stellarator, magnetohydrodynamique, équilibre, chaos, optimisation

# Acronyms

<b>3D</b>	3-dimensional
<b>CPU</b>	central processing unit
<b>ECRH</b>	electron cyclotron resonance heating
<b>ECCD</b>	electron cyclotron current drive
<b>FOCUS</b>	flexible optimized coils using space curves
<b>GDP</b>	gross domestic product
<b>HBS</b>	high beta stellarator
<b>HDI</b>	human development index
<b>JET</b>	joint european torus
<b>LHD</b>	large helical device
<b>MHD</b>	magnetohydrodynamic
<b>MPI</b>	message passing interface
<b>MRxMHD</b>	multi-region relaxed magnetohydrodynamic
<b>NBCD</b>	neutron beam current drive
<b>NBI</b>	neutral beam injection
<b>NCSX</b>	national compact stellarator experiment
<b>QA</b>	quasi-axisymmetric
<b>QFM</b>	quadratic flux minimizing
<b>QH</b>	quasi-helically symmetric
<b>QI</b>	quasi-isodynamic

## Acronyms

---

<b>QP</b>	quasi-poloidally symmetric
<b>QS</b>	quasi-symmetry
<b>RFP</b>	reversed-field pinch
<b>SPEC</b>	stepped-pressure equilibrium code
<b>TFTR</b>	tokamak fusion test reactor
<b>UNDP</b>	United Nations development programme
<b>VMEC</b>	variational moment equilibrium code
<b>W7-A</b>	Wendelstein 7-A
<b>W7-AS</b>	Wendelstein 7-AS
<b>W7-X</b>	Wendelstein 7-X



# Contents

<b>Abstract (English/Français)</b>	<b>i</b>
<b>Acronyms</b>	<b>v</b>
<b>1 Introduction</b>	<b>1</b>
1.1 Energy consumption and quality of life . . . . .	1
1.2 The need for a new source of energy . . . . .	3
1.2.1 Renewable energies . . . . .	3
1.2.2 Fossil fuels . . . . .	4
1.2.3 Nuclear energy . . . . .	5
1.3 Nuclear fusion as a source of energy . . . . .	6
1.4 Magnetic fusion reactor concepts . . . . .	9
1.4.1 Single particle confinement . . . . .	10
1.4.2 Sources of rotational transform . . . . .	14
1.4.3 The tokamak concept . . . . .	16
1.4.4 The stellarator concept . . . . .	16
1.5 Magnetic field line topologies . . . . .	18
1.6 Magnetic equilibria . . . . .	23
1.7 Scope of this thesis . . . . .	25
<b>2 Three-dimensional magnetohydrodynamic equilibria</b>	<b>27</b>
2.1 Ideal MHD . . . . .	27
2.1.1 Figures of merit of magnetic equilibria . . . . .	29
2.1.2 Ideal magnetohydrodynamic (MHD) equilibrium solution in an axisymmetric cylinder . . . . .	32
2.1.3 Currents in ideal MHD equilibria . . . . .	34
2.1.4 Classes of well posed 3D magnetic equilibria . . . . .	37
2.2 Taylor state . . . . .	39
2.2.1 Solution in a plasma slab . . . . .	39
2.2.2 Solution in a plasma cylinder . . . . .	42
2.3 Multi-region relaxed magnetohydrodynamics . . . . .	43
2.3.1 Currents in MRxMHD . . . . .	44
2.4 Energy principles . . . . .	49
	vii

## Contents

---

2.4.1	Conservation of field line topology . . . . .	49
2.4.2	Ideal MHD equilibrium . . . . .	50
2.4.3	Taylor state . . . . .	53
2.4.4	MRxMHD . . . . .	54
2.5	Summary . . . . .	55
<b>3</b>	<b>The stepped-pressure equilibrium code</b>	<b>57</b>
3.1	stepped-pressure equilibrium code (SPEC) algorithm . . . . .	58
3.1.1	Parameterization of interfaces and magnetic field . . . . .	59
3.1.2	Beltrami solver . . . . .	61
3.1.3	Force solver . . . . .	64
3.1.4	Free-boundary iterations . . . . .	72
3.2	Implementation of the toroidal current constraint . . . . .	74
3.2.1	Constraining the toroidal current profiles in SPEC . . . . .	74
3.2.2	Force gradient . . . . .	77
3.2.3	Implementation details and parallelization . . . . .	78
3.2.4	Verification of the current constraint . . . . .	78
3.3	Implementation of a unique angle representation . . . . .	83
3.3.1	The Henneberg representation . . . . .	87
3.3.2	Construction of the Henneberg harmonics . . . . .	91
3.3.3	Implementation in SPEC . . . . .	92
3.3.4	Verification and comparison with the standard representation . .	94
3.4	Summary . . . . .	101
<b>4</b>	<b>Measures of magnetic field line topology</b>	<b>103</b>
4.1	Greene's residues . . . . .	104
4.1.1	Standard map . . . . .	107
4.2	Volume of chaos . . . . .	109
4.3	Fraction of effective parallel diffusion . . . . .	112
4.3.1	Measure of the radial magnetic field . . . . .	114
4.4	Summary . . . . .	115
<b>5</b>	<b>Equilibrium <math>\beta</math>-limits</b>	<b>117</b>
5.1	Bootstrap current . . . . .	117
5.1.1	Passing and trapped particles . . . . .	117
5.1.2	Banana and bootstrap current . . . . .	120
5.2	Equilibrium $\beta$ -limit in a classical stellarator . . . . .	121
5.2.1	Scans over $\hat{C}$ and $\beta$ . . . . .	124
5.2.2	Analytical prediction for the equilibrium $\beta$ -limits . . . . .	132
5.2.3	Dependence of the equilibrium $\beta$ -limit on design parameters . . .	134
5.3	Quasi-axisymmetric configuration . . . . .	136
5.3.1	Equilibrium $\beta$ -limit in a current-free quasi-axisymmetric (QA) stellarator . . . . .	138

5.3.2	Self-consistent bootstrap current and equilibrium $\beta$ -limit . . . . .	139
5.4	Summary . . . . .	145
<b>6</b>	<b>Optimization for nested magnetic surfaces</b>	<b>149</b>
6.1	Method . . . . .	150
6.2	Quasi-free-boundary optimization . . . . .	152
6.3	Perfectly conducting wall optimization . . . . .	154
6.4	Convergence and computation time . . . . .	156
6.5	Optimization of the equilibrium $\beta$ -limit . . . . .	159
6.6	Summary . . . . .	160
<b>7</b>	<b>Conclusion and outlooks</b>	<b>163</b>
7.1	Outlook . . . . .	165
<b>A</b>	<b>Appendices</b>	<b>167</b>
A.1	Boozer coordinates . . . . .	167
A.2	Toroidal coordinates . . . . .	171
A.3	SPEC spectral condensation . . . . .	172
A.4	Derivation of the Beltrami linear system . . . . .	173
A.5	Linear relation between surface currents and poloidal fluxes . . . . .	177
A.6	Free-boundary SPEC equilibrium computation with prescribed toroidal current profile . . . . .	178
A.7	Analytical derivation of SPEC force gradient in an axisymmetric cylinder	180
	<b>Acknowledgements</b>	<b>183</b>
	<b>Bibliography</b>	<b>185</b>
	<b>Curriculum Vitae</b>	



# 1 Introduction

In the future, nuclear fusion energy could become one additional source of energy, alongside existing energy sources, such as nuclear fission, renewable energies or fossil fuels. In this introduction, we discuss advantages and disadvantages of nuclear fusion as an energy source. We then focus on the stellarator, which is a nuclear fusion power plant concept that uses 3-dimensional (3D) magnetic fields to confine a thermonuclear plasma, in which fusion reactions take place.

## 1.1 Energy consumption and quality of life

The human development index (HDI) (UNDP, 1990) is a measure of human development, developed by the United Nations development programme (UNDP) as an alternative to traditional measures of development, such as the gross domestic product (GDP), which do not take into account other important dimensions of well-being such as health, education, and living standards. The HDI is a measure of the average achievements of a country in these three dimensions, and is calculated using life expectancy at birth, mean years of schooling, and gross national income per capita. On Figure 1.1, we show the HDI as a function of the average energy consumption per inhabitant, for a wide range of different countries. One striking observation is that the HDI grows with the energy consumption per inhabitant — in other words, the more energy is available, the higher the quality of life is. This is true up to an upper limit, where increasing the energy availability further has little to no effect on the life quality.

Indeed, energy is a critical factor in human development because it plays a vital role in supporting economic growth and improving people's quality of life. Access to energy allows people to participate in economic activities, access education and healthcare, and improve their living standards. For example, access to electricity can enable people to use lighting or other modern technologies that can improve their living conditions and increase their productivity. It can also increase access to basic services such as healthcare

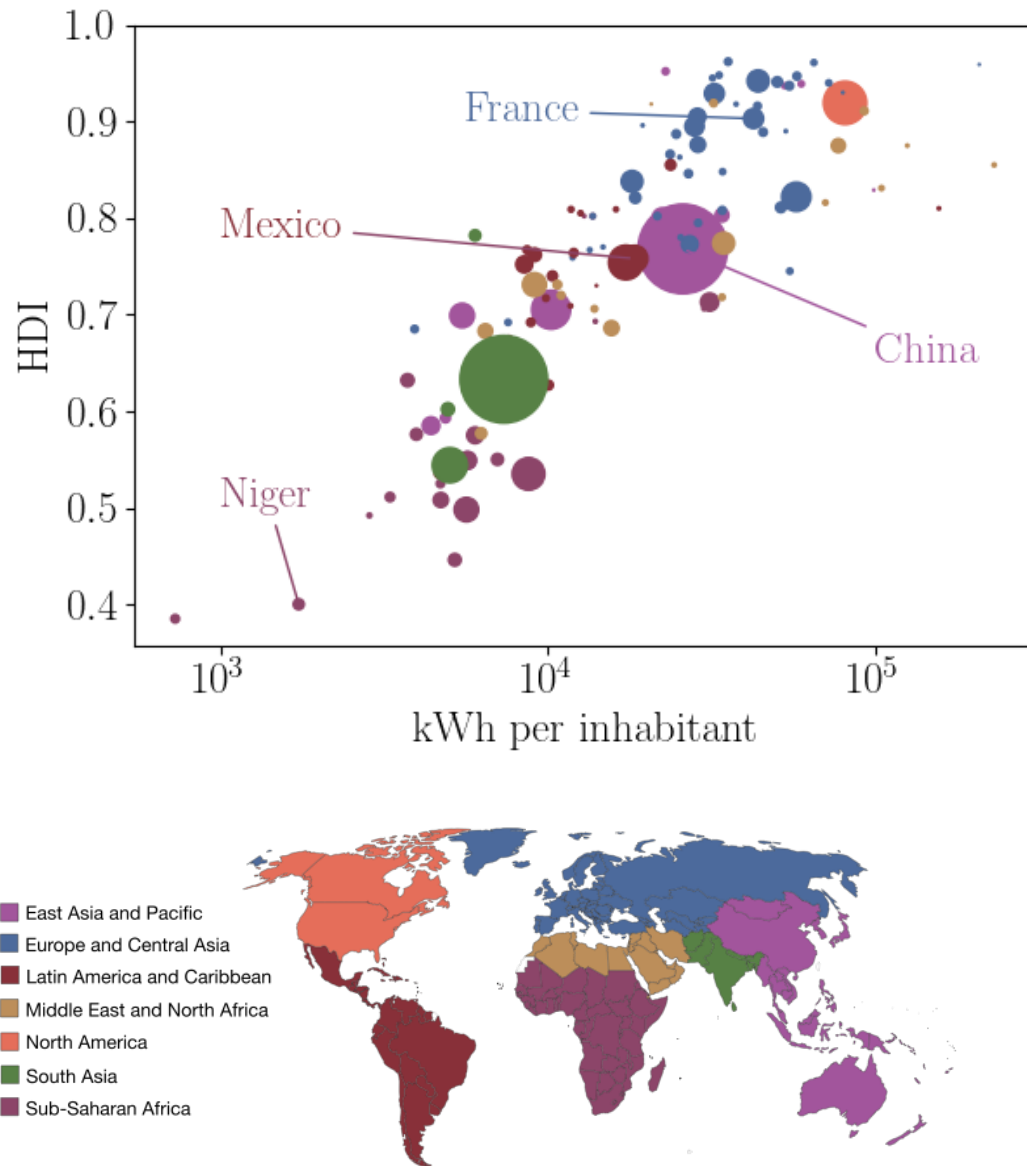


Figure 1.1: Top: HDI versus the average energy consumption per country's inhabitant. Size of dots are proportional to the total country population. Colors indicate the region the country belongs to, according to the World Bank classification, shown on the bottom map. The HDI data were obtained from the UNDP website ([hdr.undp.org](http://hdr.undp.org), consulted on the 26.12.2022), while the energy consumption in each country and its number of inhabitant were obtained from the World Bank website ([data.worldbank.org](http://data.worldbank.org), consulted on the 26.12.2022). The data dates from 2014; at the time of writing this thesis, there were no extensive dataset that postdates 2014.

and education. Similarly, the availability of energy can support economic development by enabling the production of goods and services, improving transportation, communication, and other essential activities.

While the HDI is a widely used measure of human development, it is important to recognize its limitations (McGillivray and White, 1993; Bagolin and Comim, 2008; Dervis and Klugman, 2011). The HDI is based on three indicators, but it does not capture many other important aspects of human well-being. There have been proposals for alternative measures of human development that address some of these limitations (see for example the work by Biggeri and Mauro (2018), and references therein), but none of these have gained the same level of attention as the HDI. It is also worth considering that there may be cultures where the concept of happiness and success does not align with having a high HDI. These philosophical debates about the limitations of the HDI have been ongoing for many years and are beyond the scope of this thesis. Here, we assume that development correlates with the HDI, and, according to Figure (1.1), with the available energy. It is thus primordial to develop an energy source that can support and sustain the World consumption.

## 1.2 The need for a new source of energy

There are three main categories of energy sources: renewable energies, fossil fuels, and nuclear energy. Each energy source has its own advantages and disadvantages, discussed briefly below. A more extensive discussion can be found in numerous books; for instance, see Parisi and Ball (2019).

### 1.2.1 Renewable energies

Renewable energies, such as solar, wind, hydropower, biomass, and geothermal, are not depleted once consumed and have been in use for centuries. Some examples of renewable energy include windmills powered by wind, or the use of solar panels to convert solar rays into electricity. In the recent years, these energy sources have gained increasing public and private traction as a mean to transition from a fossil energy based economy to a renewable economy, and fight the anthropologically generated climate change (Allan et al., 2021). Indeed, one of the main advantages of renewable energy sources is that they do not release additional greenhouse gases in the atmosphere, which is the main drive to climate change. In addition, renewable energies are widely available, even in the most remote areas of the globe. In consequence, the energy production can often be located close to the energy consumer. Being widely available also contributes to the geopolitical stability, as there are less dependencies between countries.

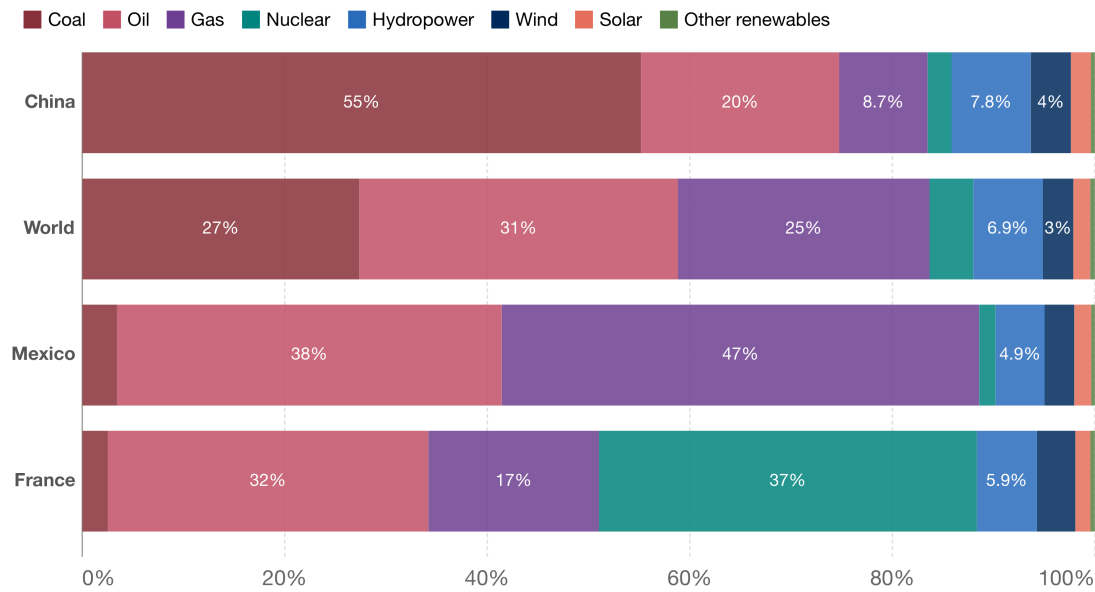


Figure 1.2: Energy consumption by source, for China, Mexico, France, and the World (Ritchie, 2021).

However, renewable energies also have disadvantages. Their energy density is relatively low, and large portion of land have to be used for power plants. For example, hydropower uses about  $0.12\text{m}^2\text{W}^{-1}$ , and solar panels  $0.11\text{m}^2\text{W}^{-1}$  (if installed on the ground) (Ritchie, 2022). This means that large areas have to be used for energy production, and large structures have to be built. Another challenge of renewable energy sources is their intermittent nature - solar panels only produce energy during the day and wind turbines only when there is wind. Energy storage, such as through water pumping, hydrogen production, or large batteries, can help mitigate this issue, but it comes with energy losses and can only be scaled up to meet global demand with massive infrastructural changes. As a result, renewable energies alone probably cannot provide a consistent base-load power supply to the grid. In 2021, about 12 % of the total consumed energy in the World was produced by renewable sources (see Figure 1.2).

### 1.2.2 Fossil fuels

The second class of energy source is the fossil fuels, such as coal, oil and natural gas. These fuels are formed from the remains of plants and animals over millions of years. Once extracted, these fuels can be burnt to generate electricity, power motors, or, in the case of oil, can be used as raw material to manufacture a wide variety of products, including plastic, chemicals and pharmaceuticals. These energy sources, thanks to their high power density, powered the industrial revolution, and are the foundation of our civilization in the 21st century. Fossil fuels do not suffer from the same shortcomings as renewable energy sources — they are not intermittent, and can easily be turned on and



off to follow the demand. Their land usage can be relatively small. For example, gas power plants use  $0.01\text{m}^2\text{W}^{-1}$ , about ten times less land than renewable energy sources.

They however have many downsides. First and foremost, the consumption of fossil fuels is one of the main sources of greenhouse gases, which contribute to global warming and climate change (Allan et al., 2021). Furthermore, the fuel often has to be transported from its extraction location to the power plant, which requires large infrastructures, and consumes energy. Fossil fuels are not globally well distributed, which is the source of multiple inequalities and to numerous geopolitical instabilities around the world. Finally, being non-renewable, there is only a limited amount of fossil fuels on Earth, which will eventually run out. Even if all disadvantages of fossil fuels are somehow avoided, our economy will have to transition away from fossil fuels because of their limited amount. Given the known reserves and the worldwide consumption of fossil fuels in 2020, coal supplies will be exhausted in 139 years, oil supplies in 54 years, and gas supplies in 49 years (BP, 2020). All these downsides motivate many to seek alternative energy sources, *i.e.* renewable and nuclear energy.

### 1.2.3 Nuclear energy

The third class of energy source is nuclear energy. Today, nuclear power plants produce electricity by leveraging the nuclear fission of Uranium. Fission power plants operation does not generate any greenhouse gases, is not intermittent, and is routinely used to generate electricity for base-load consumption. The large energy density of Uranium means that nuclear power plants have the best land use to energy production ratio, with  $2.3 \cdot 10^{-3}\text{m}^2\text{W}^{-1}$ . Tens of nuclear reactors can be enough to power a country. For instance, France produced 380TWh in 2021 with 56 reactors, about 70% of its electricity consumption (World Nuclear Association, 2023).

The Uranium is however not well distributed globally, and is mainly being mined in Kazakhstan, Canada, Australia and Niger. Again, as for fossil fuels, this uneven distribution of resources is the source of geopolitical instabilities. Uranium is not renewable, and the world will eventually run out of fuel. According to the World Nuclear Association (World Nuclear Association, 2022), the world's current annual consumption of uranium is around 61,000 tons per year. If this rate of consumption were to continue, the known land resources of uranium would last for around 90 years. However, this is a very rough estimate and does not take into account a number of factors that could affect the availability and use of uranium, such as the development of breeder reactors, changes in demand for electricity, or the exploitation of sea-water uranium (4.6 billion tons of uranium) (Dungan et al., 2017). Another downside to nuclear fission is that the reaction generates long-lived nuclear wastes dangerous for living organisms. In addition, the risk of loss of control of the power plant, such as during the infamous accidents of Chernobyl in 1986 and Fukushima in 2011, can lead to catastrophic releases of nuclear

material in the atmosphere. New power plant designs, with smaller amount of fission fuel in their core, and additional safety measures, can however make their use safer. Despite these disadvantages, nuclear fission is today the only energy source that can generate the amount of energy our civilization consumes without releasing greenhouse gases and without the inherent variability of renewable energies.

As of today, there are thus two pathways for future energy production without fossil fuels: either massive structures are built across the globe to generate enough renewable energy, or massive funding is invested in developing and constructing new generations of fission nuclear power plant, or a combination of both. An alternative is to develop a new source of energy: nuclear fusion.

### 1.3 Nuclear fusion as a source of energy

Nuclear fusion is the process of forming a nucleus from two, lighter nuclei. This is the process that powers all stars in the universe, and that is envisaged to power future fusion nuclear reactors. Nuclear *fusion* is the opposite of nuclear *fission*, where two nuclei are formed by breaking one, heavier nucleus, which is commonly used to power today's nuclear fission power plants. The advantages of nuclear fusion as a source of energy are numerous: the reaction does not generate any greenhouse gases, and, as for fission power and fossil fuels, is not intermittent. Nuclear fusion does not face the same problems as nuclear fission regarding nuclear wastes, as the reaction does not produce any radioactive byproducts. Finally, nuclear fusion reactors are intrinsically safe, as the reaction is not a chain reaction, and thus cannot undergo a core meltdown as nuclear fission reactors.

Nuclear fusion comes also with its own disadvantages. As of today, the proposed reactor prototypes are large and expensive to build, and require a large upfront investment. Reaching the conditions for fusion is extremely difficult, and there is no reactor concepts that have yet produced net electricity production. The National Ignition Facility (NIF) recently achieved a net power gain (Bishop, 2022) on the fusion fuel, but is still far from a net energy gain when taking into account all the power plant energy consumption. Tokamaks are also getting close to obtaining a net power gain, with for example the tokamak fusion test reactor (TFTR) tokamak, reaching a peak output over input power ratio of 0.27 (McGuire et al., 1995), or the joint european torus (JET) reaching an output over input power ratio of a third, sustained over five seconds (Gibney, 2022). Another disadvantage of nuclear fusion, is that the proposed reactor concepts require large amount of rare earth materials, for example to build superconducting coils.

In addition, while the fusion reaction does not generate any waste, high energy neutron fluxes are produced, that would inevitably activate the machine materials, and generate medium level radioactive waste (Gilbert et al., 2017, 2019; Bailey et al., 2021b,a; Gonzalez de Vicente et al., 2022). It is hard to predict exactly how much waste would be

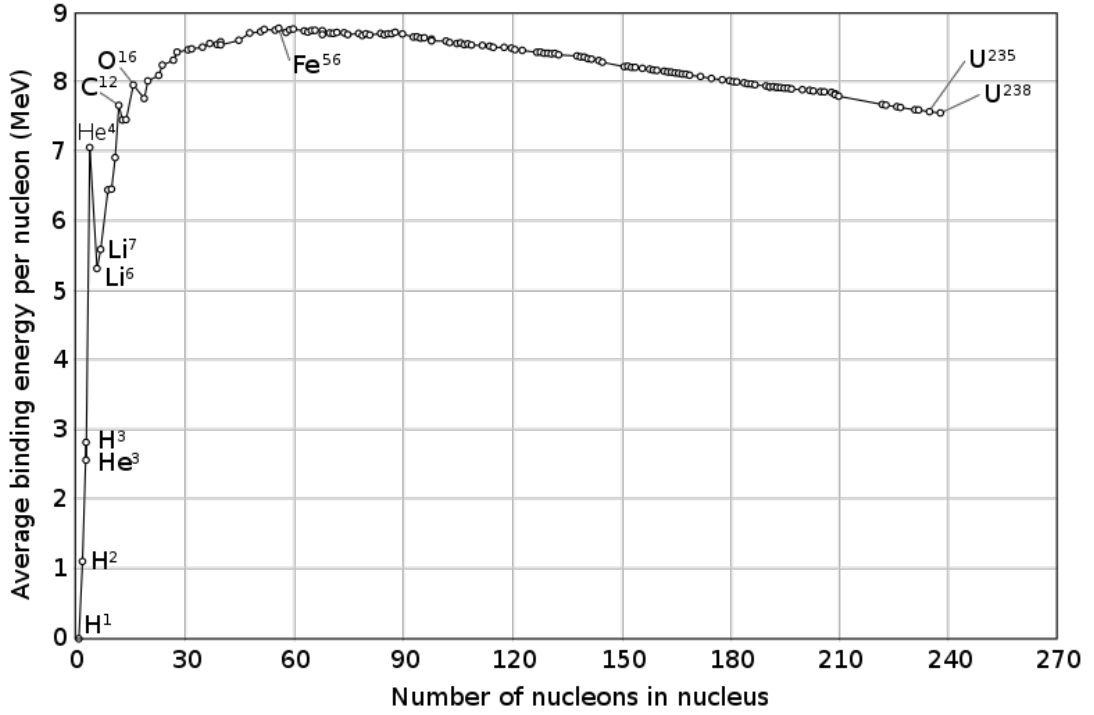
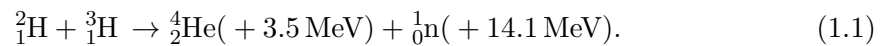


Figure 1.3: Binding energy per nucleon. Credits: Wikipedia Commons.

produced over the lifetime of a nuclear fusion reactor. Nevertheless, nuclear fusion, in comparison to fossil fuels and nuclear fission, would certainly produce smaller amounts of harmful waste.

Atomic nuclei are composed of neutron and protons, and are kept bound together by the strong nuclear interaction. The binding energy of the nucleon, defined as the minimum energy required to separate a nucleus as a collection of its nucleons, measures then how tightly bound a nucleus is. The binding energy per nucleon, shown on Figure 1.3, is low for hydrogen, grows with atomic number until reaching a maximum for the iron, and then decreases with increasing atomic number. In general, fusing two nuclei lighter than iron will then release energy, and so does breaking one nucleus heavier than iron.

Of particular interest for commercial fusion power plants is the fusion of deuterium  ${}^2_1\text{H}$  with tritium  ${}^3_1\text{H}$ , which generates a nucleus of helium  ${}^4_2\text{He}$  with 3.5MeV of kinetic energy, and a neutron  ${}^1_0\text{n}$  with 14.1MeV of kinetic energy (see Figure 1.4),



The neutron, which carries most of the reaction energy as kinetic energy, can be slowed down in water, which heats the water, creates steam, rotates turbines, and ultimately generates electricity. Deuterium can be found in sea water, at a concentration of 155

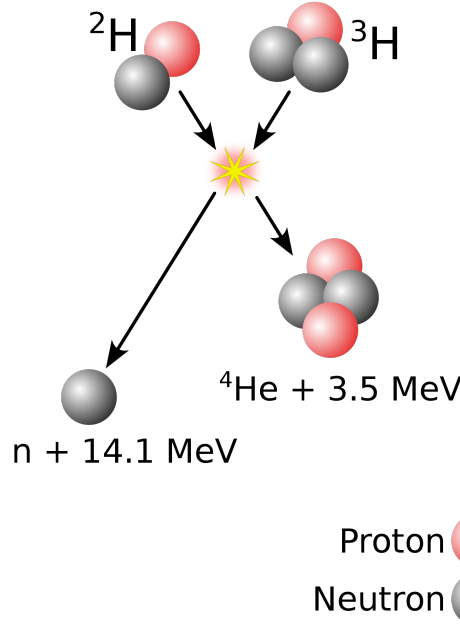


Figure 1.4: Sketch of a Deuterium-Tritium fusion reaction. Credits: Wikipedia Commons.

parts per millions (ppm), while Tritium is found in extremely small quantities on Earth, but can be produced by exposing lithium to a neutron flux,



Lithium 6 is found in natural lithium, at a concentration of 7.5%. Though lithium is not equally distributed on Earth, extraction from seawater (Zhao et al., 2019) could be a future solution to this issue. Among potential fusion reactions, the deuterium-tritium reaction is the most promising, because the reaction cross-section is the highest. Nevertheless, deuterium-tritium fusion reactions require a temperature of at least 10keV, *i.e.* about 100 millions degrees. At these temperatures, the fuel is a plasma, where electrons are stripped away from their nuclei. It is a collection of electrons and ions, interacting with one another, and with external electromagnetic fields. The challenge is then to confine the plasma for a sufficiently long time such that enough reactions have the time to occur. More specifically, we define the  $Q$ -factor as the ratio of power generated by the fusion reactions over the input power required to power the reactor,  $Q = P_{fus}/P_{in}$ . To get plasma ignition, *i.e.* to get a plasma where plasma self-heating via the helium  ${}^4_2\text{He}$  energy fully compensates the energy losses,  $Q = \infty$ , one can show that the fusion triple product, defined as the product of the plasma density,  $n$ , the plasma temperature,  $T$ , and the energy confinement time,  $\tau_E$ , has to satisfy the so-called Lawson criterion (Lawson, 1957; McNally, 1977),

$$nT\tau_E > 1.5 \cdot 10^{21} \text{keV s m}^{-3}. \quad (1.3)$$

In addition, the plasma temperature cannot be too low, otherwise the fusion cross-section would be too small and Bremsstrahlung losses would fully compensate the generated fusion power. Note that ignition, while desirable, is not a necessity, and a realistic nuclear fusion power plant could probably be economically profitable for large, but finite values of  $Q$ . From the Lawson criterion (1.3), one can identify two paths towards a nuclear fusion power plant: (i) inertial fusion, where one maximizes the density for a very short amount of time, but does not confine the plasma, or (ii) magnetic confinement, where one keeps comparatively lower densities, but increases the energy confinement time by confining the plasma using carefully designed magnetic fields. One particularly important parameter to assess the performance of a magnetic fusion reactor is the ratio between the plasma pressure  $p = nT$ , with the magnetic pressure, averaged over the plasma volume  $\mathcal{V}_P$ ,

$$\beta = \frac{1}{\mathcal{V}_P} \iiint_{\mathcal{V}_P} \frac{2\mu_0 p}{B^2} dv, \quad (1.4)$$

where  $\mu_0$  is the vacuum permeability,  $B$  is the magnetic field strength, and  $dv$  is a volume element. The fusion triple product, defined in Eq.(1.3), scales with  $\beta$  as

$$nT\tau_E \sim B^2 \beta \tau_E \sim \beta^{0.81}, \quad (1.5)$$

where the ISS04 scaling (Dinklage et al., 2007) was used to get the dependence of  $\tau_E$  on  $\beta$ . Increasing  $\beta$  thus increases the performance of the magnetic fusion reactor. We will now focus on one particular design of magnetic confinement reactor called the stellarator, which we explain in section 1.4.4.

## 1.4 Magnetic fusion reactor concepts

We discuss here how magnetic fields can be used to confine a plasma. The Virial theorem (Freidberg, 2014) states that a plasma cannot generate a magnetic field to confine itself; an external magnetic field needs to be provided. In general, electromagnets are used to generate the external magnetic field, though configurations with permanent magnets have also been proposed (Helander et al., 2019; Qian et al., 2022; Zhu et al., 2022). The first requirement on the magnetic field is that it should be able to confine a single charged particle inside the magnetic fusion reactor. We thus start by summarizing single particle dynamics in a magnetic field. Extensive discussion can be found in various textbooks; see for example Freidberg (2007) or Wesson (2011).

### 1.4.1 Single particle confinement

In a magnetic field, single particles move freely along the magnetic field lines, and rotate around the magnetic field line in the perpendicular plane, thereby describing a gyromotion, with radius  $\rho$  and frequency  $\omega$ , given by

$$\rho = \frac{v_{\perp}}{\omega} \quad (1.6)$$

$$\omega = \frac{|q|B}{m}, \quad (1.7)$$

where  $v_{\perp}$  is the velocity of the particle perpendicular to the magnetic field line,  $q$  is the charge of the particle,  $B$  is the magnetic field strength, and  $m$  is the particle's mass. The dynamics of single particles in a magnetic field can be greatly simplified if the magnetic field varies on scales larger than the gyroradius,  $\rho|\nabla B|/B = \delta_b \ll 1$ , and if the magnetic field variations in time are much slower than a gyroperiod,  $1/(\omega B)\partial B/\partial t = \delta_t \ll 1$ . The equations of motion can then be averaged over a gyroperiod, and the motion of the particle is described by the trajectory of its guiding center (see Figure 1.5).

We write the position of the particle as

$$\mathbf{x} = \mathbf{r} + \rho \mathbf{s}, \quad (1.8)$$

where  $\mathbf{r}$  is the position of the gyrocenter, and  $\mathbf{s}$  is a unit vector that rotates with the gyrophase  $\gamma$ . We require the gyroaverage of the second term on the right-hand side of Eq.(1.8) to be zero, *i.e.*

$$\langle \rho \mathbf{s} \rangle_{\gamma} = \frac{1}{2\pi} \int_0^{2\pi} \rho \mathbf{s} d\gamma = 0, \quad (1.9)$$

meaning that the vector  $\mathbf{r}$  is the gyroaveraged position  $\langle \mathbf{x} \rangle_{\gamma} = \langle \mathbf{r} \rangle_{\gamma} = \mathbf{r}$ , which we call the guiding center. The particle velocity is then

$$\mathbf{v} = \mathbf{u} + \frac{d\rho \mathbf{s}}{dt}, \quad (1.10)$$

with  $\mathbf{v} = d\mathbf{x}/dt$  the particle velocity, and  $\mathbf{u} = d\mathbf{r}/dt$  the guiding center velocity. Taking the equations of motion,

$$\frac{d\mathbf{v}}{dt} = \frac{q}{m}(\mathbf{E} + \mathbf{v} \times \mathbf{B}) \quad (1.11)$$

$$\frac{d\mathbf{x}}{dt} = \mathbf{v}, \quad (1.12)$$

with  $\mathbf{E}$  the electric field, one can show that, to the leading order in the expansion parameters  $(\delta_b, \delta_t)$ , the guiding center velocity in an electromagnetic field can be written as a combination of four different drifts (Wesson, 2011),

$$\mathbf{u} = \mathbf{V}_E + \mathbf{V}_{\nabla B} + \mathbf{V}_{\kappa} + \mathbf{V}_p + v_{\parallel} \hat{\mathbf{b}}, \quad (1.13)$$

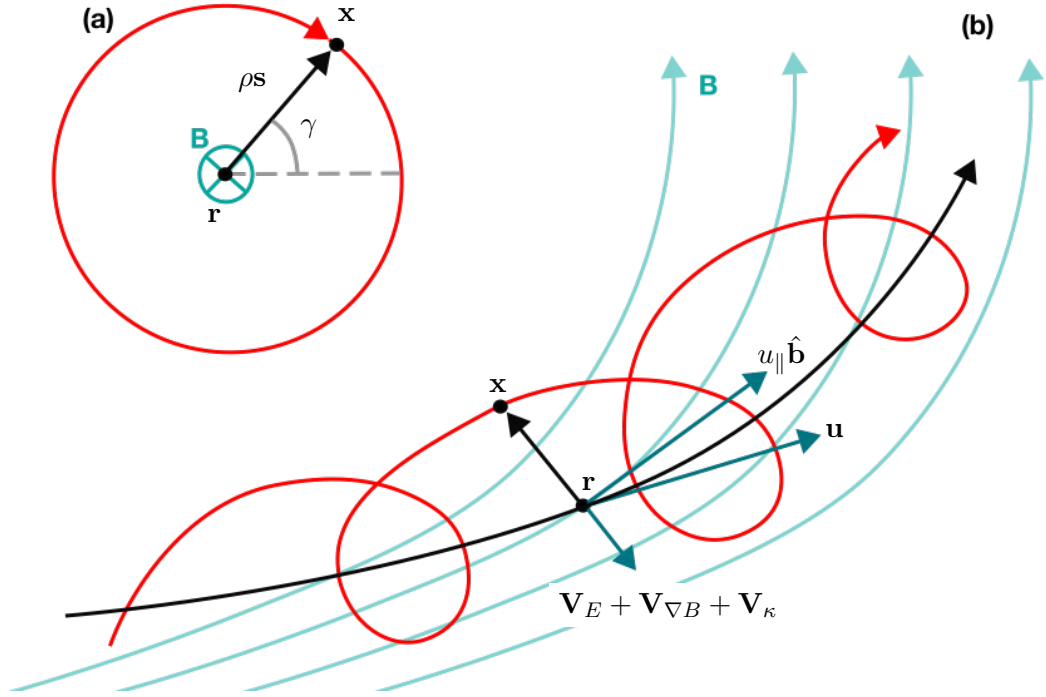


Figure 1.5: Sketch of a charged particle trajectory in a magnetic field. Figure (a) shows the trajectory in the plane perpendicular to the magnetic field, while Figure (b) shows the 3-dimensional trajectory. The light blue lines are the magnetic field lines, the red curve is the particle's trajectory, the black line is the particle's guiding center trajectory, and the dark blue arrows are the particle's velocity vectors.

with  $v_{\parallel}$  the particle velocity parallel to the magnetic field,  $\hat{\mathbf{b}} = \mathbf{B}/B$ , and

$$\text{The } \mathbf{E} \times \mathbf{B} \text{ drift} \quad \mathbf{V}_E = \frac{\mathbf{E} \times \mathbf{B}}{B^2} \quad (1.14)$$

$$\text{The } \nabla B \text{ drift} \quad \mathbf{V}_{\nabla B} = \pm \frac{v_{\perp}^2}{2\omega} \frac{\mathbf{B} \times \nabla B}{B^2} \quad (1.15)$$

$$\text{The curvature drift} \quad \mathbf{V}_{\kappa} = \pm \frac{v_{\parallel}^2}{\omega} \frac{\mathbf{B} \times \nabla B}{B^2} \quad (1.16)$$

$$\text{The polarization drift} \quad \mathbf{V}_p = \pm \frac{1}{\omega B} \frac{d\mathbf{E}_{\perp}}{dt}, \quad (1.17)$$

where the positive and negative signs are taken for ions and electrons respectively,  $\mathbf{E}_{\perp}$  is the electric field perpendicular to  $\mathbf{B}$ , and  $v_{\perp}$  is the particle velocity perpendicular to the magnetic field. Because of these drifts, the guiding center trajectory does not necessarily follow a magnetic field line (see Figure 1.5 (b)).

To confine a plasma, one must then design a magnetic field that does not cancel anywhere in space — otherwise the plasma would escape through this "hole" in the magnetic field. A straight magnetic field,  $\mathbf{B} = B_z \mathbf{e}_z$  confines a charged particle in the direction perpendicular to the magnetic field, but lets the particle move freely in the direction parallel to the magnetic field. We therefore also need the magnetic field to close upon itself. One could attempt to confine the plasma in a torus, using a purely toroidal magnetic field,  $\mathbf{B} = B \mathbf{e}_\phi$ , where  $\mathbf{e}_\phi$  is a unit vector in the toroidal direction. In this thesis, the toroidal direction is defined as the long way around the torus, and the poloidal direction as the short way around it (see Figure 1.6). To generate such a field, circular coils surrounding the plasma poloidally can be used. Assuming that a current  $I_c$  flows through the torus hole, we get, by Ampere's law,  $B \sim I_c / 2\pi R$ , with  $R$  the torus major radius, *i.e.* the magnetic field is stronger close to the torus hole, and weaker on the outer side of the machine, thereby defining a *high-field side* and a *low-field side* to the machine. In such magnetic field, a single particle will experience both a  $\nabla B$  drift and a curvature drift in the same vertical direction  $\mathbf{e}_z$ . Because both drift directions depend on the sign of the particle electric charge, electrons will drift in the opposite direction as the ions, and a charge separation will appear. A vertical electric field will emerge, which, due to the  $\mathbf{E} \times \mathbf{B}$  drift, will push the particles outside the torus, thereby losing confinement (see Figure 1.7). A purely toroidal magnetic field is thus not sufficient for confining a plasma.

Adding a poloidal component to the magnetic field solves this problem — due to their motion parallel to the magnetic field lines, particles will move from the upper portion of the torus to the lower one, and vice versa, which prevents the charge separation to occur, stops the electric field to emerge, and ultimately provides confinement within the torus to the particles. A magnetic field with a toroidal and a poloidal component wraps around the torus both in the poloidal and toroidal directions, foliating nested toroidal surfaces, thereafter called *magnetic surfaces*. One can then define a radial like coordinate  $r$ , with  $r = 0$  at the innermost surface in the plasma core, and  $r = a$  at the plasma edge, and such that  $\mathbf{B} \cdot \nabla r = 0$  on magnetic surfaces (see Figure 1.8). At  $r = 0$ , the magnetic surface is degenerate and is a curve, called the magnetic axis, which we assume here to be unique. The existence of magnetic surfaces is beneficial for particle confinement; thanks to the finite poloidal magnetic field, the guiding center drift averages to zero over a particle poloidal orbit, subsequently confining a particle to a magnetic surface, and preventing the particle to move radially towards the plasma edge. This property can be formally proven for instance in axisymmetric fields by looking at symmetries of the particle's Lagrangian (Helander and Sigmar, 2002). As we shall see in section 1.5, magnetic surfaces are however not guaranteed to exist, and different magnetic field line topologies can deteriorate confinement.



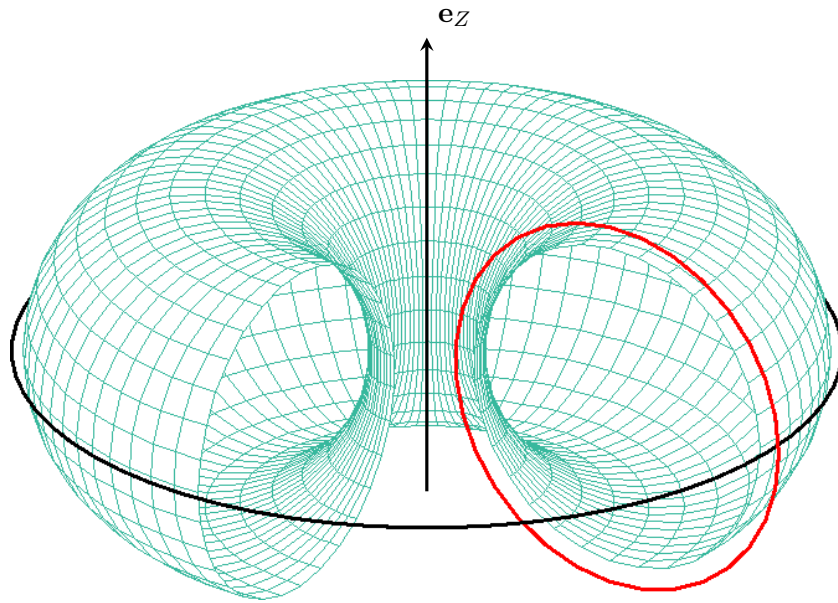


Figure 1.6: Sketch of a torus. The red line follows the poloidal direction, while the black line follows the toroidal direction.

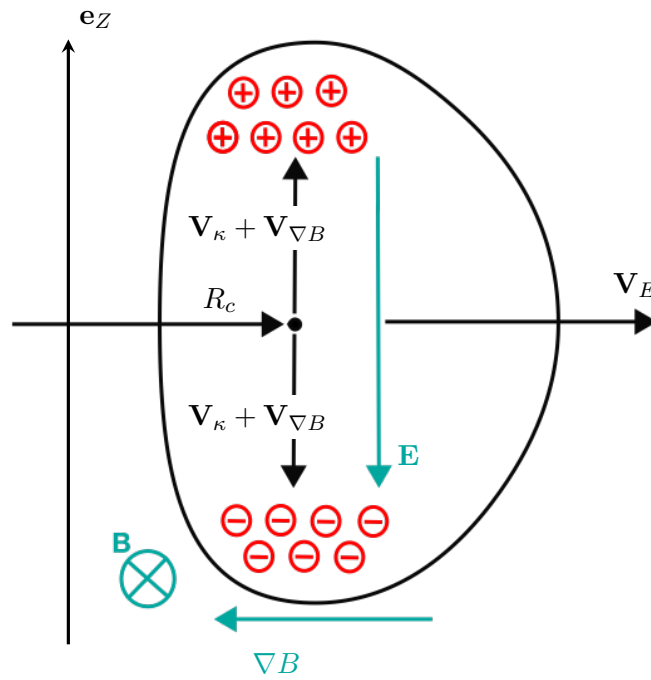


Figure 1.7: Sketch of the guiding center drifts in a purely toroidal magnetic field (zero rotational transform).

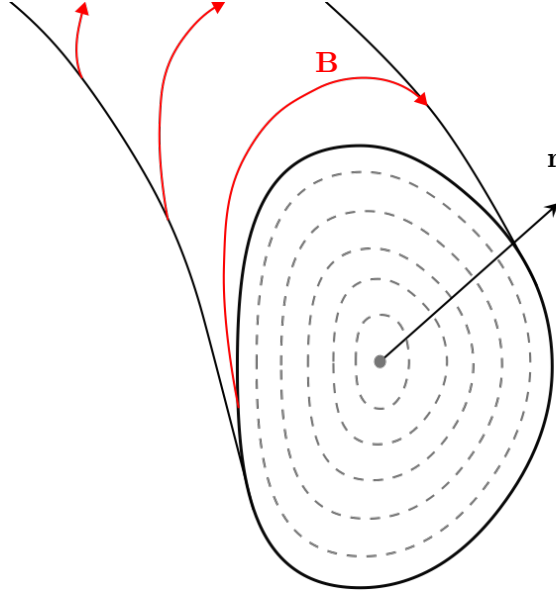


Figure 1.8: Sketch of a toroidal magnetic field with magnetic surfaces. In black: plasma boundary. Dashed gray lines: magnetic surfaces with  $r = \text{const}$ . Red arrow: magnetic field line on the plasma boundary.

The magnetic field line twist generated by the poloidal magnetic field is described mathematically by the *rotational transform*, defined as

$$\iota = \frac{\mathbf{B} \cdot \nabla \theta_s}{\mathbf{B} \cdot \nabla \phi}, \quad (1.18)$$

where  $\theta_s$  and  $\phi$  are the straight field line poloidal angle and toroidal angles respectively (see appendix A.1). The rotational transform is thus a measure of how many poloidal turns a magnetic field line does per toroidal turn around the torus. In the next section, we discuss the different ways rotational transform can be generated.

#### 1.4.2 Sources of rotational transform

We discuss now how a rotational transform can be generated in a toroidal magnetic configuration. The discussion is based on an expansion of the magnetostatic Maxwell's equations,  $\nabla \cdot \mathbf{B} = 0$  and  $\nabla \times \mathbf{B} = \mu_0 \mathbf{J}$ , around the magnetic axis, which we denote by  $\mathbf{x}_0(l)$ , with  $l$  the arc length. Assuming that magnetic field lines lie on magnetic surfaces, it can be shown that these surfaces must be ellipses close to the magnetic axis (Helander, 2014). An ellipse in the  $(x, y)$  plane can be parametrized by

$$\frac{x^2}{r_{min}^2} + \frac{y^2}{r_{max}^2} = 1, \quad (1.19)$$

with  $r_{min} = re^{-\eta/2}$  and  $r_{max} = re^{\eta/2}$  the minor and major radii of the ellipse respectively, which are controlled by the parameter  $\eta$  ( $\eta = 0$  for a circle). On the magnetic axis, we can define the so-called Frenet-Serret coordinate system ( $\hat{\mathbf{e}}_1, \hat{\mathbf{e}}_2, \hat{\mathbf{e}}_3$ ), with

$$\text{The tangent unit vector} \quad \hat{\mathbf{e}}_1 = \frac{d\mathbf{r}_0}{dl} = \frac{\mathbf{B}}{B} \equiv \hat{\mathbf{b}} \quad (1.20)$$

$$\text{The normal unit vector} \quad \hat{\mathbf{e}}_2 = \frac{1}{\kappa} \frac{d\hat{\mathbf{e}}_1}{dl} \quad (1.21)$$

$$\text{The binormal unit vector} \quad \hat{\mathbf{e}}_3 = \hat{\mathbf{e}}_1 \times \hat{\mathbf{e}}_2, \quad (1.22)$$

with  $\kappa$  the curvature. Furthermore,

$$\frac{d\hat{\mathbf{e}}_3}{dl} = -\tau \hat{\mathbf{e}}_2, \quad (1.23)$$

where  $\tau$  is the torsion, which measures the departure of a curve (here the magnetic axis) from a plane (here, the plane  $Z = \text{const}$ ). It can be shown (Mercier, 1964; Helander, 2014) that the rotational transform on the magnetic axis, defined as the  $\lim_{r \rightarrow 0} \iota$ , is

$$\iota_{axis} = \frac{1}{2\pi} \int \left[ \frac{\mu_0 J}{2B_0} - (\cosh \eta - 1)d' - \tau \right] \frac{dl}{\cosh \eta} - N, \quad (1.24)$$

with  $\mu_0$  the vacuum permeability,  $J$  and  $B_0$  the parallel current density and the magnetic field magnitude on the axis respectively,  $d$  the angle between the minor radius of the elliptical magnetic surfaces and the normal unit vector  $\hat{\mathbf{e}}_2$ , the prime denotes a derivative with respect to  $l$ , and  $N$  counts the number of rotations of  $\hat{\mathbf{e}}_2$  around the magnetic axis for one toroidal transit (see Figure 1.9).

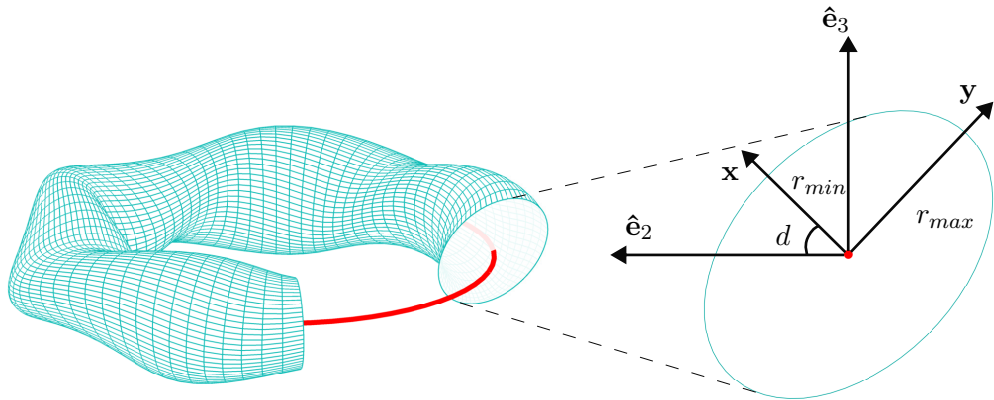


Figure 1.9: Illustration of an elliptical magnetic surface close to the magnetic axis. In red: the magnetic axis; In blue: the magnetic surface. The  $\mathbf{x}$  and  $\mathbf{y}$  axes are in the direction of the ellipse minor and major radii respectively.

The rotational transform can thus be generated by three mechanisms: either (i) by driving a toroidal current  $J \neq 0$  in the plasma, or (ii) by shaping the magnetic surfaces close to the magnetic axis as ellipses that rotate around the magnetic axis as the toroidal angle changes, namely  $\eta \neq 0$  and  $d' \neq 0 \forall \phi$ , or (iii) by having magnetic axis torsion, *i.e.*  $\tau \neq 0$ . The two main classes of magnetic confinement devices, the tokamak and the stellarator, do not use the same mechanisms to generate rotational transform. This is discussed in the following section.

### 1.4.3 The tokamak concept

The tokamak, arguably the most advanced concept for a magnetic fusion reactor, uses generally an external transformer to drive a strong toroidal current in the plasma in order to generate the rotational transform (see Figure 1.10). With regard to Eq.(1.24), the tokamak thus uses the first mechanism,  $J \neq 0$ . Note that there are tokamak scenarios, *i.e.* the so-called *advanced scenarios*, that would not need any inductively-driven plasma current, and instead would rely on currents externally driven by electromagnetic waves and neutral beam injection, and on currents self-generated by the plasma (Taylor, 1997). The tokamak greatest advantage is that the configuration is axisymmetric — *i.e.* there are no dependencies on the toroidal position. This property implies good single particle confinement, and, from an engineering point of view, makes the tokamak a relatively simple reactor to build. Driving a strong toroidal current comes however at a cost — if the current is driven by an external transformer, the operation of the machine is pulsed, forbidding continuous operation and generating stress on the different components, ultimately reducing the lifetime of the machine. The current in the plasma is also a source of free energy, which can drive violent instabilities that have to be controlled. Many types of instabilities can ultimately cause plasma disruptions, characterized by a sudden loss of the plasma confinement. Tokamaks therefore require extensive diagnostics and real time control for operation (Degraeve et al., 2022). We can summarize the tokamak concept as a device that is relatively simple to build, but complex to operate.

### 1.4.4 The stellarator concept

The stellarator uses all three mechanisms to generate the rotational transform. In general, the stellarator mainly relies on the ellipticity of the magnetic surfaces and their rotation,  $\eta \neq 0$  and  $d' \neq 0$ , and on the magnetic axis torsion,  $\tau \neq 0$ . This means that the magnetic field can be entirely generated by external coils, there is no need for a central transformer, and the machine can be operated continuously. There are no current-driven instabilities (unless the plasma generates a large current by itself), meaning that disruptions are less common in stellarators than in tokamaks. The rotation of the elliptical magnetic surfaces and the magnetic axis torsion come however at the cost of losing axisymmetry: the configuration is now fully 3-dimensional (see of Figure 1.11). Single particle confinement

is in general worse than in tokamaks, and extensive additional optimization is required to obtain good particle confinement properties. In particular, fast ions confinement, *i.e.* the confinement of fusion-born helium ions, is a great challenge in stellarators (Faustin et al., 2016a,b; Velasco et al., 2021). In addition, the 3-dimensionality of the coils and their necessary precise positioning is a formidable engineering challenge, and can increase the cost of the machine substantially. The national compact stellarator experiment (NCSX),

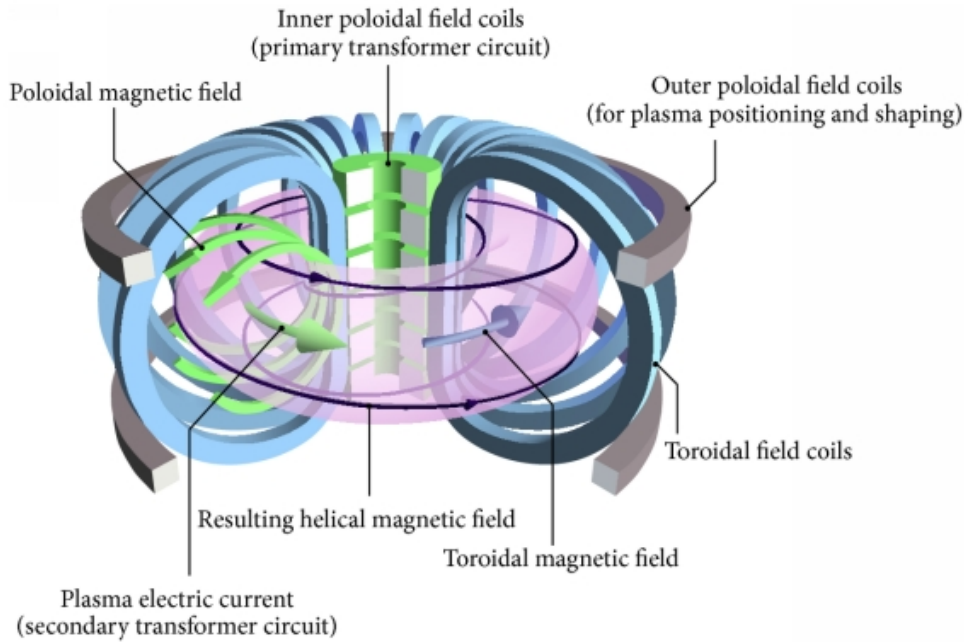


Figure 1.10: Schematic of a tokamak (Li et al., 2014).

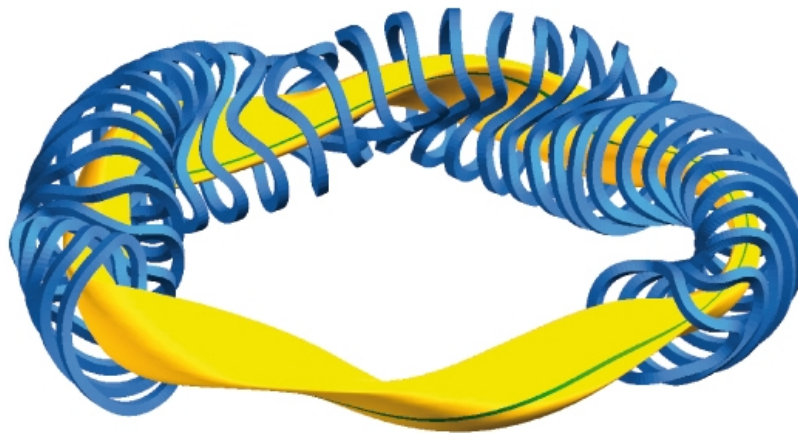


Figure 1.11: Schematic of a stellarator, credits: Max-Planck Institut für Plasmaphysik, <https://www.ipp.mpg.de/en>.

for example, was canceled in May 2008 (Orbach, 2008), due to "the budget increases, schedule delays and continuing uncertainties" of the NCSX experiment. The stellarator concept can then be summarized as a machine that is hard to build but easy to operate.

In addition, thanks to the 3D nature of stellarators, their configuration space is orders of magnitude greater than tokamaks. Stellarators can thus be optimized for different properties, for example quasi-symmetry (QS) (Landreman and Paul, 2022), quasi-isodynamicity (Goodman et al., 2022), or low turbulent transport (Xanthopoulos et al., 2014). For instance, the Wendelstein 7-X (W7-X) stellarator built in Greifswald, Germany, has been optimized for low neo-classical transport (*i.e.* non-turbulent transport), which has been verified experimentally (Beidler et al., 2021). Recent advances in stellarator optimization improved the confinement properties of stellarators beyond what can be achieved by a tokamak (Landreman et al., 2022).

One of the challenges related to stellarators is related to the topology of their magnetic field lines. In tokamaks, it can be shown (Grad and Rubin, 1958; Shafranov, 1966; Freidberg, 2014) that all magnetic field lines lie on toroidally nested magnetic surfaces, which is ideal for particle and energy confinement. In stellarators, other field line topologies can be present, as discussed in the next section.

### 1.5 Magnetic field line topologies

We discuss here the magnetic field line topologies, following the discussion by Helander (2014). As  $\nabla \cdot \mathbf{B} = 0$ , any magnetic field can be expressed as the curl of a magnetic potential,  $\mathbf{B} = \nabla \times \mathbf{A}$ . Working with general toroidal coordinates  $(r, \theta, \phi)$ , with  $\theta$  and  $\phi$  the poloidal and toroidal angles respectively, we can write

$$\mathbf{A} = A_r \nabla r + A_\theta \nabla \theta + A_\phi \nabla \phi. \quad (1.25)$$

We define

$$g(r, \theta, \phi) = \int_c^r A_r dr \quad (1.26)$$

$$\psi = A_\theta - \frac{\partial g}{\partial \theta} \quad (1.27)$$

$$\chi = -A_\phi + \frac{\partial g}{\partial \phi}, \quad (1.28)$$

and thus we obtain the Clebsch representation of the magnetic field,

$$\mathbf{A} = \psi \nabla \theta - \chi \nabla \phi + \nabla g \quad (1.29)$$

$$\mathbf{B} = \nabla \psi \times \nabla \theta + \nabla \phi \times \nabla \chi. \quad (1.30)$$

Note that the magnetic field representation (1.30) is completely general, and does not assume the existence of magnetic surfaces. Now, consider a particle of charge  $Ze$  and mass  $m$ . Its Lagrangian is given by

$$\mathcal{L}_p = \frac{mv^2}{2} + Ze\mathbf{A} \cdot \mathbf{v} - Ze\Phi, \quad (1.31)$$

with  $\Phi$  the electrostatic potential. If  $\Phi = 0$  and we take the limit  $m \rightarrow 0$ , the particle exactly follows magnetic field lines. The particle's trajectory, and therefore the magnetic field line, minimizes the action  $S_p$ , with

$$S_p = \int \mathcal{L}_p dt = Ze \int \mathbf{A} \cdot \mathbf{v} dt = Ze \int \mathbf{A} \cdot d\mathbf{r} = Ze \int \psi d\theta - \chi d\phi, \quad (1.32)$$

where the  $\nabla g \cdot d\mathbf{r}$  term has been dropped since it only adds constants to the action and therefore vanishes once the variation of the action is evaluated. The action (1.32) has the familiar form of an action expressed from a Hamiltonian  $H(p, q, t)$ , where  $(q, p)$  are the generalized coordinate and momentum, and

$$S = \int p dq - H dt, \quad (1.33)$$

which is stationary when the Hamilton's equations are satisfied. Going back to the action (1.32), we identify  $\phi$  as the time  $t$ ,  $\chi$  as the Hamiltonian  $H$ ,  $\theta$  as the generalized coordinate  $q$ , and  $\psi$  as the generalized momentum  $p$ . The action is thus stationary when

$$\frac{d\psi}{d\phi} = -\frac{\partial\chi}{\partial\theta} \quad (1.34)$$

$$\frac{d\theta}{d\phi} = \frac{\partial\chi}{\partial\psi}, \quad (1.35)$$

where the derivatives are taken along the field lines. Eqs.(1.34)-(1.35) define the trajectory of our imaginary massless particle, and therefore define the magnetic field line. Magnetic field lines thus have a Hamiltonian structure, if one considers the advancement of the toroidal angle  $\phi$  as time. This important result allows the application of all the non-linear theories of dynamical systems to study magnetic field lines; see for example the review paper by Meiss (1992). In particular, it implies the existence of magnetic field lines that do not lie on nested magnetic surfaces. We discuss now a simple example of a so-called *magnetic island*.

Magnetic surfaces exist in the case where  $\chi = \chi(\psi)$ , since then  $\mathbf{B} \cdot \nabla\psi = 0$ , and thus the surface  $\psi(r = \text{const}, \theta, \phi)$  is a magnetic surface. Under the condition  $\mathbf{B} \cdot \nabla\psi = 0$ , the function  $\psi$  can then be used as a magnetic surface label, and acts as a radial coordinate. We now focus on a rational surface  $\psi = \psi_0$  where  $\iota(\psi_0) = d\chi_0/d\psi = n/m$ , with  $m, n \in \mathbb{N}$ , and consider the perturbed Hamiltonian

$$\chi = \chi_0(\psi) + \chi_1(\psi) \cos(m\alpha) = \chi_0(\psi) + f(\psi, \alpha), \quad (1.36)$$

## Chapter 1. Introduction

---

with  $\alpha = \theta - \iota(\psi_0)\phi$ . The function  $\chi$  thus only depends on  $\psi$  and  $\alpha$  and we can write the Hamiltonian in the coordinate system  $(\psi, \alpha)$ ,

$$H(\psi, \alpha, \phi) = \chi_0(\psi) + f(\psi, \alpha) - \iota(\psi_0)(\psi - \psi_0), \quad (1.37)$$

where the last term has been included to keep the Hamiltonian structure of the field line equations, *i.e.*

$$\frac{d\psi}{d\phi} = -\frac{\partial\chi}{\partial\theta} = -\frac{\partial f}{\partial\alpha} \frac{\partial\alpha}{\partial\theta} = -\frac{\partial f}{\partial\alpha} = -\frac{\partial H}{\partial\alpha} \quad (1.38)$$

$$\frac{d\alpha}{d\phi} = \frac{d\theta}{d\phi} - \iota(\psi_0) = \frac{\partial\chi}{\partial\psi} - \iota(\psi_0) = \frac{\partial H}{\partial\psi}. \quad (1.39)$$

Notice that the Hamiltonian (1.37) is independent of  $\phi$ ; we therefore have an autonomous (*i.e.* "time-independent") Hamiltonian, which guarantees the existence of surfaces. We assume that the amplitude of the perturbation to the Hamiltonian,  $\chi_1$ , is constant around the resonance,  $\chi_1'(\psi_0) = 0$ , and therefore,  $dH/d\psi = 0$  at  $\psi = \psi_0$ . Making a Taylor expansion of  $H$  around  $\psi_0$ , we thus obtain

$$H = \chi_0(\psi_0) + f(\psi_0, \alpha) + \frac{\chi''(\psi_0)(\psi - \psi_0)^2}{2} + \mathcal{O}(\psi^3) \quad (1.40)$$

$$= \frac{\chi''(\psi_0)(\psi - \psi_0)^2}{2} + \chi_1(\psi_0) \cos(m\alpha) + \mathcal{O}(\psi^3), \quad (1.41)$$

where we are free to set the constant  $\chi_0(\psi_0) = 0$  as it has no impact on the magnetic field line equations. Note that by defining  $p_\gamma = \sqrt{\chi''(\psi_0)}(\psi - \psi_0)$ ,  $g = \chi_1(\psi_0)$ ,  $\gamma = m\alpha$ , and neglecting the terms  $\mathcal{O}(\psi^3)$ , the Hamiltonian (1.41) becomes

$$U(\gamma, p_\gamma) = \frac{p_\gamma^2}{2} - g \cos \gamma, \quad (1.42)$$

which is the Hamiltonian of a classical pendulum of unit mass and unit length, with  $g$  the gravitational acceleration,  $\gamma$  the angle between the  $-\mathbf{g}$  vector and the pendulum axis, and  $p_\gamma = \dot{\gamma}$  the canonical momentum. Analyzing the phase space of the pendulum is thus equivalent to looking at the phase space of the Hamiltonian (1.41). We plot the constant- $U$  curves in the  $(\gamma, p_\gamma)$  phase space in Figure 1.12. As time evolves, the pendulum will follow the trajectory  $U = E$ , where  $E$  is the mechanical energy of the pendulum. The corresponding interpretation for the magnetic field line is that as the toroidal angle  $\phi$  increases, the magnetic field line will map the trajectory  $H = \text{const}$ , shown in black on Figure 1.12.

The phase space is separated in two regions — one region is enclosed by the *separatrix* (in red), while the other is not. The field lines enclosed by the separatrix form a so-called *magnetic island*. The separatrix passes through the point  $\psi = \psi_0$ ,  $\alpha = 0$ , meaning that on the separatrix,  $H = \chi_1$ . At  $m\alpha = \pi$ , the separatrix extends to  $\psi - \psi_0 = \pm\sqrt{4\chi_1/\chi_0''}$ .



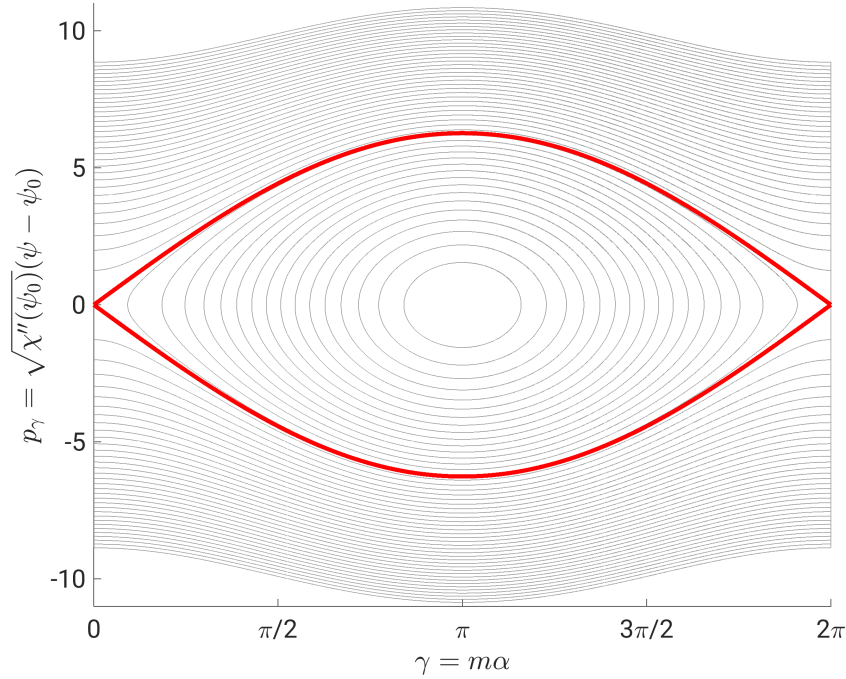


Figure 1.12: Phase space of a pendulum. In black: pendulum trajectories, defined as constant-energy curves. In red: separatrix.

Finally, noting that  $\chi_0'' = \iota'(\psi_0)$ , we find that the island width is given by

$$\Delta\psi = 4\sqrt{\frac{\chi_1}{\iota'(\chi_0)}}. \quad (1.43)$$

We thus see that in case of a perturbed Hamiltonian as described by Eq.(1.37), the existence of nested magnetic surfaces everywhere is not guaranteed. The existence of magnetic surfaces and magnetic islands has been experimentally verified, for instance via injection of an electron beam in a low-density neutral gas in the W7-X stellarator (Pedersen et al., 2016), which allowed the precise measurement of the position of magnetic surfaces (Figure 1.13a) and of the magnetic island chain at the plasma edge (Figure 1.13b). In the right panel of Figure 1.13, a single magnetic field line traces out 6 magnetic islands, where each island has the same structure as the magnetic island shown in Figure 1.12.

If the field line Hamiltonian is perturbed by more than a single harmonic as in the example (1.37), the analogy with the classical pendulum breaks down. If there are multiple rational surfaces that are excited by different harmonics, multiple island chains can open at different  $\psi$  coordinates. When two island chains overlap, the magnetic field lines become chaotic (Chirikov, 1979), and the magnetic field can fill ergodically a finite volume. To study these complicated magnetic fields, one can look at their Poincaré sections. Suppose that a magnetic field  $\mathbf{B}$  is known everywhere, *i.e.* at any position

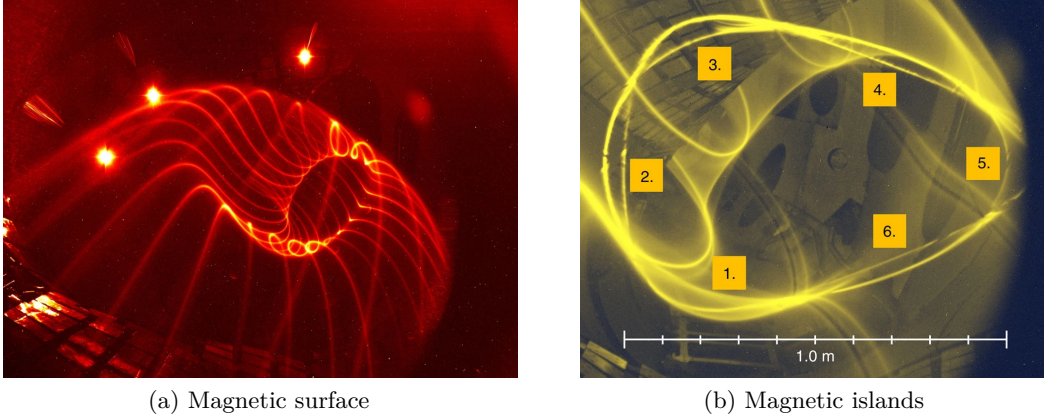


Figure 1.13: Measurement of the field line topology in W7-X via injection of an electron beam in a dilute gas (Pedersen et al., 2016).

$(r, \theta, \phi)$ . Magnetic field lines are followed by solving the differential equation

$$\frac{d\theta}{d\phi} = \frac{\mathbf{B} \cdot \nabla \theta}{\mathbf{B} \cdot \nabla \phi} \quad (1.44)$$

$$\frac{dr}{d\phi} = \frac{\mathbf{B} \cdot \nabla r}{\mathbf{B} \cdot \nabla \phi}, \quad (1.45)$$

with initial condition  $r(0) = r_0$ ,  $\theta(0) = \theta_0$  where  $(r_0, \theta_0)$  are the initial field line coordinates at  $\phi = 0$ . An example of a field line followed on a magnetic surface is shown on Figure 1.14a. The field line is followed for multiple toroidal transits, and its position  $(r_k, \theta_k)$  is saved whenever  $\phi = 2k\pi$ , with  $k \in \mathbb{N}$ . The Poincaré section is then a collection of  $(r_k, z_k)_{k=\{1, \dots, N\}}$  positions, plotted on the  $(R, Z)$  plane. An example of a Poincaré section with different field line topologies is shown on Figure 1.14b.

Magnetic field line topologies are intrinsically connected to particle confinement. At zeroth order in the Larmor radius, particles follow magnetic field lines and are constrained to remain on magnetic surfaces, *i.e.* magnetic surfaces provide radial confinement. Magnetic islands and magnetic field line chaos, on the other hand, allow particles to move in the radial direction, thereby causing a flattening of the pressure profile, which lowers the peak pressure in the plasma core, and affects the reactor's performance. Note that structures in regions occupied by chaotic field lines can still potentially support pressure gradients (Hudson and Breslau, 2008). In general however, the presence of magnetic islands and magnetic field line chaos will lower the peak pressure in the plasma core, and are thus undesirable.

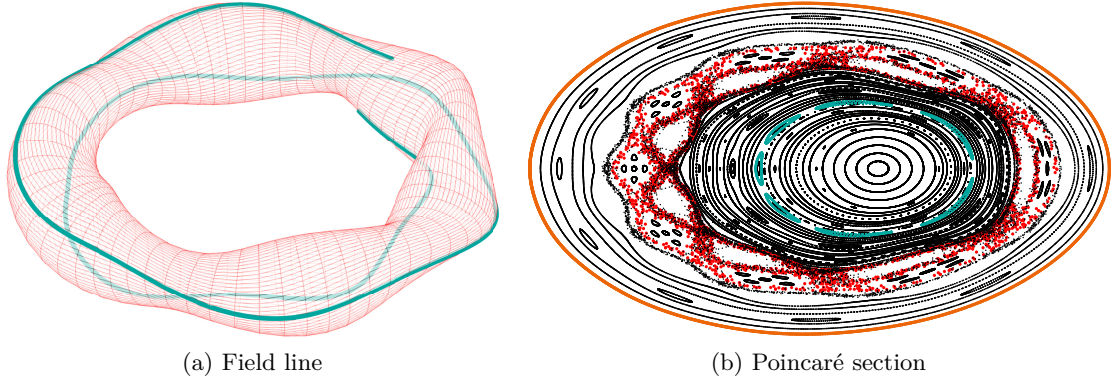


Figure 1.14: Example of field line tracing and Poincaré section in a rotating ellipse. Left: 3D mesh of a magnetic surface (red) and a traced field line over two periods (blue). Right: Poincaré section of multiple field lines, with, in particular, a magnetic surface (orange), a magnetic island (blue) and a chaotic field line (red).

## 1.6 Magnetic equilibria

It is crucial for stellarator design and operation to compute accurately the magnetic field in the plasma. This is however not a trivial task, as one has to take into account both the magnetic field produced by coils external to the plasma,  $\mathbf{B}^c$ , and the magnetic field generated by the plasma itself,  $\mathbf{B}^p$ . Indeed, complex non-linear interactions generate currents in the plasma. Consider the single particle guiding center drifts described in 1.4.1. All drift directions, at the exception of the  $\mathbf{E} \times \mathbf{B}$  drift, depend on the particle charge, and therefore generate a finite macroscopic current density  $\mathbf{J}$ . This macroscopic current density will then generate its own contribution to the total magnetic field.

Magnetic equilibria, as will be discussed in chapter 2, are steady state magnetic fields where the macroscopic plasma currents are self consistent with the magnetic field. Over the years, numerous codes have been developed to compute magnetic equilibria. The goal of equilibrium codes is to compute the magnetic field  $\mathbf{B}$ , given, for example, the pressure and the rotational transform in the plasma. Boundary conditions can be either given by the plasma shape (fixed-boundary calculation), or by information on the vacuum magnetic field generated by the coils (free-boundary calculation, Henneberg et al. (2021b)). As discussed in section 1.4.4, stellarators do not assume axisymmetry as tokamaks. Therefore their magnetic equilibria are three dimensional, and can contain magnetic islands and magnetic field line chaos, which greatly complicates their computation. Examples of 3D equilibrium codes are the variational moment equilibrium code (VMEC) (Hirshman, 1983), BETAS (Betancourt, 1988), NSTAB (Taylor, 1994), PIES (Greenside et al., 1989), HINT2 (Suzuki et al., 2006), SIESTA (Hirshman et al., 2011), SPEC (Hudson et al., 2012a, 2020), GVEC (F. Hindenlang, private communication), BIEST (O’Neil and Cerfon, 2018) or DESC (Dudt and Kolemen, 2020).

As an example of magnetic equilibria, we show on Figure 1.15 the Poincaré section of magnetic equilibria calculated in a 3D quasisymmetric stellarator configuration designed by Henneberg et al. (2019). Three different equilibria at different  $\beta$  are evaluated. The left plot is the magnetic equilibrium evaluated at  $\beta = 0.08\%$ , and in this example the plasma is filled with magnetic surfaces. The middle plot is a magnetic equilibrium at  $\beta = 1.72\%$ ; the magnetic equilibrium is only weakly affected by the plasma generated currents. On the right plot, the magnetic equilibrium is evaluated at a higher  $\beta$ , *i.e.*  $\beta = 3\%$ . We see that the magnetic equilibrium is strongly affected by the increase in  $\beta$ , as local current densities are generated by the plasma when  $\beta$  increases. These current densities then generate magnetic fields that perturb the magnetic field generated by the coils. On the right plot of Figure 1.15, the magnetic field is sufficiently perturbed for magnetic islands and chaos to emerge. In this perturbed equilibrium, the magnetic islands and magnetic field line chaos may be less efficient at confining particles than magnetic surfaces. Additional power deposited in the plasma, for example by electron cyclotron resonance heating (ECRH) or neutral beam injection (NBI), may thus leak through the damaged magnetic surfaces, and limit the maximum reachable  $\beta$  in the stellarator. This process of loss of magnetic surfaces therefore defines a so-called *equilibrium  $\beta$ -limit*, above which the magnetic surfaces present in low- $\beta$  equilibria are lost, and the radial confinement of particles is degraded in the regions of magnetic field line chaos and magnetic islands. In these regions, the pressure and temperature profiles might flatten, thereby preventing the creation of large density and pressure peaks in the plasma core, and ultimately reducing the maximum achievable fusion triple product in a stellarator.

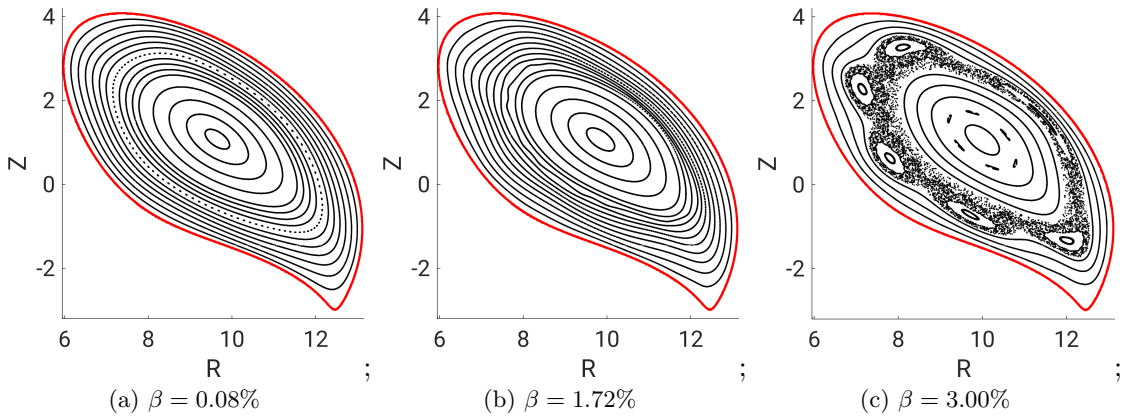


Figure 1.15: Poincaré section of three different 3D magnetic equilibria at different  $\beta$  (Henneberg et al., 2019). Here  $R$  and  $Z$  are the usual cylindrical coordinates.

There are, of course, other processes that can limit the maximum  $\beta$  in a stellarator. For example, turbulence generated by micro-instabilities in the plasma will generate a finite radial transport of particle across magnetic surfaces. The macro-stability of the equilibrium might also set a stability  $\beta$ -limit. However, as stellarators have often small currents in the plasma in comparison to tokamaks, their plasmas tend to be less prone to current-driven instabilities. The equilibrium  $\beta$ -limit is thus thought to be one of the main causes limiting the maximum  $\beta$  in stellarators (Helander, 2014; Suzuki et al., 2020), in conjunction with the stability  $\beta$ -limit set by pressure-driven macro-instabilities.

## 1.7 Scope of this thesis

In this introductory chapter, we made the case that nuclear fusion energy could become a clean, safe and abundant future energy source. Among nuclear fusion reactor concepts, we introduced in particular the stellarator, and discussed the importance of stellarator optimization — stellarators need to be optimized to obtain sufficiently good single particle confinement. We also discussed the importance of computing magnetic equilibria in stellarators while taking into account the plasma contribution in setting the total magnetic field, and we described what kind of magnetic field line topologies can be present in stellarator magnetic equilibria. Finally, we gave an example where plasma generated currents perturbed a vacuum magnetic field with magnetic surfaces sufficiently for magnetic islands and chaos to emerge, thereby defining a so-called equilibrium  $\beta$ -limit, above which magnetic surfaces start to degrade.

Various studies already analyzed the effect of  $\beta$  on the magnetic field line topologies. In the case of a classical stellarator, Loizu et al. (2017) proposed a model for the equilibrium  $\beta$ -limit of a configuration with zero net toroidal current as well as one where the rotational transform at the plasma edge is held fixed. However, as discussed in section 1.6, plasma generated currents must be taken into account in any finite  $\beta$  equilibrium calculation. In their study, Loizu et al. showed the possibility to study equilibrium  $\beta$ -limits with the stepped-pressure equilibrium code (SPEC) code, and, for the first time, modeled analytically the critical  $\beta$  at which chaotic field lines emerge. Their work must however be extended to different stellarator geometries, and more realistic pressure and current profiles. Other studies computed high  $\beta$  equilibria in a number of experimentally relevant stellarator configurations and predicted the emergence of magnetic field line chaos at sufficiently large  $\beta$ . For instance, Suzuki et al. (2020) studied the emergence of chaotic magnetic field lines in the large helical device (LHD), but assumed zero net toroidal current. Reiman et al. (2007) reconstructed equilibria with magnetic islands and chaotic field lines in Wendelstein 7-AS (W7-AS) using the PIES code, while considering the measured pressure and net toroidal current profile. These studies however required numerically expensive calculations. Extensive parameter scans were not considered due to the computational cost, and therefore the equilibrium  $\beta$ -limit dependence on design parameters could not be investigated. With the emergence of new 3D equilibrium codes,

such as the SPEC code, that can rapidly compute equilibria with magnetic islands and magnetic field line chaos, large parameter scans to model the equilibrium  $\beta$ -limit in stellarators become possible, therefore pushing further today's knowledge frontier on stellarator physics.

This thesis explores some of these fundamental plasma physics questions, attempting to understand the effect of  $\beta$  and plasma generated currents on the magnetic field line topologies, and investigates the possible applications of SPEC to compute the equilibrium  $\beta$ -limit in stellarators. In this thesis, we present work on the numerical and analytical modelling of the equilibrium  $\beta$ -limit, and, in particular, we present studies of the dependence of this equilibrium  $\beta$ -limit on the main stellarator design parameters. In addition this thesis shows potential applications of these results to stellarator optimization.

Stellarator optimization is often performed while assuming the existence of magnetic surfaces — see for example the optimizations by Strickler et al. (2004), or Henneberg et al. (2019). Once an optimum is found, additional iterations are usually made with 3D equilibrium codes to ensure that there are no large islands nor regions occupied by chaotic field lines in the volume of interest — see for example the pioneering work by Hudson et al. (2002). Recently, Landreman et al. (2021b) optimized the vacuum field for good quasi-symmetry at the same time as ensuring the existence of good magnetic surfaces, clearly showing that multi-objective optimizations that include a target on the magnetic field line topology are possible. Understanding the effect of plasma  $\beta$  and currents on the magnetic field line topology could improve our knowledge of stellarator equilibria, and facilitate the optimization of stellarators at finite  $\beta$  and current. This thesis delves into stellarator optimization, and improves on state-of-the-art optimization of stellarators by studying the possibility to optimize the equilibrium  $\beta$ -limit in a simplified stellarator geometry at finite  $\beta$  and current.

To reach these goals, we first describe different mathematical models for 3D magnetohydrodynamic (MHD) equilibria in chapter 2. In chapter 3 we describe SPEC, a 3D magnetohydrodynamic (MHD) equilibrium code, and we implement new capabilities to compute free-boundary, finite  $\beta$ , finite current, 3D MHD equilibria with magnetic islands and magnetic chaos. In chapter 4 different numerical diagnostics to measure the confining properties of the magnetic equilibrium computed by SPEC are discussed. The so-called Greene's residues (Greene, 1968, 1979), and the volume of chaos (Meiss, 1992; Loizu et al., 2017) are reviewed, and a new metric, called the fraction of effective parallel diffusion, is introduced. These diagnostics are then exploited in chapter 5 to evaluate the equilibrium  $\beta$ -limit in different stellarator configurations. Finally, we describe how SPEC was coupled with the SIMSOPT python framework for stellarator optimization (Landreman et al., 2021a), and explore the different degrees of freedom available for optimizing the equilibrium  $\beta$ -limit in chapter 6. Chapter 7 provides a summary and outlook of the research presented in this thesis.

## 2 Three-dimensional magnetohydrodynamic equilibria

The description of a plasma in a fusion reactor starts with a mathematical model for its equilibrium. In this chapter, we introduce the ideal MHD model, and in particular its equilibrium equations. Some important properties of ideal 3D MHD equilibria are discussed, and we present briefly the problem of the Pfirsch-Schlüter diverging current singularities associated with the assumption of the existence of magnetic surfaces (Grad, 1967). We introduce the multi-region relaxed magnetohydrodynamic (MRxMHD) equilibrium model (Hole et al., 2006), which models magnetic equilibria with stepped-pressure profiles and that are weak solutions to the ideal MHD equilibrium model. The MRxMHD equilibrium model is of particular interest as it can describe magnetic equilibria with finite pressure gradients and with magnetic islands and chaos, which is crucial for studying the effect of pressure on magnetic field line topology. Furthermore, these equilibria are mathematically well defined as they can be constructed to avoid the Pfirsch-Schlüter singularities. Finally we discuss how these different equilibrium models can be derived by extremizing the MHD energy functional under different constraints.

### 2.1 Ideal MHD

Ideal MHD is probably the most well-known and used model to describe macroscopic plasma equilibria. It describes relatively slow phenomena on macroscopic scales. In MHD, quasi-neutrality is assumed, *i.e.*  $n_e = n_i = n$ , where  $n_e$  and  $n_i$  are the electron and ion densities respectively. The plasma is modeled with a single fluid approximation, where the pressure is isotropic and defined as the sum of the ion and electron pressure,  $p = p_i + p_e = 2nT$ , and the temperature is defined as the average of the ion and electron temperature,  $T = (T_i + T_e)/2$ . Isotropic pressure is achieved in plasmas with sufficiently large collisionality,  $v_{Ti}\tau_{ii}/a \sim v_{Te}\tau_{ee}/a \ll 1$ , where  $v_{T\alpha} = (k_b T_\alpha / m_\alpha)^{1/2}$  is the species  $\alpha$  thermal velocity,  $k_b$  the Boltzmann constant,  $\tau_{ii}$  and  $\tau_{ee}$  are the typical ion and electron collision times respectively,  $m_\alpha$  is the mass of species  $\alpha$ , and  $a$  is the plasma characteristic length. In addition, it is assumed that electromagnetic waves have phase velocities

negligible in comparison to the speed of light,  $\omega/k \ll c$ , with  $k$  the wave number, and that the thermal velocities of ions and electrons are non-relativistic,  $v_{Ti} \ll v_{Te} \ll c$ . Phenomena described by MHD have frequencies smaller than the electron plasma frequency,  $\omega \ll \omega_{pe} = (n_e e^2 / m_e \epsilon_0)^{1/2}$ , with  $e$  the elementary charge, and  $\epsilon_0$  the vacuum permittivity, and smaller than the ion gyrofrequency,  $\omega \ll \omega_{ci} = q_i B / m_i$ , with  $q_i$  the ion electric charge, and  $B$  the magnetic field strength. In addition, the plasma gradients have a characteristic length larger than the Debye length,  $a \gg \lambda_D = (kT_e / 4\pi n_e e^2)^{1/2}$ . It is also assumed that the ion gyroradius is smaller than the characteristic plasma gradient scale,  $\rho_i / a \ll 1$ , and, if there is a finite plasma flow  $u > 0$ , it is also assumed that  $(\rho_i / a)(v_{Ti} / u) \ll 1$ . Ideal MHD is finally obtained by neglecting the effect of resistivity,  $\eta = 0$ . This is typically justified when

$$\left(\frac{m_e}{m_i}\right)^{1/2} \left(\frac{\rho_i}{a}\right)^2 \left(\frac{a}{v_{Ti} \tau_{ii}}\right) \ll 1, \quad (2.1)$$

which defines an upper bound on the collisionality.

The ideal MHD equations are (Freidberg, 2014),

$$\frac{\partial \rho}{\partial t} + \nabla \cdot (\rho \mathbf{u}) = 0 \quad (2.2)$$

$$\rho \frac{d\mathbf{u}}{dt} = \mathbf{J} \times \mathbf{B} - \nabla p \quad (2.3)$$

$$\frac{d}{dt} \left( \frac{p}{\rho^\gamma} \right) = 0 \quad (2.4)$$

$$\mathbf{E} + \mathbf{u} \times \mathbf{B} = 0 \quad (2.5)$$

$$\nabla \times \mathbf{B} = \mu_0 \mathbf{J} \quad (2.6)$$

$$\nabla \cdot \mathbf{B} = 0 \quad (2.7)$$

$$\nabla \times \mathbf{E} = -\frac{\partial \mathbf{B}}{\partial t}, \quad (2.8)$$

where  $\mathbf{J}$  and  $\rho$  are the current and mass densities,  $\mu_0$  is the vacuum permeability,  $\mathbf{E}$  is the electric field,  $\gamma$  is the heat capacity ratio, and  $\mathbf{u}$  is the fluid velocity. Note that Ampere's law, Eq.(2.6), implies charge conservation,

$$\nabla \cdot \mathbf{J} = 0. \quad (2.9)$$

It can be shown that the plasma dynamics across magnetic field lines is well described by the MHD model. The plasma dynamics along the magnetic field lines is, however, poorly described, unless time scales are long compared to the typical time between particles collision (Freidberg, 2014). In this thesis, we are interested in the plasma equilibrium, that the plasma tends to reach after an infinite time,  $t \rightarrow \infty$ . Thus, for equilibrium calculations, the physics across *and* along the magnetic field lines is well described by the MHD model.



At equilibrium, all time derivatives vanish ( $\partial/\partial t = 0$ ), and assuming zero flow ( $\mathbf{u} = 0$ ), we get the *ideal MHD equilibrium equations*,

$$\mathbf{J} \times \mathbf{B} = \nabla p \quad (2.10)$$

$$\nabla \times \mathbf{B} = \mu_0 \mathbf{J} \quad (2.11)$$

$$\nabla \cdot \mathbf{B} = 0. \quad (2.12)$$

Note that flows are damped in general magnetic equilibria, making the assumption  $\mathbf{u} = 0$  reasonable. Special cases are QS fields (Boozer, 1983; Nührenberg and Zille, 1988; Helander, 2014; Rodríguez et al., 2020), where strong flows can be generated in the direction of the symmetry (Spong, 2005; Helander and Simakov, 2008; Simakov and Helander, 2011). In tokamaks, spontaneous rotation occurs (Diamond et al., 2009), and can be generated by external drives, such as NBI (Suckewer et al., 1979), and can reach orders of sound speed  $C_s = \sqrt{(T_e + \gamma T_i)/m_i}$ . In this thesis however, we neglect plasma flow, as indeed this is a good approximation for the highly non-symmetric magnetic configurations studied here.

Writing the current density as the curl of the magnetic field, and using the relation  $\mathbf{a} \times (\nabla \times \mathbf{a}) = \nabla(a^2)/2 - (\mathbf{a} \cdot \nabla)\mathbf{a}$ , the force balance equation (2.10) becomes

$$\frac{(\mathbf{B} \cdot \nabla)\mathbf{B}}{\mu_0} = \nabla \left( \frac{B^2}{2\mu_0} + p \right), \quad (2.13)$$

where the term on the left hand side can be identified to a magnetic tension force density, which opposes the bending of field lines, while the right hand side can be understood as a pressure force, composed of the plasma pressure in addition to the magnetic pressure, which pushes to expand the plasma outwards and opposes the compression of magnetic field lines.

### 2.1.1 Figures of merit of magnetic equilibria

In the previous section, we introduced the ideal MHD model; before discussing some of its properties, we introduce here important figures of merit of ideal MHD equilibria. We consider a toroidal plasma volume  $\mathcal{V}_P$  at equilibrium, in which the pressure  $p$  and magnetic field  $\mathbf{B}$  are known everywhere. We assume an arbitrary poloidal angle  $\theta$  and a toroidal angle  $\phi$ , and their corresponding basis vector  $\mathbf{e}_\theta$  and  $\mathbf{e}_\phi$ . We assume that the magnetic field has a unique magnetic axis, and construct a radial coordinate  $s = r/a$ , where  $s = 0$  on the magnetic axis,  $s = 1$  at the plasma boundary, and  $s = c$  on a magnetic surface parametrized by  $\mathbf{x}(\theta, \phi) = R(\theta, \phi)\hat{\mathbf{e}}_R + Z(\theta, \phi)\hat{\mathbf{e}}_Z$ , with  $(\hat{\mathbf{e}}_R, \hat{\mathbf{e}}_\phi, \hat{\mathbf{e}}_Z)$  the usual cylindrical coordinate basis. For more details about the toroidal coordinate system, and the derivation of the covariant basis vectors, the contravariant basis vectors, and the

jacobian, see appendix A.2. On the magnetic surface,

$$\mathbf{e}_\theta = \frac{\partial R}{\partial \theta} \hat{\mathbf{e}}_R + \frac{\partial Z}{\partial \theta} \hat{\mathbf{e}}_Z \quad (2.14)$$

$$\mathbf{e}_\phi = \frac{\partial R}{\partial \phi} \hat{\mathbf{e}}_R + R \hat{\mathbf{e}}_\phi + \frac{\partial Z}{\partial \phi} \hat{\mathbf{e}}_Z \quad (2.15)$$

$$\mathbf{n} = \hat{\mathbf{e}}_\theta \times \hat{\mathbf{e}}_\phi, \quad (2.16)$$

where  $\mathbf{n}$  is a vector normal the magnetic surface and pointing outwards. We can define the *toroidal flux*  $\psi_t$  and *poloidal flux*  $\psi_p$  as the magnetic flux through a toroidal surface  $S[\phi = \text{const}]$  and through a poloidal ribbon  $S[\theta = \text{const}]$  respectively, *i.e.*

$$\psi_t = \iint_{S[\phi=\text{const}]} \mathbf{B} \cdot d\mathbf{S} = \int_0^{2\pi} \int_0^c B^\phi \sqrt{g} d\theta ds \quad (2.17)$$

$$\psi_p = \iint_{S[\theta=\text{const}]} \mathbf{B} \cdot d\mathbf{S} = \int_0^{2\pi} \int_0^c B^\theta \sqrt{g} d\phi ds, \quad (2.18)$$

where  $\sqrt{g}$  is the jacobian of the coordinate  $(s, \theta, \phi)$ . In the presence of nested magnetic surfaces, and if  $\psi_t$  is a monotonously increasing function of  $s$ , one can use  $\psi_t$  as a radial-like coordinate to replace  $s$ . When possible in this thesis, we will then use  $\psi_t$  as radial coordinate.

As  $S[s = c]$  is a magnetic surface, the magnetic field is everywhere tangential to the surface,  $\mathbf{B} \cdot \mathbf{n} = 0$ , and wraps around the surface. A crucial figure of merit is the *rotational transform*  $\iota$  which is a measure of the tilt of the field line in the  $(\theta, \phi)$  plane, that was introduced in section 1.4.1. The rotational transform is the inverse of the safety factor  $q = 1/\iota$ , more common in the tokamak literature. We have

$$\iota(s) = \left\langle \frac{\mathbf{B} \cdot \nabla \theta}{\mathbf{B} \cdot \nabla \phi} \right\rangle, \quad (2.19)$$

where  $\langle \cdot \rangle$  denotes the flux surface average, defined as the volume average between two neighboring magnetic surfaces (Helander, 2014). The volume enclosed by a magnetic surface is

$$V(\psi_t) = \int_0^{\psi_t} d\psi \int_0^{2\pi} d\theta \int_0^{2\pi} \sqrt{g} d\phi, \quad (2.20)$$

with  $\sqrt{g}$  the  $(\psi_t, \theta, \phi)$  coordinate jacobian. The flux surface average of any function  $f$  is then

$$\langle f \rangle = \frac{1}{V'(\psi_t)} \iint \frac{f dS}{|\nabla \psi_t|} = \iint \frac{f dS}{|\nabla \psi_t|} \bigg/ \iint \frac{dS}{|\nabla \psi_t|}, \quad (2.21)$$

with  $dS = \sqrt{g} |\nabla \psi_t| d\theta d\phi$ . Using straight field line coordinates  $(\theta_s, \phi)$  (see appendix A.1), field lines are straight in the  $(\theta_s, \phi)$ -plane (see Figure 2.1) and the rotational transform, Eq.(2.19), is thus

$$\iota(s) = \frac{\mathbf{B} \cdot \nabla \theta_s}{\mathbf{B} \cdot \nabla \phi}, \quad (2.22)$$

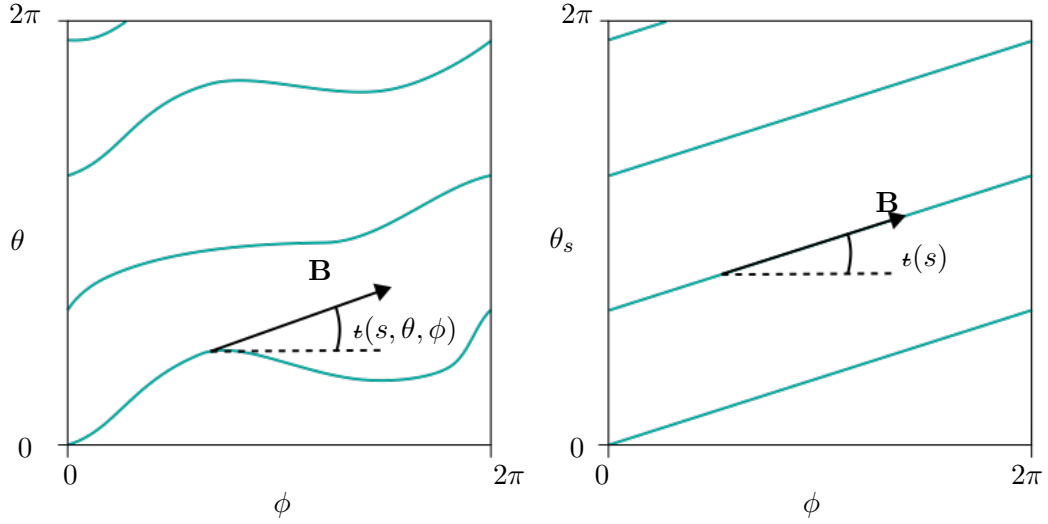


Figure 2.1: Sketch of a field line. Left: using general coordinates  $(\theta, \phi)$  and right: using straight field line coordinates  $(\theta_s, \phi)$ .

retrieving Eq.(1.18). We will differentiate the case of a *rational* magnetic surface, where  $\iota = n/m \in \mathbb{Q}$ , from an *irrational* magnetic surface, where  $\iota \in \mathbb{R} \setminus \mathbb{Q}$ . On an irrational surface, a magnetic field line virtually closes on itself after an infinite number of toroidal transits, thereby passing through virtually every point on the magnetic surface, while on a rational surface, a field line will close on itself after  $n$  poloidal and  $m$  toroidal transits.

Equation (2.10) implies that  $\mathbf{B} \cdot \nabla p = 0$ , *i.e.* the pressure is constant along a field line. If the pressure profile is smooth and not constant in any region, then equation (2.10) implies that magnetic field lies on surfaces of constant pressure, which are thus magnetic surfaces. Assuming the existence of rational magnetic surfaces where  $\nabla p \neq 0$  is however the source of potentially diverging currents, as we shall discuss in sections (2.1.3)-(2.1.4).

Another figure of merit is the normalized pressure, that we already introduced in section 1.4.1. We remind here that  $\beta$  is defined as the ratio between the plasma pressure and the magnetic pressure. It is often evaluated on the magnetic axis,

$$\beta_0 = \frac{2\mu_0 p_0}{B_0^2}, \quad (2.23)$$

or averaged over the plasma volume,

$$\beta = \frac{1}{\mathcal{V}_P} \iiint_{\mathcal{V}_P} \frac{2\mu_0 p}{B^2} dv, \quad (2.24)$$

with  $\mathcal{V}_P$  the plasma volume and  $dv$  a volume element. We also define here two useful quantities to describe plasma equilibria from energy principles (see section 2.4): the

plasma potential energy  $W$  and the magnetic helicity  $K$ , defined as

$$W = \iiint_{V_P} dv \left( \frac{\mathbf{B}^2}{2\mu_0} + \frac{p}{\gamma - 1} \right), \quad (2.25)$$

and

$$K = \iiint_{V_P} dv \mathbf{A} \cdot \mathbf{B}, \quad (2.26)$$

with  $\mathbf{A}$  the magnetic vector potential,  $\mathbf{B} = \nabla \times \mathbf{A}$ . In ideal MHD, the magnetic helicity is exactly conserved in every plasma volume bounded by magnetic surfaces, as we shall see in section 2.4.1.

### 2.1.2 Ideal MHD equilibrium solution in an axisymmetric cylinder

As an illustration, we solve here the ideal MHD equilibrium equations (2.10)-(2.12) in an axisymmetric cylinder of length  $2\pi L$  and radius  $a$ , sometimes referred to as a screw-pinch (see Figure 2.2). We work with cylindrical coordinates  $(r, \theta, z)$ . We assume that the cylinder boundary is a magnetic surface, *i.e.*  $\mathbf{B} \cdot \nabla r = 0$  at  $r = a$ . Assuming symmetries along  $\theta$  and  $z$  (equivalent to axisymmetry in a toroidal geometry), we immediately get from Eq.(2.10) that  $p = p(r)$ , *i.e.* isopressure surfaces are cylinders with constant radii. Since the magnetic field lies on constant pressure surfaces, axisymmetry implies the existence of magnetic surfaces everywhere.

We now search for a solution to the equilibrium equation. One gets from Eq.(2.12)

$$\frac{1}{r} \frac{\partial}{\partial r} (r B_r) = 0, \quad (2.27)$$

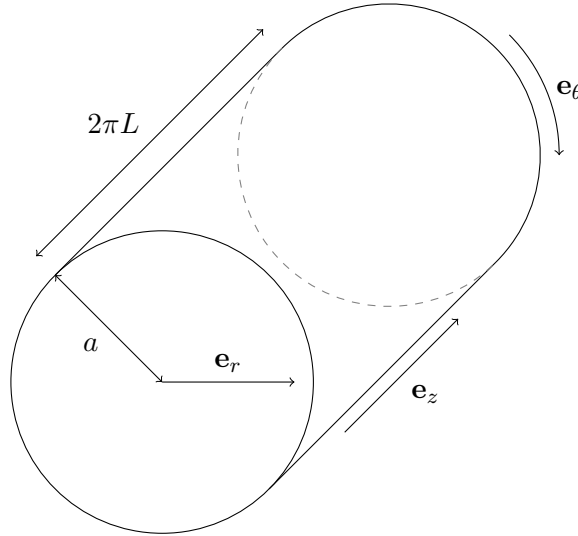


Figure 2.2: Sketch of a plasma cylinder

which, once the boundary condition is applied, leads to  $B_r = 0$ , confirming that surfaces  $S[r = \text{const}]$  are magnetic surfaces. In addition, exploiting Ampere's law, we write the current densities as

$$\mu_0 J_r = 0 \quad (2.28)$$

$$\mu_0 J_\theta = -\frac{\partial B_z}{\partial r} \quad (2.29)$$

$$\mu_0 J_z = \frac{1}{r} \frac{\partial}{\partial r} (r B_\theta). \quad (2.30)$$

Finally, taking the cross product of the current density with the magnetic field in the radial direction and rearranging the terms, one gets

$$\frac{d}{dr} \left( \mu_0 p + \frac{B_\theta^2 + B_z^2}{2} \right) + \frac{B_\theta^2}{r} = 0. \quad (2.31)$$

This equation describes the force balance in a cylindrical plasma. The first term is the gradient of the total pressure, *i.e.* the plasma pressure  $p$  and the magnetic pressure  $B^2/2$ , and it is compensated by the second term, which is the magnetic field line tension, as described by Eq.(2.13).

The equilibrium is thus completely determined if one provides (i) a pressure profile  $p(r)$  and (ii) a constraint on either the poloidal or toroidal magnetic field — for example by providing the poloidal flux profile  $\psi_p(r)$ , or the rotational transform profile  $\iota(r)$ , given here by

$$\iota(r) = \frac{L B_\theta}{r B_z}. \quad (2.32)$$

The equation (2.31) can then be rewritten as

$$\frac{d}{dr} \left[ \mu_0 p + \frac{1}{2} \left( 1 + \frac{L^2}{r^2 \iota^2} \right) B_\theta^2 \right] + \frac{B_\theta^2}{r} = 0, \quad (2.33)$$

which can be solved for  $B_\theta$  if the profiles  $p(r)$  and  $\iota(r)$  are given as inputs. Similarly, the magnetic field in the cylinder is completely determined if one provides the profiles  $p(r)$  and  $I_z(r)$ , *i.e.* the net toroidal current enclosed by a surface  $r = \text{const}$ . Applying Ampere's law, we can express the poloidal magnetic field as

$$B_\theta(r) = \frac{I_z(r)}{2\pi r}, \quad (2.34)$$

and Eq.(2.31) becomes

$$\frac{d}{dr} \left( \mu_0 p + \frac{I_z^2}{8\pi^2 r^2} + \frac{B_z^2}{2} \right) + \frac{I_z^2}{4\pi^2 r^3} = 0. \quad (2.35)$$

which can be solved for  $B_z$  numerically or analytically depending on the profiles  $p(r)$  and

$I_z(r)$ . When integrating Eq.(2.35), one has to set an integration constant, usually by providing the magnetic field on axis,  $B_z(0) = B_0$ , or by constraining the toroidal flux enclosed by the cylinder. Notice how the magnetic field in the cylinder depends on the pressure profile — the magnetic field has to reorganize itself to satisfy the force balance according to the pressure profile. From this simple example, we understand that (i) the magnetic equilibrium depends on the pressure profile and (ii) the magnetic field is fully determined if one provides the pressure and the net toroidal current profiles. In the next section, we explore the different kinds of current densities that are present in ideal MHD equilibria.

### 2.1.3 Currents in ideal MHD equilibria

The MHD equilibrium equations, Eq.(2.10), imply the existence of a finite current density  $\mathbf{J}$  to support the pressure gradient  $\nabla p$ . We discuss here the properties of these current densities. First, we write the current density as the sum of a component parallel to the magnetic field  $J_{\parallel} \hat{\mathbf{b}}$ , with  $\hat{\mathbf{b}} = \mathbf{B}/B$ , and of a component perpendicular to the magnetic field,  $\mathbf{J}_{\perp}$ . We express the perpendicular current by taking the cross product of  $\mathbf{B}$  with Eq.(2.10), and obtain

$$\mathbf{J}_{\perp} = \frac{\mathbf{B} \times \nabla p}{B^2}, \quad (2.36)$$

called the diamagnetic current. In general, the diamagnetic current density  $\mathbf{J}_{\perp}$  is however not divergence free; parallel currents  $J_{\parallel}$  are then generated by the plasma to ensure charge conservation, Eq.(2.9). We write the parallel current density as the sum of two parts (Helander, 2014),

$$J_{\parallel} = u(\psi_t, \theta, \phi) \frac{dp}{d\psi_t} B + \frac{\langle J_{\parallel} B \rangle B}{\langle B^2 \rangle}, \quad (2.37)$$

with the second term on the right hand side being a contribution to the parallel current density that is divergence-free. Note that here we assume that magnetic surfaces exist, and that the toroidal flux is monotonically increasing from the plasma core to the plasma edge so that it can be used as a radial coordinate. To satisfy the charge conservation equation, we impose  $\nabla \cdot (J_{\parallel} \hat{\mathbf{b}}) = -\nabla \cdot \mathbf{J}_{\perp}$ , and the function  $u(\psi_t, \theta, \phi)$  must then satisfy

$$\nabla \cdot \left( u \mathbf{B} p' + \frac{\mathbf{B} \times \nabla \psi_t}{B^2} p' \right) = 0, \quad (2.38)$$

with  $p' = dp/d\psi_t$ . Using the vectorial identity  $\nabla \cdot (f \mathbf{v}) = \mathbf{v} \cdot \nabla f + f \nabla \cdot \mathbf{v}$ , with  $f$  a scalar and  $\mathbf{v}$  a vector, we get

$$\nabla \cdot \left( u \mathbf{B} + \frac{\mathbf{B} \times \nabla \psi_t}{B^2} \right) = 0, \quad (2.39)$$

which can be casted as a magnetic differential equation for  $u$ ,

$$\mathbf{B} \cdot \nabla u = -(\mathbf{B} \times \nabla \psi_t) \cdot \nabla \left( \frac{1}{B^2} \right). \quad (2.40)$$

The total current density is thus

$$\mathbf{J} = \frac{\mathbf{B} \times \nabla p}{B^2} + \left( u(\psi_t, \theta, \phi) \frac{dp}{d\psi_t} + \frac{\langle J_{\parallel} B \rangle}{\langle B^2 \rangle} \right) \mathbf{B}, \quad (2.41)$$

where the first term on the right hand side of Eq.(2.41) is the *diamagnetic current*, the second is the *Pfirsch-Schlüter current*, determined by Eq.(2.40), and the last term encompasses other parallel currents, such as externally driven currents (Ohmic, electron cyclotron current drive (ECCD), neutron beam current drive (NBCD)) or bootstrap current (see section 5.1). The function  $u(\psi_t, \theta, \phi)$  is only determined up to the addition of an integration constant  $C(\psi_t)$  (Coronado and Wobig, 1992). There is some freedom in the choice of this constant, as the corresponding current density,  $\mathbf{J}_C = C(\psi_t) p' \mathbf{B}$ , is divergence-free and can be absorbed by the last term of Eq.(2.41). One choice is to fully determine this constant by considering the parallel momentum balance equation; the resulting Pfirsch-Schlüter current density would then depend on diverse neo-classical effects. Another choice, common in equilibrium calculations, is to choose the integration constant  $C$  such that the flux surface average of the Pfirsch-Schlüter toroidal current density vanishes. Working in Boozer coordinates (see appendix A.1), we obtain

$$\langle u \mathbf{B} \cdot \nabla \phi_b p' \rangle = p' \left\langle \frac{u}{\sqrt{g_b}} \right\rangle = \frac{p'}{G + \epsilon I} \langle u B^2 \rangle, \quad (2.42)$$

where we used the general relation  $\mathbf{B} \cdot \nabla \phi_b = \sqrt{g_b}^{-1}$ . The condition that the flux surface average of the Pfirsch-Schlüter toroidal current density vanishes,  $\langle u \mathbf{B} \cdot \nabla \phi_b p' \rangle = 0$ , is then satisfied when the integration constant  $C(\psi_t)$  is chosen such that

$$\langle u B^2 \rangle = 0. \quad (2.43)$$

As discussed in the example of a cylindrical plasma in section 2.1.2, the net toroidal current in the plasma plays a central role in setting the magnetic equilibrium. It is thus interesting to discuss which current density described in equation (2.41) dominates when setting the net toroidal current. To evaluate each contribution, it is convenient to work in Boozer coordinates (see appendix A.1). We take the flux surface average of the total current density projected in the Boozer toroidal direction,  $\mathbf{J} \cdot \nabla \phi_b$ , following notes by J. A. Alonso (personal communication, 2023). Starting by looking at the contribution from the diamagnetic current density, we write the magnetic field in its contravariant form,

$$\mathbf{B} = I(\psi_t) \nabla \theta_b + G(\psi_t) \nabla \phi_b + K(\psi_t, \theta_b, \phi_b) \nabla \psi_t, \quad (2.44)$$

## Chapter 2. Three-dimensional magnetohydrodynamic equilibria

---

with  $I(\psi_t) = \mu_0 I_\phi / 2\pi$ , where  $I_\phi$  is the net toroidal current enclosed inside a magnetic surface,  $G(\psi_t) = \mu_0 I_\theta / 2\pi$ , where  $I_\theta$  is the net poloidal current outside a magnetic surface, and  $K(\psi_t, \theta_b, \phi_b)$  a function. The flux average of the diamagnetic current density is then

$$\langle \mathbf{J}_\perp \cdot \nabla \phi_b \rangle = p' \left\langle \left( \frac{\mathbf{B} \times \nabla \psi_t}{B^2} \right) \cdot \nabla \phi_b \right\rangle \quad (2.45)$$

$$= p' \left\langle \frac{1}{\sqrt{g_b} B^2} (I(\psi_t) \mathbf{e}_{\phi_b} - G(\psi_t) \mathbf{e}_{\theta_b}) \cdot \nabla \phi_b \right\rangle = p' I(\psi_t) \left\langle \frac{1}{B^2 \sqrt{g_b}} \right\rangle, \quad (2.46)$$

where we used the relation  $\mathbf{e}_{\theta_b} = \sqrt{g_b} \nabla \phi_b \times \nabla \psi_t$  and  $\mathbf{e}_{\phi_b} = \sqrt{g_b} \nabla \psi_t \times \nabla \theta_b$ , with  $\mathbf{e}_{\theta_b}, \mathbf{e}_{\phi_b}$  the covariant basis vectors of the Boozer coordinates  $\theta_b$  and  $\phi_b$  respectively. Using the expression of the jacobian in Boozer coordinates, Eq.(A.32), we get

$$\langle \mathbf{J}_\perp \cdot \nabla \phi_b \rangle = \frac{Ip'}{G + \epsilon I}. \quad (2.47)$$

Interestingly, the diamagnetic current contributes to the net toroidal current only if there are other sources of toroidal current in the plasma,  $I \neq 0$ , which must come from externally driven or bootstrap current, as the Pfirsch-Schlüter current does not generate any net toroidal current. The contribution from the externally driven currents and the bootstrap current is

$$\frac{\langle J_\parallel B \rangle}{\langle B^2 \rangle} \langle \mathbf{B} \cdot \nabla \phi_b \rangle = \frac{\langle J_\parallel B \rangle}{\langle B^2 \rangle} \left\langle \frac{1}{\sqrt{g_b}} \right\rangle = \frac{\langle J_\parallel B \rangle}{G + \epsilon I}. \quad (2.48)$$

The flux surface average of the total current density projected on  $\nabla \phi_b$  is then

$$\langle \mathbf{J} \cdot \nabla \phi_b \rangle = \frac{Ip'}{G + \epsilon I} + \frac{\langle J_\parallel B \rangle}{G + \epsilon I}. \quad (2.49)$$

We can now estimate which current contributes the most to the net toroidal current by taking the ratio of the first and second terms on the right hand side of Eq.(2.49),

$$\frac{Ip'}{\langle J_\parallel B \rangle} \sim \frac{I_\phi \mu_0 p_0}{J_\phi B \psi_a} \sim \frac{\mu_0 p_0}{B^2} \sim \beta. \quad (2.50)$$

Here we assumed that  $p' \sim p_0 / \psi_a$ , with  $\psi_a \sim \pi a^2 B$  the toroidal flux enclosed by the plasma, and  $a$  the minor radius. We also assumed  $J_\parallel \sim J_\phi \sim I_\phi / \pi a^2$ . As  $\beta \ll 1$ , we conclude that the main contribution to the flux-surface averaged current density comes from the externally driven and bootstrap currents. The Pfirsch-Schlüter flux-surface averaged current density vanishes, and the diamagnetic flux surface averaged current density is negligible. While the diamagnetic and Pfirsch-Schlüter currents are by construction included in any magnetic equilibrium calculation, it is thus crucial to also include the contribution from the externally driven and bootstrap current to compute the full effect of the currents on the magnetic field. This will be particularly important when we discuss, in chapter 5, the equilibrium  $\beta$ -limit of a stellarator.



### 2.1.4 Classes of well posed 3D magnetic equilibria

The magnetic differential equation (2.40) has important implications on the existence of 3D magnetic equilibria with nested magnetic surfaces. In the discussion below, we solve equation (2.40) assuming the existence of magnetic surfaces and using the coordinate system  $(\psi_t, \theta_b, \phi_b)$ , where  $(\theta_b, \phi_b)$  are the poloidal and toroidal Boozer angles (see appendix A.1). We first write the left hand side of Eq.(2.40) as

$$\mathbf{B} \cdot \nabla u = \mathbf{B} \cdot \nabla \theta_b \frac{\partial u}{\partial \theta_b} + \mathbf{B} \cdot \nabla \phi_b \frac{\partial u}{\partial \phi_b} + \mathbf{B} \cdot \nabla \psi_t \frac{\partial u}{\partial \psi_t} \quad (2.51)$$

$$= \left( \epsilon \frac{\partial u}{\partial \theta_b} + \frac{\partial u}{\partial \phi_b} \right) \mathbf{B} \cdot \nabla \phi_b. \quad (2.52)$$

Then, expressing the magnetic field  $\mathbf{B}$  on the contravariant Boozer coordinate basis,

$$\mathbf{B} = I(\psi_t) \nabla \theta_b + G(\psi_t) \nabla \phi_b + K(\psi_t, \theta_b, \phi_b) \nabla \psi_t, \quad (2.53)$$

we write the right hand side of Eq.(2.40) as

$$(\mathbf{B} \times \nabla \psi_t) \cdot \nabla \frac{1}{B^2} = (I \nabla \theta_b \times \nabla \psi_t + G \nabla \phi_b \times \nabla \psi_t) \cdot \nabla \frac{1}{B^2} \quad (2.54)$$

$$= \frac{1}{\sqrt{g_b}} \left( G \frac{\partial}{\partial \theta_b} - I \frac{\partial}{\partial \phi_b} \right) \frac{1}{B^2}, \quad (2.55)$$

with  $\nabla \psi_t \cdot (\nabla \theta_b \times \nabla \phi_b) = 1/\sqrt{g_b}$  the inverse of the Boozer coordinate jacobian. Writing the functions  $u(\psi_t, \theta_b, \phi_b)$  and  $B^{-2}(\psi_t, \theta_b, \phi_b)$  as double Fourier series,

$$u(\psi_t, \theta_b, \phi_b) = \sum_{m,n} u_{mn}(\psi_t) e^{i(m\theta_b - n\phi_b)} \quad (2.56)$$

$$B^{-2}(\psi_t, \theta_b, \phi_b) = \sum_{m,n} h_{mn}(\psi_t) e^{i(m\theta_b - n\phi_b)}, \quad (2.57)$$

we can substitute Eqs.(2.52) and (2.55) in Eq.(2.40) and obtain

$$(m\epsilon - n)u_{mn} = -(mG + nI)h_{mn}, \quad (2.58)$$

where we used the general property that  $\sqrt{g_b}^{-1} = \mathbf{B} \cdot \nabla \phi_b$ . The solution for  $u_{mn}$  in (2.58) is then

$$u_{mn} = \Delta_{mn} \delta(\psi_t - \psi_{t,mn}) - \frac{(mG + nI)}{m\epsilon - n} h_{mn}, \quad (2.59)$$

where  $\Delta_{mn}$  is a constant and  $\psi_{t,mn}$  is the toroidal flux enclosed by the rational magnetic surface where  $\epsilon = n/m$  (Helander, 2014). Note that the delta function appears since the general solution to the equation  $xf(x) = h(x)$ , for two arbitrary functions  $f(x)$  and  $h(x)$ , is  $f(x) = h(x)/x + c\delta(x)$ , with  $c$  a constant. This delta function describes a current sheet with zero width. It is physically meaningful because the corresponding net current, given by the integral over a surface  $S[\phi = \text{const}]$  of the delta function, is finite. This current

sheet arises when the topological constraint of the existence of a magnetic surface is enforced on a resonance, which prevents magnetic field lines forming magnetic islands. A current sheet must then be generated to "untangle" the magnetic field lines so that they remain on the magnetic surface (Loizu et al., 2015a; Helander, 2014). The existence of delta-function current sheets is thus a necessary condition when constraining magnetic surfaces to exist, instead of letting magnetic islands form.

The second term on the right hand side of equation (2.59) leads to the Pfirsch-Schlüter current density,

$$J_{mn}^{PS} = -\frac{(mG + nI)}{m\iota - n} h_{mn} p'(\psi_\iota). \quad (2.60)$$

At rational surfaces, where  $\iota = n/m$ , the current density (2.60) seems to diverge as a  $1/x$  singularity if the pressure gradient is finite and if the magnetic field harmonic  $h_{mn}$  is non zero. This particular singularity might be unphysical since the integrated net toroidal current could diverge. To circumvent the issue of unphysical diverging currents and obtain well defined, ideal MHD solutions, one has to consider restricted classes of equilibria.

One possibility is to consider equilibria for which the inverse magnetic field squared resonant harmonic is zero at each rational surface, *i.e.*  $h_{mn} = 0$ , discussed by Weitzner (2014). Another is to relax the assumption of smooth, continuous solutions, and consider rotational transform profiles that are stepped — essentially jumping from irrational to irrational values, and entirely avoiding rational surfaces. This has been discussed by Loizu et al. (2015b). Similarly, one could consider equilibria where the pressure is constant around resonant surfaces. Since rationals are dense in  $\mathbb{R}$ , the pressure profile is either stepped (Bruno and Laurence, 1996) or fractal (Grad, 1967). A combination of the second and third class discussed above, where the rotational transform profile and the pressure profile are alternatively constant, can be constructed to obtain solutions with continuous profiles (Hudson and Kraus, 2017). Recently, a final class of equilibria has been proposed by Y.-M. Huang (Huang et al., 2023), where the delta function current densities in Eq.(2.59) would modify the radial dependency of  $G$ ,  $I$ ,  $p$  and  $\iota$  such that the Pfirsch-Schlüter current density  $J_{mn}^{PS}$  remains integrable.

In the remaining of this thesis, we will work with stepped-pressure equilibria. The reasons are threefold: (i) these equilibria are numerically tractable, *e.g.* there are no fractal structures in the considered profiles, (ii) solutions with magnetic islands and chaos can be obtained and (iii) solutions have been proven to exist close to axisymmetry by Bruno and Laurence (1996). In particular, we will work with MRxMHD equilibria, which are a specific class of stepped-pressure equilibria and can be seen as a combination of Taylor states, described in the following section.

## 2.2 Taylor state

In stepped-pressure equilibria there are regions with flat pressure profiles,  $\nabla p = 0$ . In these regions, the Pfirsch-Schlüter current density, Eq.(2.60), vanishes, meaning that the issue of diverging currents discussed in the previous section is avoided. According to equation (2.10), in these regions the magnetic field and the total current density must satisfy  $\mathbf{J} \times \mathbf{B} = 0$ , meaning that the current density is parallel to the magnetic field,  $\mathbf{J} = \mu(\mathbf{x})\mathbf{B}$ . These magnetic fields are called *force-free fields*, and are the building blocks of the stepped-pressure equilibria.

The Taylor state (Taylor, 1974, 1986) is a particular case of force-free fields where the function  $\mu$  is a constant, which gives the Taylor equilibrium equation, also called Beltrami equation,

$$\nabla \times \mathbf{B} = \mu \mathbf{B}. \quad (2.61)$$

Solutions to the equation (2.61) in a slab and a cylinder are derived below.

### 2.2.1 Solution in a plasma slab

We solve equation (2.61) in a plasma slab. We use cartesian coordinates  $(x, y, z)$  with  $(\mathbf{e}_x, \mathbf{e}_y, \mathbf{e}_z)$  the basis vectors. The plasma slab is bounded by two surfaces at  $x = x^- = 0$  and  $x = x^+ = a$ , and we assume that these surfaces are magnetic surfaces, *i.e.*  $\mathbf{B} \cdot \mathbf{e}_x = 0$ . We first assume periodic boundary conditions in the  $y$  and  $z$  directions, and assume that the equilibrium is independent of the  $y$  and  $z$  coordinates, *i.e.*  $\mathbf{B} = \mathbf{B}(x)$  (see Figure 2.3).

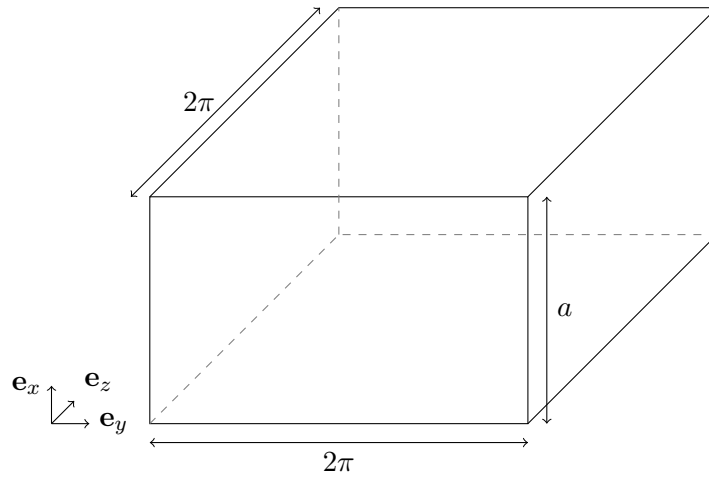


Figure 2.3: Sketch of a plasma slab

## Chapter 2. Three-dimensional magnetohydrodynamic equilibria

---

The equation  $\nabla \cdot \mathbf{B} = 0$  implies that  $B_x = 0$ , while equation (2.61) can be written as

$$\frac{\partial B_z}{\partial x} = -\mu B_y \quad (2.62)$$

$$\frac{\partial B_y}{\partial x} = \mu B_z, \quad (2.63)$$

whose solution is

$$B_y = B_0 \cos(\mu(x - x_0)) \quad (2.64)$$

$$B_z = -B_0 \sin(\mu(x - x_0)), \quad (2.65)$$

where  $B_0$  and  $x_0$  are integration constants, which can be fixed by providing, for example, a constraint on the poloidal and toroidal fluxes. Note that, in this geometry, three constants (or constraints),  $(\mu, B_0, x_0)$ , have to be provided to fully determine the equilibrium. The rotational transform is then given by

$$t = \frac{B_y}{B_z} = -\frac{1}{\tan(\mu(x - x_0))}. \quad (2.66)$$

In this problem, we assumed that  $\mathbf{B}$  was independent of  $y$  and  $z$ . As a consequence, we obtained a solution filled with magnetic surfaces, defined by  $x = \text{const}$ , as  $B_x = 0$  everywhere (see the left panel of Figure 2.4). If we relax the  $y$ - and  $z$ -symmetry assumption, and perturb the plasma slab boundaries, magnetic islands and magnetic field line chaos can be generated. As an example, we solve numerically the Beltrami equation (2.61), in a plasma slab where we perturb both boundaries with three different modes,

$$x^+ = a + x_{21} \cos(2y - z) + x_{31} \cos(3y - z) + x_{32} \cos(3y - 2) \quad (2.67)$$

$$x^- = x_{21} \cos(2y - z) + x_{31} \cos(3y - z) + x_{32} \cos(3y - 2). \quad (2.68)$$

The values of  $\mu$  and  $\psi_p$ , necessary to fully define the Taylor state in a plasma slab, have been chosen such that the rotational transform profile goes through the  $(m, n) = (3, 1)$ ,  $(2, 1)$ ,  $(3, 2)$  resonances (see Figure 2.5). The Poincaré section for small and large values of  $x_{mn}$  is plotted in the middle and right panel of Figure (2.4) respectively. In the case of small perturbations, islands open in the plasma, but they do not overlap, and magnetic surfaces still exist between each main island chain. In the case of larger perturbations, the  $(2, 1)$  island overlaps with the  $(3, 2)$  island and chaotic magnetic field lines emerge. The rotational transform profile, shown on Figure (2.5), shows the expected flattening around the magnetic islands. Clearly, the Taylor state can describe force-free fields with magnetic surfaces, magnetic islands and magnetic field line chaos.

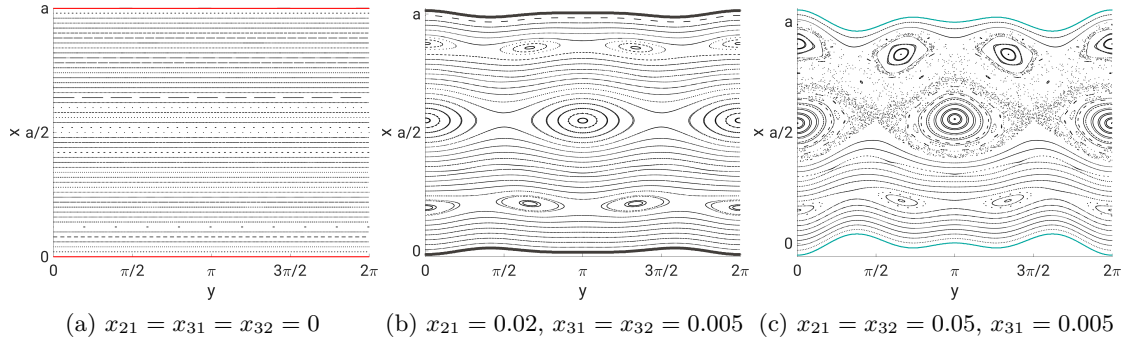


Figure 2.4: Taylor state in a plasma slab, with unperturbed boundary (left), weakly perturbed boundary (middle), and strongly perturbed boundary (right). Colored surfaces are the slab lower and upper boundary,  $x^-$  and  $x^+$  respectively.

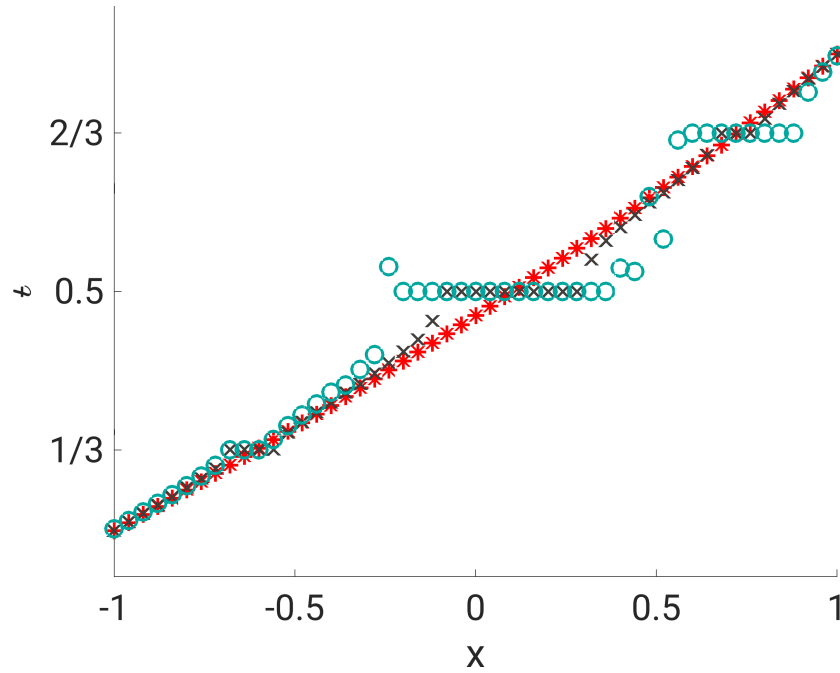


Figure 2.5: Rotational transform of a Taylor state in a plasma slab. Red: unperturbed boundary. Gray: weakly perturbed boundary. Blue: strongly perturbed boundary.

### 2.2.2 Solution in a plasma cylinder

We now solve equation (2.61) in a plasma cylinder. We use cylindrical coordinates  $(r, \theta, z)$ , and assume that the  $z$  coordinate is  $2\pi$ -periodic. The plasma cylinder is bounded by a single surface at  $r = a$ , which we assume to be a magnetic surface, *i.e.*  $\mathbf{B} \cdot \nabla r = 0$  at  $r = a$ . Again, we assume the equilibrium to be axisymmetric, *i.e.*  $\mathbf{B} = \mathbf{B}(r)$ , and assume periodic boundary conditions in the  $\theta$  and  $\phi$  directions (see Figure 2.2), analogous to the  $x - y$  symmetry in the equilibrium slab calculation (see section 2.2.1).

The equation  $\nabla \cdot \mathbf{B} = 0$  implies that  $B_r = 0$ , and equation (2.61) leads to

$$\mu B_\theta = -\frac{\partial B_z}{\partial r} \quad (2.69)$$

$$\mu B_z = \frac{1}{r} \frac{\partial}{\partial r} (r B_\theta). \quad (2.70)$$

Defining  $x = \mu r$ , we thus obtain

$$x^2 \frac{\partial^2 B_\theta}{\partial x^2} + x \frac{\partial B_\theta}{\partial x} + (x^2 - 1) B_\theta = 0, \quad (2.71)$$

which we identify to be Bessel's differential equation. The solutions are then

$$B_\theta = B_0 J_1(\mu r) \quad (2.72)$$

$$B_z = B_0 J_0(\mu r), \quad (2.73)$$

where  $J_i$  is the Bessel function of the  $i^{\text{th}}$  order, and we set  $B_\theta = 0$  at  $r = 0$ . Here  $B_0$  is an integration constant, which can be fixed by providing an additional constraint, for example the toroidal flux. Note that in a cylinder only two constants (or constraints)  $(\mu, B_0)$  have to be provided to fully determine the equilibrium. This is in opposition to the plasma slab case, where three constants had to be provided. This difference is intrinsically linked to the topology of the domain; in a slab, there are two boundaries to the plasma, one at  $x = 0$  and one at  $x = a$ , while in a cylinder there is only one boundary, at  $r = a$ . These important topological properties are also true in toroidal geometries; two constants are required to fully determine the Taylor state in a torus, while three constants are required in a toroidal annulus (see Figure 2.6).

As a side note, we remark that the Taylor state in an axisymmetric cylinder, described by Eqs.(2.72)-(2.73), is given by a combination of Bessel functions — the sign of  $B_z$  or  $B_\theta$  can thus switch from positive to negative (if  $B_0 > 0$ ), depending on the value of  $\mu$ . This would typically apply to describe the magnetic equilibrium of a reversed-field pinch (RFP), which was historically Taylor's motivation to develop this model.

## 2.3 Multi-region relaxed magnetohydrodynamics

Taylor states alone cannot describe plasma equilibria with pressure profiles. An alternative is proposed by the MRxMHD equilibrium model, which describes weak solutions to the ideal MHD equilibrium equations, Eqs.(2.10)-(2.12), assuming stepped-pressure profiles. The pressure steps are supported by magnetic surfaces  $\mathcal{I}_l$ ,  $l \in \{1, \dots, N_{vol}\}$ , with irrational rotational transform, *i.e.*  $t \in \mathbb{R} \setminus \mathbb{Q}$ , which define a finite number of volumes  $\mathcal{V}_l$  between each adjacent pair of interfaces (see Figure 2.6). In each volume, the magnetic field is described by a Taylor state,

$$\nabla \times \mathbf{B} = \mu_l \mathbf{B}. \quad (2.74)$$

We remark that while ideal MHD equilibria are defined by two free functions (*e.g.* the pressure and the rotational transform profiles,  $p(\psi_t)$  and  $t(\psi_t)$ , or the pressure and the net toroidal current profiles,  $p(\psi_t)$  and  $I_\phi(\psi_t)$  — see section 2.1.2), MRxMHD equilibria require two scalars to determine the solution in an annular volume  $\mathcal{V}_l$ , in addition to the pressure and toroidal flux — this is similar to what has been discussed in section 2.2.1. This can be considered as three independent discrete profiles that are required to determine an equilibrium. Examples are  $\{p_l, \mu_l, \Delta\psi_{p,l}\}_{l=1,\dots,N_{vol}}$ , with  $\psi_{p,l}$  the poloidal flux enclosed by the interface  $\mathcal{I}_l$ , or  $\{p_l, \mu_l, K_l\}_{l=1,\dots,N_{vol}}$ , with  $K_l$  the magnetic helicity in volume  $\mathcal{V}_l$ , or  $\{p_l, t_l^-, t_l^+\}_{l=1,\dots,N_{vol}}$ , with  $t_l^\pm$  the rotational transform on the inner and outer side of the interface  $\mathcal{I}_l$ , as functions of  $\{\psi_{t,l}\}_{l=1,\dots,N_{vol}}$ , *i.e.* the toroidal flux enclosed by the interface  $\mathcal{I}_l$ . The innermost volume is a special case, since it only has one boundary; the magnetic field in the innermost volume is thus fully determined by two scalars, for example  $(\mu_1, \psi_{t,1})$ , as discussed in section 2.2.2.

The geometry of the volumes' boundary is obtained such that force balance is achieved, *i.e.* the total pressure (plasma and magnetic pressure) is continuous across each volume's interface  $\mathcal{I}_l$ ,

$$\left[ \left[ p + \frac{B^2}{2\mu_0} \right] \right]_l = 0, \quad (2.75)$$

where  $[[x]]_l \equiv x_{l+1} - x_l$  denotes the discontinuity across interface  $l^{\text{th}}$ . The MRxMHD equilibrium can then be seen as a collection of nested Taylor states at equilibrium with one another.

MRxMHD equilibria are thus stepped-pressure equilibria that extend the Taylor state to equilibria with pressure gradients. Magnetic field lines are discretely constrained to lay on magnetic surfaces at the volumes' boundaries, while magnetic islands and magnetic field line chaos can be present in the volumes between the interfaces. Diverging currents, as described in section 2.1.4, are avoided if pressure gradients are only supported by irrational magnetic surfaces. There are however some drawbacks; the magnetic field, and so the rotational transform, pressure and other physical profiles, are in general discontinuous across the interfaces. Furthermore, interfaces may not always exist. If an interface is close to a magnetic island chain or chaotic field lines, the surface might be

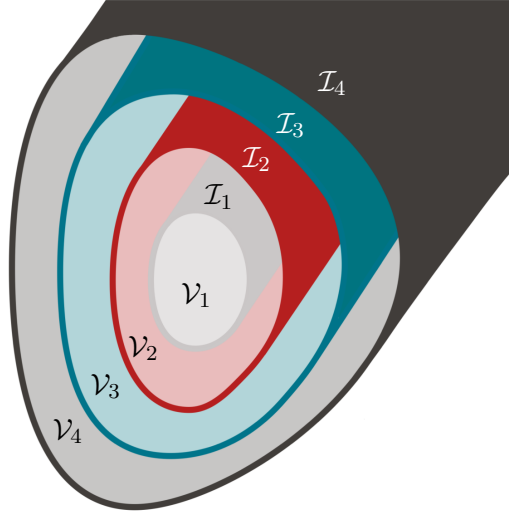


Figure 2.6: Illustration of 4 nested volumes,  $\mathcal{V}_1$  to  $\mathcal{V}_4$ , separated by 4 interfaces,  $\mathcal{I}_1$  to  $\mathcal{I}_4$ . Volume  $\mathcal{V}_1$  is a torus, while volumes  $\mathcal{V}_{2-4}$  are toroidal annuli.

fractal and thus can not be represented with analytical basis functions, *e.g.* a Fourier basis (Qu et al., 2021). Another possibility is that the pressure jump is too large for a single surface to support it and no solutions to Eq.(2.75) exist (McGann et al., 2010). Therefore, care must be taken when constructing MRxMHD equilibria, and in their analysis.

### 2.3.1 Currents in MRxMHD

One important part of the work presented in this thesis is the implementation of a new capability in the stepped-pressure equilibrium code (SPEC) (introduced in Chapter 3) to run at fixed net toroidal current profile. The numerical implementation will be explained in great details in section 3.2; we describe in this section how currents are represented in the MRxMHD theory. This section is adapted from parts of the publication by A. Baillod *et. al.*, Computation of multi-region, relaxed magnetohydrodynamic equilibria with prescribed toroidal current profile, *Journal of Plasma Physics* **87**, 4, 905870403 (2021), published under the license CC BY 4.0.

In MRxMHD, two spatially distinct net toroidal current profiles co-exist, namely currents flowing in the volumes,  $\{I_{l,\phi}^v\}_{l=\{1,\dots,N_{vol}\}}$ , and surface currents flowing at the volumes' interfaces,  $\{I_{l,\phi}^s\}_{l=\{1,\dots,N_{vol}-1\}}$  (current sheets), where the subscript  $\phi$  refers to the toroidal angle.



### 2.3 Multi-region relaxed magnetohydrodynamics

The volume current  $I_{l,\phi}^v$  in volume  $\mathcal{V}_l$  is easily evaluated using Eq.(2.74),

$$\mu_0 I_{l,\phi}^v = \mu_0 \iint_{S[\phi=\text{const}]} \mathbf{J} \cdot d\mathbf{S} = \mu_l \iint_{S[\phi=\text{const}]} \mathbf{B}_l \cdot d\mathbf{S} = \mu_l (\psi_{t,l} - \psi_{t,l-1}), \quad (2.76)$$

where  $S[\phi = \text{const}]$  is a constant- $\phi$  surface in volume  $\mathcal{V}_l$  and  $d\mathbf{S}$  is the differential surface element. Volume currents represent externally driven currents such as ECCD, NBCD or Ohmic current. Eq.(2.76) might be surprising since toroidal currents are usually expressed in terms of functions of the poloidal fluxes and not the toroidal fluxes. In essence, the poloidal flux dependence is contained in  $\mu_l$ , which is related to the parallel current density, as  $\mu_l = \mu_0 \mathbf{J}_l \cdot \mathbf{B}_l / B_l^2$ , with  $\mathbf{j}_l$  the current density in volume  $\mathcal{V}_l$ .

The surface current  $I_{l,\phi}^s$  at interface  $\mathcal{I}_l$  can be evaluated using Ampere's law,

$$\mu_0 I_{l,\phi}^s = \int_{\Gamma_{\theta,l}} [[\mathbf{B}]]_l \cdot d\mathbf{l} = \oint_0^{2\pi} [[B_\theta]]_l d\theta \equiv 2\pi [[\tilde{B}_\theta]]_l, \quad (2.77)$$

where  $\Gamma_{\theta,l}$  is a closed curve following the interface  $\mathcal{I}_l$  poloidally and  $\tilde{B}_\theta$  is the  $m = n = 0$  Fourier mode of the covariant component of the poloidal magnetic field. In Eq.(2.77), the poloidal and toroidal angles,  $\theta$  and  $\phi$ , are as-of-yet arbitrary. However the surface currents  $I_{l,\phi}^s$  are, as expected, independent of these angles choice, since the surface currents only depend on the  $m = n = 0$  mode of the field. Surface currents represent all equilibrium pressure-driven currents, such as diamagnetic, Pfirsch-Schlüter, and bootstrap currents, as well as shielding currents arising when an ideal interface is positioned on a resonance (Loizu et al., 2015a) — see section 2.1.3. Note that the net poloidal current at the interface  $\mathcal{I}_l$  can be obtained by considering integrals over  $\Gamma_{\phi,l}$ , *i.e.* a closed curve following the interface toroidally, as

$$\mu_0 I_{l,\theta}^s = \int_{\Gamma_{\phi,l}} [[\mathbf{B}]]_l \cdot d\mathbf{l} = \oint_0^{2\pi} [[B_\phi]]_l d\phi \equiv 2\pi [[\tilde{B}_\phi]]_l, \quad (2.78)$$

where  $\tilde{B}_\phi$  is the  $m = n = 0$  Fourier mode of the covariant component of the toroidal magnetic field.

Furthermore, it is interesting to note that the current density at the interface  $\mathcal{I}_l$  is

$$\mu_0 \mathbf{J}_l^s = \hat{\mathbf{n}} \times [[\mathbf{B}]] \delta(\mathbf{x} - \mathbf{x}_l), \quad (2.79)$$

where  $\hat{\mathbf{n}} = \nabla s / |\nabla s|$ ,  $s$  is a radial coordinate with  $s = s_l$  on  $\mathcal{I}_l$ , and  $\mathbf{x}_l \in \mathcal{I}_l$ . Equation (2.79) can be proven in its weak form by taking surface integrals. Since  $\mathbf{B} \cdot \nabla s = 0$  at the interface  $\mathcal{I}_l$ , we find

$$\mu_0 \mathbf{J}_l^s = (\nabla s \times \nabla \theta [[B_\theta]] + \nabla s \times \nabla \phi [[B_\phi]]) \frac{\delta(\mathbf{x} - \mathbf{x}_l)}{|\nabla s|}. \quad (2.80)$$

Integrating over a toroidal surface  $S[\phi = \text{const}]$ , and using the relation  $\delta(\mathbf{x} - \mathbf{x}_l) =$

$\delta(s - s_l)|\nabla s|$ , we obtain the net toroidal current at the interface,

$$\mu_0 \iint_{S[\phi=\text{const}]} \mathbf{J}_l^s \cdot d\mathbf{S} = \iint_{S[\phi=\text{const}]} \nabla s \times \nabla \theta [[B_\theta]] \cdot \nabla \phi \delta(s - s_l) \sqrt{g} ds d\theta \quad (2.81)$$

$$= \iint_{S[\phi=\text{const}]} [[B_\theta]] \delta(s - s_l) ds d\theta \quad (2.82)$$

$$= \oint [[B_\theta]]_l d\theta = \mu_0 I_{l,\phi}^s, \quad (2.83)$$

retrieving Eq.(2.77). The net poloidal current at the interface is obtained similarly by integrating over a poloidal surface  $S[\theta = \text{const}]$ ,

$$\mu_0 \iint_{S[\theta=\text{const}]} \mathbf{J}_l^s \cdot d\mathbf{S} = \iint_{S[\theta=\text{const}]} \nabla s \times \nabla \phi [[B_\phi]] \cdot \nabla \theta \delta(s - s_l) \sqrt{g} ds d\phi \quad (2.84)$$

$$= \iint_{S[\theta=\text{const}]} [[B_\phi]] \delta(s - s_l) ds d\phi \quad (2.85)$$

$$= \oint [[B_\phi]]_l d\phi = \mu_0 I_{l,\theta}^s. \quad (2.86)$$

Equations (2.83) and (2.86) show that the current density (2.79) leads to the same net toroidal and poloidal current as obtained with Ampere's law in Eqs.(2.77)-(2.78).

### Currents discretization

Typically, continuous current profiles are provided by theoretical models or after equilibrium reconstruction using experimental data. We now discuss how these profiles can be represented in the framework of MRxMHD. Consider an externally driven current profile, *e.g.* ECCD, provided as the enclosed toroidal current as a function of the toroidal magnetic flux, *i.e.*  $I_{\phi,ECCD}(\psi_t)$ , and a pressure-driven current profile, *e.g.* the bootstrap current, provided similarly as the enclosed toroidal current as a function of the toroidal flux,  $I_{\phi,BS}(\psi_t)$ . We also assume that the pressure profile,  $p(\psi_t)$ , the number of volumes,  $N_{vol}$ , and their enclosed toroidal fluxes,  $\{\psi_{t,l}\}_{l=1,\dots,N_{vol}}$ , are given (see Figure 2.7). The question of how many volumes and where to position their interfaces to best represent a given pressure profile is not addressed in this chapter.

A proposed representation of these current density profiles in MRxMHD is achieved as follows. The ECCD current is an externally driven, parallel current and is thus represented as a volume current since it flows parallel to the field lines; on the other hand, the bootstrap current is a pressure-driven, self-generated current and is represented as a surface current, since it is localized at the pressure gradients. Volume currents are obtained by integrating the externally driven current density in each volume (Figure 2.8), which is simply given by the difference

$$I_{l,\phi}^v = I_{\phi,ECCD}(\psi_{t,l}) - I_{\phi,ECCD}(\psi_{t,l-1}), \quad (2.87)$$

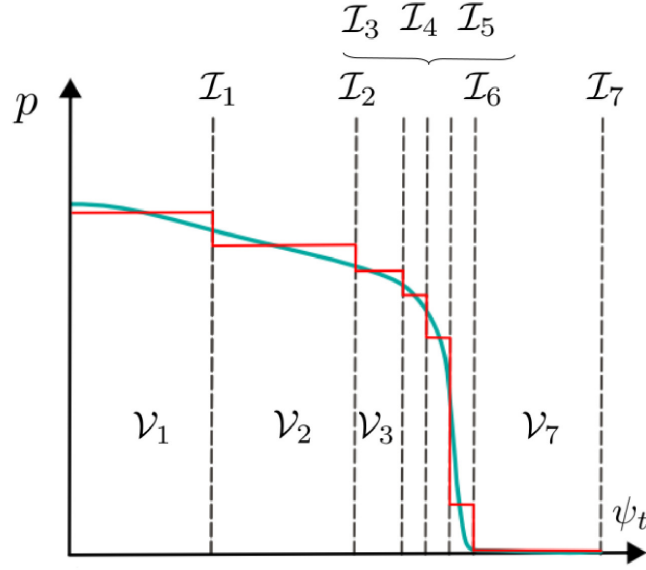


Figure 2.7: Sketch of a pressure profile as a function of the toroidal flux. Blue: continuous pressure profile obtained via experiment or analytical model. Red: MRxMHD discretized pressure profile. Black dashed lines: volumes' interfaces.

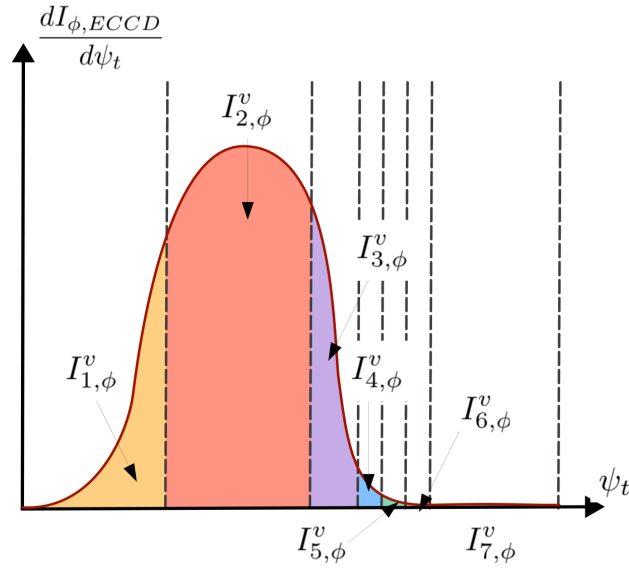


Figure 2.8: Sketch of externally driven current density (red curve). Colored area correspond to the MRxMHD volume current. Black dashed lines represent volumes' interfaces.

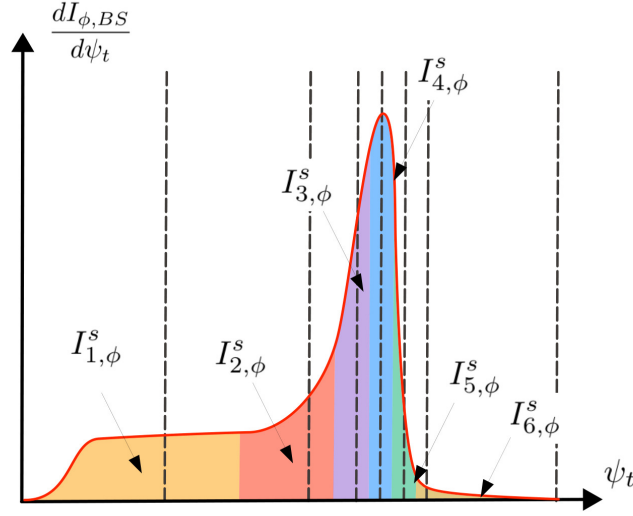


Figure 2.9: Sketch of pressure driven current density. Colored area correspond to the MRxMHD surface current. Black dashed lines represent volumes' interfaces.

and the surface currents are obtained by integrating the pressure driven current density around each interface (Figure 2.9), which is expressed as

$$I_{l,\phi}^s = I_{\phi,BS}(\psi_{l,out}) - I_{\phi,BS}(\psi_{l,in}), \quad (2.88)$$

with

$$\psi_{l,in} = \begin{cases} 0 & \text{if } l = 1 \\ \frac{\psi_{t,l-1} + \psi_{t,l}}{2} & \text{otherwise} \end{cases} \quad (2.89)$$

$$\psi_{l,out} = \begin{cases} \psi_a & \text{if } l = N_{vol} - 1 \\ \frac{\psi_{t,l} + \psi_{t,l+1}}{2} & \text{otherwise} \end{cases}, \quad (2.90)$$

with  $\psi_a$  the total toroidal magnetic flux enclosed by the plasma. In Eqs.(2.89)-(2.90), care has been taken for the first and last interfaces, where the surface of integration has been extended to include the current density from the magnetic axis and up to the plasma boundary. Note that this difference in the definition of the first and last surface currents vanishes as the number of volumes  $N_{vol}$  is increased. Eqs.(2.87)-(2.90) are only one possible discretization of the continuous current profiles, proposed here for illustration. Advantages of this particular representation are (1) that the total toroidal current is always preserved and (2) that the currents are approximately localized at the same location in the discretized than in the continuous case.

## 2.4 Energy principles

To complete this chapter, we discuss here how the ideal MHD equilibrium equations, Eqs.(2.10)-(2.12), the Taylor state, Eq.(2.61), and the MRxMHD equilibrium equations can all be derived from an energy principle, Eqs.(2.74)-(2.75). In fact, all three models derive from the same energy functional, which is extremized under different topological constraints. We first start by discussing the relation between magnetic helicity and field line topology conservation.

### 2.4.1 Conservation of field line topology

An important property of the ideal MHD model is that the magnetic helicity  $K$ , defined in Eq.(2.26) is conserved everywhere under ideal MHD evolution (Woltjer, 1958). Indeed, we find

$$\frac{\partial K}{\partial t} = \iiint_{\mathcal{V}} d\mathbf{x}^3 \frac{\partial}{\partial t} (\mathbf{A} \cdot \mathbf{B}) + \iint_{\delta\mathcal{V}} \mathbf{A} \cdot \mathbf{B} (\mathbf{n} \cdot \mathbf{v}) d\mathbf{x}^2. \quad (2.91)$$

where  $\mathcal{V}$  is any volume in the plasma bounded by magnetic surfaces,  $\mathbf{n}$  is a unit vector normal to  $\delta\mathcal{V}_i$ , and  $\mathbf{v}$  is the velocity describing the motion of the boundary  $\delta\mathcal{V}$ . The first term of the right hand side of Eq.(2.91) can be simplified using Faraday's law,

$$\frac{\partial}{\partial t} (\mathbf{A} \cdot \mathbf{B}) = \frac{\partial \mathbf{A}}{\partial t} \cdot \mathbf{B} - \mathbf{A} \cdot (\nabla \times \mathbf{E}) \quad (2.92)$$

$$= \mathbf{E} \cdot \mathbf{B} + \mathbf{B} \cdot \frac{\partial \mathbf{A}}{\partial t} - \nabla \cdot (\mathbf{E} \times \mathbf{A}) \quad (2.93)$$

$$= -\nabla \cdot (\Phi \mathbf{B} + \mathbf{E} \times \mathbf{A}), \quad (2.94)$$

where we used the relation  $\nabla \cdot (\mathbf{A} \times \mathbf{E}) = \mathbf{A} \cdot \nabla \times \mathbf{E} + \mathbf{E} \cdot \nabla \times \mathbf{A}$  to get to the second equation, and the electric field was expressed in terms of the electrostatic potential  $\Phi$  as  $\mathbf{E} = -\nabla\Phi - \partial\mathbf{A}/\partial t$  to get the third equation. Using the divergence theorem to rewrite the second term of Eq.(2.94) as a surface integral, and noting that  $\mathbf{B} \cdot \mathbf{n} = 0$  since  $\delta\mathcal{V}$  are magnetic surfaces, we obtain

$$\frac{\partial K}{\partial t} = \iint_{\delta\mathcal{V}} (\mathbf{A} \cdot \mathbf{B} (\mathbf{n} \cdot \mathbf{v}) - (\mathbf{E} \times \mathbf{A}) \cdot \mathbf{n}) d\mathbf{x}^2 \quad (2.95)$$

$$= \iint_{\delta\mathcal{V}} (\mathbf{n} \times \mathbf{A}) \cdot (\mathbf{E} + \mathbf{v} \times \mathbf{B}) d\mathbf{x}^2. \quad (2.96)$$

Applying the ideal Ohm's law (Eq.(2.5)), we obtain  $\partial K/\partial t = 0$ , *i.e.* the magnetic helicity is conserved everywhere in the plasma according to ideal MHD. Interestingly, it has been shown that the magnetic helicity is also approximately conserved during certain non-ideal processes, such as fast reconnection events (Berger, 1999), and tokamak sawtooth crashes (Heidbrink and Dang, 2000).

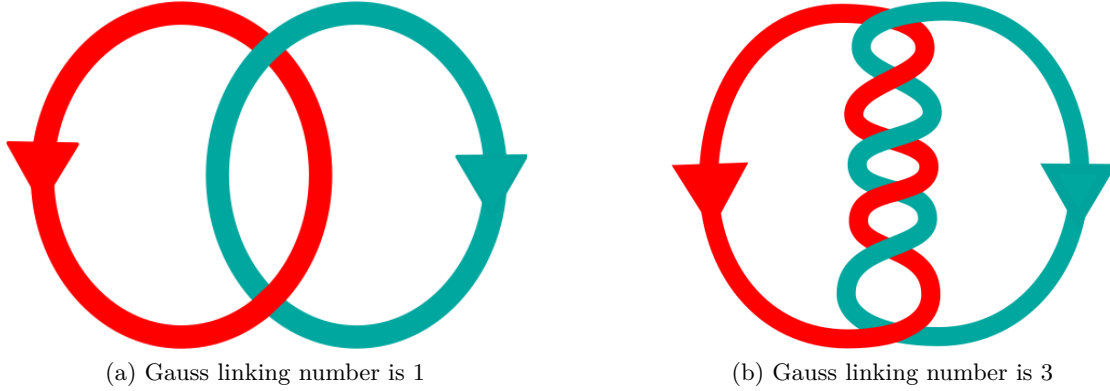


Figure 2.10: Sketch of two intertwined curves (one in red, one in blue), and their related Gauss linking number

Magnetic helicity can be linked to the magnetic field line topologies. Using the Coulomb gauge to express the magnetic vector potential,  $\nabla \cdot \mathbf{A} = 0$ , one can show (Moffatt, 1969; Arnold and Khesin, 2021; Berger, 1999) that the magnetic helicity is the sum of the Gauss linking number over every pair of field lines within a volume, where the Gauss linking number is a measure of how intertwined field lines are (see Figure 2.10). Note the following implication: in ideal MHD, the magnetic helicity is conserved *everywhere*, meaning that the magnetic topology is conserved during plasma motion, a reflection of Alfvén’s frozen-in-flux theorem (Alfvén, 1942). Therefore, no magnetic reconnection event can be described by ideal MHD dynamics.

### 2.4.2 Ideal MHD equilibrium

Consider a plasma filled with nested magnetic surfaces and initially at rest with potential energy  $W$  given by Eq.(2.25). In general, this initial state will not be at equilibrium. We follow Kruskal and Kulsrud (1958) to minimize  $W$  under ideal MHD motions.

The first step in the derivation is to find a new time-invariant of the system. From Eq.(2.4), we find that  $p^{1/\gamma} = k\rho$ , with  $k$  a constant. Multiplying both sides by a volume element  $dv$ , we get  $p^{1/\gamma}dv = k\rho dv = kdm$ , with  $dm$  the mass contained in  $dv$ . Mass conservation implies that  $dm$  is a constant, and thus  $p^{1/\gamma}dv$  is also constant in time. We can thus define the conserved quantity  $M(c)$ , which is proportional to the plasma mass, as

$$M(c) = \int_{\psi_t \leq c} p^{1/\gamma} dv, \quad (2.97)$$

where  $c$  is a flux surface label, and  $c = C$  is the plasma boundary. Variation of  $M$  with

respect to  $p$  gives

$$0 = \delta M = \frac{1}{\gamma} \int_{\psi_t \leq c} p^{1/\gamma-1} \delta p dv \quad (2.98)$$

$$= \frac{1}{\gamma} \int_0^c dc \iint_{S[\psi_t=c]} p^{1/\gamma-1} \delta p \frac{dS}{|\nabla \psi_t|}. \quad (2.99)$$

The plasma will dissipate its energy until reaching an equilibrium, characterized by the minimum of its energy, where  $\delta W = 0$ . Variation of the energy with respect to  $p$  thus gives

$$0 = \delta W = \frac{1}{\gamma-1} \int_0^C dc \iint_{S[\psi_t=c]} \frac{dS}{|\nabla \psi_t|} \delta p. \quad (2.100)$$

Both equation (2.99) and (2.100) have to be satisfied for any variation  $\delta p$ ; in particular, we can choose a variation such that  $p^{1/\gamma-1} \delta p / |\nabla \psi_t| = \delta(\mathbf{x} - \mathbf{x}_1) - \delta(\mathbf{x} - \mathbf{x}_2)$ , with  $\mathbf{x}_i$  a point on the surface  $\psi_t = c$ . Then equation (2.99) is satisfied by construction, and equation (2.100) implies

$$0 = \iint_{S[\psi_t=c]} \frac{\delta p dS}{|\nabla \psi_t|} = \iint_{S[\psi_t=c]} \frac{dS}{p^{1/\gamma-1}} [\delta(\mathbf{x} - \mathbf{x}_1) - \delta(\mathbf{x} - \mathbf{x}_2)], \quad (2.101)$$

which is satisfied if  $p(\mathbf{x}_1) = p(\mathbf{x}_2)$ . Since the  $\mathbf{x}_i$  are arbitrary, the pressure must be a function of  $c$ , *i.e.*  $p = p(c)$ . Taking the derivative of equation (2.97) with respect to  $c$ , we can write

$$p(c) = \left[ \frac{M'(c)}{\int_{\psi_t=c} dS / |\nabla \psi_t|} \right]^\gamma. \quad (2.102)$$

We now use the assumption of the existence of magnetic surfaces to express the magnetic field using straight-field line coordinates  $(c, \theta, \phi)$  (see appendix A.1) using the Clebsch form,

$$\mathbf{B} = \nabla \psi_t \times \nabla \alpha, \quad (2.103)$$

with

$$\alpha = \theta + \lambda(c, \theta, \phi) - \epsilon \phi, \quad (2.104)$$

and  $\lambda$  a function that transforms arbitrary toroidal coordinates  $(c, \theta, \phi)$  into straight field line coordinates with  $\theta_s = \theta + \lambda$ . Variation of the energy function  $W$  with respect to  $\lambda$  gives

$$0 = \delta W = \int_{\mathcal{V}_P} \mathbf{B} \cdot (\nabla \psi_t \times \nabla \delta \lambda) dv = - \int_{\mathcal{V}_P} \delta \lambda \nabla \cdot (\mathbf{B} \times \nabla \psi_t) dv, \quad (2.105)$$

which implies

$$\nabla \psi_t \cdot (\nabla \times \mathbf{B}) = 0, \quad (2.106)$$

*i.e.* magnetic surfaces are current surfaces as well. The final stage of the derivation is to consider variations of  $W$  with respect to the toroidal flux. Careful consideration of how

the pressure varies as the toroidal flux is varied leads to

$$\int_{\mathcal{V}_P} \delta p(c) dv = \iiint_{\mathcal{V}_P} p \delta \log p dv = \int_0^C dc \int_{S[\psi_t=c]} \frac{dS}{|\nabla \psi_t|} p \gamma \delta \left[ \log \left( \frac{M'(c)}{\iint dS/|\nabla \psi_t|} \right) \right]. \quad (2.107)$$

Let us define  $I(c) = \int_{\psi_t=c} dS/|\psi_t|$  to lighten the notation. Expanding the variation of the logarithm, we obtain

$$\delta \left[ \log \left( \frac{M'(c)}{I(c)} \right) \right] = \frac{I(c)}{M'(c)} \frac{\delta(M'(c))I(c) - M'(c)\delta(I(c))}{I(c)^2} \quad (2.108)$$

$$= \frac{\delta(I(c))}{I(c)}, \quad (2.109)$$

where we used that  $M(c)$  is an ideal MHD invariant, *i.e.*  $\delta M(c) = 0$  and thus  $\delta M'(c) = 0$ . Note that the variation of  $I(c)$  can be written as

$$\delta(I(c)) = \delta \left( \iint_{S[\psi_t=c]} \frac{dS}{|\nabla \psi_t|} \right) = \delta \frac{d}{dc} \iiint_{\mathcal{V}_P} dv = -\frac{d}{dc} \int_{S[\psi_t=c]} dS \frac{\delta \psi_t}{|\nabla \psi_t|}, \quad (2.110)$$

which leads to

$$\iiint_{\mathcal{V}_P} \delta p(c) dv = \gamma \int_0^c dp(c) \frac{d}{dc} \iint_{S[\psi_t=c]} dS \frac{\delta \psi_t}{|\nabla \psi_t|} \quad (2.111)$$

$$= -\gamma \int_0^c dp'(c) \iint_{S[\psi_t=c]} dS \frac{\delta \psi_t}{|\nabla \psi_t|} \quad (2.112)$$

$$= -\gamma \iiint_{\mathcal{V}_P} dv p'(\psi_t) \delta \psi_t, \quad (2.113)$$

where we integrated by part the first equation, and used the assumption that  $\delta \psi_t = 0$  on the plasma boundary. We can now finally write the variation of the energy,

$$0 = \delta W = \iiint_{\mathcal{V}_P} dv \left[ \mathbf{B} \cdot \delta \mathbf{B} + \frac{p' \delta \psi_t + \delta p}{\gamma - 1} \right] \quad (2.114)$$

$$= \iiint_{\mathcal{V}_P} dv [\mathbf{B} \cdot (\nabla \delta \psi_t \times \nabla \alpha + \nabla \psi_t \times \nabla \delta \lambda) - p' \delta \psi_t] \quad (2.115)$$

$$= \iiint_{\mathcal{V}_P} dv [\mathbf{B} \cdot (\nabla \delta \psi_t \times \nabla \alpha) - p' \delta \psi_t] \quad (2.116)$$

$$= \iiint_{\mathcal{V}_P} dv \delta \psi_t [(\nabla \times \mathbf{B}) \cdot \nabla \alpha - p'], \quad (2.117)$$

To obtain the force balance equation, one needs to take the cross product between  $\nabla \times \mathbf{B}$  and  $\mathbf{B}$ . We get

$$\mathbf{B} \times (\nabla \times \mathbf{B}) = [(\nabla \times \mathbf{B}) \cdot \nabla \psi_t] \nabla \alpha + [(\nabla \times \mathbf{B}) \cdot \nabla \alpha] \nabla \psi_t = -p' \nabla \psi_t, \quad (2.118)$$



which is equivalent to

$$(\nabla \times \mathbf{B}) \times \mathbf{B} = \nabla p, \quad (2.119)$$

thereby retrieving the force balance equation (2.10). The plasma state that extremizes the energy  $W$  under ideal MHD variations is thus described by the MHD equilibrium equation. Since only ideal MHD variations were allowed, the magnetic field line topologies are conserved between the initial and final state — the equilibrium is thus filled with nested magnetic surfaces.

### 2.4.3 Taylor state

Taylor states do not assume the existence of magnetic surfaces; as a matter of fact, the magnetic helicity is conserved globally, as opposed to its local conservation in ideal MHD. To enforce this constraint in the energy minimization, we employ the Lagrange multiplier method and minimize the functional

$$F = \int_{\mathcal{V}_P} \left( \frac{p}{\gamma - 1} + \frac{B^2}{2\mu_0} \right) dv - \frac{\mu}{\mu_0} (K - K_0), \quad (2.120)$$

where  $K_0$  is the magnetic helicity of the initial state. Variation with respect to  $\mu$  enforces the constraint  $K = K_0$ , while variation with respect to the vector potential  $\mathbf{A}$  gives

$$0 = \delta F = \delta W - \frac{\mu}{\mu_0} (\delta K - K_0) \quad (2.121)$$

$$= \int_{\mathcal{V}_P} \mathbf{B} \delta \mathbf{B} dv - \mu \int_{\mathcal{V}_P} (\delta \mathbf{A} \cdot \mathbf{B} + \mathbf{A} \cdot \delta \mathbf{B}) dv \quad (2.122)$$

$$= \int_{\mathcal{V}_P} (\mathbf{B} \cdot \nabla \times \delta \mathbf{A} - \mu \mathbf{A} \cdot \delta \mathbf{B} - \mu \mathbf{B} \cdot \delta \mathbf{A}) dv, \quad (2.123)$$

where  $\delta \mathbf{B} = \nabla \times \delta \mathbf{A}$ . We now write the first term as  $\mathbf{B} \cdot \nabla \times \delta \mathbf{A} = (\nabla \times \mathbf{B}) \cdot \delta \mathbf{A} + \nabla \cdot (\delta \mathbf{A} \times \mathbf{B})$ , and apply the divergence theorem to write

$$\int_{\mathcal{V}_P} \mathbf{B} \cdot \nabla \times \delta \mathbf{A} dv = \int_{\mathcal{V}_P} (\nabla \times \mathbf{B}) \cdot \delta \mathbf{A} dv + \int_{\delta \mathcal{V}_P} (\delta \mathbf{A} \times \mathbf{B}) \cdot d\mathbf{S}. \quad (2.124)$$

Without loss of generality, we can choose a gauge such that  $\delta \mathbf{A} \times d\mathbf{S} = 0$  on  $\delta \mathcal{V}_P$ ; the second term in equation (2.124) thus vanishes, and we find

$$\delta F = \int_{\mathcal{V}_P} (\nabla \times \mathbf{B} - \mu \mathbf{B}) \cdot \delta \mathbf{A} dv - \mu \int_{\mathcal{V}_P} \mathbf{A} \cdot \nabla \times \delta \mathbf{A} dv. \quad (2.125)$$

Note that here, the variation  $\delta \mathbf{A}$  is completely arbitrary, reflecting the possibility of magnetic field line reconnection. We wish now to prove that the second term of equation (2.125) vanishes. We write  $\nabla \times \delta \mathbf{A} = \delta \mathbf{B}$  and we make use of Faraday's law to write  $\delta \mathbf{B} = \nabla \times \mathbf{E} \delta t$  where  $\delta t$  is an infinitesimal time over which the plasma motion takes

place. We thus get

$$\mathbf{A} \cdot \delta \mathbf{B} = [\nabla \cdot (\mathbf{E} \times \mathbf{A} - \mathbf{E} \cdot \mathbf{B})] \delta t \quad (2.126)$$

$$= \nabla \cdot (\mathbf{E} \times \mathbf{A}) \delta t, \quad (2.127)$$

where we used Ohm's law (2.5) to find  $\mathbf{E} \cdot \mathbf{B} = 0$ . Finally, taking the integral over the plasma volume and applying the divergence theorem, we get

$$\int_{\mathcal{V}_P} \mathbf{A} \cdot \nabla \times \delta \mathbf{A} dv = \int_{\Gamma_{PB}} (\mathbf{E} \times \mathbf{A}) \cdot d\mathbf{S} \delta t = \int_{\Gamma_{PB}} \mathbf{A} \cdot (d\mathbf{S} \times \mathbf{E}) \delta t = 0, \quad (2.128)$$

where we applied the boundary condition  $d\mathbf{S} \times \mathbf{E} = 0$  on the plasma boundary  $\Gamma_{PB}$ . Equation (2.125) reduces then to

$$\int_{\mathcal{V}_P} (\nabla \times \mathbf{B} - \mu \mathbf{B}) \cdot \delta \mathbf{A} dv = 0, \quad (2.129)$$

which implies the Taylor equilibrium equation (2.61).

### 2.4.4 MRxMHD

The MRxMHD equilibrium equations derive as well from an energy principle (Dewar et al., 2015). As described in section 2.3, MRxMHD equilibria can be seen as a combination of nested Taylor states at equilibrium with one another. It is thus natural to define the energy functional as the sum of the Taylor's state energy functional relative to each volume, *i.e.*

$$F = \sum_{l=1}^{N_{vol}} \int_{\mathcal{V}_l} \left[ \frac{p}{\gamma - 1} + \frac{\mathbf{B}^2}{2\mu_0} \right] d\mathbf{x}^3 + \mu_l (K_l - K_{l,0}). \quad (2.130)$$

Minimization with respect to variations in the magnetic field leads to the Taylor state equation (2.74) in each volume  $\mathcal{V}_l$ , while variation with respect to the volume's boundary motion leads to the equilibrium condition (2.75). The derivation is rather tedious — further details can be found in the publication by Dewar et al. (2015).

## 2.5 Summary

This chapter introduced the ideal MHD model which can be used to describe plasma equilibria in stellarators. Important figures of merit were defined, in particular the normalized pressure,  $\beta$ , which is a crucial parameter for the efficiency of the reactor. We also discussed the different kinds of currents that are present in ideal MHD equilibria. The diamagnetic current is generated by the plasma to satisfy the force balance equation, while the Pfirsch-Schlüter current emerges in order to satisfy the charge conservation equation. Calculating the flux averaged current density of both currents, we showed that only the diamagnetic current contributes to setting a net toroidal current in the plasma, and only if there are other sources of net toroidal current — for example the bootstrap current, or externally driven currents. Furthermore, estimates showed that the net toroidal current in the system is dominated by the bootstrap and externally driven currents, which strongly motivates their inclusion in the calculation of any magnetic equilibria. As we shall see in chapter 5, the bootstrap current has indeed a strong effect on the equilibrium.

Furthermore, we discussed the singular properties of the Pfirsch-Schlüter current. Different classes of equilibria were proposed to keep the Pfirsch-Schlüter current integrable. In particular, we discussed the Taylor state, which is a force-free field that allows the emergence of magnetic islands and chaos, and the stepped-pressure equilibrium, where the pressure gradient is supported by a finite number of interfaces. We introduced the MRxMHD equilibrium equations, which describes the plasma as a set of nested Taylor states at constant pressure, with pressure discontinuities at the volume's interfaces. This class of equilibrium is of particular interest because it (i) allows the emergence of magnetic islands and magnetic field line chaos, (ii) describes equilibria with finite pressure gradients, (iii) does not have singular Pfirsch-Schlüter current densities, and (iv) has been proven to have solutions in 3D under some conditions. In this thesis, we will uniquely work with MRxMHD equilibria.

In this chapter, we also discussed some of the properties of the MRxMHD equilibria. We showed that there are two types of currents in MRxMHD equilibria, namely volume currents, that are parallel to the magnetic field and flow in the volumes, and surface currents, that are current sheets with zero width that flow at the volume's interfaces. Volume currents encompass all externally driven currents, while interface currents represent the pressure-driven currents and shielding currents that emerge when an ideal interface is positioned on a resonance.

Finally, we discussed how the ideal MHD, the Taylor state and the MRxMHD equilibrium equations could be derived from an energy principle. This property is exploited by different numerical codes to find 3D equilibria — indeed, the equilibrium can be directly computed from an initial state by minimizing an energy functional instead of computing the entire time evolution and trajectory of the plasma. While the

time evolution can be of great importance for some applications, it is often a waste of computational time and resources if only the equilibrium state is sought. For example, the VMEC code (Hirshman, 1983; Hirshman et al., 1986a) finds ideal 3D MHD equilibria by minimizing Eq.(2.25), and the SPEC code (Hudson et al., 2012a, 2020) can find MRxMHD equilibria by minimizing the equation (2.130). The next chapter will focus on describing the SPEC code, and how the capability to constraint the toroidal current profiles was implemented.

## 3 The stepped-pressure equilibrium code

The stepped-pressure equilibrium code (SPEC) was developed in the past decade to solve the MRxMHD equilibrium equations (see section 2.3). In 2012, Hudson et al. published a first version that computes fixed-boundary, stepped-pressure equilibria. Since then, SPEC has been upgraded to allow free-boundary calculations (Hudson et al., 2020) and to allow the prescription of a net toroidal current profile (Baillod et al., 2021) — the implementation of this constraint is explained in more detail in section 3.2. The numerical robustness of the code was (and is still being) continuously improved: Qu et al. (2020) improved the radial discretization and the numerical solvers in the innermost volume of the plasma, and a new representation for the interfaces of neighboring volume domains, based on the work by Henneberg et al. (2021a), has been implemented. Details about the implementation of this new representation in SPEC are given in section 3.3.

In addition to these numerical developments, SPEC has been extensively used in the past decade to study diverse physics topics. The code has been rigorously verified in stellarator geometry (Loizu et al., 2016), and has been successfully applied to study current sheets at rational surfaces (Loizu et al., 2015a,b; Huang et al., 2022), tearing mode stability (Loizu and Hudson, 2019) and nonlinear tearing saturation (Loizu et al., 2020), equilibrium  $\beta$ -limits in a classical stellarator (Loizu et al., 2017), the penetration and amplification of resonant magnetic perturbations in the ideal limit (Loizu et al., 2016), the modelling of the non-linear plasma response to resonant magnetic perturbations by allowing islands formation (Wright et al., 2022), the stability of MRxMHD equilibria (Kumar et al., 2021, 2022), relaxation phenomena in reversed field pinches such as the formation of helical states (Dennis et al., 2013) or the relaxation of flow during sawteeth (Dennis et al., 2014; Qu et al., 2020), and the modelling of ECCD induced sawteeth crashes in W7-X (Aleynikova et al., 2021).

In this chapter, an overview of the SPEC code is given. In section 3.1 some important parts of the SPEC algorithm are explained. In section 3.2 the implementation of the net toroidal current constraint is described. Section 3.3 discusses some limitations of SPEC that are related to its numerical fragility, and presents the implementation of a new angle representation, which is shown to be a step towards improving SPEC robustness. Finally, section 3.4 concludes the chapter with some summarizing remarks.

### 3.1 SPEC algorithm

We recall that MRxMHD describes the plasma as a collection of nested neighboring volumes  $\mathcal{V}_l$ , separated by interfaces  $\mathcal{I}_l$  (see Figure 2.6). The SPEC code solves the MRxMHD equilibrium equations (2.74)-(2.75), which we rewrite here for convenience:

$$\text{in } \mathcal{V}_l : \quad \nabla \times \mathbf{B} = \mu_l \mathbf{B} \quad (3.1)$$

$$\text{at } \mathcal{I}_l : \quad \left[ \left[ p + \frac{B^2}{2\mu_0} \right] \right]_l = 0 \quad (3.2)$$

$$\text{at } \mathcal{I}_l : \quad \mathbf{B} \cdot \mathbf{n} = 0, \quad (3.3)$$

with  $\mathbf{B}$  the magnetic field,  $\mu_l$  a constant specific to the volume  $\mathcal{V}_l$ ,  $[[\cdot]]_l$  denotes the discontinuity across the interface  $\mathcal{I}_l$ ,  $p$  is the pressure,  $\mu_0$  the vacuum permeability, and  $\mathbf{n}$  a vector normal to the interface  $\mathcal{I}_l$ . To solve these equations, SPEC is constructed as a number of nested loops. The innermost loop solves equation (3.1) to obtain the magnetic field in each volume  $\mathcal{V}_l$ , that satisfies the boundary condition, Eq.(3.3), given the geometry of their interfaces and some constraints — for example the rotational transform on each boundary of the volume can be imposed. Given the magnetic field in each volume, the force imbalance at each interface,  $[[p + B^2/2\mu_0]]_l$ , can be evaluated. The second loop is then an iteration over the geometry of the volume interfaces until the force balance condition (3.2) is satisfied. Finally, an additional but optional final loop iterates on the boundary condition of the outermost volume in case of free-boundary calculations (see section 3.1.4).

For a fixed-boundary calculation, one needs to provide a plasma boundary  $\Gamma_{PB}$ , a number of volumes  $N_{vol}$ , the pressure  $p_l$ , and the enclosed toroidal flux  $\Delta\psi_{t,l} = \psi_{t,l+1} - \psi_{t,l}$  in each volume, with  $\psi_{t,l}$  the toroidal flux enclosed by the interface  $\mathcal{I}_l$ , and with  $l \in \{1, \dots, N_{vol}\}$ . As discussed in section 2.2, the magnetic field in each annular volume requires two additional constraints to be fully determined, for example  $\mu_l$  and the poloidal flux  $\Delta\psi_{p,l} = \psi_{p,l+1} - \psi_{p,l}$ , with  $\psi_{p,l}$  the poloidal flux enclosed by the interface  $\mathcal{I}_l$ . In the first volume, only one additional constant,  $\mu_1$ , is required to fully determine the magnetic field. Note that SPEC can be run with different constraints; one can constrain for example the toroidal flux in each volume and the rotational transform on each side of the volume's interfaces ( $\Delta\psi_{t,l}, t_-, t_+$ ). We will in particular describe in section 3.2 how

the capability to run at fixed net toroidal current profile has been implemented, *i.e.* how one can constrain the net toroidal current in each volume and at each volume interface (see section 2.3.1). We discuss now how, given these inputs, SPEC finds fixed-boundary equilibria.

### 3.1.1 Parameterization of interfaces and magnetic field

Using the standard cylindrical coordinate system  $(R, \phi, Z)$ , the plasma boundary  $\Gamma_{PB}$  is parameterized by  $R(\theta, \phi)$ ,  $Z(\theta, \phi)$ , where  $\theta$  is an as-of-yet undetermined poloidal angle, and  $\phi$  is the usual cylindrical angle. Toroidal surfaces can be written as double Fourier series in the toroidal and poloidal directions, thereafter named the *standard representation*,

$$R(\theta, \phi) = \sum_{m=0}^{M_{pol}} \sum_{n=-N_{tor}}^{N_{tor}} R_{mn} \cos(m\theta - nN_{fp}\phi) \quad (3.4)$$

$$Z(\theta, \phi) = \sum_{m=0}^{M_{pol}} \sum_{n=-N_{tor}}^{N_{tor}} Z_{mn} \sin(m\theta - nN_{fp}\phi), \quad (3.5)$$

where  $M_{pol}$  and  $N_{tor}$  are the maximum poloidal mode number  $m$  and toroidal mode number  $n$  respectively,  $R_{mn}$  and  $Z_{mn}$  are the Fourier modes of  $R$  and  $Z$  respectively, and  $N_{fp}$  is the number of field periods (discrete symmetry) of the system. Note that we assumed stellarator symmetry (Dewar and Hudson, 1998) to lighten the notation. If stellarator symmetry was not assumed, both  $R$  and  $Z$  Fourier series would have odd and even terms (sine and cosine series), thereby doubling the number of Fourier harmonics required to describe the surface.

Each volume's interface  $\mathcal{I}_l$  is represented by such Fourier series, with modes  $\{R_{mn}^l, Z_{mn}^l\}$ . Between each interface, SPEC uses toroidal coordinates  $(s, \theta, \phi)$  (see Figure 3.1), where  $s \in [-1, 1]$  is a radial-like coordinate. In each volume  $\mathcal{V}_l$ , coordinates  $\mathbf{x} = R(s, \theta, \phi)\mathbf{e}_R + Z(s, \theta, \phi)\mathbf{e}_Z$  are constructed by interpolation between the volumes' interfaces, *i.e.*

$$R(s, \theta, \phi) = R_{l-1}(\theta, \phi) + [R_l(\theta, \phi) - R_{l-1}(\theta, \phi)]f_{lmn}(s) \quad (3.6)$$

$$Z(s, \theta, \phi) = Z_{l-1}(\theta, \phi) + [Z_l(\theta, \phi) - Z_{l-1}(\theta, \phi)]f_{lmn}(s), \quad (3.7)$$

with  $f_{lmn}$  given by

$$f_{lmn} = \begin{cases} \frac{1+s}{2} & \text{if } l \neq 1 \text{ or } m = 0 \\ \left(\frac{1+s}{2}\right)^m & \text{if } l = 1 \text{ and } m \neq 0, \end{cases} \quad (3.8)$$

where the power law in  $m$  is chosen in order to regularize the coordinates in the innermost volume ( $l = 1$ ) close to the magnetic axis. The innermost volume, which contains the magnetic axis, is particular in the sense that a coordinate axis,  $(R_0(\phi), Z_0(\phi))$ , has to be chosen. A clever algorithm that maximizes the coordinate jacobian in the first volume

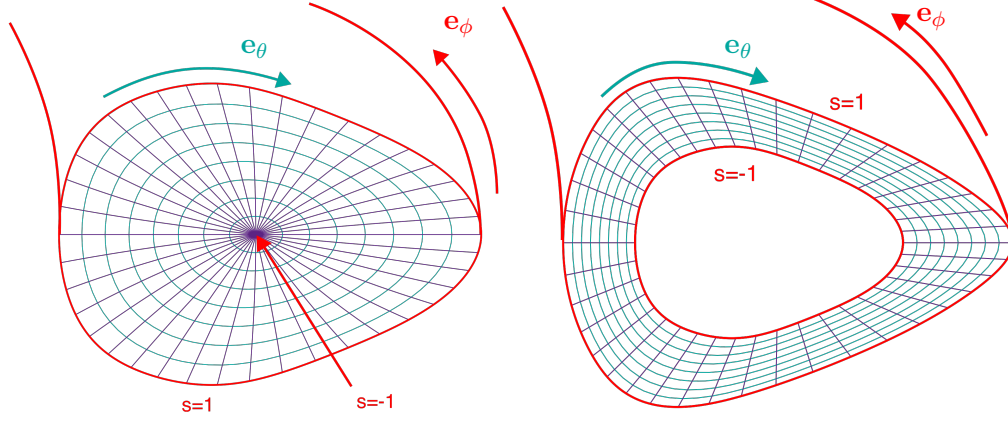


Figure 3.1: Sketch of the coordinate system used in SPEC, in a toroidal volume (left) and an annular volume (right). In red: volume interfaces, at  $s = \pm 1$ . In blue: constant- $s$  surfaces. In purple: constant- $\theta$  surfaces.

by moving the coordinate axis was implemented, so that ill-defined coordinate systems are more easily avoided, ensuring well-defined coordinate mappings for star-like domains (Qu et al., 2020). Coordinate covariant and contravariant basis are easily computed (see appendix A.2).

The poloidal angle  $\theta$  is an as-of-yet undetermined angle. In SPEC, the poloidal angle on an interface  $\mathcal{I}_l$  is chosen so that the required number of Fourier harmonics is minimized. In appendix A.3 we discuss how this so-called spectral condensation is implemented. For the purpose of the discussion, we simply mention here that the poloidal angle on  $\mathcal{I}_l$  is chosen such that a certain function, which we call here  $Y_l(\theta, \phi)$ , is set to zero. Expressed on a Fourier basis, we get

$$Y_l = \sum_{m=0}^{M_{pol}} \sum_{n=-N_{tor}}^{N_{tor}} Y_{lmn} \sin(m\theta - nN_{fp}\phi), \quad (3.9)$$

where again stellarator symmetry has been assumed.

In each volume  $\mathcal{V}_l$ , the covariant component of the magnetic field vector potential  $\mathbf{A}_l$ ,

$$\mathbf{A}_l = A_{l,s} \nabla s + A_{l,\theta} \nabla \theta + A_{l,\phi} \nabla \phi, \quad (3.10)$$

is expanded on a polynomial basis in the radial direction and a double Fourier series in the poloidal and toroidal directions,

$$A_{l,i} = \sum_{k=0}^{L_{rad}} \sum_{m=0}^{M_{pol}} \sum_{n=-N_{tor}}^{N_{tor}} A_{likmn} T_{km}(s) \cos(m\theta - nN_{fp}\phi), \quad (3.11)$$

where  $i = \{s, \theta, \phi\}$ , the polynomials  $T_{km}(s)$  are Zernike polynomials in the innermost



volume (Qu et al., 2020), and  $T_{km} = T_k$  are Chebyshev polynomials in the other volumes, and  $L_{rad}$  is the highest considered order of the polynomials. Note that gauge freedom is used to set  $A_{l,s} = 0 \forall l$ . The magnetic field is then given by

$$\mathbf{B}_l = \frac{\mathbf{e}_s}{\sqrt{g}} \sum_{k=0}^{L_{rad}} \sum_{m=0}^{M_{pol}} \sum_{n=-N_{tor}}^{N_{tor}} -(mA_{l\phi kmn} + nA_{l\theta kmn})T_{km}(s) \sin(m\theta - nN_{fp}\phi) \quad (3.12)$$

$$+ \frac{\mathbf{e}_\theta}{\sqrt{g}} \sum_{k=0}^{L_{rad}} \sum_{m=0}^{M_{pol}} \sum_{n=-N_{tor}}^{N_{tor}} -A_{l\phi kmn}T'_{km}(s) \cos(m\theta - nN_{fp}\phi) \quad (3.13)$$

$$+ \frac{\mathbf{e}_\phi}{\sqrt{g}} \sum_{k=0}^{L_{rad}} \sum_{m=0}^{M_{pol}} \sum_{n=-N_{tor}}^{N_{tor}} A_{l\theta kmn}T'_{km}(s) \cos(m\theta - nN_{fp}\phi), \quad (3.14)$$

where the prime denotes the derivative.

### 3.1.2 Beltrami solver

At the core of SPEC stands the *Beltrami solver*, which finds the magnetic field that satisfies the Beltrami equation (2.74) given the volume interfaces geometry and the input profiles. We first remark that the constraints given by the fluxes ( $\Delta\psi_{p,l}, \Delta\psi_{t,l}$ ) depend linearly on the vector potential harmonics. Indeed, using Eqs(3.13)-(3.14), we obtain

$$\Delta\psi_{t,l} = \iint_{S[\phi=\text{const}]} B^\phi \sqrt{g} d\theta ds = 2\pi \sum_{k=0}^{L_{rad}} A_{l\theta k00} [T_{k0}(1) - T_{k0}(-1)] \quad (3.15)$$

$$\Delta\psi_{p,l} = \iint_{S[\theta=\text{const}]} B^\theta \sqrt{g} d\phi ds = -2\pi \sum_{k=0}^{L_{rad}} A_{l\phi k00} [T_{k0}(1) - T_{k0}(-1)] \quad (3.16)$$

Similarly, the boundary conditions, *i.e.* enforcing the volumes interfaces to be magnetic surfaces, is set by requiring  $B^s = 0$ . Using Eq.(3.12), we obtain

$$\sum_{k=0}^{L_{rad}} (mA_{l\phi kmn} + nA_{l\theta kmn})T_{km}(\pm 1) = 0. \quad (3.17)$$

Finally, the Beltrami equation (2.74) can be written as a linear system by minimizing the MHD energy functional, Eq.(2.120), while constraining the enclosed poloidal and toroidal fluxes, and while satisfying the boundary conditions (3.17) — see appendix A.4 for more details. We can then construct matrices  $\mathbf{G}_l$ ,  $\mathbf{D}_l$  and  $\mathbf{C}_l$ , and we write

$$\left( \mathbf{G}_l[X_{mn}^l, X_{mn}^{l+1}] - \mu_l \mathbf{D}_l[X_{mn}^l, X_{mn}^{l+1}] \right) \mathbf{a}_l = \mathbf{C}_l[\Delta\psi_{p,l}, \Delta\psi_{t,l}], \quad (3.18)$$

where  $\mathbf{a}_l$  is an array where, in particular, the coefficients  $A_{likmn}$  are packed, and the  $X_{mn}^l$  are the  $R_{mn}^l$  and  $Z_{mn}^l$  harmonics.

Solving Eq.(3.18) provides the vector potential harmonics  $\mathbf{a}_l$  consistent with the volume's geometry, the constant  $\mu_l$ , and the enclosed fluxes  $(\Delta\psi_{t,l}, \Delta\psi_{p,l})$ . If the input profiles are the rotational transform  $\iota_l^\pm$  on the inner and outer boundary of the volume  $\mathcal{V}_l$ , initial guesses for  $(\mu_l, \Delta\psi_{p,l})$  are used for a first Beltrami solve. The Beltrami field is then solved multiple times for different values of  $(\mu_l, \Delta\psi_{p,l})$  until the rotational transform constraint is matched. Note that the matrices  $\mathbf{G}_l$  and  $\mathbf{D}_l$ , which require multiple volume integral evaluations, are expensive to evaluate. They however only depend on the volume geometry. Consequently, these matrices do not have to be recalculated for each new set of values of  $(\mu_l, \Delta\psi_{p,l})$ . We finally remark that the rotational transform  $\iota_l^\pm$  only depends on the magnetic field in volume  $\mathcal{V}_l$  — we say that it is a *local constraint* to the volume  $\mathcal{V}_l$ . This is different from *global constraints*, that depend on the magnetic field in multiple volumes. An example of a global constraint is the net toroidal current constraint, discussed in section 3.2.

The output of the Beltrami solver is the magnetic field  $\mathbf{B}_l$  in agreement with the constraint and the volume geometry. As an example, we compute now the solution to the Beltrami equation (2.74) in the W7-X geometry (see Figure 3.2a). We consider here only one volume,  $N_{vol} = 1$ , meaning that the pressure is flat in all the plasma. There is no pressure gradient, thus the absolute value of the pressure is irrelevant and we set it to zero. As we consider a single volume, there are no interfaces where the magnetic field line topology is constrained, excepted on the plasma boundary. Finally, we set the toroidal flux enclosed by the plasma boundary to  $\psi_{t,1} = 2\text{Tm}^2$  — note however that this parameter only scales the modulus of the magnetic field. We solve the Beltrami equation for  $\mu_1 = 0$  (*i.e.* in a vacuum), and for  $\mu_1 = -8 \cdot 10^{-2}$ , meaning that a net toroidal current is flowing in the volume, as  $I_{\phi,1}^v = \mu_1 \psi_{t,1}$ . Here, we set  $M_{pol} = N_{tor} = 10$ , and  $L_{rad} = 16$ . The Poincaré section of the magnetic field is plotted for different toroidal angles on the middle and lower panels of Figure 3.2, and the rotational transform profile for both cases is plotted on Figure 3.3. Note that the negative sign of  $\iota$  is due to the definition of the poloidal angle  $\theta$  (see Figure 3.1). We see that, as expected, imposing a net toroidal current in the plasma shifts the rotational transform profile — in vacuum, the rotational transform crosses the  $\iota = 5/6$  resonance, and an island chain opens with a 6-fold periodicity in the poloidal direction, as measured experimentally (see Figure 1.13b). With  $\mu = -8 \cdot 10^{-2}$ , the rotational transform crosses now the  $\iota = 5/5$  resonance, and an island chain with a 5-fold periodicity in the poloidal direction opens.

To evaluate MRxMHD equilibria with multiple volumes,  $N_{vol} > 1$ , the SPEC code needs to evaluate the force at each interface  $\mathcal{I}_l$ , given the magnetic field  $\mathbf{B}$  in each volume. We discuss now how the force is evaluated, and how SPEC iterates on the geometrical degrees of freedom to set the force to zero.

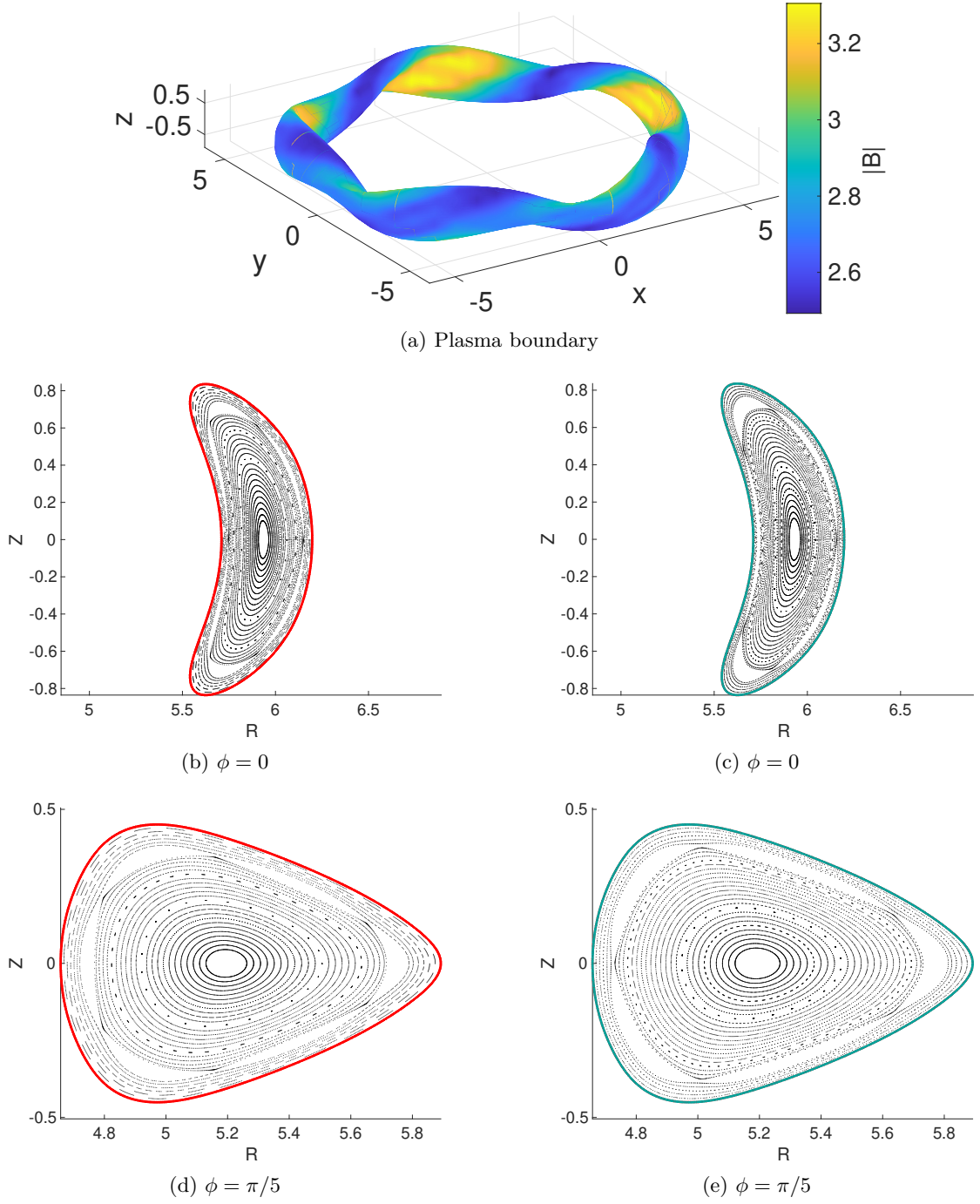


Figure 3.2: Top: W7-X geometry. Colors indicate the magnetic field strength obtained with SPEC on the plasma boundary in vacuum. Middle and bottom: Poincaré section of the Beltrami field evaluated by SPEC in W7-X geometry. Left: vacuum field, with  $\mu = 0$ . Right:  $\mu = -0.08$ .

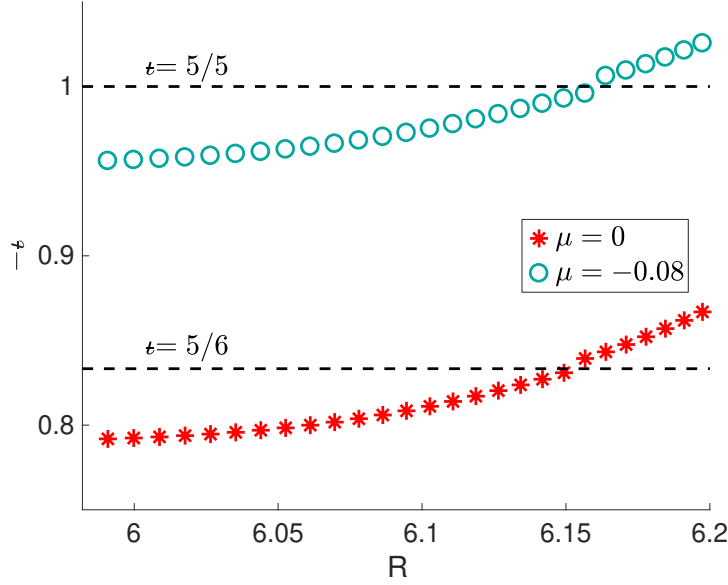


Figure 3.3: Rotational transform profiles in W7-X for two different values of  $\mu$ , as evaluated by SPEC. The value of  $R$  labels the starting point of the field-line tracing, at  $\phi = 0$ ,  $Z = 0$ .

### 3.1.3 Force solver

SPEC searches the geometry of the volume interfaces  $\mathcal{I}_l$ ,  $l \in \{1, \dots, N_{vol} - 1\}$ , that minimizes (i) the physical force density, *i.e.* Eq.(2.75) and (ii) the spectral constraint, *i.e.* Eq.(3.9). We denote by  $\mathbf{X}$  the array where all geometrical degrees of freedom, *i.e.* all  $\{X_{mn}^l\} = \{R_{mn}^l, Z_{mn}^l\}$ , are packed. In total, there are  $(N_{vol} - 1)N_x$  geometrical degrees of freedom, with  $N_x$  the number of Fourier harmonics per interface,

$$N_x = 2[N_{tor} + M_{pol}(2N_{tor} + 1)] + 1. \quad (3.19)$$

The physical force density is an even function of the poloidal and toroidal angles, and can be written as a double Fourier series

$$F_l(\theta, \phi) = \left[ \left[ p + \frac{B^2}{2\mu_0} \right] \right]_l = \sum_{m=0}^{\infty} \sum_{n=-\infty}^{\infty} F_{lmn} \cos(m\theta - nN_{fp}\phi). \quad (3.20)$$

The double Fourier series requires an infinite number of Fourier harmonics, because of the nonlinear  $B^2$  term in the force. In SPEC, the assumption is however made that the Fourier resolution set by the user is high enough to capture the dominant force harmonics by truncating the force at  $(M_{pol}, N_{tor})$ , *i.e.*

$$F(\theta, \phi) \approx \sum_{m=0}^{M_{pol}} \sum_{n=-N_{tor}}^{N_{tor}} F_{lmn} \cos(m\theta - nN_{fp}\phi). \quad (3.21)$$

Only the force harmonics with  $m \leq M_{pol}$ ,  $|n| \leq N_{tor}$  are then considered in SPEC algorithm. As discussed later in the conclusion of this chapter, this particular choice in SPEC's implementation might be one source of numerical fragility in the case of strongly shaped stellarator geometries, *i.e.* in configuration with either large torsion or elongation.

Given the magnetic field in each volume computed by the Beltrami solver (see section 3.1.2), one can evaluate the magnetic field on a  $(\theta, \phi)$  grid on each side of each interface using Eqs.(3.12)-(3.14). Taking the difference between the outer and inner side, and performing a Fourier transformation gives the Fourier harmonics  $F_{lmn}$ . All Fourier harmonics of the (truncated) physical force and of the spectral constraint are packed in a single array, thereafter named  $\mathbf{F}$ . Using a hybrid-Powell method (Powell, 1971), which is a modified Newton method, SPEC will then iterate on all geometric degrees of freedom of the interfaces,  $\mathbf{X}$ , until all elements of  $\mathbf{F}$  are smaller than a tolerance set by the user. Analytical derivatives of  $\mathbf{F}$  with respect to the interface geometry harmonics  $\mathbf{X}$  are provided to speed up the calculation. Details about the computation of the force derivatives are given in the case of the toroidal current constraint in section 3.2.2.

It is important to remark that while Newton-like methods are fast to converge towards the root of a function if a good initial guess is provided, these methods can also get stuck in local minima, or diverge, if the initial guess is too far from the solution. As it will be illustrated in section 3.3, SPEC sometimes requires a very good initial guess for the geometry of the interfaces to find the solution to  $\mathbf{F} = 0$ , when considering strongly shaped stellarator geometries with large elongation or torsion.

Let us finally introduce a useful scalar, thereafter named *force scalar*, to represent the force-balance convergence of SPEC, provided by the  $L^2$ -norm of  $\mathbf{F}$ ,

$$|f| = \frac{1}{N_f} \sqrt{\sum_{l=1}^{N_{vol}-1} \sum_{m=0}^{M_{pol}} \sum_{n=-N_{tor}}^{N_{tor}} (F_{lmn})^2 + (Y_{lmn})^2}, \quad (3.22)$$

with  $N_f$  the number of elements in  $\mathbf{F}$ , which can be easily evaluated to

$$N_f = (N_{vol} - 1) \{2[N_{tor} + M_{pol}(2N_{tor} + 1)] + 1\}, \quad (3.23)$$

which is equal to the number of geometrical degrees of freedom  $N_x(N_{vol} - 1)$ , with  $N_x$  given by Eq.(3.19).

As an example, let us consider once again the W7-X geometry (see Figure 3.2a). We now compute a MRxMHD equilibrium with two volumes,  $N_{vol} = 2$ , and attempt at retrieving the vacuum field obtained with  $N_{vol} = 1$  (see Figure 3.2). We set the profiles to  $p_l = \mu_l = 0$  for  $l = \{1, 2\}$ , and choose the toroidal flux enclosed by each interface to be  $\psi_{t,1} = 0.75\text{Tm}^2$ , and  $\psi_{t,2} = 2\text{Tm}^2$ . The poloidal flux enclosed by the second interface,  $\psi_{p,2}$ , needs to be carefully chosen to ensure that there is no net toroidal current at the

volume's interface  $\mathcal{I}_1$ . Here, we assume that this particular poloidal flux is known, and we set  $\psi_{p,2} = -5.22 \cdot 10^{-1} \text{Tm}^2$ ; we will describe in section 3.2 how it can be obtained. We interpolate an initial guess for the geometry of  $\mathcal{I}_1$  from the geometry of the plasma boundary. Evaluating the Beltrami field using the initial guess for the geometry of  $\mathcal{I}_1$ , SPEC evaluates a force scalar of  $|f| = 3.14 \cdot 10^{-2}$ . After 150 iterations on the interface geometry, SPEC eventually finds the  $\mathcal{I}_1$  geometry for which  $|f|$  is of the order of machine precision, and thus satisfies the equations (2.74) and  $F_{lmn} = Y_{lmn} = 0$  for  $m \leq M_{pol}$ ,  $|n| \leq N_{tor}$  — see the top left panel of Figure 3.4. As expected, SPEC retrieves the same magnetic field as obtained with a single vacuum volume, with the same rotational transform profile (see top right panel of Figure 3.4). Again, we observe an island chain with a 6-fold periodicity in the poloidal direction (see the bottom panels of Figure 3.4).

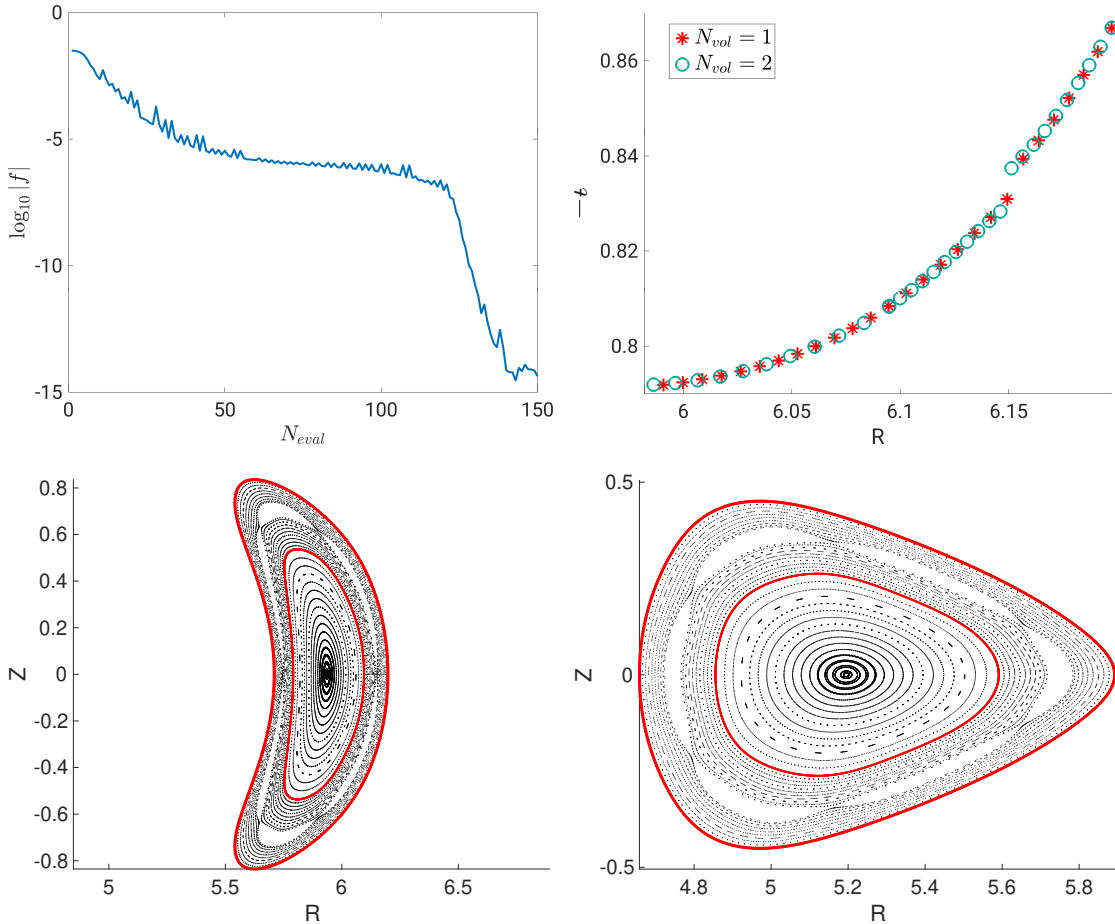


Figure 3.4: SPEC computation of a W7-X vacuum field with  $N_{vol} = 2$ . Top left: force scalar (3.22) as a function of the number of Beltrami solve. Top right: rotational transform profile. Bottom: Poincaré section, with  $\phi = 0$  on the left and  $\phi = \pi/5$  on the right. The innermost red surface is  $\mathcal{I}_1$ , while the outermost red surface is the plasma boundary.

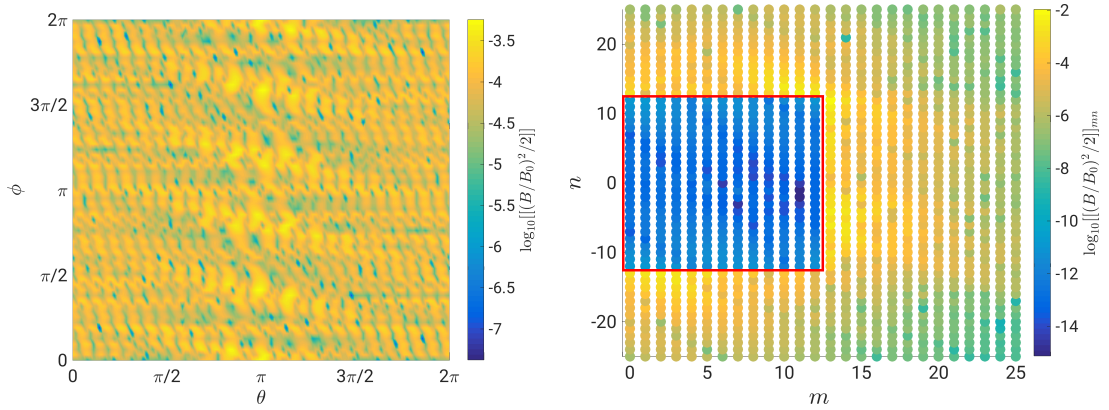


Figure 3.5: Normalized residual force on an interface of a W7-X vacuum SPEC equilibrium. Left: real space. Right: Fourier space. The red box surrounds the space of Fourier harmonics that are not truncated.

On Figure 3.5 is plotted the normalized force residual evaluated at the interface  $\mathcal{I}_1$ ,  $[(B/B_0)^2/2]$ , with  $B_0$  the magnetic field strength on axis. In real space (left panel), we see that the force is *not* zero, and is of the order of  $10^{-2}$ . In Fourier space (right panel) however, the Fourier modes  $F_{lmn}$  with  $m \leq M_{pol}$  and  $|n| \leq N_{tor}$  are all of the order of  $10^{-12}$ , *i.e.* close to machine precision. The Fourier modes  $F_{lmn}$  with  $m > M_{pol}$  or  $|n| > N_{tor}$ , are however much larger, of the order of  $10^{-2}$ . Interestingly, the largest Fourier modes of the force are the modes  $(m, n) = (M_{pol} + 1, n)$  and  $(m, n) = (m, \pm(N_{tor} + 1))$ . Clearly, SPEC only minimizes the Fourier harmonics of the force that are not truncated, meaning that the force in real space is not necessarily minimized. One must then be careful to set the truncation  $M_{pol}, N_{tor}$  sufficiently high so that SPEC minimizes all relevant modes of the force. Indeed, one can show that the residual force evaluated in real space decreases as the resolution is increased (Loizu et al., 2016).

We remark that the agreement between the vacuum calculations with  $N_{vol} = 1$  and  $N_{vol} = 2$  only occurs because the vacuum magnetic field possesses magnetic surfaces, and, in particular, because we positioned  $\mathcal{I}_1$  on a magnetic surface for the  $N_{vol} = 2$  calculation. Note that computing this vacuum magnetic field while assuming the existence of magnetic surfaces everywhere, for example by using the VMEC code, would lead to a different result than what has been obtained with SPEC. Indeed, if one enforces the existence of a magnetic surface at the  $\iota = 5/6$  resonance, a current sheet  $\Delta_{65}\delta(\psi_t - \psi_{t,65})$  would emerge (see section 2.1.4), with  $\psi_{t,65}$  the toroidal flux enclosed by the  $\iota = 5/6$  resonance. Resolving such current sheet in VMEC requires an infinite radial resolution. Even if this current sheet was resolved, it would modify the global solution for the magnetic field, and therefore not provide the correct solution.

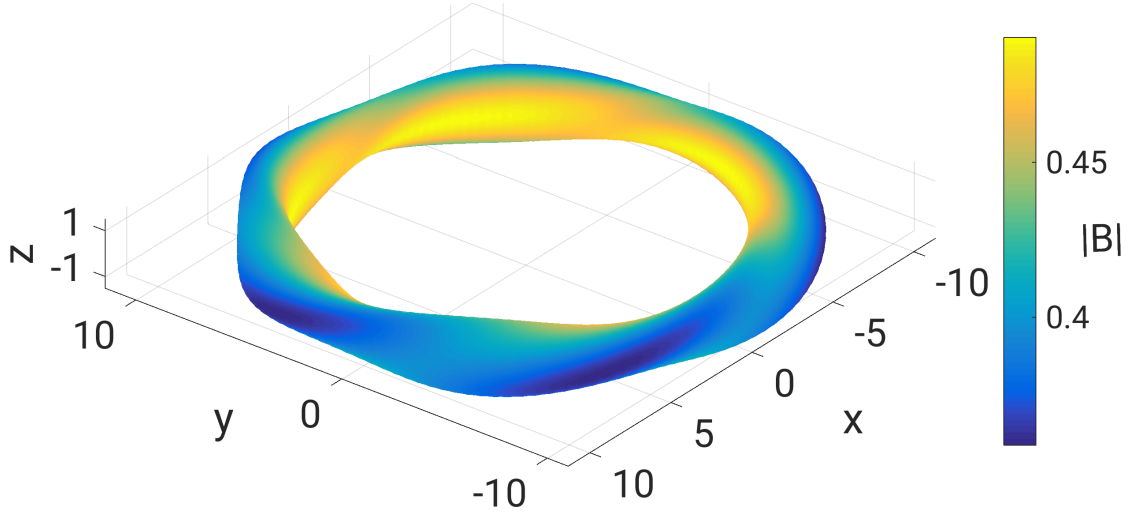


Figure 3.6: Rotating ellipse. Colors indicate the magnetic strength on the boundary in vacuum, as evaluated by SPEC.

We now show an example where the magnetic equilibrium is evaluated in a plasma with a non-trivial pressure profile. We consider a five field period classical stellarator geometry, also called a rotating ellipse (see Figure 3.6), whose boundary is described by

$$R(\theta, \phi) = 10 - 0.25 \cos \theta - 1.25 \cos(\theta - 5\phi) \quad (3.24)$$

$$Z(\theta, \phi) = -0.25 \sin \theta + 1.25 \sin(\theta - 5\phi). \quad (3.25)$$

We construct a continuous pressure profile  $p = p_0(1 - \psi_t/\psi_a)^2$ , and approximate it with seven equi-pressure steps supported by seven interfaces,  $\mathcal{I}_l$ ,  $l = \{1, \dots, 7\}$ , which, together with the plasma boundary, define eight plasma volumes (see top panel of Figure 3.7). We interpolate an initial guess for the geometry of each  $\mathcal{I}_l$  from the plasma boundary, and run SPEC once in vacuum, and once at finite  $\beta$ . For the vacuum calculation, we set  $p_0 = 0$ ,  $\mu_l = 0$  for  $l = \{1, \dots, 8\}$ , and choose the poloidal flux in each volume such that there are no current sheets at the volume interfaces. For the finite- $\beta$  calculation, we keep the same  $\mu$ - and  $\psi_p$ -profiles, but raise the pressure to  $\mu_0 p_0 = 5 \cdot 10^{-3} \text{T}^2$ , which gives a plasma averaged  $\beta$  of 0.67%. The Poincaré section of both equilibria are plotted at  $\phi = 0$  on the lower panels of Figure 3.7. We observe that the magnetic surfaces in the finite-pressure equilibrium are pushed outwards; this is the so-called *Shafranov shift* (Freidberg, 2014). On the top left panel, the force scalar (3.22) is shown to decrease from  $\sim 10^{-2}$  down to machine precision in 38 and 81 iterations on the  $\mathcal{I}_l$  geometries, respectively. As expected, the finite pressure equilibrium calculation requires more iterations, as the surfaces are further away from the initial guess that is provided for the volumes' interfaces geometry. The rotational transform profiles are plotted on the top right panel of Figure 3.7. While the vacuum field rotational transform profile is continuous, the rotational transform profile of the finite- $\beta$  equilibrium is not. This is expected, since in order to satisfy the



constraint on the poloidal flux, current sheets are generated at the volumes' interfaces (see section 2.3.1).

The normalized force residual on the seventh interface,  $[(B/B_0)^2/2]_7$ , evaluated for the finite- $\beta$  equilibrium found by SPEC, is shown in Figure 3.8. As in the case of the W7-X geometry, the residual force in real space is larger than machine precision, though in the case of the rotating ellipse, the force residual is about an order of magnitude smaller. Again, the Fourier harmonics of the force with  $m \leq M_{pol}$  and  $|n| \leq N_{tor}$  are successfully minimized by SPEC down to machine precision; there are however other modes, with  $m > M_{pol}$  or  $|n| > N_{tor}$ , that are of the order of  $10^{-4}$ . We remark that in the case of the rotating ellipse, the spectrum of modes that are not minimized is more narrow than in the case of the W7-X geometry. This is a reflection of the fact that the magnetic field, and therefore the interface geometry, require less Fourier modes to be accurately described in a simple geometry as a rotating ellipse than in a complex geometry as W7-X. We conclude that while SPEC is able to find an interface geometry that minimizes the Fourier harmonics of the force below a certain truncation, the truncation has to be large enough to represent both the magnetic field and the geometry of the interfaces.

It is worth noting that even though the magnetic helicity is not conserved when SPEC iterates on  $\{R_{mn}^l, Z_{mn}^l\}$  to find an equilibrium that matches a given input  $\{\Delta\psi_{t,l}, \Delta\psi_{p,l}, \mu_l\}_{l=1,\dots,N_{vol}}$  or  $\{\Delta\psi_{t,l}, \epsilon_l^+, \epsilon_l^-\}_{l=1,\dots,N_{vol}}$ , the final equilibrium satisfies the MRxMHD equilibrium equations given by Eqs.(2.74)-(2.75). There is in fact a magnetic helicity profile  $\{K_l\}_{l=1,\dots,N_{vol}}$  corresponding to this equilibrium which is unknown *a priori*. Thus, the same equilibrium could have been found by minimizing the MRxMHD energy functional while keeping the magnetic helicity profile constant if the initial state had the same magnetic helicity profile (bifurcations are not considered in this thesis). This capability is also available in SPEC, and details can be found in the literature (Hudson et al., 2012b; Dennis et al., 2013).

We have thus far discussed how SPEC evaluates fixed-boundary equilibria. First, the Beltrami solver finds the magnetic field in each volume consistent with the volume's geometry and the input profiles. Then SPEC evaluates the force on each interface, and iterates on the interfaces geometry until the force is below a tolerance set by the user. This algorithm is summarized in Figure 3.9. In the next section, we explain how an additional loop on fixed-boundary calculations can be used to evaluate free-boundary equilibria.

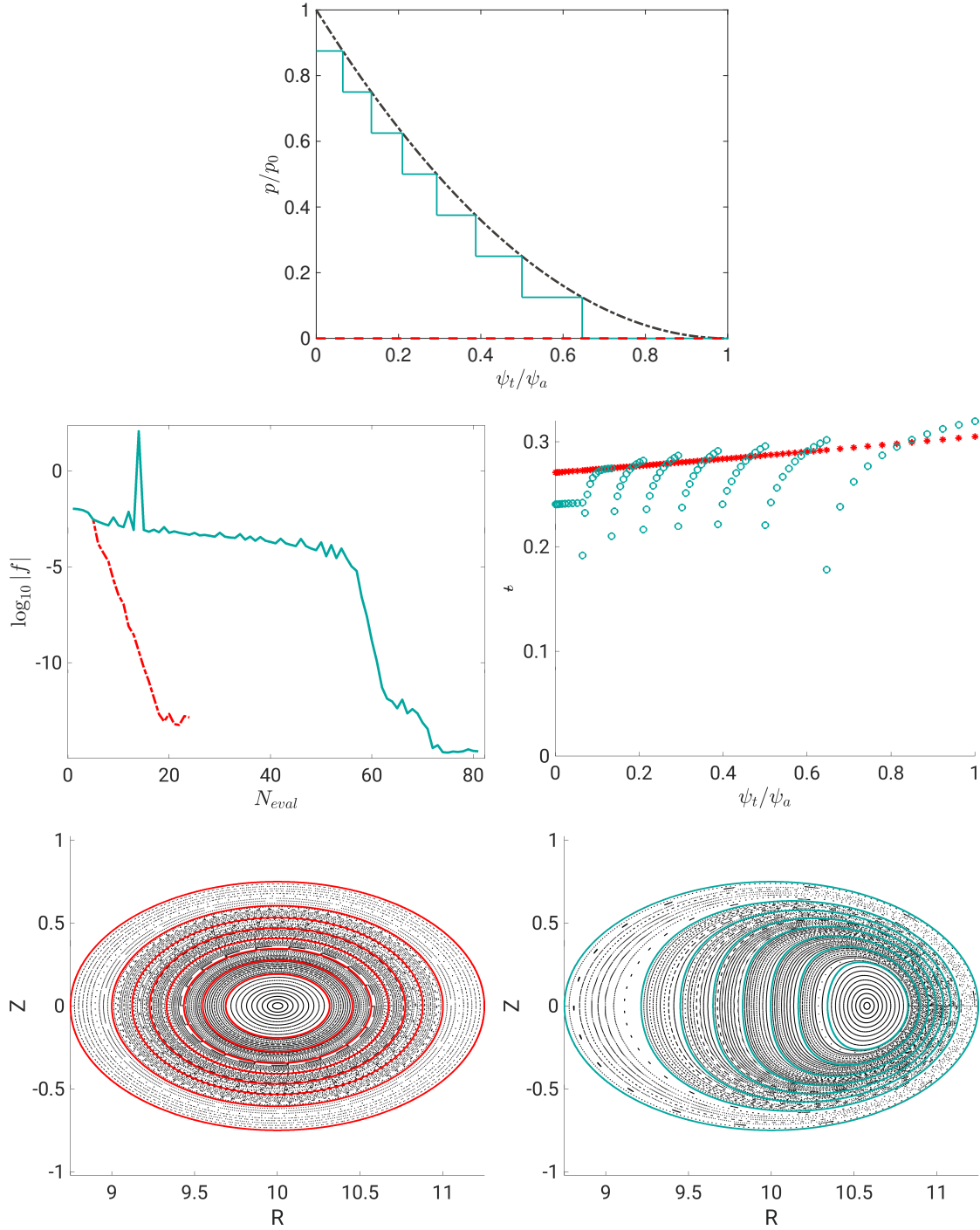


Figure 3.7: Vacuum and finite  $\beta$  fixed-boundary equilibria computed with the SPEC code. Top: Pressure profile. Black: continuous pressure profile. In blue: finite pressure ( $p_0 = 5 \cdot 10^{-3}$ ), and in red: vacuum field ( $p_0 = 0$ ). Middle left: force scalar, as defined by Eq.(3.22), as a function of the number of iterations on the volumes' interfaces geometry. Middle right: rotational transform profile. Bottom: Poincaré section at  $\phi = 0$ , in vacuum (left) and at  $\beta = 0.67\%$  (right). Colored lines are the volumes interface.

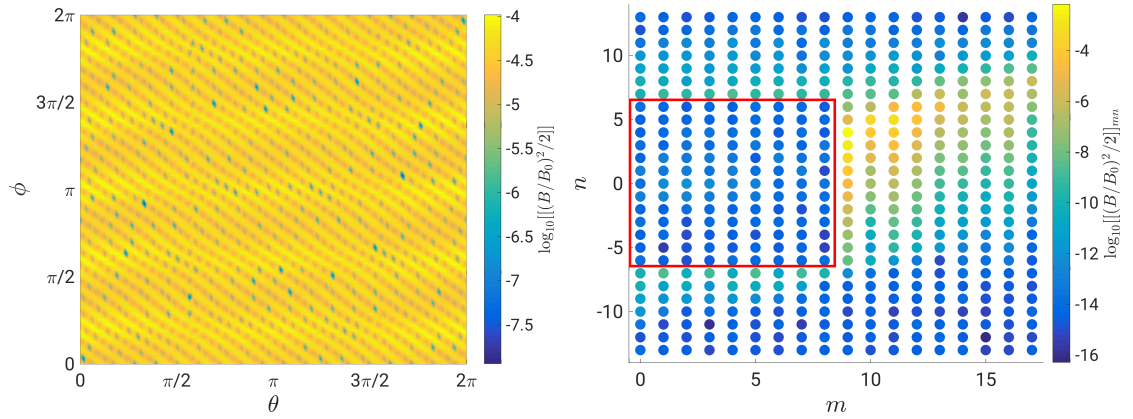


Figure 3.8: Normalized residual force in real space (left) and in Fourier space (right) on an interface of an equilibrium found by SPEC in a rotating ellipse geometry at finite  $\beta$ . The red box surrounds the space of Fourier harmonics that are not truncated.

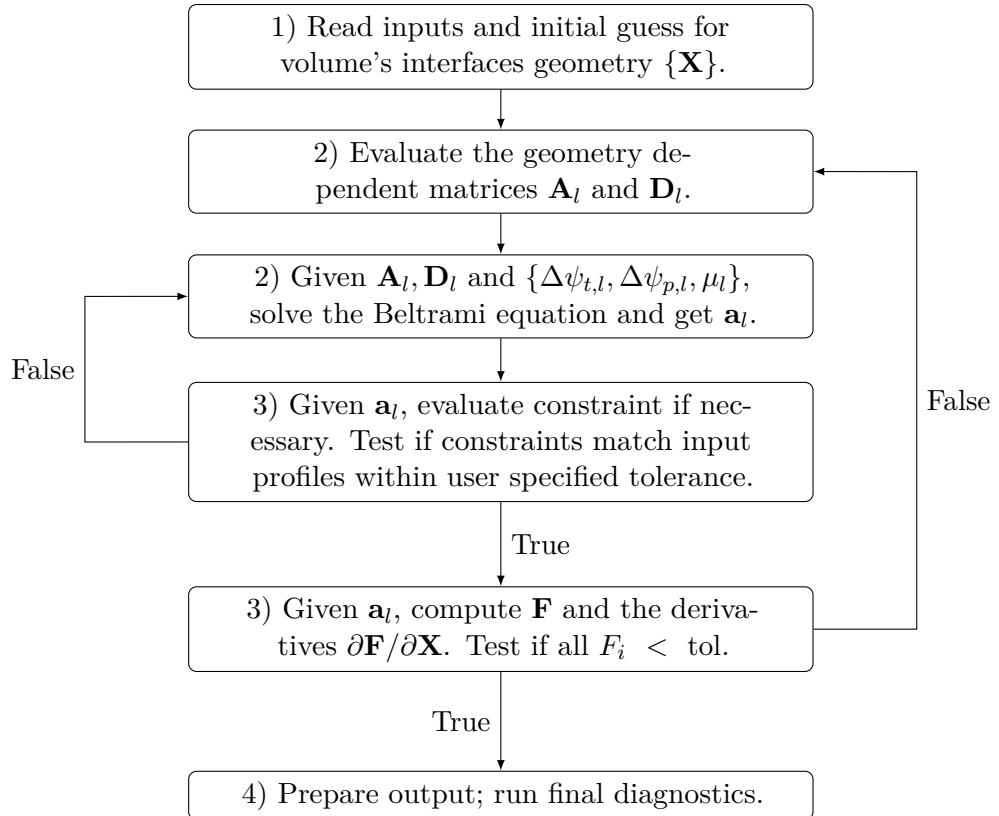


Figure 3.9: Main components of the fixed-boundary SPEC algorithm

### 3.1.4 Free-boundary iterations

In the case of free-boundary calculations, the plasma is allowed to move in a vacuum. We define a toroidal computational boundary  $\Gamma_{CB}$  outside the plasma and inside the coils (see Figure 3.10). This boundary is an otherwise arbitrary mathematical surface, and is generally not a magnetic surface, *i.e.*  $\mathbf{B} \cdot \mathbf{n} = (\mathbf{B}^c + \mathbf{B}^p) \cdot \mathbf{n} \neq 0$ , with  $\mathbf{B}^c$  the magnetic field produced by the coils,  $\mathbf{B}^p$  the magnetic field produced by the plasma, and  $\mathbf{n}$  the normal to  $\Gamma_{CB}$ . The vacuum region, outside  $\Gamma_{PB}$  and inside  $\Gamma_{CB}$ , can be seen as an additional MRxMHD volume surrounding the plasma where  $\mu = 0$ ,  $p = 0$ .

The computational boundary, parametrized with Fourier harmonics  $(R_{mn}^{CB}, Z_{mn}^{CB})$ , and the normal magnetic field produced by the coils on the computational boundary,  $\mathbf{B}^c \cdot \mathbf{n}$  are inputs to SPEC. As for fixed-boundary calculations, the pressure, toroidal flux, and two additional constraints have to be provided in each plasma volume. To fully define the magnetic field in the vacuum region, the total toroidal current flowing in the plasma,  $I_\phi$ , and the total poloidal current flowing outside  $\Gamma_{CB}$  through the torus hole,  $I_{coil}$ , have to be provided as well.

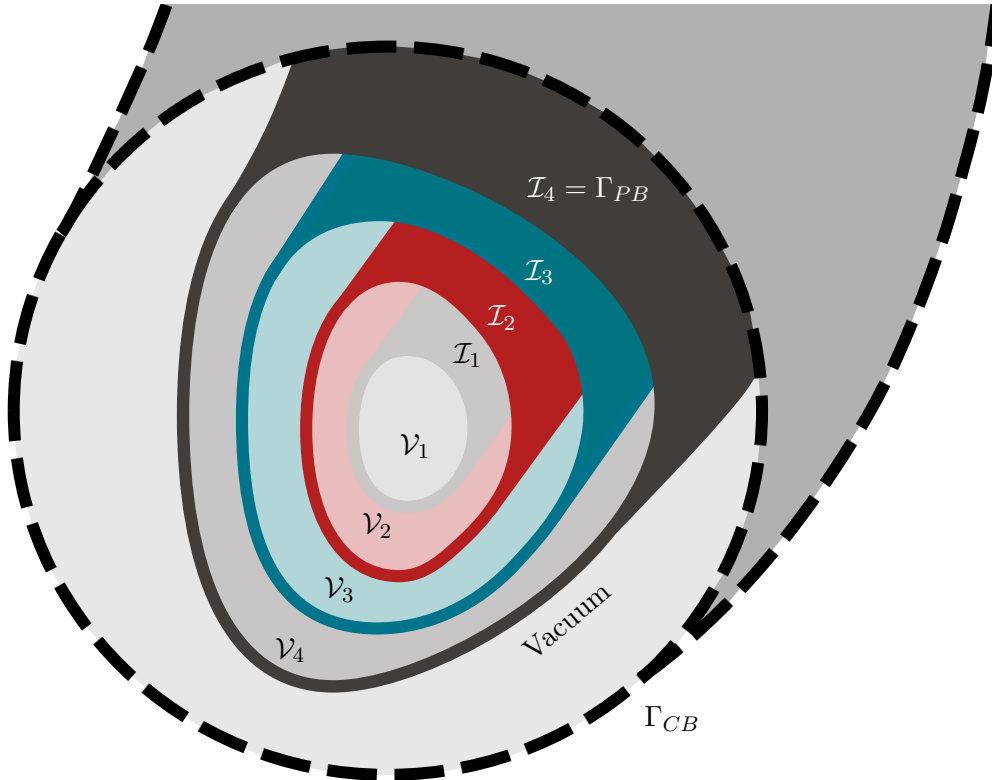


Figure 3.10: Sketch of a SPEC equilibrium with four volumes. The plasma boundary,  $\Gamma_{PB} = \mathcal{I}_4$ , is the dark gray surface and the computational boundary,  $\Gamma_{CB}$ , is the light gray surface.

While the piece of magnetic field on the computational boundary that is produced by the coils,  $\mathbf{B}^c \cdot \mathbf{n}$ , is an input, the contribution from the plasma,  $\mathbf{B}^p \cdot \mathbf{n}$  is not known *a priori*. This information is however required for the Beltrami solver in the vacuum region to find the magnetic field in agreement with the boundary condition  $(\mathbf{B}^p + \mathbf{B}^c) \cdot \mathbf{n}$ . To find self consistent solutions, an additional loop in SPEC is thus implemented. An initial guess for the Fourier harmonics of  $\mathbf{B}^p \cdot \mathbf{n}$ , denoted  $B_{mn}^0$ , is given as input; SPEC finds the magnetic field and plasma geometry in agreement with the corresponding boundary condition and recomputes the Fourier harmonics of  $\mathbf{B}^p \cdot \mathbf{n}$ , denoted  $\tilde{B}_{mn}^1$ , using a virtual casing method (Lazerson, 2012; Hanson, 2015). Generally,  $B_{mn}^0 \neq \tilde{B}_{mn}^1$ . Thus, a Piccard iteration is performed,

$$B_{mn}^1 = \alpha B_{mn}^0 + (1 - \alpha) \tilde{B}_{mn}^1, \quad (3.26)$$

with  $\alpha \in [0, 1[$ , and SPEC re-evaluates the equilibrium with  $B_{mn}^1$  as a new guess for the Fourier harmonics of  $\mathbf{B}^p \cdot \mathbf{n}$ . This loop wraps around fixed-boundary SPEC calculations and continues until  $B_{mn}^i - \tilde{B}_{mn}^{i+1}$  is smaller than a tolerance set by the user.

In free-boundary calculations, the plasma boundary  $\Gamma_{PB}$  is not an input. Its geometry is modified by SPEC to find force balance for each iteration of the free-boundary loop. As an output, SPEC will then provide the plasma geometry  $\Gamma_{PB}$  as well as the interfaces geometry  $\mathcal{I}_l$ , the magnetic field inside the plasma, and the magnetic field in the vacuum region. In its current implementation, free-boundary SPEC calculations require substantially more computational time than fixed-boundary calculations, since it requires multiple fixed-boundary evaluations. Recently, Henneberg et al. (2021b) reformulated the free-boundary problem of MRxMHD equilibria such that the free-boundary loop is no longer necessary, and free-boundary calculations become as fast as fixed-boundary calculations. This new algorithm is currently being implemented in SPEC; all calculations presented in this thesis will however use the free-boundary algorithm that was presented in this section.

## 3.2 Implementation of the toroidal current constraint

The computation of equilibria at fixed toroidal current profile is crucial for basic physic studies (Loizu et al., 2017; Suzuki et al., 2020), equilibrium reconstruction (Lao et al., 1985; Hanson et al., 2009), and stellarator optimization (Geiger et al., 2010, 2015; Landreman et al., 2022). Most MHD equilibrium codes (VMEC (Hirshman, 1983; Hirshman et al., 1986a), SIESTA (Hirshman et al., 2011; Peraza-Rodriguez et al., 2017), HINT (Harafuji et al., 1989; Suzuki et al., 2006), or PIES (Reiman and Greenside, 1986; Drevlak et al., 2005)) can calculate equilibria at chosen rotational transform or toroidal current profile. SPEC could run at fixed rotational transform but only recently its capability to run at fixed toroidal current profile has been implemented (Baillod et al., 2021). This capability is crucial for studying the effect of toroidal current on 3D magnetic equilibria. Examples are the study of the effect of bootstrap current on equilibrium  $\beta$ -limits, or the study of the sensitivity of a given equilibrium to toroidal current perturbations. In this chapter we describe the implementation of the new capability for SPEC, that allows MRxMHD equilibria to be calculated at prescribed toroidal current profiles.

This section is adapted from parts of the publication by A. Baillod *et al.*, Computation of multi-region, relaxed magnetohydrodynamic equilibria with prescribed toroidal current profile, Journal of Plasma Physics **87**, 4, 905870403 (2021), published under the license CC BY 4.0.

### 3.2.1 Constraining the toroidal current profiles in SPEC

As described in section 2.3.1, two kinds of net toroidal currents co-exist in MRxMHD equilibria: the volume currents  $\{I_{\phi,l}^v\}_{l=\{1,\dots,N_{vol}\}}$  and the surface currents  $\{I_{\phi,l}^s\}_{l=\{1,\dots,N_{vol}-1\}}$ . The SPEC code has been extended to allow the triplet  $\{\Delta\psi_{t,l}, I_{l,\phi}^v, I_{l,\phi}^s\}_{l=1,\dots,N_{vol}-1}$  as a constraint, herein *current constraint*. In the case of the rotational transform constraint, SPEC finds the solution to the linear system (2.74) volume by volume and iterates on  $\{\mu_l, \Delta\psi_{p,l}\}$  until the field has the desired rotational transform at the volume's interfaces. In the case of the current constraint, the constants  $\{\mu_l\}_{l=1,\dots,N_{vol}}$  are determined using Eq.(2.76), without the need for iterations, and this directly constrains the value of the volume currents  $\{I_{l,\phi}^v\}_{l=1,\dots,N_{vol}}$ .

Regarding the poloidal fluxes, it can be shown (Appendix A.5) that the surface currents depend linearly on the poloidal fluxes, *i.e.*

$$\mathbf{I}^s = \mathbf{M}\boldsymbol{\psi}_p + \mathbf{Q}, \quad (3.27)$$

where  $\mathbf{I}^s$  and  $\boldsymbol{\psi}_p$  are arrays containing all  $\{I_l^s\}_{l=1,\dots,N_{vol}-1}$  and all  $\{\Delta\psi_{p,l}\}_{l=2,\dots,N_{vol}}$  respectively, and the matrix  $\mathbf{M}$  and the array  $\mathbf{Q}$  depend only on the geometry of the interfaces  $\{\mathbf{X}\}$ . In this section, we consider the geometry, toroidal fluxes and the constants  $\{\mu_l\}_{l=1,\dots,N_{vol}}$  to be fixed and seek how the poloidal flux profile  $\boldsymbol{\psi}_p$  has to be constrained

### 3.2 Implementation of the toroidal current constraint

in order to obtain a surface current profile matching the input profile  $\mathbf{I}^s$ . The unknown  $\mathbf{Q}$  is eliminated by subtracting Eq.(3.27) evaluated at two different values of  $\psi_p$ , *i.e.* evaluated once at  $\overline{\psi_p}$  and once at  $\psi_p$ ,

$$\mathbf{M}(\overline{\psi_p} - \psi_p) = \overline{\mathbf{I}^s} - \mathbf{I}^s, \quad (3.28)$$

where  $\overline{\psi_p}$  is an arbitrary choice of poloidal fluxes, and  $\overline{\mathbf{I}^s}$  is the surface current profile calculated from the Beltrami fields  $\{\bar{\mathbf{a}}_l\}_{l=1,\dots,N_{vol}}$  obtained when the poloidal fluxes are constrained to the values  $\overline{\psi_p}$ .

The matrix  $\mathbf{M}$  is evaluated by taking the derivatives of Eq.(3.27) with respect to the poloidal fluxes, *i.e.*

$$M_{ij} = \frac{\partial I_{i,\phi}^s}{\partial \Delta \psi_{p,j}}, \quad (3.29)$$

which, when taking the derivative of Eq.(2.77), leads to the following bi-diagonal matrix

$$\mathbf{M} = \frac{2\pi}{\mu_0} \begin{bmatrix} \frac{\partial \tilde{B}_{\theta,2}^-}{\partial \Delta \psi_{p,2}} & 0 & \dots & \dots & 0 \\ \frac{\partial \tilde{B}_{\theta,2}^+}{\partial \Delta \psi_{p,2}} & \frac{\partial \tilde{B}_{\theta,3}^-}{\partial \Delta \psi_{p,3}} & 0 & \dots & 0 \\ 0 & -\frac{\partial \tilde{B}_{\theta,3}^+}{\partial \Delta \psi_{p,3}} & \frac{\partial \tilde{B}_{\theta,4}^-}{\partial \Delta \psi_{p,4}} & 0 & 0 \\ \vdots & \ddots & \ddots & \ddots & 0 \\ 0 \dots & \dots & 0 & -\frac{\partial \tilde{B}_{\theta,N_{vol}-1}^+}{\partial \Delta \psi_{p,N_{vol}-1}} & \frac{\partial \tilde{B}_{\theta,N_{vol}}^-}{\partial \Delta \psi_{p,N_{vol}}} \end{bmatrix}, \quad (3.30)$$

where we remind that  $\tilde{B}_{\theta,l}^\pm$  is the  $(m,n) = (0,0)$  Fourier harmonic of the covariant poloidal magnetic field on the inner and outer side of volume  $\mathcal{V}_l$  respectively. Derivatives of  $\tilde{B}_{\theta,l}^\pm$  with respect to the poloidal flux can be obtained by applying matrix perturbation theory on the linear system (3.18) (Hudson et al., 2012a),

$$(\mathbf{G}_l - \mu_l \mathbf{D}_l) \cdot \left[ \frac{\partial}{\partial \Delta \psi_{p,l}} \mathbf{a}_l \right] = - \left[ \frac{\partial \mathbf{G}_l}{\partial \Delta \psi_{p,l}} - \mu_l \frac{\partial \mathbf{D}_l}{\partial \Delta \psi_{p,l}} \right] \cdot \mathbf{a}_l + \frac{\partial}{\partial \Delta \psi_{p,l}} \mathbf{C}_l, \quad (3.31)$$

Solving Eq.(3.31) for  $\partial \mathbf{a}_l / \partial \Delta \psi_{p,l}$ , one can then evaluate  $\partial \tilde{B}_{\theta,l}^\pm$  using Eq.(3.13). Due to the linear nature of Eq.(3.27), the coefficients of the matrix  $\mathbf{M}$ , *i.e.* Eq.(3.29), are independent of  $\psi_p$  and thus can be evaluated once at any arbitrary value of  $\psi_p$ . We thus conveniently evaluate them at  $\overline{\psi_p}$ . Equation (3.28) is then solved to obtain the poloidal flux profile  $\psi_p$ .

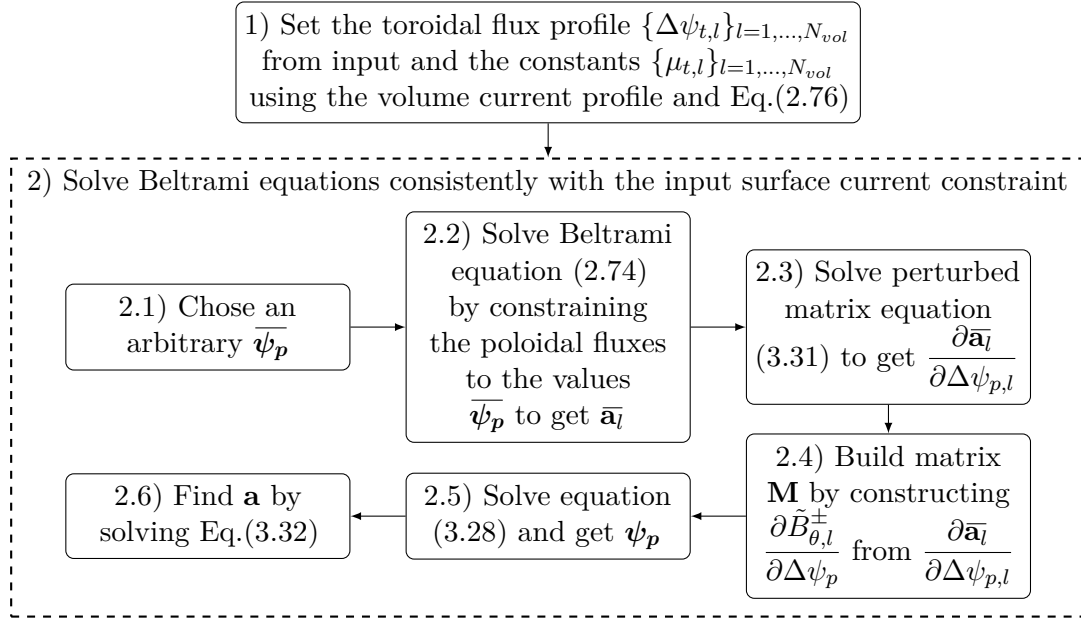


Figure 3.11: Flow of the algorithm used to constrain the net toroidal current profile for a given toroidal flux profile and geometry.

Finally, instead of solving a second time the Beltrami equation, Eq.(2.74), at  $\psi_p$ , we take advantage of the linear dependence of  $\mathbf{a}$  on  $\psi_p$ , Eq.(3.18), and solve

$$A_{l,i} = \overline{A_{l,i}} - \frac{\partial A_{l,i}}{\partial \Delta \psi_{p,l}} (\overline{\Delta \psi_{p,l}} - \Delta \psi_{p,l}), \quad (3.32)$$

where  $\overline{A_{l,i}}$  is one element of  $\overline{\mathbf{a}_l}$ . The algorithm flow is summarized in Figure 3.11. In the case of a free-boundary computation, the toroidal flux in the vacuum region is varied to satisfy the poloidal linking current  $I_{coil}$ . This slightly modifies the linear system (3.28). Details can be found in Appendix A.6.

Note that the current constraint is a global constraint, in the sense that the net toroidal current at the interface  $\mathcal{I}_l$  depends on the magnetic field on each side of the interface, and thus, on the solution to the Beltrami equation in volume  $\mathcal{V}_l$  and  $\mathcal{V}_{l+1}$ . This has important implication for the parallelization of the code, as we will discuss in section 3.2.3.

Constraining the toroidal current profile takes away the control of other profiles such as the rotational transform or the magnetic helicity. However, as for the case of the rotational transform constraint, the equilibrium can be accessed by a relaxation process at constant magnetic helicity if the final magnetic helicity is known *a priori*. The MRxMHD equilibrium equations are thus still satisfied by an equilibrium obtained by constraining the toroidal current profiles.



### 3.2.2 Force gradient

The hybrid-Powell algorithm used in SPEC to iterate on the interfaces geometry uses analytic derivatives, which is faster than finite differentiation. To keep good performance while using the current constraint, derivatives of the force Fourier coefficients,  $\{F_{lmn}\}$ , with respect to the interfaces degrees of freedom,  $\{x_i\}$ , at constant  $\{\Delta\psi_{t,l}, I_{l,\phi}^v, I_{l,\phi}^s\}_{l=1,\dots,N_{vol}}$  are derived here. Here  $x_i$  is one of the Fourier harmonics  $X_{mn}^k$ , one of the  $R_{mn}^k$  or  $Z_{mn}^k$  of an interface  $\mathcal{I}_k$ . Derivatives are first evaluated in real space and then Fourier-transformed. Using the chain rule,

$$\frac{d}{dx_i} \left[ \left[ p + \frac{B^2}{2\mu_0} \right]_l \right] = \frac{1}{\mu_0} \left( B_{l+1}^- \frac{dB_{l+1}^-}{dx_i} - B_l^+ \frac{dB_l^+}{dx_i} \right) \quad (3.33)$$

$$\text{with} \quad \frac{dB_l^\pm}{dx_i} = \frac{\partial B_l^\pm}{\partial x_i} + \frac{\partial B_l^\pm}{\partial \Delta\psi_{p,l}} \frac{d\Delta\psi_{p,l}}{dx_i} + \frac{\partial B_l^\pm}{\partial \mu_l} \frac{d\mu_l}{dx_i} + \frac{\partial B_l^\pm}{\partial \Delta\psi_{t,l}} \frac{d\Delta\psi_{t,l}}{dx_i} \quad (3.34)$$

where  $B_l^-$ ,  $B_l^+$  are the magnetic field strength on the inner and outer side of volume  $l$ , respectively, and the pressure,  $p_l$ , is considered constant in each volume with respect to variations in the geometry,  $\mu_l$  and  $\Delta\psi_{p,l}$ . Note that all derivatives are taken at constant toroidal flux, volume current and surface current. Enforcing  $d\Delta\psi_{t,l}/dx_i = 0$  and  $dI_{l,\phi}^v/dx_i = 0$  leads to  $d\mu_l/dx_i = 0$  using Eq.(2.76). The surface current constraint,  $dI_{l,\phi}^s/dx_i = 0$ , leads to a system of coupled equations using Eq.(2.77),

$$\frac{\partial \tilde{B}_{l+1,\theta}^-}{\partial x_i} + \frac{\partial \tilde{B}_{l+1,\theta}^-}{\partial \Delta\psi_{p,l+1}} \frac{\partial \Delta\psi_{p,l+1}}{\partial x_i} - \frac{\partial \tilde{B}_{l,\theta}^+}{\partial x_i} - \frac{\partial \tilde{B}_{l,\theta}^+}{\partial \Delta\psi_{p,l}} \frac{\partial \Delta\psi_{p,l}}{\partial x_i} = 0, \quad (3.35)$$

which can be written as a linear system using the matrix  $\mathbf{M}$  defined in Eq.(3.30),

$$\mathbf{M} \begin{bmatrix} \frac{d\Delta\psi_{p,2}}{dx_i} \\ \vdots \\ \frac{d\Delta\psi_{p,N_{vol}}}{dx_i} \end{bmatrix} = \frac{2\pi}{\mu_0} \begin{bmatrix} \frac{\partial \tilde{B}_{\theta,1}^+}{\partial x_i} - \frac{\partial \tilde{B}_{\theta,2}^-}{\partial x_i} \\ \vdots \\ \frac{\partial \tilde{B}_{\theta,N_{vol}-1}^+}{\partial x_i} - \frac{\partial \tilde{B}_{\theta,N_{vol}}^-}{\partial x_i} \end{bmatrix}. \quad (3.36)$$

Derivatives of  $\tilde{B}_{\theta,l}$  with respect to  $\Delta\psi_{p,l}$  and  $x_i$  can be obtained by applying matrix perturbation theory to the Beltrami system (3.18). The solution of Eq.(3.36), together with Eq.(3.33) provides the required derivatives of the force with respect to the geometry. Derivatives of the Fourier components of the force,  $dF_{lmn}/dx_i$ , are obtained by taking the Fourier transform of equation (3.33) and, together with the derivatives of the spectral condensation  $Y_{mn}$  with respect to  $x_i$ , are packed in a matrix  $\nabla F$  of size  $N^2$ , henceforth named *force gradient*.

Note that here we only discussed how the physical force could be derived with respect to the volumes' interfaces geometry, and did not describe how the derivatives of the spectral constraint  $Y_{mn}$  are evaluated. These are however relatively easy to compute,

since the spectral constraint depends only explicitly on the geometrical degrees of freedom  $x_i$  (see appendix A.3). Appendix A.6 provides details on the free-boundary case.

### 3.2.3 Implementation details and parallelization

The new current constraint has been parallelized with message passing interface (MPI) in a similar way to the other constraints: each volume is associated to one central processing unit (CPU); since the solution to the Beltrami equation (2.74) in a volume is independent from other volumes, each CPU can solve the linear system (3.18) in parallel. In the case of a local constraint, each volume iterates on the  $(\mu_l, \Delta\psi_{p,l})$  until its local constraint is satisfied. In the case of a global constraint, additional communications between CPUs are required. In the case of the current constraint, the master CPU gathers all required derivatives to construct the matrix  $\mathbf{M}$  and solves the linear systems (3.28) and (3.32), before broadcasting the values of  $\{\Delta\psi_{p,l}\}_{l=2,\dots,N_{vol}}$  and  $\{\mathbf{a}_l\}_{l=1,\dots,N_{vol}}$  to all CPUs.

Regarding communications, we reduced them to a minimum. The global toroidal current constraint is computed using Eq.(2.77), which only depends on the first even Fourier coefficient of  $B_\theta$  in each volume. We thus compute locally (by each MPI task) these coefficients before sending them to the master task. This requires the communication of  $2(N_{vol} - 1)$  doubles. All communications are implemented using basic MPI point-to-point communications, though a gathering communication could be more efficient. The master task then solves Eqs.(3.28) and (3.32) and broadcasts the elements  $\bar{\mathbf{a}}_l$  and  $\bar{\psi}_p$ . We don't expect a communication bottleneck due to the reasonably low amount of communications.

### 3.2.4 Verification of the current constraint

In this section we present a rigorous verification of the new capability of SPEC against analytical solutions in a screw pinch geometry and against a reference SPEC solution obtained with the rotational transform constraint in a classical stellarator geometry. All results presented in this section were obtained with SPEC version 2.10.

#### Verification in cylindrical geometry

We consider a fixed-boundary screw pinch MRxMHD equilibrium that only depends on the radius  $R$  and whose solutions can be written analytically (Appendix A.7). We choose a set of somewhat arbitrary input parameters, *i.e.* a cylinder of minor radius  $a = 1$  and length  $L = 2\pi$ ,  $N_{vol} = 3$ ,  $p_l = 0 \ \forall l \in \{1, 2, 3\}$ ,  $\psi_t = \{1/9, 4/9, 1\}\text{Tm}^2$ ,  $\mu_0 \mathbf{I}^v = \{0.2, 0.2, 0.4\}\text{Tm}$  and  $\mu_0 \mathbf{I}^s = \{-0.4, 0.5\}\text{Tm}$ , which uniquely define the analytical solution. SPEC is then run with the same input parameters and the solutions are compared (Figure 3.12). Very good agreement between the analytical solution and the SPEC solution is obtained.

Note that by constraining the toroidal current profiles, we lose control on the rotational transform profile, since only two profiles can be constrained in addition to the pressure profile. Hence discontinuities in the magnetic field components arise at the volumes' interfaces, even when there is no pressure, unless the input parameters are carefully selected.

The force gradient, which is here a matrix of size  $2 \times 2$ ,  $(\nabla F)_{ij} = \partial F_i / \partial R_j$ , with  $R_j$  the position of the interfaces, can also be expressed in terms of Bessel functions integrals (see Appendix A.7). Figure 3.13 shows the normalized maximum absolute error between the force gradient obtained with SPEC and that obtained analytically as a function of the radial resolution  $L_{rad}$ . As  $L_{rad}$  is increased, exponential convergence is observed up until  $10^{-13}$ , where the error in the evaluation of the Bessel integrals starts to dominate.

#### Verification in toroidal geometry

A verification is proposed here in the more complex case of a free-boundary, rotating ellipse with seven plasma volumes ( $N_{vol} = 7$ ). The pressure is set to zero and the computational boundary is defined by Eqs.(3.24)-(3.25) — see Figure 3.6. We suppose here that some hypothetical coils with a total current of  $\mu_0 I_{coil} = 42.87 \text{Tm}$  are able to generate a vacuum field without normal component to the computational boundary. The total toroidal magnetic flux in the plasma is set to  $\psi_a = 0.61 \text{Tm}^2$  and the toroidal magnetic flux in the vacuum region is set to  $\Delta\psi_{t,V} = 1.39 \text{Tm}^2$ , adding up to a total toroidal magnetic flux enclosed by the computational boundary of  $\Delta\psi_{t,V} + \psi_a = 2 \text{Tm}^2$ .

To our knowledge, no analytical solution to Eqs.(2.74) and (2.75) exists in this geometry. The verification is thus carried out as follows: first, a rotational transform constraint case is run with an input  $\iota$ -profile that is chosen to be 10% larger than the vacuum rotational transform  $\iota_{vac}$ , *i.e.*  $\iota = 1.10 \cdot \iota_{vac}$ , so that there is a non-zero contribution from the current to the rotational transform. Note that the rotational transform is only prescribed at the interfaces  $\mathcal{I}_i$ , and is free within the volumes. In particular, the rotational transform is unconstrained at the computational boundary. The volume and surface currents are evaluated from the fixed rotational transform equilibrium and used to run a second calculation where the net toroidal current is constrained. The same initial guess for the geometry and the interfaces is used for both calculations. The rotational transform profile  $\bar{\iota}$  is then extracted from the second equilibrium and compared to the reference  $\iota$ -profile.

The vacuum rotational transform profile, as well as the profiles  $\iota$  and  $\bar{\iota}$  are shown in Figure 3.14 (left). The toroidal current enclosed by the plasma is mostly contained in the volumes and adds up to a total of  $\sim 2.7 \text{kA}$ , see Figure 3.14 (right). As expected the surfaces currents,  $I_{\phi,l}^s$ , remain small ( $< 10^{-2} \text{kA}$ ), since there are no pressure gradients to drive them. The constraint on the rotational transform  $\iota$  is enforced on each side of

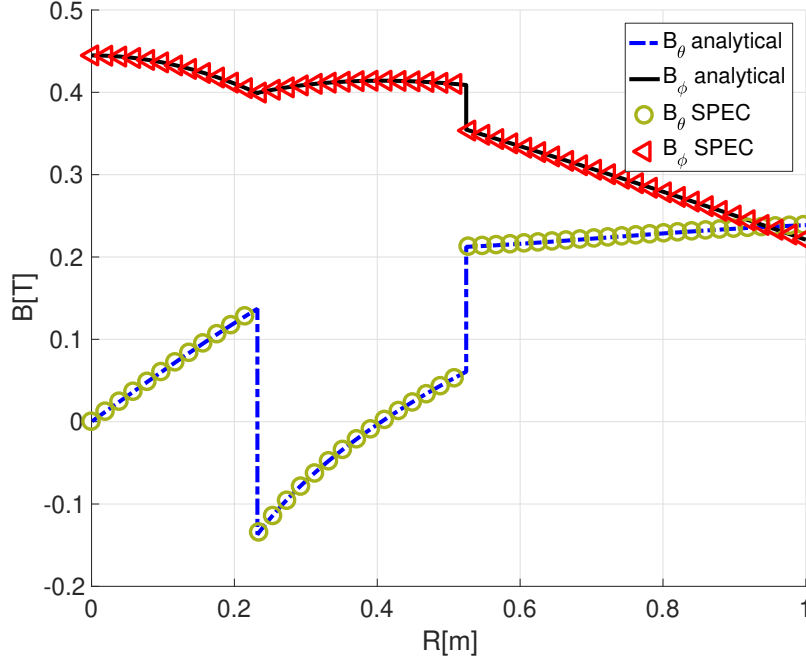


Figure 3.12: Magnetic field components as a function of the radius in the case of a screw pinch. Solid and dashed lines: analytical solution as given in Appendix A.7. Circles and triangles: SPEC solution using the current constraint.

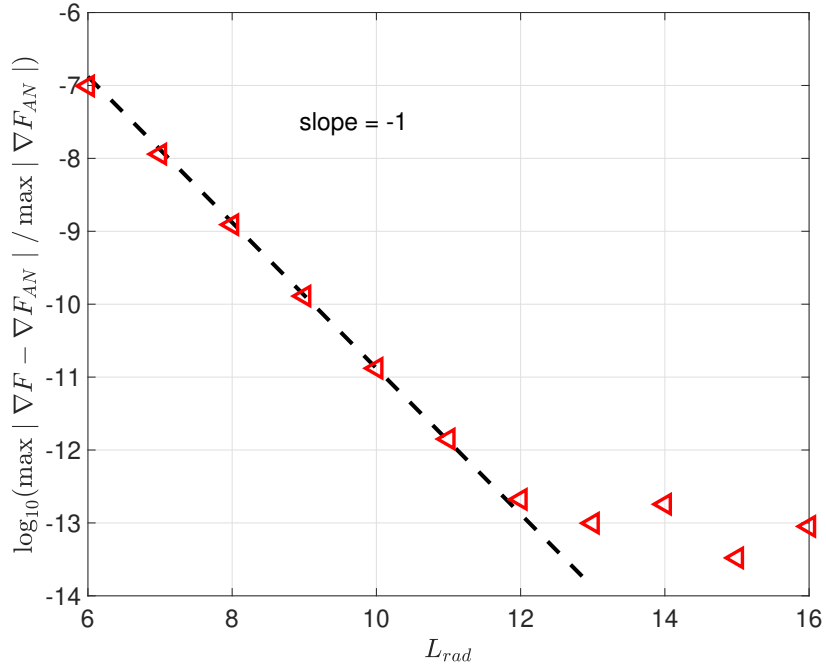


Figure 3.13: Maximal absolute error between the analytical force gradient,  $\nabla F_{AN}$ , and the force gradient obtained from SPEC,  $\nabla F$ , as a function of the radial resolution for the screw pinch case.

### 3.2 Implementation of the toroidal current constraint

the volumes' interfaces, indicated by gray dashed lines on Figure 3.14 (left). The value of  $\iota$  at the computational boundary is not constrained. Agreement between  $\iota$  and  $\bar{\iota}$  up to a relative error of  $\max(|\iota - \bar{\iota}| / |\iota|) \sim 10^{-5}$  is observed, showing that the same equilibrium can be obtained using either constraint. The maximum error between both profiles decreases as the numerical resolution is increased (data not shown).

To verify the force gradient components, we use a fourth-order centered finite difference formula (Fornberg, 1988),

$$\frac{df}{dx} = \frac{f(x - 2\Delta x) - 8f(x - \Delta x) + 8f(x + \Delta x) - f(x + 2\Delta x)}{12\Delta x} + \mathcal{O}(\Delta x^4), \quad (3.37)$$

to obtain  $\nabla F_{FD}$ , *i.e.* a finite-difference estimate of the force gradient, and compare it to  $\nabla F$ , *i.e.* the force gradient calculated in SPEC by using analytical derivatives (see section 3.2.2). The finite difference estimate is evaluated by perturbing each geometrical degree of freedom  $\{x_i\}_{i=1,\dots,N}$  by a constant value  $\Delta R$ . Convergence as  $\Delta R \rightarrow 0$  is shown in Figure 3.15. A convergence of order  $\mathcal{O}(\Delta R^4)$  is observed down to  $\sim 10^{-11}$  for  $\Delta R \sim 10^{-4}$ . For lower values of  $\Delta R$ , the finite difference approximation error is dominated by round-off error. This shows that the analytical derivatives (the force gradient) is correctly implemented in SPEC.

In this section, we have explained how the net toroidal current in SPEC can be

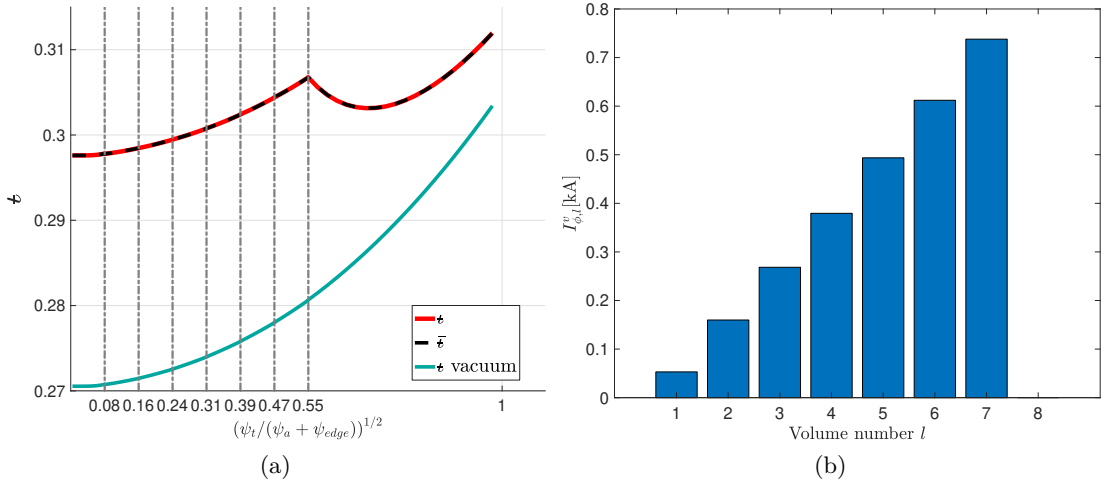


Figure 3.14: Left: rotational transform profile versus effective minor radius. Red line:  $\iota$ , the rotational transform profile obtained by SPEC when the rotational transform is prescribed. Note that here  $\iota$  is only constrained at the interfaces  $\mathcal{I}_l$ , indicated by gray dashed vertical lines. Black, dashed line:  $\bar{\iota}$ , the output profile obtained from SPEC when run at fixed toroidal current profile. Blue line:  $\iota$ -profile in vacuum. Right: total toroidal current enclosed by each volume. Surface currents (not plotted),  $I_{\phi,l}^s$ , are smaller than  $10^{-2}$ [kA] and are negligible in comparison to the volume current.

constrained, and how this new constraint has been implemented. This will, in particular, be used in chapter 5 to include bootstrap current effects in SPEC calculations, and in chapter 6 to optimize the injected current profile to minimize the size of magnetic islands in an equilibrium. This new capability of the SPEC code is also useful to evaluate vacuum fields with multiple volumes (see for example the W7-X vacuum field evaluated in section 3.1.3), or for predicting the nonlinear saturation of tearing modes (Loizu et al., 2020). Before looking at applications of the SPEC code, we discuss in the following section some of its limitations and an attempt to remove them.

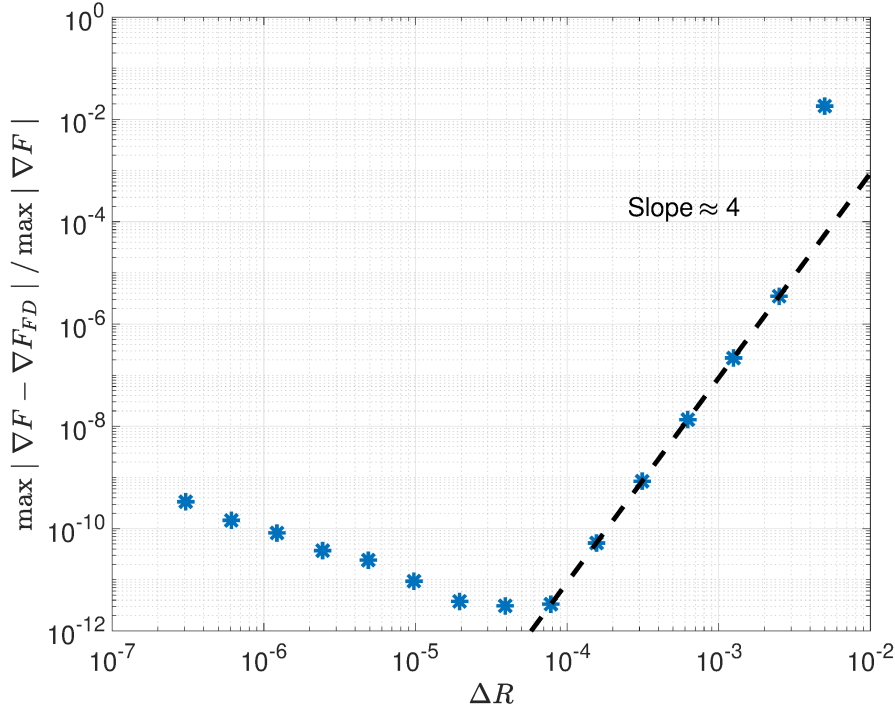


Figure 3.15: Normalized maximum absolute error between SPEC force gradient and a finite difference estimate in the case of a rotating ellipse. The dashed line has slope of 4.

### 3.3 Implementation of a unique angle representation

In simple geometries, SPEC provides solutions to the MRxMHD equations in a fast and reliable way. For example, see the studies of Qu et al. (2021); Loizu et al. (2020) in slab geometry, Kumar et al. (2021) in cylindrical geometries, Kumar et al. (2022) or Baillod et al. (2022) in some toroidal geometries, or the examples presented in section 3.1.3. However, any attempt in strongly shaped geometries, *i.e.* geometries with large elongation or torsion, and with multiple volumes will require an initial guess for the geometry of the interfaces  $\mathcal{I}_l$  very close to the solution for SPEC to find the geometry that satisfies the equilibrium equations. In some extreme cases, SPEC does not find an equilibrium, as it will be now illustrated.

As an example, let's consider a strongly shaped quasi-isodynamic (QI) stellarator with one field period and  $\iota \approx 0.6$  in vacuum on the magnetic axis, obtained by Goodman et al. (2022), and plotted on the top panel of Figure 3.16. We start by computing the vacuum field by solving the Beltrami equation (2.74) with  $\mu = 0$  in the volume enclosed by the provided boundary. The Poincaré section of the vacuum magnetic field is shown on the middle and lower panels of Figure 3.16. We remark that most of the volume is occupied by nested magnetic surfaces, excepted for a small  $(m, n) = (5, 3)$  island chain. As for the W7-X example presented in section 3.1.3, we thus expect that the same magnetic field can be retrieved in a two-volume SPEC calculation, if the volume's interface is positioned on one of the magnetic surfaces.

We thus attempt a two-volume SPEC calculation of the vacuum magnetic field. We set the toroidal flux to  $\psi_{t,1} = 8 \cdot 10^{-4} \text{Tm}^2$  and  $\psi_{t,2} = 0.01 \text{Tm}^2$ , which corresponds to the position of a magnetic surface as computed by the single volume SPEC calculation. To constrain the field to be in vacuum, we leverage the current constraint (see section 3.2) to impose the net toroidal current in both volumes and at the interface to be zero, *i.e.*  $I_{\phi,1}^v = I_{\phi,2}^v = I_{\phi,1}^s = 0$  and set the pressure to zero in both volumes. As a first attempt, we let SPEC interpolate an initial guess for the interface geometry from the plasma boundary. We show on the middle and lower panels of Figure 3.16 SPEC's interpolated initial guess, in green, in comparison to the Poincaré section of the vacuum field. To the eye, the initial guess seems to be very different than the magnetic surfaces. Nevertheless, we see on Figure 3.17 (green curve) that  $|f| \sim 3 \cdot 10^{-4}$  initially; then SPEC iterates on the geometrical degrees of freedom  $\sim 120$  times to lower the force scalar down to  $|f| \sim 4 \cdot 10^{-5}$ , where it saturates. Obviously, the Hybrid-Powell method used in SPEC got stuck in a local minimum. To improve the result, it is attempted below to construct a better initial guess.

To construct a good initial guess for the interface separating both volumes, we proceed as follows. We start by running a field line tracing algorithm on the single-volume SPEC vacuum calculation, as described in section 1.5, and extract a set of points  $\mathbf{x}_i$  along a selected field line. Then, we use the DESCUR code (Hirshman and Meier, 1985) to

obtain the spectrally condensed harmonics  $(R_{mn}^1, Z_{mn}^1)$  of a surface that fits the points  $\mathbf{x}_i$ . Finally, we use the  $(R_{mn}^1, Z_{mn}^1)$  harmonics as initial guess for the two-volumes SPEC calculation. The comparison between the Poincaré plot obtained from the single volume SPEC calculation and the DESCUR computed initial guess is shown on Figure 3.16 (blue surface). We first remark that this method generates, to the eye, a better initial guess than the interpolation method. There are no visible differences between the DESCUR surface and the Poincaré section of SPEC single volume calculation. When used as initial guess in the SPEC two-volumes calculation however, the initial force scalar is of the order of  $|f| \sim 5 \cdot 10^{-4}$ , and SPEC does not find the interface's geometry that satisfies force balance, since after  $\sim 130$  iterations on the geometry, the force scalar is still of the order of  $10^{-4}$  (see Figure 3.17). One may think that this is because the Fourier resolution used in SPEC is too low; increasing the Fourier resolution does however not solve the problem (see blue curve on Figure 3.17).

We plot on Figure 3.18 the normalized residual force,  $[(B/B_0)^2/2]$ , in real space and in Fourier space, at the local minimum found by SPEC. Two local minima are compared; the first is obtained by SPEC when the initial guess for the inner interface geometry is provided by the DESCUR procedure, while the second one is obtained when the initial guess for the inner interface geometry is provided by an interpolation of the plasma boundary. In real space (see the left panels of Figure 3.18), both local minima have very different structures. Clearly, both local minima found by SPEC are different. This indicates that the force Fourier harmonics probably have multiple minima in the space spanned by the interface's geometrical degrees of freedom, in which the hybrid-Powell method gets stuck, thereby preventing SPEC to find the solution to the MRxMHD equilibrium equations. In Fourier space, we remark that at both local minima, the Fourier harmonics of the force that are minimized by SPEC remain large, in contrast to what has been observed in the case of the W7-X geometry (see Figure 3.5), or in the case of a rotating ellipse (see Figure 3.8). This again confirms that SPEC got stuck in a local minimum, and could not find an interface geometry that would lower further down the target Fourier harmonics of the force.

Why SPEC is not able to find the interface geometry that satisfies the equilibrium equation, despite having such a good initial guess, is a truly puzzling question. We expect that, even in a space filled with local minima, a sufficient good initial guess would let SPEC find the solution. One hypothesis is that the spectrally condensed angle from DESCUR is different from the spectrally condensed angle from SPEC (DESCUR does not include the "spectral length" constraint as in SPEC — see appendix A.3). This means that while the initial guess is close geometry-wise, its parametrization might be far from the one that satisfies SPEC's spectral constraint. Another hypothesis is that the spectral condensation harmonics  $Y_{lmn}$  is the source of the numerous local minima in the space of degrees of freedom describing the interface geometry. A potential solution to these problems would be to choose a representation of the interface geometries where spectral condensation is not required. This can be achieved by defining a *unique angle*



### 3.3 Implementation of a unique angle representation

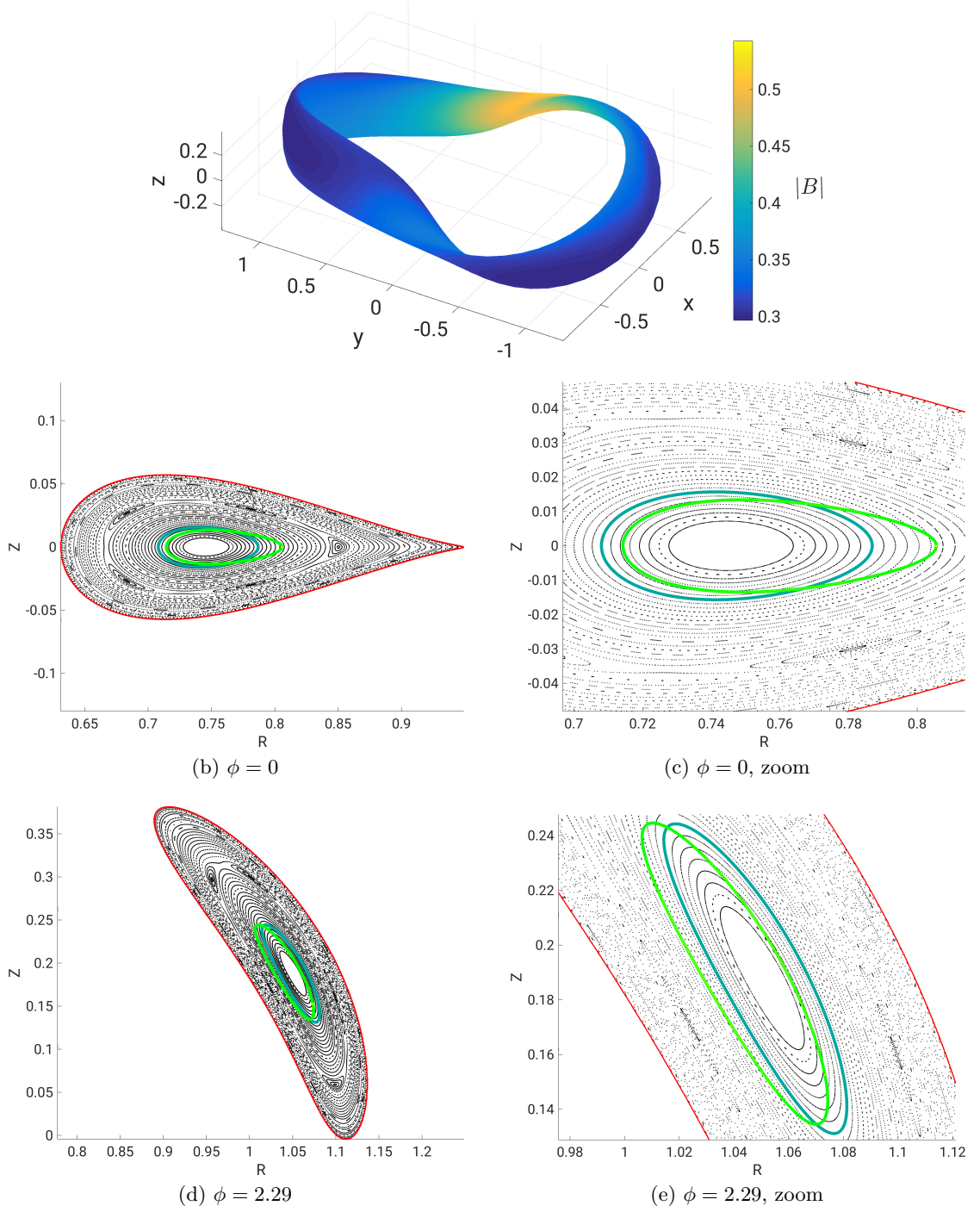


Figure 3.16: Strongly shaped QI stellarator. Top: 3D-plot of the computational boundary. Colors indicate the magnetic field strength calculated by SPEC in vacuum. Middle and bottom: Comparison between SPEC Poincaré section, the interpolated initial guess, and the DESCUR constructed initial guess. The SPEC calculation was performed with a single plasma volume. In red: plasma boundary. In green: SPEC interpolated initial guess for the interface geometry. In blue: DESCUR surface reconstructed from SPEC Poincaré data.

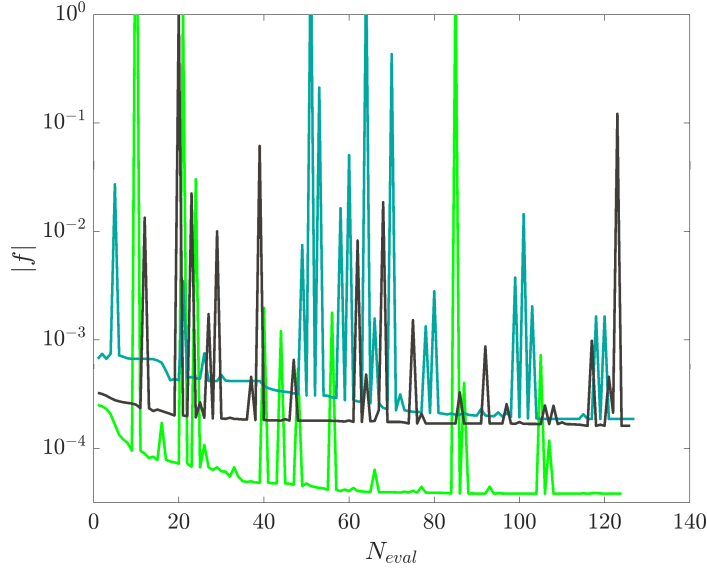


Figure 3.17: Strongly shaped QI geometry, two-volume SPEC calculation. Force scalar as a function of the number of iteration on the interface geometry. Green:  $M_{pol} = 8$ ,  $N_{tor} = 6$ , interpolated initial guess. Blue:  $M_{pol} = 8$ ,  $N_{tor} = 6$ , initial guess constructed from the vacuum field using DESCUR. Black:  $M_{pol} = 8$ ,  $N_{tor} = 10$ , initial guess constructed from the vacuum field using DESCUR.

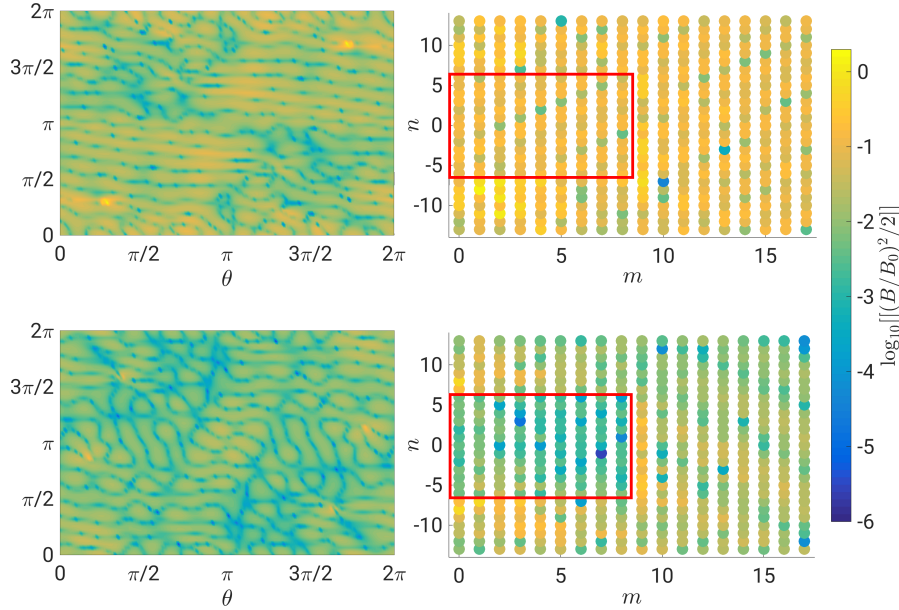


Figure 3.18: Normalized residual force on an interface from a QI equilibrium obtained with SPEC, in real space (left) and in Fourier space (right). Top: local minimum found by SPEC when using the DESCUR-generated initial guess for the inner interface geometry. Bottom: local minimum found by SPEC when using an interpolated initial guess from the plasma boundary for the inner interface geometry. The red box surrounds the Fourier harmonics of the force that are not truncated.

### 3.3 Implementation of a unique angle representation

$\theta_h$ . Of course, there are an infinite number of choices for the poloidal angle  $\theta_h$ , and many have been proposed in the literature — see, for example, Hirshman and Weitzner (1985), Hirshman and Breslau (1998) and Carlton-Jones et al. (2021). In the following section, we will discuss the implementation of an alternative parametrization for the toroidal surfaces proposed by Henneberg et al. (2021a), which uses a unique poloidal angle optimal for representing elliptical surfaces.

#### 3.3.1 The Henneberg representation

One potentially advantageous choice of angle  $\theta_h$ , called thereafter the *Henneberg angle*, is to choose  $\theta_h$  to be the optimal angle to represent rotating ellipses. Since magnetic surfaces close to the magnetic axis have elliptical cross-sections (Helander, 2014), we expect this particular choice of poloidal angle to be efficient to represent magnetic surfaces, at least close to the magnetic axis. This angle was first proposed by Henneberg et al. (2021a), and was shown to reduce the number of local minima in stellarator optimization problems. With this angle, a toroidal surface is parametrized by

$$R(\theta_h, \phi) = R_0(\phi) + \rho(\theta_h, \phi) \cos(\alpha\phi) - \zeta(\theta_h, \phi) \sin(\alpha\phi), \quad (3.38)$$

$$Z(\theta_h, \phi) = Z_0(\phi) + \rho(\theta_h, \phi) \sin(\alpha\phi) + \zeta(\theta_h, \phi) \cos(\alpha\phi), \quad (3.39)$$

where  $\alpha$  is the number of poloidal rotations of the elliptical magnetic surfaces close to the magnetic axis per field period — typically,  $\alpha = 1/2$ . Here  $(\rho, \zeta)$  describes a coordinate system, defined by  $(\mathbf{e}_\rho, \mathbf{e}_\zeta)$ , centered at  $(R_0(\phi), Z_0(\phi))$ , and tilted by an angle  $\alpha\phi$  with respect to the the coordinate system  $(\mathbf{e}_R, \mathbf{e}_Z)$  (see Figure (3.19)).

For each plane  $\phi = \text{const}$ , we now construct a circle  $\mathcal{C}(\phi)$ , centered at  $(R_0(\phi), Z_0(\phi))$ , and with radius  $b(\phi)$ ,

$$b(\phi) = \frac{1}{2} \left( \max_{\phi=\text{const}} \zeta - \min_{\phi=\text{const}} \zeta \right) \quad (3.40)$$

$$= \frac{1}{2} \left( \max_{\phi=\text{const}} [Z \cos(\alpha\phi) - R \sin(\alpha\phi)] - \min_{\phi=\text{const}} [Z \cos(\alpha\phi) - R \sin(\alpha\phi)] \right). \quad (3.41)$$

For any magnetic surface  $(R(\theta, \phi), Z(\theta, \phi))$ , with a single maximum and single minimum along the  $\zeta$  direction for all  $\phi$ , there is thus a one-to-one mapping between the magnetic surface and the torus generated by the circle  $\mathcal{C}(\phi)$ . We project the magnetic surface on  $\mathcal{C}(\phi)$  by writing

$$\zeta(\theta_h, \phi) = b(\phi) \sin(\theta_h - \alpha\phi), \quad (3.42)$$

which uniquely defines the angle  $\theta_h$  as

$$\theta_h = \arcsin \left( \frac{\zeta}{b} \right) + \alpha\phi. \quad (3.43)$$

Finally, we write the functions  $\rho(\theta, \phi)$ ,  $b(\phi)$ ,  $R_0(\phi)$ , and  $Z_0(\phi)$  as Fourier series,

$$\rho(\theta_h, \phi) = \sum_{m=1}^M \sum_{n=-N}^N \rho_{mn} \cos(m\theta_h + n\phi - \alpha\phi), \quad (3.44)$$

$$b(\phi) = \sum_{n=0}^N b_n \cos(n\phi), \quad (3.45)$$

$$R_0(\phi) = \sum_{n=0}^N r_n \cos(n\phi) \quad (3.46)$$

$$Z_0(\phi) = \sum_{n=1}^N z_n \sin(n\phi). \quad (3.47)$$

Note that this representation of the magnetic surface is unique, in the sense that two different sets of harmonics  $\{r_n, z_n, \rho_{mn}, b_n\}$  will always describe two different surfaces.

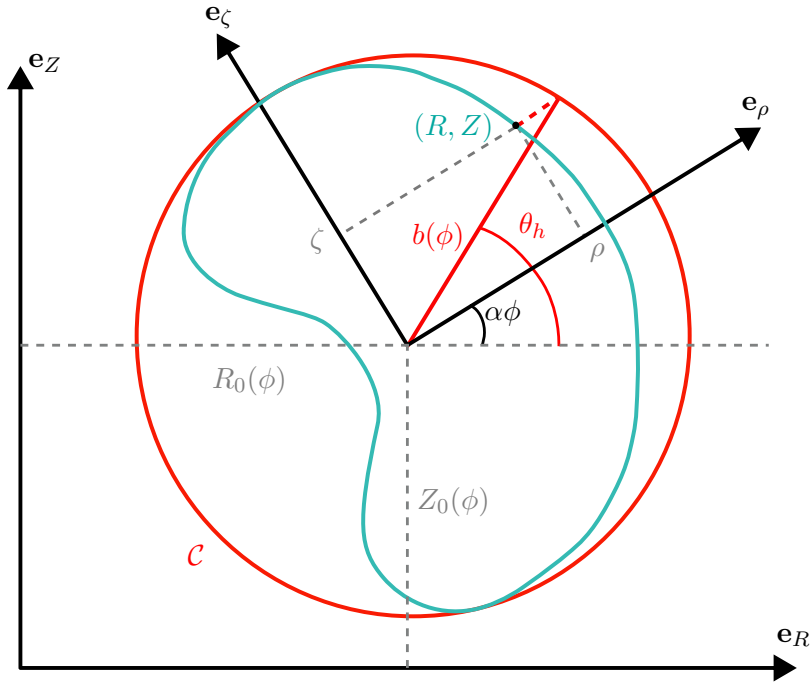


Figure 3.19: Sketch of a toroidal surface (blue) in the  $(R, Z)$  plane, and the corresponding coordinates of the Henneberg representation. The coordinate system  $(\rho, \zeta)$  is tilted with an angle  $\alpha\phi$ . A point  $(R, Z)$  on the toroidal surface is projected in the  $\mathbf{e}_\rho$  direction onto a circle of radius  $b(\phi)$  and centered in  $(R_0(\phi), Z_0(\phi))$ .

### 3.3 Implementation of a unique angle representation

One can easily derive a linear relation between the Fourier harmonics  $(R_{mn}, Z_{mn})$  and  $(r_n, z_n, \rho_{mn}, b_n)$ . Expanding equation (3.38) with the Fourier series (3.44)-(3.47), we get

$$R(\theta_h, \phi) = + \sum_{n=0}^N r_n \cos(n\phi) + \sum_{m=1}^M \sum_{n=-N}^N \rho_{mn} \cos(m\theta_h + n\phi - \alpha\phi) \cos(\alpha\phi) \quad (3.48)$$

$$- \sum_{n=0}^N b_n \cos(n\phi) \sin(\theta_h - \alpha\phi) \sin(\alpha\phi) \quad (3.49)$$

$$= + \sum_{m=1}^M \sum_{n=-N}^N \frac{\rho_{mn}}{2} [\cos(m\theta_h + n\phi - 2\alpha\phi) + \cos(m\theta_h + n\phi)] \quad (3.50)$$

$$- \sum_{n=0}^N \frac{b_n}{4} [\cos(\theta_h - (n + 2\alpha)\phi) + \cos(\theta_h - (-n + 2\alpha)\phi)] \quad (3.51)$$

$$- \cos(\theta_h - n\phi) - \cos(\theta_h + n\phi)] + \sum_{n=0}^N r_n \cos(n\phi), \quad (3.52)$$

from which we easily identify

$$R_{0n} = r_n \quad (3.53)$$

$$R_{mn} = \frac{1}{2}(\rho_{m, -n+2\alpha} + \rho_{m, -n}) + \frac{\delta_{m1}}{4} [b_n + b_{-n} - b_{n-2\alpha} - b_{-n+2\alpha}], \quad \forall m > 0. \quad (3.54)$$

Similarly, we get

$$Z_{0n} = z_n \quad (3.55)$$

$$Z_{mn} = \frac{1}{2}(-\rho_{m, -n+2\alpha} + \rho_{m, -n}) + \frac{\delta_{m1}}{4} [b_n + b_{-n} + b_{n-2\alpha} + b_{-n+2\alpha}], \quad \forall m > 0. \quad (3.56)$$

Note that the relations (3.54) and (3.56) assume that the  $(R_{mn}, Z_{mn})$  are constructed using the same angle  $\theta_h$  as the Henneberg representation. In addition, in order not to lose information, if the  $(R_{mn}, Z_{mn})$  are non-zero for  $m < M_{pol}$ ,  $|n| < N_{tor}$ , the Fourier series of  $\rho$  must have non-zero modes for  $m < M$ ,  $|n| < N$ , with

$$M = M_{pol} \quad (3.57)$$

$$N = N_{tor} + 2\alpha. \quad (3.58)$$

Packing the geometrical modes  $(R_{mn}, Z_{mn})$  in a one-dimensional array  $\mathbf{X}$  and the modes  $(r_n, z_n, \rho_{mn}, b_n)$  in another one-dimensional array  $\mathbf{x}_h$ , one can thus write

$$\mathbf{X} = \mathbf{H}\mathbf{x}_h, \quad (3.59)$$

### Chapter 3. The stepped-pressure equilibrium code

---

where  $\mathbf{H}$  is a matrix of size  $(N_h \times N_x)$ , with

$$N_h = 3N + M(2N + 1) + 2 \quad (3.60)$$

$$= 3N_{tor} + M_{pol}(2N_{tor} + 1) + 4\alpha M_{pol} + 6\alpha - 1, \quad (3.61)$$

and  $N_x$  is given by Eq.(3.19). In general,  $N_h \neq N_x$ , and  $\mathbf{H}$  is not a square matrix. Note that, when  $M_{pol} \gg 1$  and  $N_{tor} \gg 1$ ,  $N_h/N_x \sim 1/2$ , *i.e.* the Henneberg representation uses about half the number of Fourier harmonics used by the standard representation, as long as both are using the same poloidal angle. Of course, in general  $N_h > N_x$  if the standard representation uses a spectrally condensed angle.

As an example, consider a rotating ellipse (see Figure 3.6) parametrized by

$$R_0(\phi) = R_0 \quad (3.62)$$

$$Z_0(\phi) = Z_0 \quad (3.63)$$

$$\rho(\theta_h, \phi) = \rho_{10} \cos \theta_h \quad (3.64)$$

$$b(\phi) = b_0 \quad (3.65)$$

$$\alpha = 0.5. \quad (3.66)$$

Applying the forward map (3.59), we immediately find

$$R(\theta_h, \phi) = R_0 + \frac{\rho_{10} + b_0}{2} \cos \theta_h + \frac{\rho_{10} - b_0}{2} \cos(\theta_h - N_{fp}\phi) \quad (3.67)$$

$$Z(\theta_h, \phi) = Z_0 + \frac{\rho_{10} + b_0}{2} \sin \theta_h - \frac{\rho_{10} - b_0}{2} \sin(\theta_h - N_{fp}\phi). \quad (3.68)$$

We remark here that  $\rho_{10}$  and  $b_0$  are the major and minor radii of the ellipse respectively. With this simple example we have shown that if one knows the harmonics  $\{r_n, z_n, b_n, \rho_{mn}\}$ , it is straightforward to obtain the harmonics  $\{R_{mn}, Z_{mn}\}$ . It is however not trivial to obtain the harmonics  $\{r_n, z_n, b_n, \rho_{mn}\}$  from a geometry  $R(\theta, \phi)$ ,  $Z(\theta, \phi)$ , as it will be discussed in the following section.

#### 3.3.2 Construction of the Henneberg harmonics

Here we suppose that a general surface  $(R(\theta, \phi), Z(\theta, \phi))$  is given, and we develop an algorithm to find the Fourier harmonics  $(r_n, z_n, \rho_{mn}, b_n)$  that fit best the input surface. We can first construct the function  $b(\phi)$ . As  $b(\phi)$  is independent of  $(R_0, Z_0)$ , we can set  $R_0 = Z_0 = 0$  and identify the poloidal angle  $\theta$  that extremizes the  $\zeta$  coordinate for each angle  $\phi$ ,

$$\tilde{\zeta}(\theta_+, \phi) = \max_{\theta \in [0, 2\pi]} \tilde{\zeta}(\theta, \phi) \quad (3.69)$$

$$\tilde{\zeta}(\theta_-, \phi) = \min_{\theta \in [0, 2\pi]} \tilde{\zeta}(\theta, \phi) \quad (3.70)$$

with  $\tilde{\zeta}$  the coordinate  $\zeta$  if  $R_0 = Z_0 = 0$ ,

$$\tilde{\zeta}(\theta, \phi) = Z \cos(\alpha\phi) - R \sin(\alpha\phi). \quad (3.71)$$

Then we can evaluate the radius of the circle  $\mathcal{C}$  as

$$b(\phi) = \frac{1}{2} [\tilde{\zeta}(\theta_+, \phi) - \tilde{\zeta}(\theta_-, \phi)], \quad (3.72)$$

Working in the  $\phi = \text{const}$  plane, the position  $(R_0(\phi), Z_0(\phi))$  must then be at equal distance from the point  $(R(\theta_+, \phi), Z(\theta_+, \phi))$  than from the point  $(R(\theta_-, \phi), Z(\theta_-, \phi))$ . We can thus write

$$R_0(\phi) = -Z_0(\phi) \frac{R(\theta_+, \phi) - R(\theta_-, \phi)}{Z(\theta_+, \phi) - Z(\theta_-, \phi)}. \quad (3.73)$$

Equation (3.73) only constrains  $R_0$  as function of  $Z_0$ , but does not fully determine the position of the point  $(R_0, Z_0)$ . The idea is now to write an optimization problem to fit the input surface, using as degrees of freedom the Fourier harmonics  $r_n$ . First, given the harmonics  $r_n$ , we can evaluate  $R_0(\phi)$  from Eq.(3.46) and  $Z_0(\phi)$  from Eq.(3.73) in real space. Then, the coordinate  $\rho(\theta, \phi)$  can be evaluated with

$$\rho(\theta, \phi) = (R - R_0) \cos(\alpha\phi) + (Z - Z_0) \sin(\alpha\phi), \quad (3.74)$$

and the Henneberg angle  $\theta_h$  can be evaluated via equation (3.43). The Fourier harmonics  $(b_n, \rho_{mn})$  can then be obtained by standard Fourier transforms. The corresponding surface, reconstructed in real space using Eqs.(3.38)-(3.47), can then be compared with the input surface  $(R(\theta, \phi), Z(\theta, \phi))$ . The algorithm then iterates on the  $r_n$  harmonics until both surfaces match. This method can be used to transform inputs that use the more conventional standard representation, Eqs.(3.4)-(3.5), into inputs that use the Henneberg representation. The only free parameter in this transformation is the parameter  $\alpha$ , that has to be chosen by the user. Note that a similar algorithm has been implemented in the ROSE optimization code (Drevlak et al., 2019).

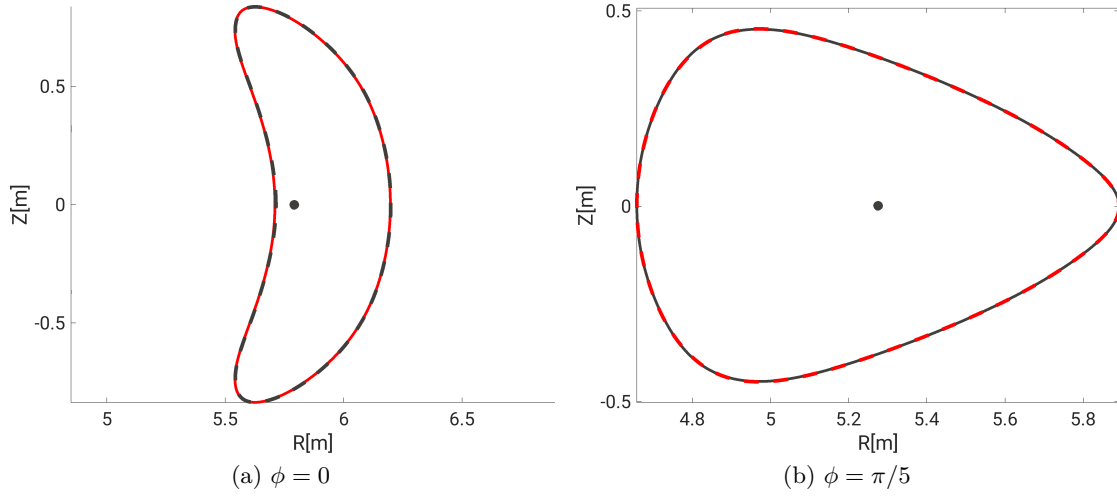


Figure 3.20: Plasma boundary of W7-X. In black: using the standard representation, and in red: using the Henneberg representation.

As an example, we compute the harmonics  $\{\rho_{mn}, b_n, r_n, z_n\}$  that best fit the W7-X geometry (see Figure 3.2a). The W7-X boundary is represented using the standard representation with  $M_{pol} = N_{tor} = 10$ , meaning that there are 442 different  $\{R_{mn}, Z_{mn}\}$  Fourier harmonics. Using the Henneberg representation, we set  $M = 12$ ,  $N = 10$ , and use the algorithm presented above to compute the harmonics  $\{\rho_{mn}, b_n, r_n, z_n\}$ , for a total of 295 different Fourier harmonics. The obtained boundary parametrized by the Henneberg representation is compared to the boundary parametrized using the standard representation on Figure 3.20. We see that, to the eye, there are no significant differences between both boundaries, which confirms that the Henneberg representation is suitable for parameterizing complex stellarator geometries. Clearly, in this particular case, the number of Fourier harmonics required by the Henneberg representation is smaller than those required by the standard representation. This is however not true in general; using a spectrally condensed angle might only require the same amount or less Fourier modes than the Henneberg representation to parametrize a surface.

### 3.3.3 Implementation in SPEC

To use the Henneberg representation in SPEC, the geometrical degrees of freedom on which SPEC iterates to find force balance need to be the  $\mathbf{x}_h = \{r_n^l, z_n^l, b_n^l, \rho_{mn}^l\}$  harmonics. Then, before entering the Beltrami solver, the mapping (3.59) is applied to get the corresponding  $\mathbf{X} = \{R_{mn}^l, Z_{mn}^l\}$  harmonics (notice that this is a direct evaluation of Eq.(3.59), there is no need to invert  $\mathbf{H}$ ). Once the field has been computed and the force has been evaluated, a new iteration on the geometry can be made by changing the  $\mathbf{x}_h$  harmonics. No backward map from the standard representation to the Henneberg representation is thus required.



### 3.3 Implementation of a unique angle representation

Note that the matrix  $\mathbf{H}$  is independent of the geometry, and can be evaluated once at the beginning of SPEC execution. This is of course very advantageous for SPEC speed. The force gradient, *i.e.* the derivatives of the force Fourier harmonics  $F_{lmn}$  with respect to the harmonics  $\mathbf{x}_h$ , can be easily obtained by applying the chain rule,

$$\frac{dF_{lmn}}{dx_{h,i}} = \frac{dF_{lmn}}{dx_k} \frac{\partial x_k}{\partial x_{h,i}}, \quad (3.75)$$

where the matrices elements  $dF_{lmn}/dx_k$  are the force gradient derivatives computed using the standard representation, described in section 3.2.2, and the matrices element  $\partial x_k/\partial x_{h,i}$  are obtained by taking the derivative of equation (3.59).

Finally, one has to be careful about the truncation of the force in Fourier space. The hybrid-Powell method used to iterate on the interfaces geometry requires the same number of degrees of freedom as equations, *i.e.* the force must be truncated such that it has  $N_h$  Fourier harmonics. This is possible if

$$m \leq M_{pol}^f = M_{pol} + 1 \quad (3.76)$$

$$|n| \leq N_{tor}^f = N_{tor}, \quad (3.77)$$

where  $M_{pol}^f$  and  $N_{tor}^f$  refer to the truncation of the force harmonics. The magnetic field and vector potential are, however, still truncated at the same resolution as the standard representation,  $M_{pol}$  and  $N_{tor}$ . The Fourier truncation used to represent different physical quantities in SPEC is summarized in table 3.1.

	$R_{mn}, Z_{mn}, B_{mn}$	$F_{lmn}$	$Y_{lmn}$	$\rho_{mn}^l, b_n^l, r_n^l, z_n^l$
Standard representation	$m \leq M_{pol}$ $ n  \leq N_{tor}$	$m \leq M_{pol}$ $ n  \leq N_{tor}$	-	-
Henneberg representation	$m \leq M_{pol} = M$ $ n  \leq N_{tor} = N + 2\alpha$	$m \leq M_{pol}^f = M + 1$ $ n  \leq N_{tor}^f = N$	-	$m \leq M$ $ n  \leq N$

Table 3.1: Summary of the different truncations in Fourier space used in SPEC, for the standard representation and the Henneberg representation. A dash indicated that the corresponding quantity is not used in SPEC with this representation of the geometry.

### 3.3.4 Verification and comparison with the standard representation

We compare here the solutions obtained by SPEC using the Henneberg representation to the ones obtained using the standard representation. In this section, we will only consider fixed-boundary calculations. We run SPEC using both the standard representation and the Henneberg representation in different stellarator geometries, and compare its outputs. To compare the convergence properties, we plot the scalar force  $|f|$  from Eq.(3.22), which usually goes down to machine precision ( $\sim 10^{-16}$ ) when the equilibrium is found, as a function of the number of force evaluations.

#### Bean shaped tokamak

We first look at an axisymmetric configuration with a bean shaped cross-section (see Figure 3.21), proposed by Hirshman and Meier (1985). The boundary is described by

$$R(\theta, \phi) = -0.32 + 1.115 \cos \theta + 0.383 \cos 2\theta - 0.0912 \cos 3\theta \quad (3.78)$$

$$+ 0.0358 \cos 4\theta - 0.0164 \cos 5\theta \quad (3.79)$$

$$Z(\theta, \phi) = 1.408 \sin \theta + 0.154 \sin 2\theta - 0.0264 \sin 3\theta. \quad (3.80)$$

The same boundary can be represented using the Henneberg representation. The harmonics  $\{r_n, z_n, b_n, \rho_{mn}\}$  are obtained using the algorithm presented in section 3.3.2,

$$R_0(\phi) = -0.32 \quad (3.81)$$

$$Z_0(\phi) = 0 \quad (3.82)$$

$$\rho(\theta, \phi) = 1.184 \cos \theta + 0.208 \cos 2\theta - 0.1433\theta \quad (3.83)$$

$$+ 0.064 \cos 4\theta - 0.032 \cos 5\theta + 0.011 \cos 6\theta \quad (3.84)$$

$$b(\phi) = 1.419 \quad (3.85)$$

$$\alpha = 0. \quad (3.86)$$

We attempt a two-volume fixed-boundary SPEC calculation, with  $\psi_{t,1} = 0.61 \text{Tm}^2$  and  $\psi_{t,2} = 2 \text{Tm}^2$ , and where we impose the rotational transform to be equal of  $\epsilon_1 = 0.28$  on each side of the inner plasma interface, and  $\epsilon_2 = 0.31$  at the plasma boundary. We set the Fourier resolution to  $M_{pol} = M = 6$ ,  $N_{tor} = N = 2$ , and the radial resolution to  $L_{rad} = 12$  in both volumes. Note that due to Eqs.(3.76)-(3.77), SPEC seeks a geometry that minimizes more Fourier harmonics of the physical force when using the Henneberg representation, but does not have to minimize the numerical force related to the spectral condensation (see table 3.2). Finally, we construct an initial guess for the inner plasma interface geometry via interpolation of the plasma boundary. This initial guess is the same for both SPEC calculations, running either with the standard or the Henneberg representation.

### 3.3 Implementation of a unique angle representation

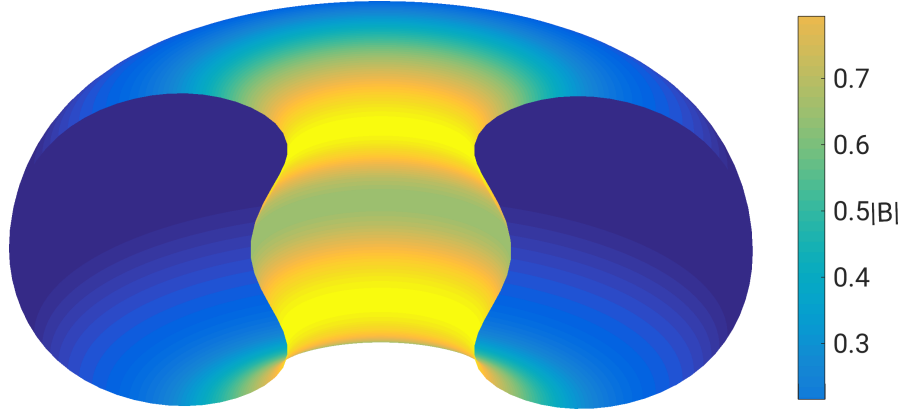


Figure 3.21: Tokamak with bean shaped cross-section as described by Eqs.(3.78)-(3.80). Colors indicate the magnetic field strength in vacuum.

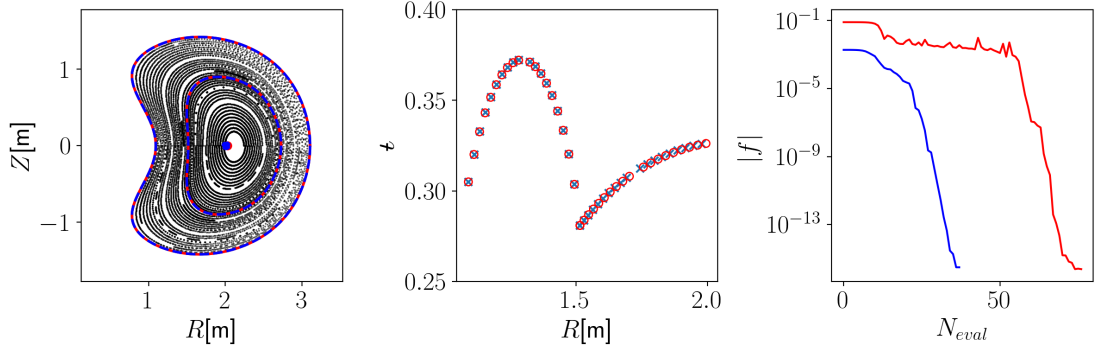


Figure 3.22: Bean shaped tokamak. Left: Poincaré section, with the volume's interface and plasma boundary highlighted in color. Middle: rotational transform profile, and right: scalar force as a function of the iteration number. Red: standard representation and blue: Henneberg representation.

	$R_{mn}, Z_{mn}, B_{mn}$	$F_{lmn}$	$F_{lmn}$	$\rho_{mn}, b_n, r_n, z_n$
Standard representation	$m \leq 6$ $ n  \leq 2$	$m \leq 6$ $ n  \leq 2$		- -
Henneberg representation	$m \leq M_{pol} = 6$ $ n  \leq N_{tor} = 2$	$m \leq 7$ $ n  \leq 2$	- -	$m \leq 6$ $ n  \leq 2$

Table 3.2: Bean shaped tokamak test case, summary of the different Fourier resolutions used in SPEC calculation using the standard and Henneberg representation.

The poincaré section of the obtained equilibria, rotational transform profile and force scalar are plotted on Figure 3.22. Both representations are able to find the same equilibrium; the inner volume interface is visually the same, and the rotational transform profiles are very close. Interestingly, we see that SPEC using the standard representation (in red) requires about twice more force evaluations to find the equilibrium than those required when using the Henneberg representation. This is expected since SPEC needs to satisfy the spectral constraints when running with the standard representation, which almost doubles the amount of force harmonics to minimize. In addition, the standard representation has more degrees of freedom than the Henneberg representation.

#### Circular cross-section, large torsion configuration

The second case of interest is a stellarator with circular cross-section and large magnetic torsion (see Figure 3.23), described in the Henneberg representation by  $\alpha = 0$ , and

$$R_0(\phi) = 10 + \cos(5\phi) \quad (3.87)$$

$$Z_0(\phi) = -\sin(5\phi) \quad (3.88)$$

$$\rho(\theta, \phi) = 1.25 \cos \theta \quad (3.89)$$

$$b(\phi) = -1.25 \quad (3.90)$$

which can be expressed by the standard representation by using Eq.(3.59),

$$R(\theta, \phi) = 10 + 1.25 \cos \theta + \cos(5\phi) \quad (3.91)$$

$$Z(\theta, \phi) = -1.25 \sin \theta - \sin(5\phi). \quad (3.92)$$

We evaluate a vacuum field by performing a two-volume fixed-boundary SPEC calculation. We set the toroidal flux to  $\psi_{t,1} = 0.3$  and  $\psi_{t,2} = 1\text{Tm}^2$ , and constraint the net toroidal current in each volume and at their interface to be zero, *i.e.*  $I_{\phi,1}^s = 0$  and  $I_{\phi,1}^v = I_{\phi,2}^v = 0$ , in order to reproduce a vacuum field. We set the poloidal resolution to  $M_{pol} = M = 6$ , toroidal resolution to  $N_{tor} = N = 4$  and radial resolution to  $L_{rad} = 14$  in both volumes. The different Fourier resolution used in both SPEC calculations are written in table 3.3 . The initial guess for the interface geometry is interpolated from the plasma boundary, and is the same for either representation.

The Poincaré section, rotational transform profile and force scalar are plotted on Figure 3.24. SPEC finds the equilibrium in about  $\sim 50$  force evaluations using either representation. The equilibrium found with the Henneberg representation is the same as the one found with the standard representation. This test case, in addition to the bean shaped tokamak presented above, shows that the Henneberg representation is correctly implemented in SPEC for a tokamak or stellarator boundary that has  $\alpha = 0$ . We will now explore cases where  $\alpha \neq 0$ .

### 3.3 Implementation of a unique angle representation

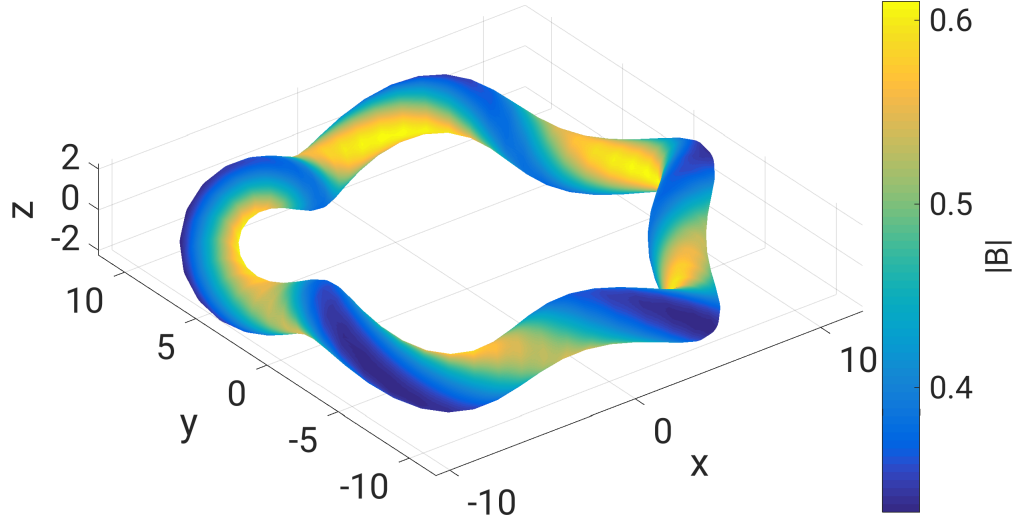


Figure 3.23: Circular cross-section, large torsion configuration. Colors indicate the magnetic field strength in vacuum.

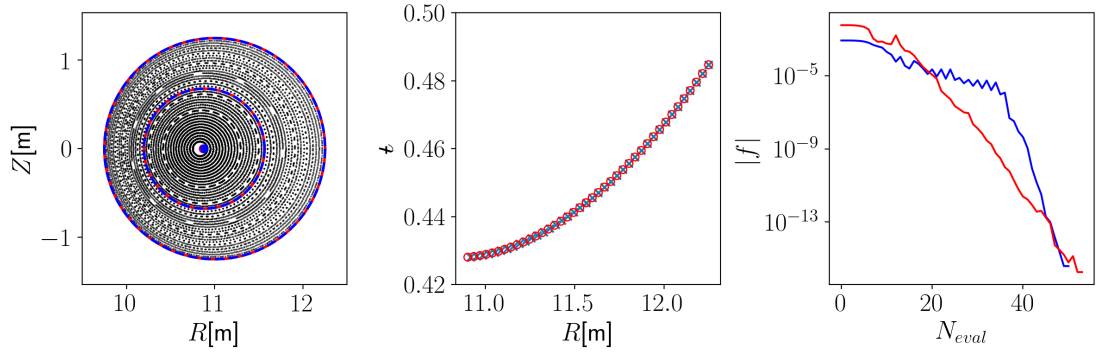


Figure 3.24: Circular cross-section, large torsion configuration. Left: Poincaré section, with the volume's interface and the plasma boundary highlighted in color. Middle: rotational transform profile, and right: scalar force as a function of the iteration number. Red: standard representation, and blue: Henneberg representation.

	$R_{mn}, Z_{mn}, B_{mn}$	$F_{lmn}$	$F_{lmn}$	$\rho_{mn}, b_n, r_n, z_n$
Standard representation	$m \leq 6$ $ n  \leq 4$	$m \leq 6$ $ n  \leq 4$		- -
Henneberg representation	$m \leq M_{pol} = 6$ $ n  \leq N_{tor} = 4$	$m \leq 7$ $ n  \leq 4$	- -	$m \leq 6$ $ n  \leq 4$

Table 3.3: Circular cross-section and large torsion test case. Fourier resolutions used in SPEC calculation using the standard and Henneberg representation.

### Rotating ellipse

We now look at the case of a rotating ellipse (see Figure 3.6), whose boundary is described by setting  $\alpha = 0.5$ , and

$$R_0(\phi) = 10 \quad (3.93)$$

$$Z_0(\phi) = 0 \quad (3.94)$$

$$\rho(\theta, \phi) = 1.5 \cos \theta \quad (3.95)$$

$$b(\phi) = -1 \quad (3.96)$$

which can again be expressed with the standard representation by using Eq.(3.59),

$$R(\theta, \phi) = 10 + 0.25 \cos \theta + 1.25 \cos(\theta - 5\phi) \quad (3.97)$$

$$Z(\theta, \phi) = 0.25 \sin \theta - 1.25 \sin(\theta - 5\phi), \quad (3.98)$$

Note that  $b_0 < 0$  ensures a right-handed coordinate system. We again attempt a two-volumes, fixed-boundary, vacuum SPEC calculation, and set the toroidal flux in each volume to  $\psi_{t,1} = 0.3$  and  $\psi_{t,2} = 1\text{Tm}^2$  respectively. We constrain the equilibrium to be a vacuum by setting the pressure in each volume to zero,  $p_l = 0$ , as well as the net toroidal current in the volumes and at the interface,  $I_{\phi,l}^s = I_{\phi,l}^v = 0$ . The standard representation is run with  $M_{pol} = 6$ ,  $N_{tor} = 5$ , while the Henneberg representation is run with  $M = 5$ ,  $N = 5$ . The Fourier resolution has been chosen such that both SPEC calculations truncates the force at the same Fourier resolution (table 3.4). The initial guess for the geometry of the interface is obtained by interpolating the plasma boundary, and is the same for each SPEC calculation.

	$R_{mn}, Z_{mn}, B_{mn}$	$F_{lmn}$	$\rho_{mn}, b_n, r_n, z_n$
Standard	$m \leq 6$	$m \leq 6$	-
representation	$ n  \leq 5$	$ n  \leq 5$	-
Henneberg	$m \leq 5$	$m \leq 6$	$m \leq 5$
representation	$ n  \leq 6$	$ n  \leq 5$	$ n  \leq 5$

Table 3.4: Rotating ellipse test case, summary of the different Fourier resolutions used in SPEC calculation using the standard and Henneberg representation.

Again, the Poincaré section, rotational transform profile and force scalar are plotted on Figure 3.25. While it seems that both SPEC runs find the same equilibrium, we remark that the force scalar  $|f|$  saturates at  $\sim 3 \cdot 10^{-8}$  when using the Henneberg representation. This is surprising, since this representation is supposed to be using an optimal angle for representing ellipses. We would thus expect that, at equilibrium, the geometry of the inner interface could be expressed using the Henneberg representation, and thus that SPEC would be able to find it.

### 3.3 Implementation of a unique angle representation

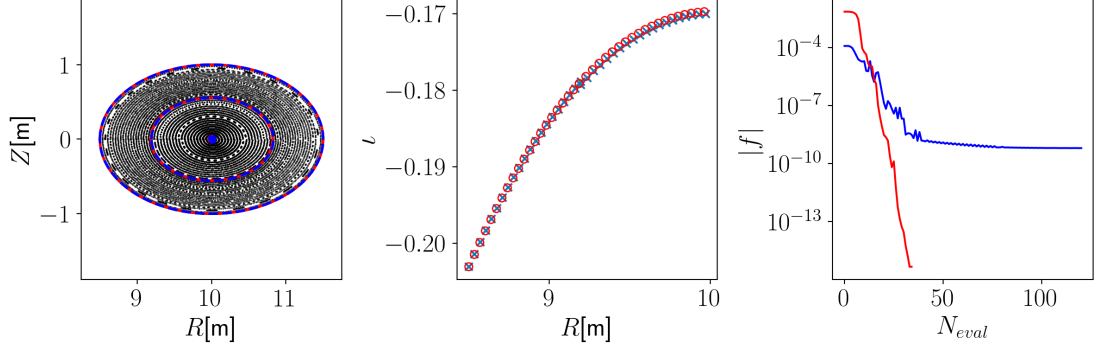


Figure 3.25: Classical stellarator. Left: Poincaré section, with the volume’s interface and the plasma boundary highlighted in color. Middle: rotational transform profile, and right: scalar force as a function of the iteration number. Red: standard representation and blue: Henneberg representation.

The normalized residual force,  $[(B/B_0)^2/2]$ , evaluated in real space, and its Fourier harmonics, calculated at the equilibrium found by SPEC using the standard representation, are shown on the top panels of Figure 3.26. Not surprisingly, as only the Fourier harmonics of the force with  $m \leq M_{pol}$ , and  $|n| \leq N_{tor}$ , are minimized to zero by SPEC, the force in real space is *not* zero — it is of order  $10^{-4}$ . This is also clearly visible on the top right panel of Figure 3.26. The same analysis can be done for the equilibrium obtained with SPEC using the Henneberg representation (see lower panels of Figure 3.26). Again, we observe that higher order Fourier modes keep the force in real space relatively large. In real space, the force residuals have structures different than in the case where the standard representation was used. The Fourier modes of the force that are minimized by SPEC are of the order of  $10^{-4}$ , *i.e.* orders of magnitude larger than machine precision.

This example suggests that the implementation of the Henneberg representation in the SPEC code does not solve its robustness issues — it actually made it worse, since SPEC could not find the equilibrium in a rotating ellipse geometry using this new representation. The hypothesis, that unfortunately could not be verified in the time frame of this thesis, is that the different truncations of the Fourier series in SPEC when using the Henneberg representation are causing the issue when  $\alpha \neq 0$ . Indeed, potential implementation errors are possible but unlikely, as each submodule implemented in SPEC, namely the mapping (3.54)-(3.56), and the implementation of the chain rule to evaluate the force gradient (3.75), have been both verified independently to return the right values.

In summary, we have implemented the Henneberg representation as an alternative representation for the toroidal surfaces in SPEC in an attempt to solve its robustness issues. Unfortunately, SPEC does not converge towards an equilibrium when  $\alpha \neq 0$ . For that reason, all further results in this thesis will use the standard representation. In addition, only simplified stellarator geometries, or, in some cases, more shaped geometries but with a limited number of volumes will be considered.

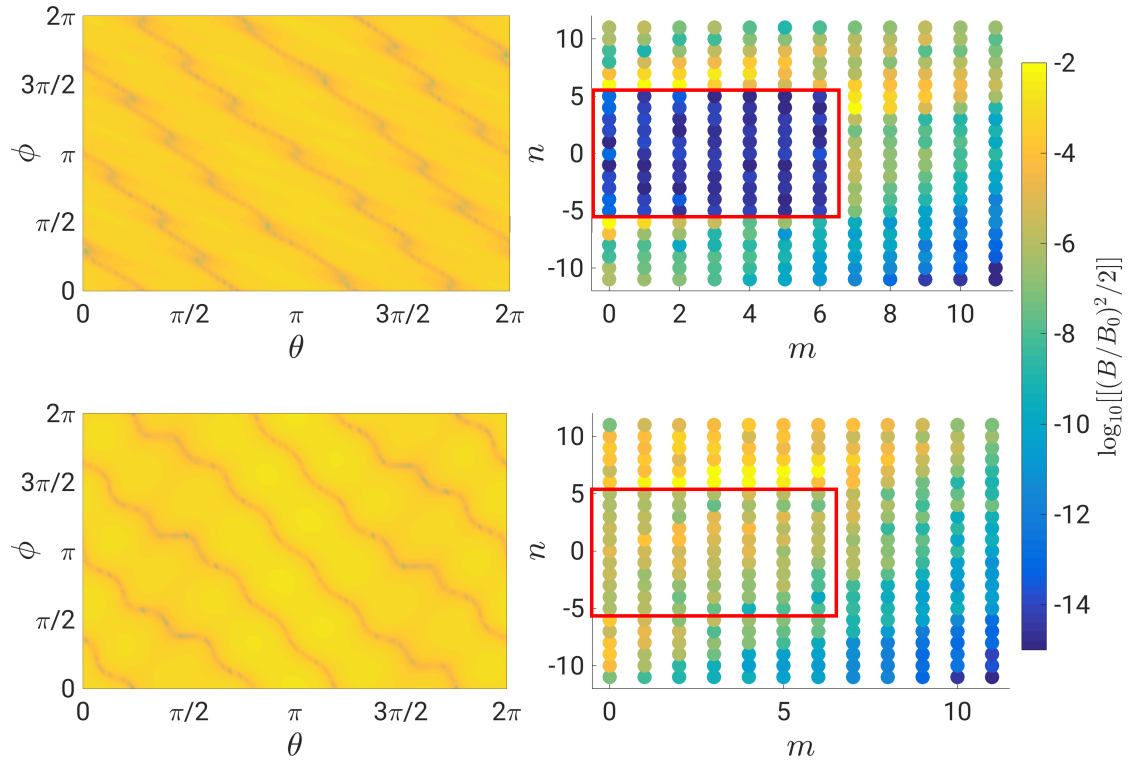


Figure 3.26: Normalized residual force on an interface from a rotating ellipse equilibrium obtained with SPEC. Left: real space, right: Fourier space. Top: standard representation. Bottom: Henneberg representation. The red box surrounds the space of modes that are not truncated.



### 3.4 Summary

In this chapter, we explained some important features of the SPEC algorithm. Details were given on the main loops of the SPEC algorithm, namely the Beltrami solver, the force minimization, and the free-boundary iterations. In addition, we showed how the net toroidal current profile could be constrained in SPEC. Two different net toroidal current profiles co-exist in MRxMHD: the volume current profile, flowing through the volumes, and the surface current profile, flowing at each volume's interface. Both profiles were implemented as new constraints in the SPEC code, which can now compute MRxMHD equilibria for a given toroidal current profile. Analytical derivatives of the force on each volume's interface with respect to the geometry of the interfaces at fixed toroidal current have been derived and implemented in SPEC. These derivatives speed up substantially the hybrid-Powell iterations on the geometry of the interfaces. Both the new constraint and the force gradient implementation have been verified in cylindrical and toroidal geometries. In cylindrical geometry, we considered an axisymmetric screw pinch, where the equilibria and force gradient obtained with SPEC could be compared to analytical solutions. In toroidal geometry, a classical stellarator has been considered. The equilibrium at fixed toroidal current profile has been verified to match the equilibrium obtained by constraining the rotational transform profile in SPEC, and the force gradient has been compared to a finite difference estimate.

In addition to the capability to constrain the net toroidal current in SPEC, the Henneberg representation was implemented as an alternative way of parameterizing the geometry of the interfaces. This representation uses a unique poloidal angle, which allows SPEC to be run without the spectral condensation, and was foreseen to be a potential solution to SPEC robustness issues in finding force-balance in strongly shaped geometries. In addition, the derivatives of the force with respect to the new geometrical degrees of freedom were implemented. The implementation was verified in multiple geometries, namely a bean-shaped tokamak, a stellarator with circular cross-section and strong torsion, and a rotating ellipse. While promising results in the case of the stellarator with circular cross-section and torsion were obtained, it showed disappointing results in the case of a rotating ellipse. It is thought that the different Fourier truncations used in SPEC when  $\alpha \neq 0$  might be the source of the issue. The robustness issues in SPEC that arise in strongly shaped calculations thus remains unsolved.

It is however important to emphasize that while this new representation does not solve SPEC robustness issues, it greatly simplifies the problem of numerical fragility. Essentially, we decoupled the issues related to the spectral condensation to the potential robustness issues related to the physical force. The next obvious step is to make SPEC more robust using the Henneberg representation. Once SPEC is able to reliably find a solution with zero physical force, one can look at implementing a more robust spectral condensation algorithm. Ideas to improve SPEC convergence are numerous. We could try to combine both representations — use the Henneberg representation when SPEC

is far from the equilibrium, and switch to the standard representation once the force is already quite small. Another proposition would be to change the hybrid-Powell method for another algorithm that might be more adapted to the MRxMHD equilibrium problem (*e.g.* descent-like methods). Finally, one could improve how the force is numerically evaluated. Indeed, the force is a quadratic function of the magnetic field; by truncating its Fourier series with the same modes as the magnetic field, one might lose important information. A solution would be to evaluate the force in real space on a number of cleverly chosen collocation points (as proposed by the DESC team (Dudt and Kolemen, 2020)), and to minimize the  $L^2$ -norm of the force. This would have the benefit of considering all Fourier modes of the force. These ideas could unfortunately not be explored further in the time frame of this thesis.

## 4 Measures of magnetic field line topology

In magnetic fusion devices such as stellarators, zeroth order confinement of particles and energy is obtained by constructing an equilibrium with magnetic surfaces. Magnetic islands and magnetic field line chaos are detrimental to confinement, *i.e.* they contribute to increased radial transport of particle and energy (Hudson and Nakajima, 2010). While it is possible to design equilibria with good magnetic surfaces in a vacuum (Cary and Kotschenreuther, 1985; Cary and Hanson, 1986; Pedersen et al., 2016), pressure-driven plasma currents, such as diamagnetic, Pfirsch-Schlüter and bootstrap currents, perturb finite  $\beta$  equilibria, and, at a sufficiently large pressure, magnetic islands and chaos emerge.

A pressure increase can also sometimes heal magnetic islands (Bhattacharjee et al., 1995). While this mechanism can improve confinement locally, other islands might open elsewhere in the plasma as  $\beta$  increases. Starting from a vacuum magnetic field with magnetic surfaces, there is thus a critical value of  $\beta$  at which magnetic islands open and magnetic field line chaos emerges. This defines an *equilibrium  $\beta$ -limit*. Note however that the equilibrium  $\beta$ -limit is a *soft limit*, since crossing it does not lead to a loss of control of the plasma. Additional input power may however leak through the damaged magnetic surfaces more easily (Rechester and Rosenbluth, 1978), thereby preventing a further increase of  $\beta$ . Crossing the equilibrium  $\beta$ -limit may thus not be as concerning as crossing a stability limit (which may lead to plasma disruptions), but it still limits the overall performance of the reactor, and by definition its  $Q$ -factor. It is consequently of crucial importance to understand these equilibrium  $\beta$ -limits better, especially for the operation of existing experiments and the design of new machines. Configurations where good magnetic surfaces are preserved over a large range of  $\beta$  have to be sought, which will help to ultimately identify configurations whose equilibrium  $\beta$ -limit is large enough for good plasma performance.

In view of assessing the capability of a magnetic equilibrium to confine a plasma, and ultimately calculating its equilibrium  $\beta$ -limit, one has to define metrics to measure the confinement properties of magnetic equilibria, such as numerical diagnostics that

can determine the topology of a magnetic field line. In this chapter, we first review two different metrics, namely the Greene's residue (Greene, 1968, 1979), and the volume of chaos (Loizu et al., 2017). We then propose a new metric, the fraction of net parallel diffusion (Baillod et al., 2022), and develop an associated numerical diagnostic that does not have the same limitations as the volume of chaos, and provides more physics-based insights on the effect of magnetic field line topology on particle transport. In subsequent chapters, these metrics will be used in different applications. The volume of chaos and the fraction of parallel diffusion will be used to measure the equilibrium  $\beta$ -limit in a classical stellarator (chapter 5), while objective functions will be constructed using the Greene's residues of some specific resonances to optimize stellarator equilibria for good magnetic surfaces (chapter 6).

Parts of this chapter are adapted from the following publication: A. Baillod *et al.*, Equilibrium  $\beta$ -limits dependence on bootstrap current in classical stellarators, arXiv:2211.12948v2 (2022) (Baillod et al., 2022).

### 4.1 Greene's residues

The first metric discussed in this chapter is the Greene's residue (Greene, 1968, 1979). This measure is a local indicator of the presence of an island on a rational surface. First, note that the Poincaré section of a magnetic equilibrium can be understood as the map  $T(R, Z) : \mathbb{R}^2 \rightarrow \mathbb{R}^2$ , that maps any point  $(R_i, Z_i)$  of the  $RZ$ -plane to another point  $(R_{i+1}, Z_{i+1})$  after each toroidal transit of the magnetic field. We remark here that, as magnetic field lines are described by a Hamiltonian set of equations (1.34)-(1.35), the map  $T(R, Z)$  is symplectic (Lichtenberg and Lieberman, 2013). In 2 dimensions, symplectic maps are maps that preserve the area (Meiss, 1992).

Orbits are then characterized by a sequence of points  $\{(R_0, Z_0), \dots, (R_n, Z_n)\}$ , and can form either periodic orbits, which correspond to rational magnetic surfaces, or quasiperiodic orbits, which correspond to irrational surfaces. In case of a resonance, periodic orbits fill a finite volume of the space, *i.e.* a magnetic island is formed. Of particular interest are the O- and X-points of the island chain, thereafter denoted  $\mathbf{x}_o$  and  $\mathbf{x}_x$  respectively, located at the center and at the edge of the islands. These points are fixed-points of the map  $T$ , that is  $T(\mathbf{x}_{o/x}) = \mathbf{x}_{o/x}$ . The asymptotic behavior of the orbits close to these points can be studied by looking at the Taylor expansion of the map  $T$  around  $\mathbf{x}_{o/x}$ ,

$$T(\mathbf{x}_{o/x} + \delta\mathbf{x}) = \mathbf{x}_{o/x} + J_T(\mathbf{x}_{o/x})\delta\mathbf{x}, \quad (4.1)$$

where  $\delta\mathbf{x}$  is a small displacement from  $\mathbf{x}_{o/x}$ , and  $J_T(\mathbf{x}_{o/x})$  is the jacobian of  $T$ . As  $T$  is symplectic (Meiss, 1992),  $\det(J_T) = 1$ , and the eigenvalues of the jacobian are

$$\lambda_{\pm} = \frac{1}{2} \left( \text{Tr}(J_T) \pm \sqrt{\text{Tr}(J_T)^2 - 4} \right), \quad (4.2)$$

with  $Tr(J_T)$  the trace of the jacobian matrix, and, as expected by the symplectic property of  $T$ , we have  $\lambda_+ = 1/\lambda_-$ . At a fixed point  $\mathbf{x}_{o/x}$ , the following cases are then possible (Lichtenberg and Lieberman, 2013):

1. The eigenvalues are real, with  $\lambda_+ < -1$  and  $-1 < \lambda_- < 0$ . The trace of the jacobian matrix is then  $Tr(J_T) < -2$ . In this case, orbits close to the fixed-point trace hyperbolas, and are reflected on the opposite side of the fixed-point at each map iteration. The orbits are therefore called *reflective hyperbolic* orbits, and the fixed-point is an X-point (see Figure 4.1(a)).
2. The eigenvalues are real, with  $\lambda_+ > 1$  and  $0 < \lambda_- < 1$ . The trace of the jacobian matrix is then  $Tr(J_T) > 2$ . Again, orbits close to the fixed-point trace hyperbolas. In this case however, orbits stay on the same side of the fixed-point at each map iteration; they are therefore called *hyperbolic* orbits, and the fixed-point is also an X-point (see Figure 4.1(e)).
3. The eigenvalues are two complex conjugate values,  $\lambda_{\pm} = e^{\pm 2\pi i \omega}$ , with  $\omega$  a constant, and corresponds to the case where the trace of the jacobian matrix is  $|Tr(J_T)| < 2$ . Orbits close to the fixed point are *elliptic* orbits; the fixed-point is thus an O-point (see Figure 4.1(c)).
4. The two remaining cases describe the transition between hyperbolic and elliptic orbits, and are called *parabolic* orbits. The transition between reflective hyperbolic orbits and elliptic orbits occurs when  $\lambda_+ = \lambda_- = -1$ , and  $Tr(J_T) = -2$ . Using Eqs.(1.34)-(1.35) to describe a magnetic field line, the Poincaré map of a magnetic field line around a fixed-point is characterized by a sequence of points with alternating signs of  $\chi$  (see Figure 4.1(b)).
5. The transition between elliptic and hyperbolic orbits occur when  $\lambda_+ = \lambda_- = 1$ , and  $Tr(J_T) = 2$ . In this case, the Poincaré map of magnetic field lines around the fixed-point is characterized by a sequence of points with  $\chi = \text{const}$ , *i.e.* a magnetic surface (see Figure 4.1(d)).

The Greene's Residue  $R$  is a measure used to differentiate between the cases (1)-(5), which is more practical than the eigenvalues  $\lambda_{\pm}$ . It is defined as

$$R = \frac{1}{4} (2 - Tr(J_T)) . \quad (4.3)$$

For reflection hyperbolic orbits,  $R > 1$ ; for elliptic orbits,  $0 < R < 1$ ; for parabolic orbits,  $R = 1$ ; for hyperbolic orbits,  $R < 0$ ; and for orbits that trace magnetic surfaces,  $R = 0$ . We will discuss in chapter 6 how stellarators can be optimized for good magnetic surfaces by minimizing the square of the Greene's residue of some targeted resonances. As an illustrative example, we describe in the next section the standard map and compute its Greene's Residue.

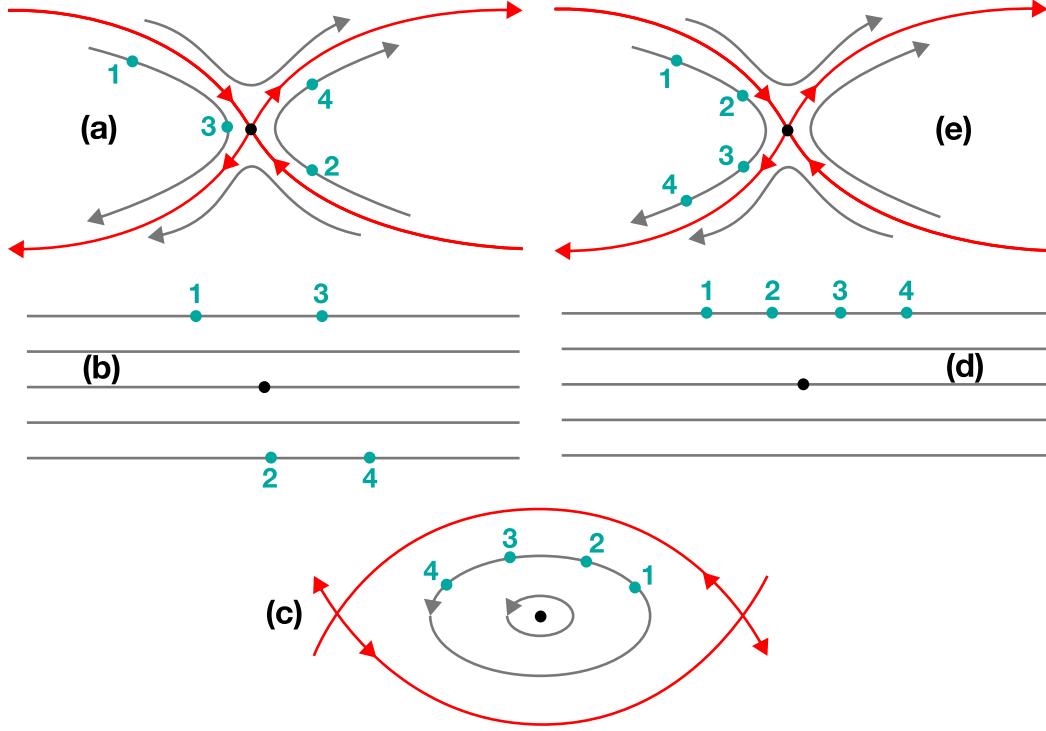


Figure 4.1: Sketch of a reflective hyperbolic orbit (a), a hyperbolic orbit (e), an elliptic orbit (c) and of two parabolic orbits (b) and (d). The order (a)-(e) follows the increasing value of  $Tr(J_T)$ . Red lines: island separatrix and grey: magnetic field line orbits. Black dot: position of the fixed-point. In the case of parabolic orbits (b) and (d), the separatrix is not well defined and is not traced. Arrows indicate the direction the magnetic field line moves along the orbit after each toroidal transit. Blue points are the position of a magnetic field line after 1 – 4 toroidal transits.

### 4.1.1 Standard map

The standard map is a canonical example of a 2-dimensional non-linear map. It is defined as  $(x', y') = T(x, y)$ , with

$$y' = y - \frac{k}{2\pi} \sin(2\pi x) \quad (4.4)$$

$$x' = x + y', \quad (4.5)$$

with  $k$  a parameter, that controls the non-linearity strength in the system. We plot the phase space of the standard map for four different values of  $k$  in Figure 4.2. For  $k = 0$ , the map is linear, and there are no islands nor chaos in the system. For  $k = 0.3$ , some resonances are excited, but their corresponding islands remain small. At  $k = 0.9$ , islands start to overlap, and the phase space is filled with islands, and some chaotic orbits. At  $k = 1.3$ , most orbits are chaotic.

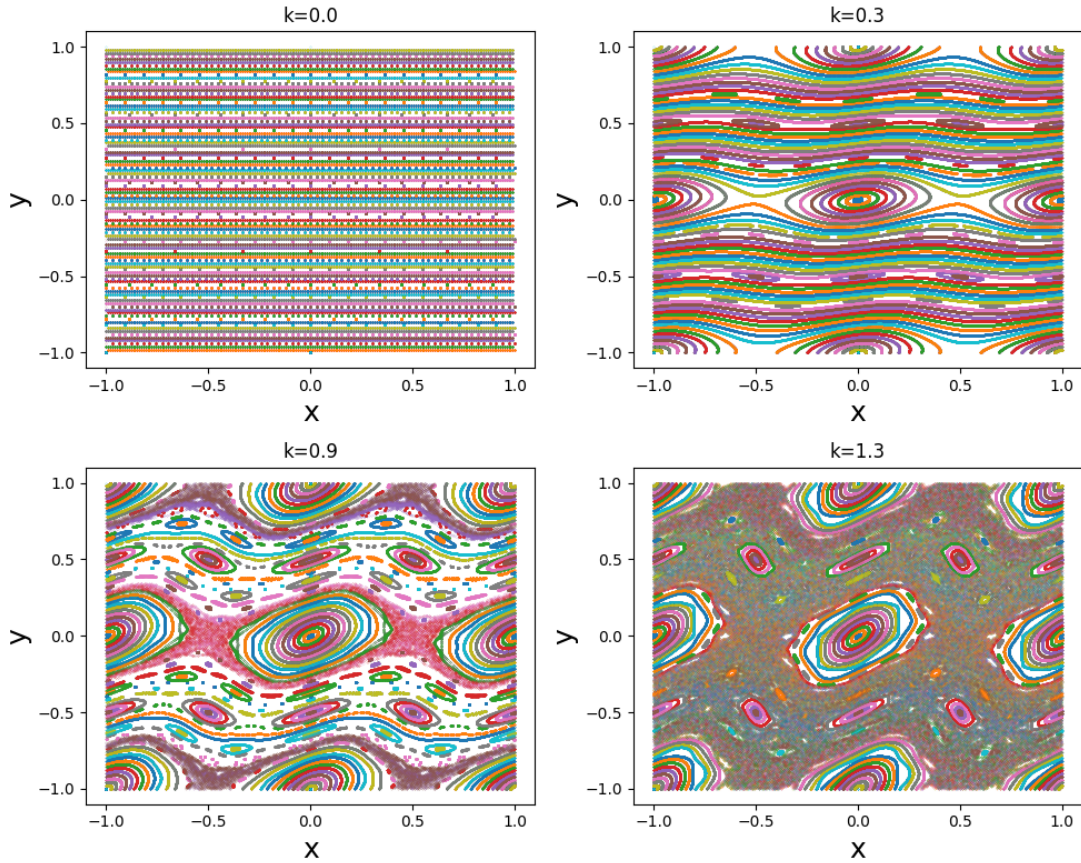


Figure 4.2: Phase space of the standard map for four different values of  $k$ , as described by Eqs.(4.4)-(4.5). Colors indicate different orbits. Here we plot 200 orbits, with initial condition  $x = 0, 1$  and  $y = k/100$ , with  $k = \{0, \dots, 99\}$ , and plot 4000 iterations of the map for each orbit.

## Chapter 4. Measures of magnetic field line topology

---

The points  $\mathbf{x}_o = (x = 0, y = 0)$  and  $\mathbf{x}_x = (x = 1/2, y = 0)$  are both fixed points of the standard map, as  $T(\mathbf{x}_{o/x}) = \mathbf{x}_{o/x}$ . We study the behavior of the orbits close to these points by looking at the jacobian of  $T$ ,

$$J_T = \begin{pmatrix} 1 - k \cos(2\pi x) & 1 \\ -k \cos(2\pi x) & 1 \end{pmatrix}. \quad (4.6)$$

The eigenvalues of  $J_T$  are then

$$\lambda_{\pm} = \frac{1}{2} \left( 2 - k \cos(2\pi x) \pm \sqrt{(2 - k \cos(2\pi x))^2 - 4} \right), \quad (4.7)$$

and the Greene's residue is

$$R = \frac{k}{4} \cos(2\pi x). \quad (4.8)$$

At  $\mathbf{x}_o$ , the Greene's residue is zero if and only if  $k = 0$ , which, as seen on top left panel of Figure 4.2, corresponds to a phase space without island. For  $0 < k < 4$ , the Greene's residue is  $0 < |R| < 1$ , which corresponds to the existence of an island. The orbits around the  $\mathbf{x}_o$  fixed points are elliptic, which corresponds to an O-point at  $\mathbf{x}_o$ . Finally, for  $k > 4$ , the orbits become hyperbolic. For such large values of  $k$  however, the phase space is mostly filled with chaotic orbits, making any observation difficult. Regarding the  $\mathbf{x}_x$  fixed-point, it is again zero if and only if  $k = 0$ . For any values of  $k > 0$  however, the residue is smaller than 0. Orbits close to the fixed point are hyperbolic, which correspond to an X-point at  $\mathbf{x}_x$ .

The Greene's residues are a great measure to assess whether or not a rational surface is resonant, or more generally if magnetic islands are present. This does however require that the fixed points of the magnetic field Poincaré map are known. In practice, this means that for any given magnetic equilibrium, resonances of interest must be selected, and the location of their fixed point must then be found. The Greene's residue is thus a local measure — as it will be discussed in chapter 6, this can be a limitation when performing stellarator optimization. In addition, the Greene's residue gives no information on the impact of the field line topology on the plasma confinement.



## 4.2 Volume of chaos

We build here an alternative global metric, that measures the volume occupied by chaotic field lines. We first seek to discriminate between a chaotic field line and other magnetic field line topologies by evaluating the fractal dimension  $D$  of the field line Poincaré section, for example using a box-counting algorithm (Meiss, 1992). Assuming that a field line Poincaré section is provided as a set of  $N_p$  points in the  $RZ$ -plane, we split the  $RZ$ -plane into a grid made of squares of dimension  $L \times L$  and count the number  $N$  of grid elements that contain at least one point from the field line (see top panel of Figure 4.3). The box-counting dimension (also called fractal dimension or Hausdorff dimension) is then given by

$$D = \lim_{L \rightarrow 0} \frac{\log N(L)}{\log L_0/L}, \quad (4.9)$$

with  $L_0$  the typical dimension of the map. The value of  $N(L)$  as a function of  $L$  is plotted on the lower panel of Figure 4.3. For large values of  $L$ , all points from a magnetic field line Poincaré section are contained in a single grid element, and  $N = 1$ . For small values of  $L$ , each grid element contains at most one point from the magnetic field line Poincaré section, and  $N = N_p$ . Between these two saturated values, the curve can be approximated by a linear function,  $\log(N) \approx D \log(L_0/L) + C$ , with  $C$  an irrelevant constant. The fractal dimension  $D$  can thus be extracted by fitting the linear part of the curve (Arbez, 2021).

An almost binary behavior is then observed: either a magnetic field line stays on a magnetic surface whose Poincaré section is a one-dimensional object,  $D = 1$ , or the magnetic field line has a fractal dimension  $D > D_{crit}$ , with  $1 < D_{crit} < 2$ . For example, for the two lines showed on Figure 4.3, we find  $D = 1.0$  for the blue line and  $D = 1.4$  for the red line. Loizu et al. (2017) proposed to evaluate the volume occupied by chaotic field lines with

$$V_{chaos} = V_P \sum_{i=1}^{N_{lines}} \frac{(\psi_{t,i} - \psi_{t,i-1})}{\psi_a} \mathcal{H}(D_i - D_{crit}), \quad (4.10)$$

where  $N_{lines}$  is the number of considered field lines,  $D_i$  is the fractal dimension of the  $i^{\text{th}}$  line,  $\mathcal{H}$  is the Heaviside function,  $V_P$  is the total plasma volume,  $\psi_{t,i} - \psi_{t,i-1}$  measures the enclosed toroidal flux between field lines  $i$  and  $i - 1$ , and  $\psi_a$  is the toroidal flux enclosed by the plasma.

As an illustration of the volume of chaos, we evaluate it for the standard map defined in Eqs.(4.4)-(4.5) as a function of the parameter  $k$  for different values of  $D_{crit}$  (see Figure 4.4). The same trend is observed for the three considered values of  $D_{crit}$ : for low values of  $k$ , the volume of chaos is zero; a critical value of  $k$ , between 0.5 and 0.8, marks the emergence of chaotic orbits; for large values of  $k$ , the normalized volume of chaos tends to 0.8 — the remaining non chaotic orbits are those close to O-points inside islands (Arbez, 2021).

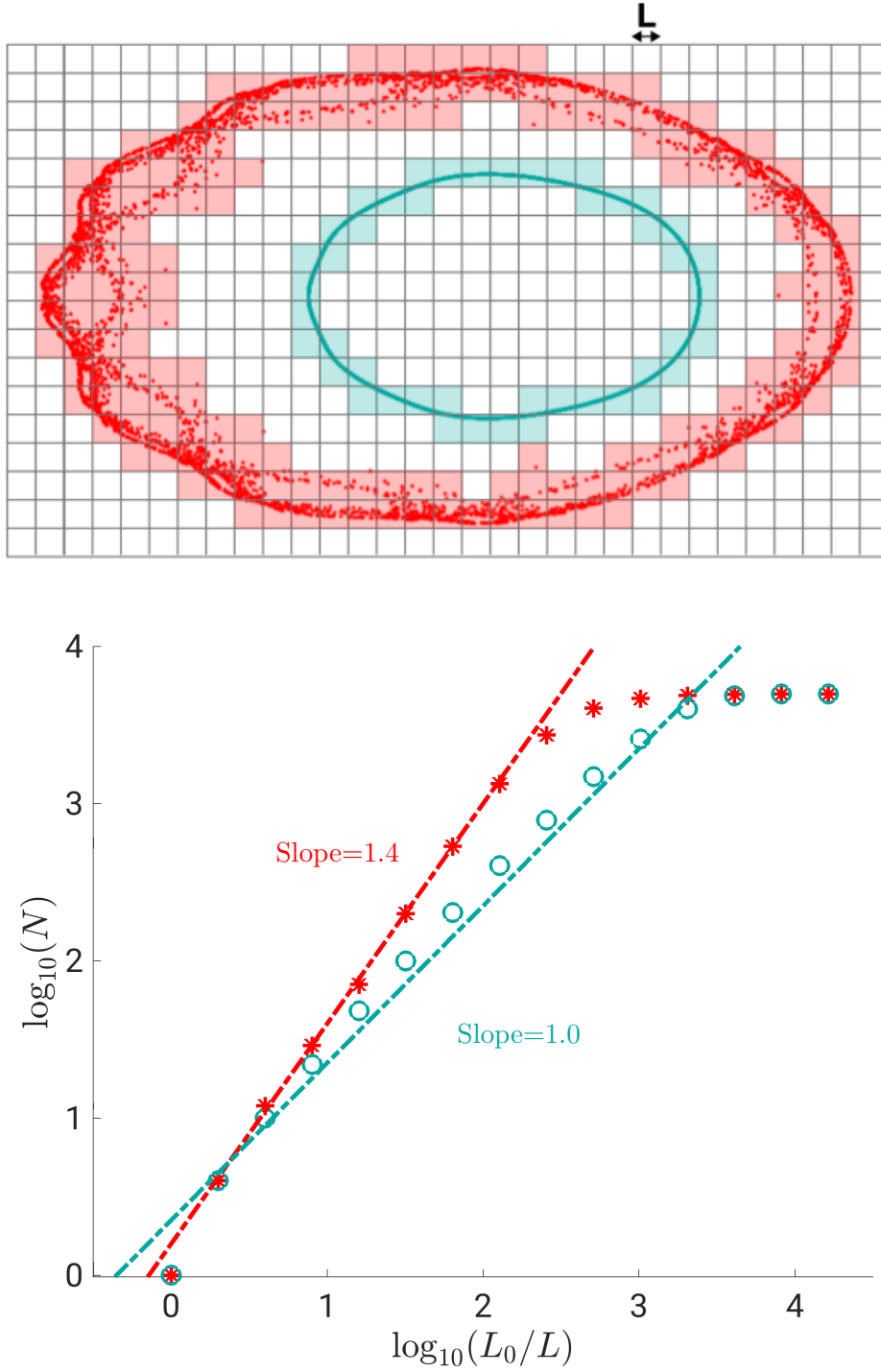


Figure 4.3: Evaluation of the fractal dimension of two field lines Poincaré section. Top: Poincaré section of two field lines. A grid with elements of size  $L$  is plotted over; each grid cell that contains at least a point from the field line is colored with the field line color. In this example,  $N(L) = 46$  for the blue line and  $N(L) = 177$  for the red line. Bottom: Number  $N$  of grid element with at least one point as a function of the grid element size  $L$ .

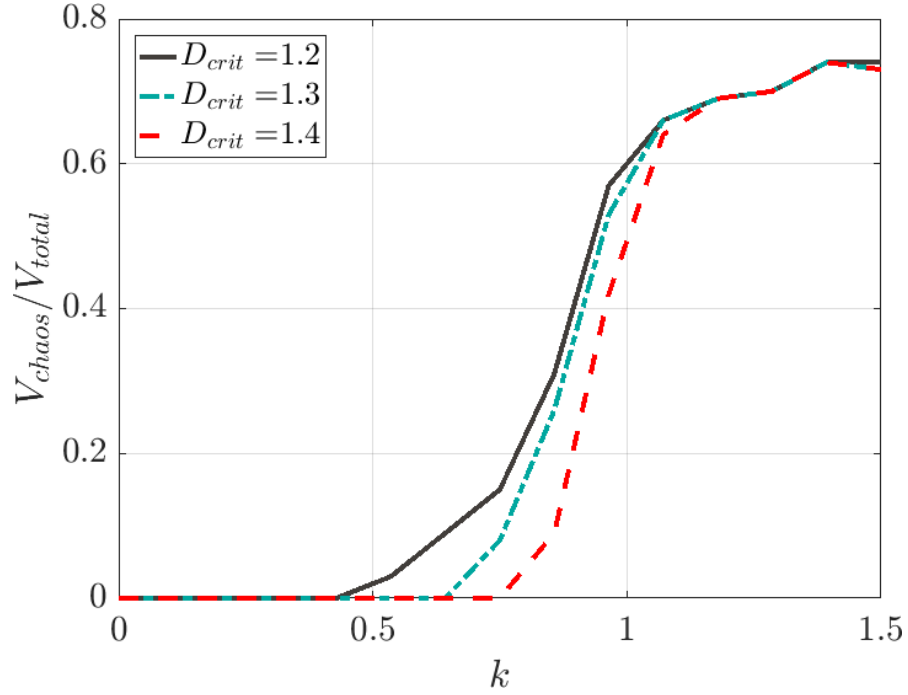


Figure 4.4: Normalized volume of chaos in the standard map as a function of  $k$  for different values of  $D_{crit}$  (Arbez, 2021).

When applied to Poincaré maps of magnetic field lines, the volume of chaos is a global measure of the amount of chaotic field lines in the system, in opposition to the Greene’s residue, which was a local measure of the field line topology (see section 4.1). The equilibrium  $\beta$ -limit could then be defined as the  $\beta$  above which  $V_{chaos} > 0$ . This criterion, however, is uniquely based on the magnetic field lines topology, and does not take into account the possibility that a chaotic magnetic field could still confine the plasma, at least to a certain level. Indeed, structures present in chaotic magnetic field lines and magnetic islands can, potentially, support temperature and density gradients (Hudson and Breslau, 2008; Hudson and Dewar, 2009). Considering all magnetic islands and chaotic field lines as detrimental for confinement can thus be a pessimistic diagnostic of the confinement properties of the magnetic equilibrium. In the next section, we propose an alternative measure, specific to the Poincaré map of stellarator magnetic fields, that counts the fraction of resonances in the equilibrium that are important sources of transport.

### 4.3 Fraction of effective parallel diffusion

We now introduce a novel, alternative measure to the volume of chaos to determine if the destruction of magnetic surfaces significantly impacts the radial transport. In what follows, the parallel and perpendicular directions are defined as the directions along and across the magnetic field respectively, and the radial direction  $r$  as the direction perpendicular to isotherms,  $\nabla T \times \nabla r = 0$ , with  $T$  the temperature. In recent work, Paul et al. (2022) discussed the properties of the anisotropic heat diffusion equation,  $\nabla \cdot (\kappa_{\parallel} \nabla_{\parallel} T + \kappa_{\perp} \nabla_{\perp} T) = 0$ , where  $\kappa_{\parallel}$  and  $\kappa_{\perp}$  are the parallel and perpendicular heat conductivities. In particular, Paul et al. demonstrated that, under the assumption that  $\kappa_{\parallel}$ ,  $\kappa_{\perp}$ , and  $\nabla \cdot \kappa$  are analytical, isotherms are topologically constrained to be toroidal surfaces — this forbids isotherms to align with the magnetic field in regions occupied by magnetic islands and magnetic field line chaos. Here  $\kappa$  is the diffusion tensor,  $\kappa = \kappa_{\perp} I + (\kappa_{\parallel} - \kappa_{\perp}) \mathbf{B}\mathbf{B}/B^2$ , with  $I$  the identity tensor. Motivated by comparing the local parallel diffusion to the local perpendicular diffusion, Paul et al. introduced the *volume of effective parallel diffusion*, which is the volume of plasma where the parallel heat transport dominates over perpendicular heat transport,

$$V_{PD} = \frac{1}{V_P} \int_{V_P} \mathcal{H}(\kappa_{\parallel} |\nabla_{\parallel} T|^2 - \kappa_{\perp} |\nabla_{\perp} T|^2) d\mathbf{x}^3, \quad (4.11)$$

where  $\mathcal{H}$  is the Heaviside function, and the parallel and perpendicular gradients are defined as  $\nabla_{\parallel} = \mathbf{B}(\mathbf{B} \cdot \nabla)/B^2$  and  $\nabla_{\perp} = \nabla - \nabla_{\parallel}$  respectively. In regions occupied by magnetic islands and magnetic field line chaos, the constraint on the isotherms topology implies that the magnetic field has a non-zero radial component, thus  $\nabla_{\parallel} T > 0$ . Depending on the ratio  $\kappa_{\parallel}/\kappa_{\perp}$ , the volume of effective parallel diffusion can then be greater than zero. On the contrary, in regions occupied by magnetic surfaces, isotherms largely coincide with magnetic surfaces, which means that  $\nabla_{\parallel} T$  is negligible, and consequently the volume  $V_{PD}$  is zero. We can thus define the equilibrium  $\beta$ -limit as the  $\beta$  above which  $V_{PD} > 0$ .

To determine the equilibrium  $\beta$ -limit, it is only required to determine if  $V_{PD}$  is zero or not; its absolute value is irrelevant. We thus construct a proxy function for  $V_{PD}$  that does not depend on the temperature profile, but only on the magnetic field. We start by noticing that the Heaviside function in Eq.(4.11) is greater than zero when  $\kappa_{\parallel} |\nabla_{\parallel} T|^2 \geq \kappa_{\perp} |\nabla_{\perp} T|^2$ . As we expect the radial magnetic field to be small in comparison to the total magnetic field,  $B_r = \mathbf{B} \cdot \hat{\mathbf{e}}_r \ll B$ , with  $\hat{\mathbf{e}}_r$  a unitary vector perpendicular to the isotherms, we can write  $\nabla_{\parallel} T \sim \nabla T B_r/B$ , and  $\nabla_{\perp} T \sim \nabla T$ . The volume of effective parallel diffusion is then greater than zero if there is a finite volume where

$$\left(\frac{B_r}{B}\right)^2 \geq \frac{\kappa_{\perp}}{\kappa_{\parallel}} \equiv \left(\frac{B_{r,crit}}{B}\right)^2. \quad (4.12)$$

We now consider the electron heat transport as a figure of merit for the confinement properties of the equilibrium. We write  $\kappa_{\perp,e} = n\chi_{\perp,e}$ , where  $\chi_{\perp,e}$  is typically given by

turbulence or neoclassical transport, with  $\chi_{\perp,e} \sim 1\text{m}^2\text{s}^{-1}$ , and we use the Spitzer-Härm conductivity for  $\kappa_{\parallel,e}$  (Braginskii, 1965) to get

$$\left(\frac{B_{r,crit}}{B}\right)^2 = 5.2 \cdot 10^{-22} \frac{n_e \log \Lambda \chi_{\perp,e}}{T_e^{5/2}}, \quad (4.13)$$

where  $\log \Lambda$  is the Coulomb logarithm. Here everything is to be expressed in SI units except  $T_e$ , which is in  $eV$ . For temperatures and densities between 1 to 10 keV and  $10^{19}$  to  $10^{20}\text{m}^{-3}$  respectively,  $B_{r,crit}/B$  ranges from  $10^{-6}$  to  $10^{-4}$ . For example using typical values for W7-X high performance experiments (Klinger et al., 2019), *i.e.*  $n_e = 4 \cdot 10^{19}\text{m}^{-3}$ ,  $T_e = 5$  keV, we obtain a critical normalized radial magnetic field of  $B_{r,crit}/B \sim 10^{-5}$ . As a side note, we remark that the criterion (4.12) can also be derived by considering the radial heat flux of electrons,  $q_r = -\kappa_{\perp,e}(\nabla_{\perp} T_e)_r - \kappa_{\parallel,e}(\nabla_{\parallel} T_e)_r \sim -\kappa_{\perp,e}dT_e/dr - \kappa_{\parallel,e}dT_e/dr B_r^2/B^2$ . Magnetic islands and chaos play then an important role in setting the local heat radial transport when the second term in the expression for the electron heat flux is larger than the first, which occurs when  $B_r^2/B^2 \geq \kappa_{\perp}/\kappa_{\parallel}$ , recovering equation (4.12).

The volume of effective parallel diffusion can thus be written using the criterion on the radial magnetic field (4.12),

$$V_{PD} \sim \frac{1}{V_P} \int_{V_P} \mathcal{H} \left( \left[ \frac{B_r}{B} \right]^2 - \left[ \frac{B_{r,crit}}{B} \right]^2 \right) d\mathbf{x}^3. \quad (4.14)$$

This measure is however impractical for the purpose of this thesis, as it would require to evaluate the radial magnetic field everywhere in the plasma. Instead, the radial magnetic field is evaluated where it is expected to be the largest, *i.e.* on a selected number of rational surfaces. We then construct *the fraction of parallel diffusion*,

$$f_{PD} = \frac{1}{N_{res}} \sum_{i=1}^{N_{res}} \mathcal{H} \left( \left[ \frac{B_r}{B} \right]^2 - \left[ \frac{B_{r,crit}}{B} \right]^2 \right), \quad (4.15)$$

where  $N_{res}$  is the number of considered resonances, and the algorithm used to evaluate the radial magnetic field  $B_r$  from SPEC equilibria is described in section 4.3.1. The fraction of effective parallel diffusion is then the fraction of resonances in the plasma that contribute to the transport, *i.e.* the fraction of resonances over which the diffusion due to parallel dynamics dominates. Note that  $f_{PD} \neq V_{PD}$ , but if  $f_{PD} > 0$ , then we can expect  $V_{PD} > 0$ . The fraction of parallel diffusion can then be used as a proxy function to determine if the volume of parallel diffusion is zero or not. The equilibrium  $\beta$ -limit can thus be defined by the value of  $\beta$  above which  $f_{PD} > 0$ .

### 4.3.1 Measure of the radial magnetic field

To evaluate the radial magnetic field  $B_r$ , it is useful to construct a general set of coordinates, such as quadratic flux minimizing (QFM) surfaces (Dewar et al., 1994; Hudson and Dewar, 1996, 1998), or ghost surfaces (Hudson and Dewar, 2009), which have been shown to coincide with isotherms (Hudson and Breslau, 2008). We construct QFM surfaces using the pyoculus package<sup>1</sup>. These surfaces, thereafter named  $\Gamma_{mn}$ , are smooth toroidal surfaces that pass through the X- and O- points of the island chain corresponding to the  $\iota = n/m$  rational resonant surface, and are constructed by finding the surfaces  $\Gamma_{mn}$  minimizing the weighted quadratic flux  $\int_{\Gamma_{mn}} w(\mathbf{x})(\mathbf{B} \cdot \mathbf{n})^2 dS$ , where the weight  $w(\mathbf{x})$  is cleverly chosen such that the underlying Euler-Lagrange equation has non-singular solutions. Some examples of QFM surfaces are plotted in Figure 4.5. The radial coordinate  $r$  is then defined as the direction perpendicular to the QFM surfaces.

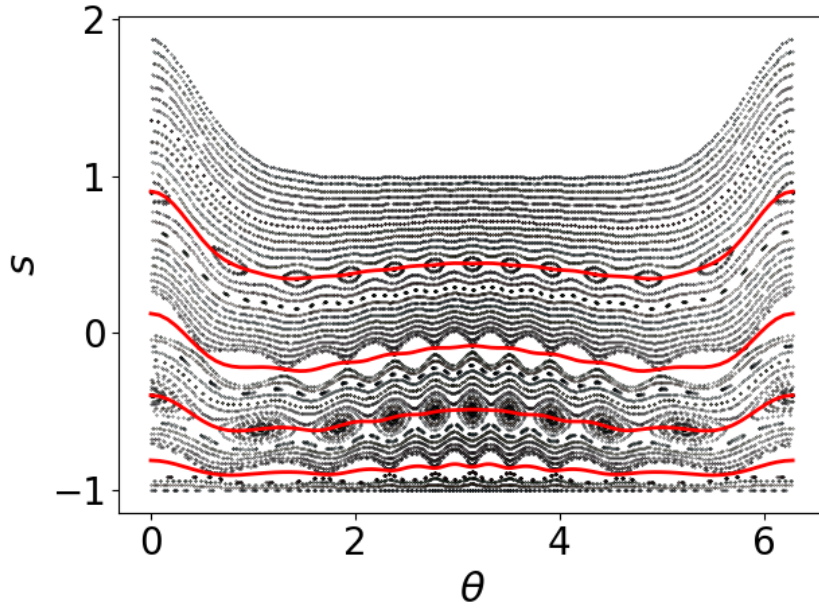


Figure 4.5: Black: Poincaré plot with magnetic surfaces and magnetic islands. Red: QFM surface  $r = \text{const}$ . The coordinate  $s$  is a radial-like coordinate.

We can now measure the radial component of the magnetic field at each resonant surface  $\iota = n/m$  in a SPEC equilibrium. We start by identifying all potential resonances  $(m, n) \in \mathbb{N}$  in each volume  $\mathcal{V}_l$  within the plasma boundary, such that (i)  $n/m$  is within the rotational transform extrema in the volume, and (ii)  $n$  is a multiple of the number of field periods. We construct QFM surfaces for each of the identified resonances  $\iota = n/m$ .

<sup>1</sup><https://github.com/zhisong/pyoculus>

The magnetic field perpendicular to the QFM surface,  $B_r$ , is obtained by projecting the magnetic field on the normal direction, and the magnetic field resonant harmonic,  $B_{r,mn}$  is obtained after a standard Fourier transform of  $B_r$ . Here, the poloidal angle is the straight-field line angle of the magnetic field tangential to the QFM surface. The Fourier spectrum of  $B_r$  is largely dominated by the  $(m, n)$  harmonic — it has been verified that  $B_{r,mn}$  is at least twice as large as other Fourier harmonics of the radial magnetic field. We can thus assume  $B_r \approx B_{r,mn}$  to filter out numerical noise that may be generated by the QFM surface construction.

Only resonances with large radial magnetic field will significantly participate to the radial transport. Since the magnetic field harmonics  $B_{r,mn}$  are expected to decrease exponentially with the square of their mode numbers  $m$  and  $n$  (Qu et al., 2021), *i.e.*  $B_{mn} \sim \exp(-m^2 - n^2)$ , we can discard resonances with large poloidal and toroidal mode number and study only harmonics with mode number smaller than a given resolution,  $m \leq M_{res}$  and  $n \leq N_{res}$ . In this thesis, we set  $M_{res} = 25$  and  $N_{res} = 10$ .

We have thus constructed the fraction of effective parallel diffusion, which is a proxy function for the volume of effective diffusion, and is greater than zero if radial transport is strongly impacted by the field line topology anywhere in the plasma. We also discussed how the radial magnetic field could be evaluated numerically by constructing QFM surfaces. In chapter 5, we will apply this diagnostic to compute the equilibrium  $\beta$ -limit in a classical stellarator.

## 4.4 Summary

This chapter introduced different metrics to evaluate the capability of a magnetic equilibrium to confine a plasma. First, we discussed the Greene’s Residue, which is a local measurement of the magnetic field line topology on rational surfaces. While very useful to define optimization target functions for minimizing an island’s width, this measure is impractical to assess the magnetic field capability at supporting pressure gradients. As an alternative, the volume of chaos is a second diagnostic that measures the volume of plasma occupied by chaotic magnetic field lines. To assess if a field line is chaotic or not, the fractal dimension of its Poincaré section is evaluated. This diagnostic has the advantage to be a global diagnostic, but, as for the Greene’s residues, fails to provide information on the magnetic field capability to support pressure gradients; indeed, structures in chaotic magnetic field can potentially support pressure gradients. The Greene’s residue and the volume of chaos will be used in different stellarator optimization applications in chapter 6.

The third diagnostic introduced in this chapter is the fraction of effective parallel diffusion. Constructing QFM surfaces, one can evaluate the radial magnetic field for any resonance in the plasma. By comparing the parallel transport in the radial direction

to the radial transport generated by turbulence, a critical radial magnetic field can be estimated, above which the resonance has an important impact on setting the net radial transport. This measure, in opposition to the Greene's residue and the volume of chaos, is not uniquely based on the topology of the magnetic field line, as it also includes information on whether or not the damaging of magnetic surface is detrimental to confinement. The fraction of effective parallel diffusion will be used in chapter 5 to measure the equilibrium  $\beta$ -limit.



# 5 Equilibrium $\beta$ -limits

In this chapter, we deploy the SPEC code, introduced in chapter 3, and the numerical diagnostics and metrics discussed in chapter 4 to study the equilibrium  $\beta$ -limit in stellarators. We perform large parameter scans of finite  $\beta$ -equilibria, including the bootstrap current contribution, to both numerically and analytically model the impact of the pressure and the bootstrap current on the equilibrium topology, and to determine how the equilibrium  $\beta$ -limit depends on the device parameters. After having introduced the mechanisms that drive the bootstrap current in a plasma, we will first compute the equilibrium  $\beta$ -limit in a classical stellarator with bootstrap current, and model these results analytically using the high beta stellarator (HBS) model. We then study a more complex quasi-axisymmetric (QA) stellarator geometry, and compute its equilibrium  $\beta$ -limit while considering the self-consistent bootstrap current.

## 5.1 Bootstrap current

The bootstrap current is a parallel current self-generated by toroidally confined plasmas. It is a kinetic effect, described by the neo-classical theory (Helander and Sigmar, 2002), and it is therefore not described by the MHD model. Nevertheless, its contribution can be taken into account in magnetic equilibrium calculations by including it as a divergence-free current density, *i.e.* the last term of Eq.(2.41). A precise derivation of bootstrap current in general stellarator geometries can be found in Helander et al. (2011) and references therein; in this section, we qualitatively explain the basic physics at the origin of this current in a tokamak. Similar arguments can be made in stellarator geometries.

### 5.1.1 Passing and trapped particles

Assuming that the magnetic field strength varies on large scales in comparison to the gyroradius,  $\rho|\nabla B| \ll B$ , and that it varies slowly in comparison to the gyrofrequency,

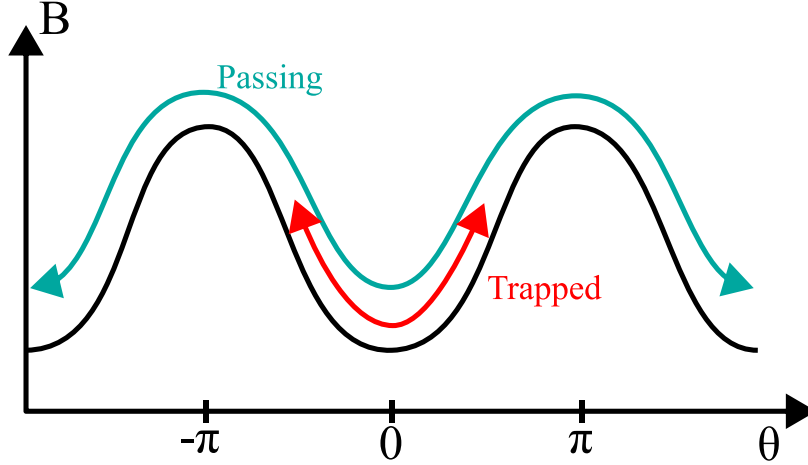


Figure 5.1: Sketch of a trapped and passing particle. Here  $\theta = 0$  and  $\theta = \pm\pi$  designate a position on the plane  $Z = 0$ , on the low-field and high-field side of the torus respectively.

$1/\omega \partial B / \partial t \ll B$ , a particle trajectory can be approximated by its guiding center motion (see section 1.4.1). Furthermore, it can be shown (Helander and Sigmar, 2002) that the magnetic moment  $mv_{\perp}^2/2B$  is approximately conserved, where  $v_{\perp}$  is the component of  $\mathbf{v}$  perpendicular to the magnetic field. In addition, in the absence of collisions, and if  $\mathbf{E} = 0$ , the particle's kinetic energy,  $W_k = mv_{\parallel}^2/2 + mv_{\perp}^2/2$ , is also conserved. Now, suppose that a charged particle follows a straight magnetic field line. If the magnetic field strength increases, by conservation of the magnetic moment, the particle's perpendicular velocity increases, which means that its parallel velocity decreases. Ultimately, if the particle's kinetic energy is not large enough, the parallel velocity will reach zero, and the particle will bounce back in the opposite direction along the field line.

In tokamaks, the magnetic field is stronger on the inner side of the torus, and weaker on the outer side, as  $B \sim 1/R$ , thereby defining the so-called high-field side and low-field side of the torus. Now suppose that an ion is located at a point  $A$ , on the midplane  $Z = 0$  and on the low-field side of the torus (see Figure 5.2). As this ion moves along a magnetic field line, it moves closer to the high-field side of the torus, where the magnetic field strength is larger, and thus the ion decelerates in the direction parallel to the field lines. Particles whose kinetic energy is large enough will complete their poloidal orbit, and are therefore called *passing particles* (see the blue curve in Figure 5.1). On the other hand, particles whose kinetic is too small will bounce back before completing a full poloidal orbit, and are thus called *trapped particles* (see the red curve in Figure 5.1).

As discussed in section 1.4.1, particles do not follow exactly magnetic field lines, as they experience guiding center drifts. Working in standard cylindrical coordinates  $(R, \phi, Z)$ , we assume a mostly toroidal magnetic field,  $\mathbf{B} \approx B\hat{\mathbf{e}}_{\phi}$ . Furthermore, we assume that the plasma current flows in the  $-\hat{\mathbf{e}}_{\phi}$  direction, which, according to Ampere's law, generates a poloidal magnetic field in the  $-\hat{\mathbf{e}}_{\theta}$  direction (see Figure 5.2). Writing

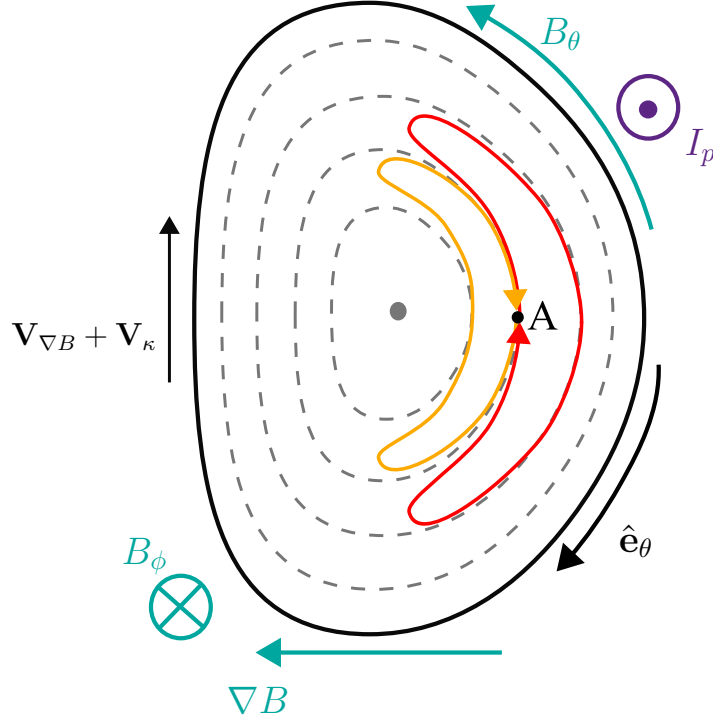


Figure 5.2: Sketch of a banana orbit. The black surface indicates the plasma boundary, while inner, dashed, grey surfaces represents magnetic surfaces. In red and orange, the banana orbit of an ion passing by  $A$  with a positive and negative parallel velocity respectively.

$\nabla B \sim -B/R\hat{e}_R$ , and using Eqs.(1.15)-(1.16), we obtain the sum of the  $\nabla B$  and curvature drifts,

$$\mathbf{V}_{\nabla B} + \mathbf{V}_{\kappa} = \pm \frac{v_{\perp}^2 + 2v_{\parallel}^2}{2R\omega} \hat{e}_Z, \quad (5.1)$$

where the positive and negative signs are taken for ions and electrons respectively. Ions thus drift in the  $\hat{e}_Z$  direction, while electrons drift in the  $-\hat{e}_Z$  direction. These drifts will generate a finite radial excursion of the particle from the trajectory traced by a magnetic field line. Take for example a trapped ion, with initially a positive parallel velocity,  $v_{\parallel} > 0$ , and positioned at a point  $A$  as shown on Figure 5.2. In the upper part of the torus,  $Z > 0$ , the ion drifts away from the plasma core, while in the lower part of the torus,  $Z < 0$ , the ion drifts towards the plasma core. The resulting orbit of the ion is sketched in red on Figure 5.2, and is called a *banana orbit*, for obvious reasons. Remark that trapped ions at the point  $A$ , with negative parallel velocity  $v_{\parallel} < 0$  will follow a different banana orbit, than ions with a positive parallel velocity. Their banana orbit is traced in orange on Figure 5.2. Trapped electrons also follow banana orbits, as discussed above for the ions. As they drift in the opposite direction than ions, electrons will however move along the banana orbit in the opposite direction than ions.

### 5.1.2 Banana and bootstrap current

The banana current is a consequence of the banana orbits and emerges in the presence of a density or temperature gradient. In general, unless the density profile is hollow, the closer the banana is to the magnetic axis, the greater is the density, meaning there are more ions with negative parallel velocity than positive parallel velocity at a point  $A$  (see Figure 5.2). There is thus a net parallel flow of ions at  $A$  in the  $-\hat{\mathbf{e}}_\phi$  direction, that generates a net parallel current density, called the banana current density, in the  $-\hat{\mathbf{e}}_\phi$  direction. This ion banana current thus increases the plasma current  $I_p$ . Electrons move in the opposite direction than ions along a banana orbit, and therefore there is a net parallel flow of electrons in the  $\hat{\mathbf{e}}_\phi$  direction. As electrons are negatively charged, this corresponds to a net electron banana current density in the  $-\hat{\mathbf{e}}_\phi$  direction. The electron banana current thus also increases the plasma current  $I_p$ . Note that the banana current is parallel to the magnetic field, and is thus mostly toroidal.

The banana current is however relatively small in comparison to the bootstrap current. The bootstrap current emerges from the interaction between the passing and trapped particle population. The net parallel momentum of trapped electrons and ions is transferred to passing particles via collisions, which generates a net momentum in the passing particle population, and ultimately the bootstrap current. Again, the bootstrap current is a parallel current, and therefore is mostly toroidal. The calculation of the bootstrap current depends on numerous parameters, for instance the plasma collisionality, the density and temperature of ions and electrons, and the geometry of the magnetic surfaces — see for example the work of Sauter et al. (1999) or, more recently, Redl et al. (2021). In a low collisionality, large aspect ratio tokamak approximation, one can show (Helander and Sigmar, 2002) that the bootstrap current density reduces to

$$j_\phi = \sqrt{\epsilon} R \frac{dp}{d\psi_p}, \quad (5.2)$$

where  $\sqrt{\epsilon}$  is the fraction of trapped particles, and  $\epsilon = r/R$  is the inverse aspect ratio.

In tokamaks, the net radial drift of a trapped particle, averaged over its banana orbit, is zero. In stellarators, particle orbits are more complex; they can be trapped in regions where the guiding center drifts do not average to zero over a banana orbit, leading to the loss of the particle. In some particular configurations, for example in quasi-symmetric (QS) stellarators, one can show that trapped particles are confined (Helander, 2014). QS stellarators are a special class of stellarators where the magnetic field strength only depends on two coordinates when expressed in Boozer coordinates,  $B = B(\psi_t, M\theta_b - N\phi_b)$ . We differentiate quasi-axisymmetric (QA) configurations, with  $M \neq 0$  and  $N = 0$ , from quasi-helically symmetric (QH) configurations, with  $M \neq 0$  and  $N \neq 0$ , and from quasi-poloidally symmetric (QP) configurations, where  $M = 0$  and  $N \neq 0$ . To compute the trajectory of trapped particles in any stellarator and the resulting bootstrap current, numerical codes are required, such as the SFINCS code (Landreman

et al., 2014). In QS configurations however, one can apply an isomorphism with tokamaks (Boozer, 1983), and use tokamak-specific semi-analytic formulas to evaluate the bootstrap current, thereby avoiding the necessity to use expensive kinetic numerical computations.

In section 5.2, we construct a classical stellarator model with bootstrap current, and evaluate its equilibrium  $\beta$ -limit using the SPEC code. We then numerically and analytically model the equilibrium  $\beta$ -limit dependence on design parameters and on the bootstrap current strength. In section 5.3, we compute the magnetic equilibrium in a QA stellarator for a wide range of temperature and densities while considering the self-consistent bootstrap current evaluated with the Redl et al. formulas.

## 5.2 Equilibrium $\beta$ -limit in a classical stellarator

This section is adapted from the following publication: A. Baillod *et. al.*, Equilibrium  $\beta$ -limits dependence on bootstrap current in classical stellarators, arXiv:2211.12948v2 (2022) (Baillod et al., 2022).

In recent work, Loizu et al. (2017) modelled numerically and analytically the equilibrium  $\beta$ -limit in a current-free classical stellarator using the SPEC code. In this chapter, we propose to extend the work of Loizu et al. (2017) to the case of a classical stellarator with bootstrap current and a more realistic pressure profile. While a rotating ellipse is arguably a simple geometry, it is relevant since all stellarators without torsion are rotating ellipses close to the magnetic axis (Helander, 2014). An experimental instance of rotating ellipse was the Wendelstein 7-A (W7-A) stellarator (Grieger et al., 1985).

We construct a free-boundary classical stellarator equilibrium. The computational boundary  $\Gamma_{CB}$ , shown on Figure 5.3, is given by

$$R_{CB}(\theta, \phi) = R_0 + R_{10} \cos(\theta) + R_{11} \cos(\theta - N_{fp}\phi) \quad (5.3)$$

$$Z_{CB}(\theta, \phi) = Z_{10} \sin(\theta) + Z_{11} \sin(\theta - N_{fp}\phi), \quad (5.4)$$

with  $N_{fp} = 5$  the number of field periods,  $R_0 = 10\text{m}$ ,  $R_{10} = -Z_{10} = 1\text{m}$ ,  $R_{11} = Z_{11} = 0.25\text{m}$ . The effective minor radius is  $a_{\text{eff}} = \sqrt{r_{\min} r_{\max}}$ , with  $r_{\min} = R_{10} - R_{11}$  and  $r_{\max} = R_{10} + R_{11}$  the minor and major radii of the ellipse, respectively. We define  $\epsilon_a = a_{\text{eff}}/R_0$  as the inverse aspect ratio.

We assume that a coil system exists such that  $\mathbf{B}_c \cdot \mathbf{n} = B_v \hat{\mathbf{e}}_z \cdot \mathbf{n}$  on  $\Gamma_{CB}$ , where  $\mathbf{B}_c$  is the magnetic field produced by the coils, and  $B_v \hat{\mathbf{e}}_z$  is a vertical field, which is applied to keep the plasma within the computational boundary at high  $\beta$ . We set  $B_v = -0.03\text{T}$ . This vertical field has little to no impact on the results presented hereafter; its only purpose is to keep the plasma within the volume defined by  $\Gamma_{CB}$ . We fix the total current flowing in the torus hole to  $I_c = 17.1\text{MA}$ , which determines the toroidal flux enclosed by the computational boundary,  $\psi_{t,V} = 1\text{Tm}^2$ .

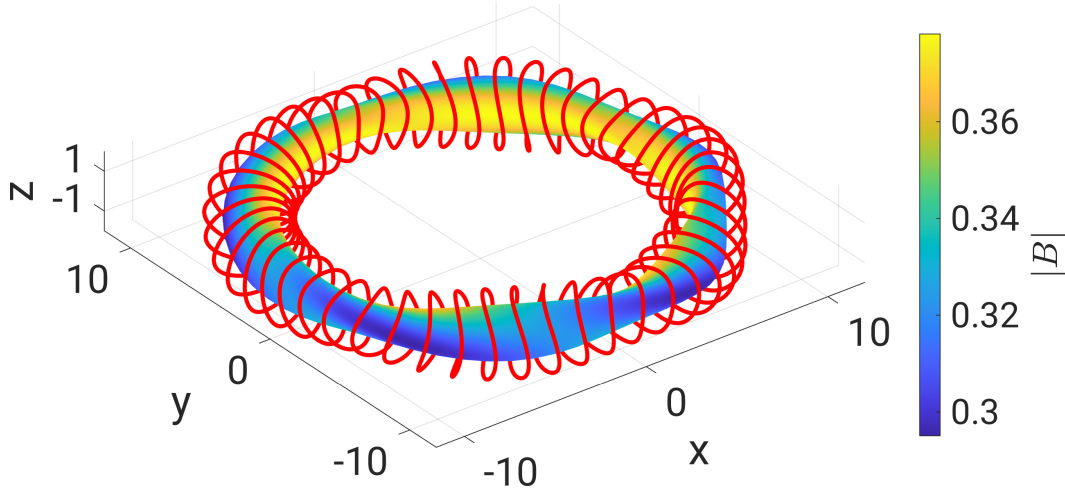


Figure 5.3: Rotating ellipse with coils. In red: tentative coil design, obtained with the flexible optimized coils using space curves (FOCUS) code (Zhu et al., 2017). The 3D-colored surface is the computational boundary,  $\Gamma_{CB}$ , described by Eqs.(5.3)-(5.4). Colors indicate the magnetic field strength in vacuum, as evaluated by SPEC, assuming  $\mathbf{B} \cdot \mathbf{n} = 0$  on  $\Gamma_{CB}$ .

We choose a pressure profile with a linear dependence on the toroidal flux, *i.e.*  $p = p_0(1 - \psi_t/\psi_a)$ , where  $p_0$  is a free parameter that controls the value of  $\beta$ , and  $\psi_a = 0.25\text{Tm}^2$  is the total toroidal flux enclosed by the plasma boundary  $\Gamma_{PB}$ . We approximate the pressure profile with seven steps of equal magnitude  $[[p]]_l = -p_0/N_{vol}$  (see Figure 5.4). We thus define seven plasma regions, *i.e.*  $N_{vol} = 7$ , surrounded by a vacuum region. This means that  $\psi_{t,l} = l\psi_a/N_{vol}$  and  $p_l = p(\psi_{t,l})$ . The number of volumes determines how the pressure profile is represented — more volumes means more and smaller pressure steps. As each interface is a discrete constraint on the magnetic topology, increasing the number of volumes reduces the available space for reconnection and thus the maximum size of magnetic islands and regions of magnetic field line chaos. In this chapter, we are however interested in the *onset* of loss of magnetic surfaces, which is not affected by the volume available for islands to grow. Therefore our results are very weakly dependent on the number of volumes.

Finally, two current profiles have to be provided to SPEC: the profile of volume currents,  $\{I_{\phi,l}^v\}$ , and the profile of surface currents  $\{I_{\phi,l}^s\}$  (see section 3.2). Here we study the case of an equilibrium with zero externally driven currents and with bootstrap current. No externally driven currents implies, in SPEC, that there are no currents in the plasma volumes, *i.e.*

$$I_{\phi,l}^v = 0. \quad (5.5)$$

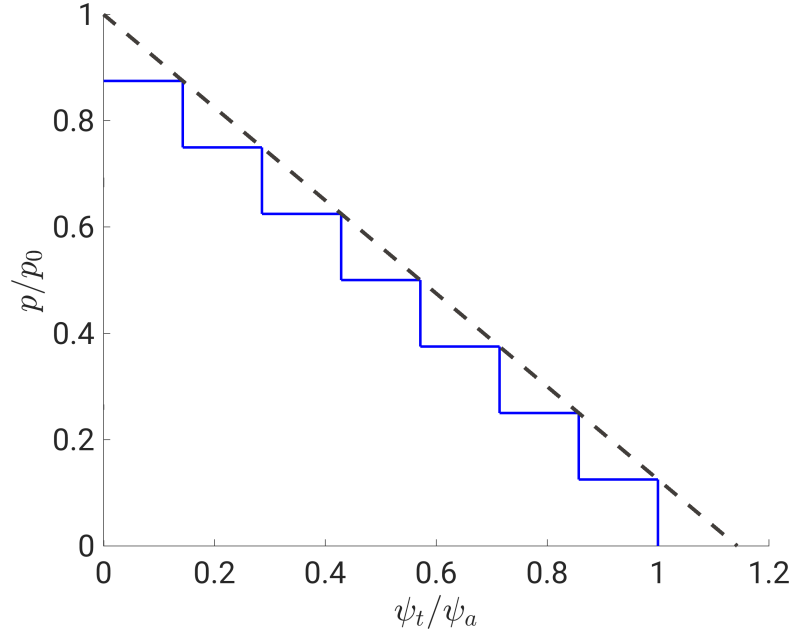


Figure 5.4: Pressure profile, with linear dependence on the toroidal flux. Black dashed line: continuous profile. Stepped blue curve: SPEC’s pressure profile. Here  $\psi_t/\psi_a = 1$  is the plasma boundary.

The bootstrap current is a pressure-driven current, and is consequently described by a surface current at the volume’s interfaces. We model it with

$$I_{\phi,l}^s = -C \left( \frac{\psi_{t,l}}{\psi_a} \right)^{1/4} [[p]]_l, \quad (5.6)$$

where  $(\psi_{t,l}/\psi_a)^{1/4} \approx \sqrt{\epsilon_l/\epsilon_{PB}}$  is related to the fraction of trapped particles, with  $\epsilon_l$  the inverse aspect ratio of interface  $\mathcal{I}_l$ , and  $\epsilon_{PB}$  the aspect ratio of the plasma boundary. Here,  $[[p]]_l$  is a measure of the local pressure gradient; and  $C$  is a coupling constant, in  $[APa^{-1}]$ , which controls the strength of the bootstrap current in the system. A full neoclassical calculation of the bootstrap current, for example with the SFINCS code (Landreman et al., 2014), would require the density and temperature profiles as inputs — and the freedom in the choice of the coupling constant  $C$  reflects the freedom in these profiles. In this chapter, we will consider a bootstrap current that increases the vacuum rotational transform, as in tokamaks or QA stellarators. This means that  $I_{\phi,l}^s > 0$ , and thus  $C > 0$ , as  $[[p]]_l < 0$ . Note that in stellarators, the bootstrap current can also decrease the vacuum rotational transform — this is in particular the case in QH stellarators (Boozer and Gardner, 1990).

The current density associated to the current in Eq.(5.6) is

$$j_{\phi,l} = -\frac{C\psi_a}{\pi a_{\text{eff}}^2} \left( \frac{\psi_{t,l}}{\psi_a} \right)^{1/4} \frac{dp}{d\psi_t}. \quad (5.7)$$

Note that if

$$C = C_0 \equiv \frac{\sqrt{\epsilon_a} R_0}{\iota_v B_0}, \quad (5.8)$$

with  $\iota_v$  the edge rotational transform in vacuum and  $B_0$  such that  $\mu_0 I_{coil} = 2\pi R_0 B_0$ , Eq.(5.7) reduces to the well-known large-aspect ratio tokamak bootstrap current approximation, Eq.(5.2). The constant  $C_0$  will be used to normalize  $C$ , *i.e.* we define  $\hat{C} \equiv C/C_0$ . In the case of a large aspect ratio circular tokamak, we thus have  $\hat{C} = 1$ , while in a stellarator with no bootstrap current,  $\hat{C} = 0$ .

We use the recently implemented capability of SPEC to prescribe the toroidal current profile (Baillod et al., 2021), with the profiles defined in Eqs.(5.5) and (5.6). Unless stated otherwise, the Fourier resolution used in all results presented in this chapter is  $|n| \leq N_{tor} = 8$ ,  $m \leq M_{pol} = 8$ , with  $n$  the toroidal mode number and  $m$  the poloidal mode number, meaning that  $2[N_{tor} + M_{pol}(2N_{tor} + 1)] + 1 = 289$  Fourier modes are used to describe each interface geometry. Results presented in this chapter have been checked for convergence with respect to Fourier resolution.

In summary, we can construct free-boundary SPEC equilibria with a simple bootstrap current model and we are left with two free parameters, namely (i)  $\beta$  which controls the total pressure in the system and (ii)  $\hat{C}$ , a dimensionless parameter, that controls the bootstrap current strength for a given plasma  $\beta$ . We start by calculating the vacuum field, *i.e.* the equilibrium corresponding to  $\beta = 0$  and  $\hat{C} = 0$ . We show on Figure 5.5a the vacuum rotational transform profile, and on Figure 5.5b-d, the Poincaré section of the vacuum field at three different poloidal planes. We remark that the vacuum rotational transform on the outer side of the plasma boundary is  $\iota = 0.27$ . The volume enclosed by the plasma boundary, and the vacuum region between the plasma boundary and the computational boundary, are all filled with magnetic surfaces. In the next section, we perform extensive scans over  $\beta$  and  $\hat{C}$  and describe the effect of the increasing pressure and bootstrap current on the magnetic field line topology.

### 5.2.1 Scans over $\hat{C}$ and $\beta$

A scan has been performed with  $\beta \in [0, 2\%]$  and  $\hat{C} \in [0, 2.26]$  representing 680 SPEC calculations, each requiring about 24 CPU-hours on the MARCONI cluster<sup>1</sup>. Figure 5.6 and 5.7 show some selected Poincaré sections at different values of  $\beta$  and  $\hat{C}$ , while Figure 5.8 shows the edge rotational transform, *i.e.* the rotational transform on the outer side of  $\Gamma_{PB}$ , as a function of  $\beta$  for four different values of  $\hat{C}$ .

For small values of  $\hat{C}$ , namely for  $\hat{C} < \hat{C}_{crit} \approx 0.59$ , the edge rotational transform decreases with increasing  $\beta$  and eventually reaches zero (Figure 5.8, black stars and red dots), at which point an  $m = 1$ ,  $n = 0$  island opens and forms a separatrix at the plasma

---

<sup>1</sup><https://www.hpc.cineca.it/hardware/marconi>



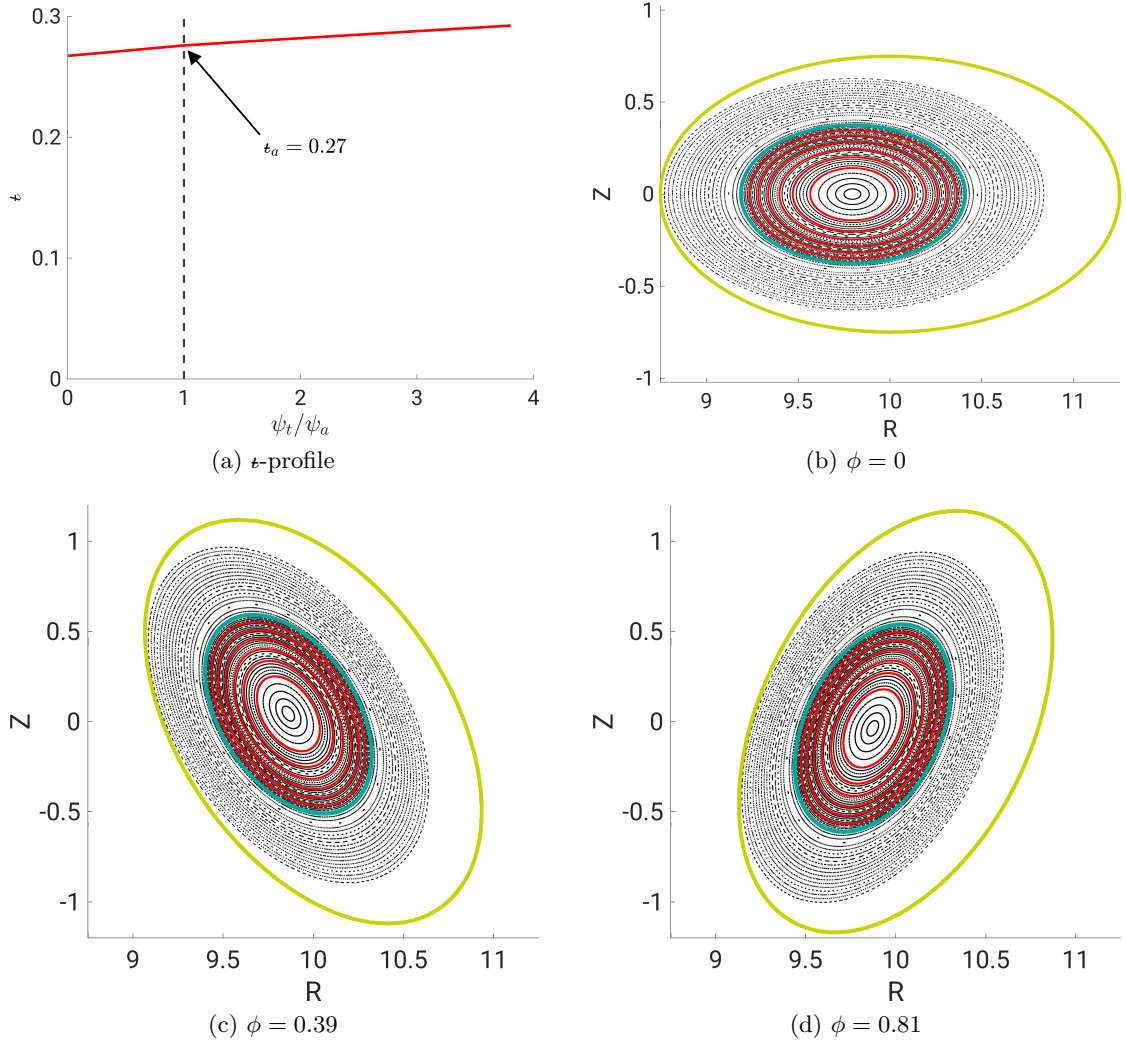


Figure 5.5: Top left: vacuum rotational transform profile (in red) in a rotating ellipse, as evaluated by the SPEC code. The black dashed line highlights the position of the plasma boundary. Here  $t_a$  is the rotational transform at the plasma edge, *i.e.* on the outer side of the plasma boundary. Top right, and bottom: Poincaré section, at three different poloidal planes, of the vacuum field as evaluated by SPEC. In yellow: computational boundary. In blue: plasma boundary. In red: interfaces  $\mathcal{I}_l$ ,  $l = \{1, \dots, 7\}$ .

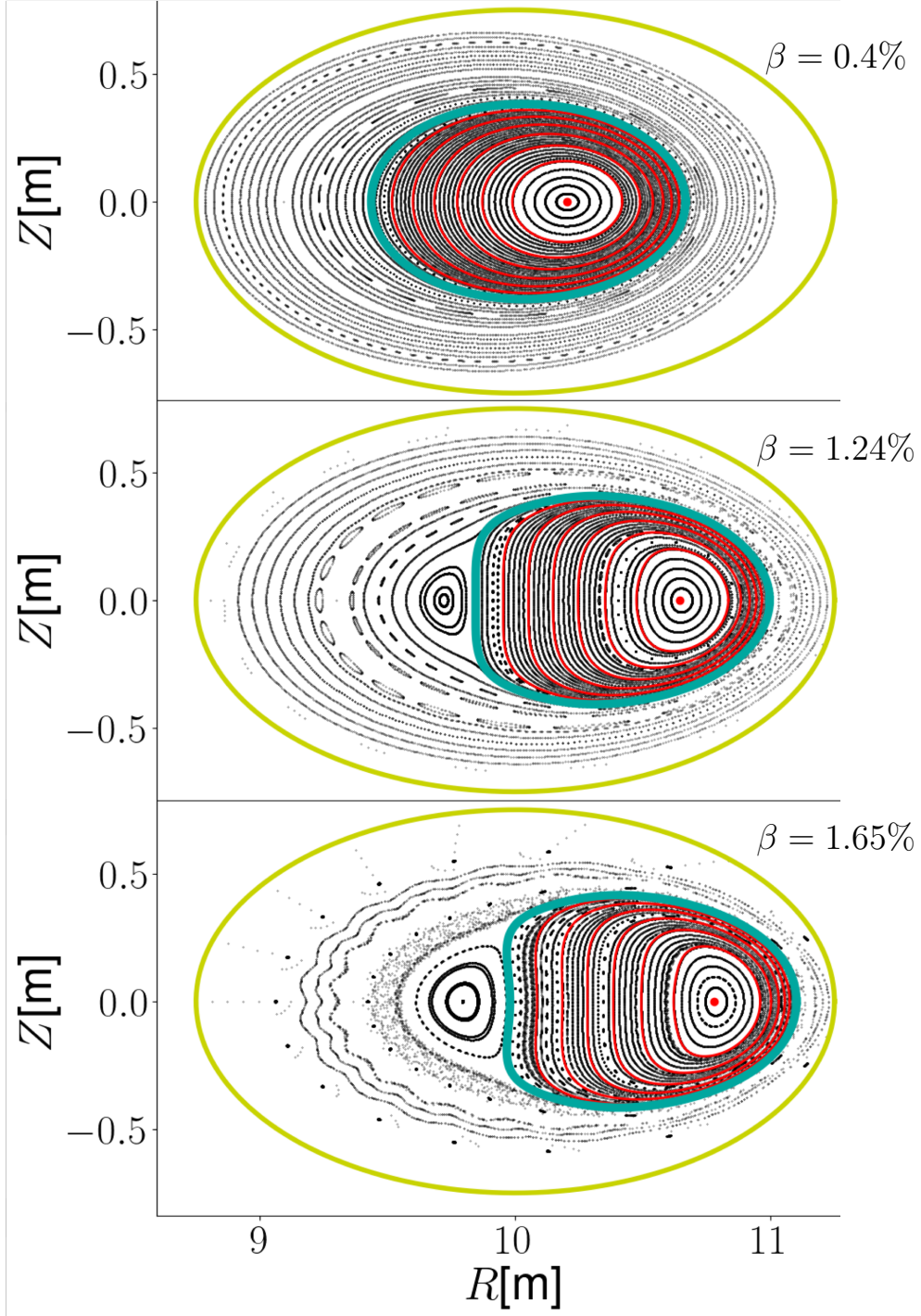


Figure 5.6: Poincaré plot (black dots) of SPEC equilibria at toroidal angle  $\phi = 0$  and at different values of  $\beta$ , for  $\hat{C} = 0.46 < \hat{C}_{crit}$ . Red lines: inner plasma volume interfaces; blue line: plasma boundary; and yellow line: computational boundary.

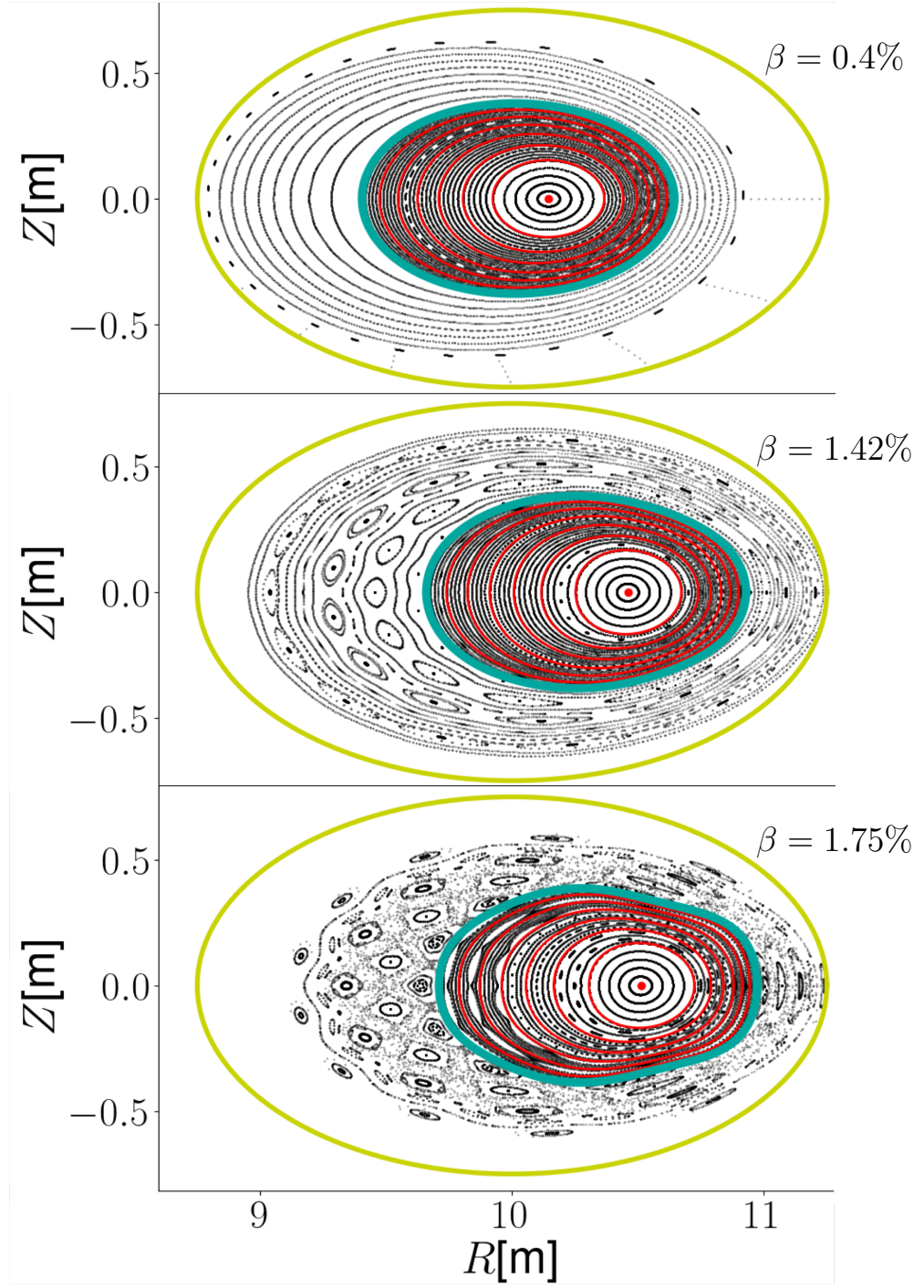


Figure 5.7: Poincaré plot (black dots) of SPEC equilibria at toroidal angle  $\phi = 0$  and at different values of  $\beta$ , for  $\hat{C} = 0.91 > \hat{C}_{crit}$ . Red lines: inner plasma volume interfaces; blue line: plasma boundary; and yellow line: computational boundary.

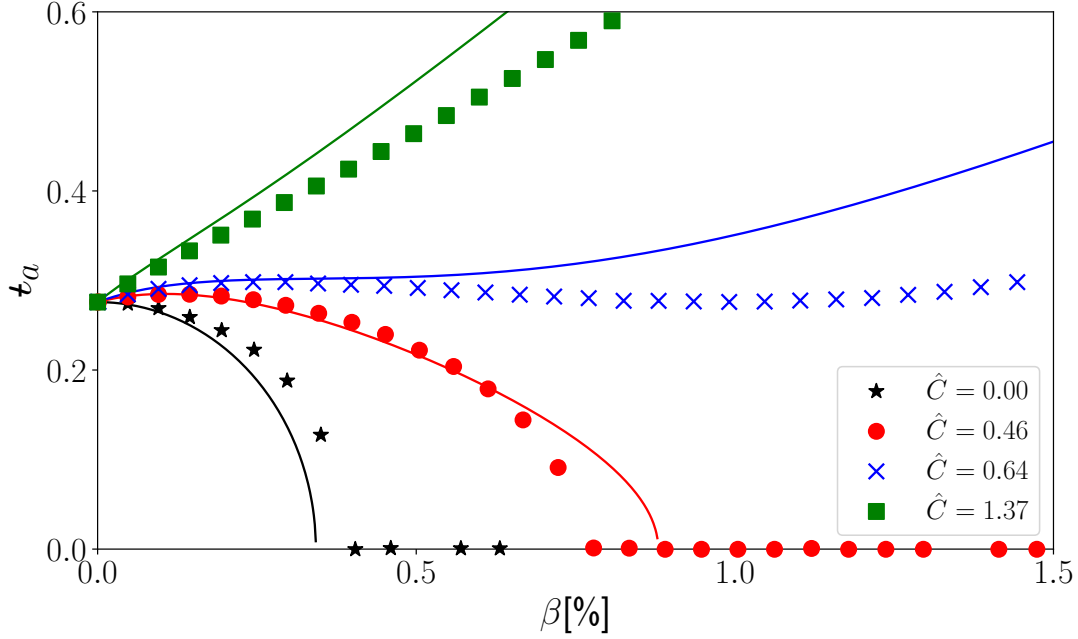


Figure 5.8: Edge rotational transform,  $t_a$ , as a function of plasma average  $\beta$ , for different values of  $\hat{C}$ ; stars, circles, crosses and squares are SPEC calculations while full lines are given by the analytical model, Eq.(5.9).

boundary (see Figure 5.6). We will refer to this  $\beta$ -limit as the *ideal equilibrium  $\beta$ -limit*, denoted by  $\beta_{lim}^{ideal}$ , since it is well described by ideal MHD theory (see section 5.2.2). The value of  $\beta_{lim}^{ideal}$  obtained with SPEC is shown as a function of  $\hat{C}$  in Figure 5.9 (red triangles).

The ideal equilibrium  $\beta$ -limit can also be observed in tokamaks, although the underlying mechanism is different. In a tokamak, the plasma may be kept centered by applying a vertical magnetic field  $B_Z$ . As  $\beta$  grows,  $B_Z$  has to be increased, until it compensates the poloidal field  $\mathbf{B}_p$  on the high field side. When this happens, the field at the plasma boundary is purely toroidal and a separatrix opens. In a stellarator, the poloidal magnetic field does not have to cancel for a separatrix to open, it merely has to be such that a field line never completes a poloidal turn. If this happens, the edge rotational transform is zero and a separatrix opens. In our calculations, the net toroidal current is constrained in the plasma volumes and at the interfaces. However the actual dependencies of the current density on the toroidal and poloidal angle are unconstrained. Pfirsch-Schlüter and diamagnetic currents angular dependencies are the source of the poloidal magnetic field perturbation, the lowering of the edge rotational transform, and ultimately the opening of the separatrix. This is why, even in a zero net-toroidal-current stellarator ( $\hat{C} = 0$ ), the edge rotational transform reaches zero as  $\beta$  is increased.

For values of  $\hat{C} > \hat{C}_{crit}$ , the (now strong enough) bootstrap current is able to prevent the edge rotational transform from reaching zero for any  $\beta$ , and hence no  $m = 1$ ,  $n = 0$  island appears anywhere (see the blue crosses and green squares in Figure 5.8). Instead, the edge rotational transform increases until many island chains open in the plasma and in the vacuum region (see Figure 5.7). When these islands are large enough to have a significant impact on the radial transport, the *chaotic equilibrium  $\beta$ -limit* is reached, denoted by  $\beta_{lim}^{chaos}$ . Finally, for all values of  $\hat{C}$ , islands start to overlap and generate large regions of chaotic field lines at sufficiently large values of  $\beta$  (bottom panels of Figures 5.6 and 5.7).

It may be argued that volume interfaces might not be able to support the pressure if islands or chaos are close by (see, for example, the lower panel of Fig.5.7) — *i.e.* that SPEC equilibria might not be trusted at large  $\beta$  without further analysis. This question has been thoroughly studied in slab geometry by Qu et al. (2021). They identified two reasons why a solution might not exist.

The first possibility is that the magnetic surface is fractal and can not be represented by Fourier series. In our calculations above the equilibrium  $\beta$ -limit, large magnetic islands and chaotic regions develop close to volumes interfaces. In this situation, it is

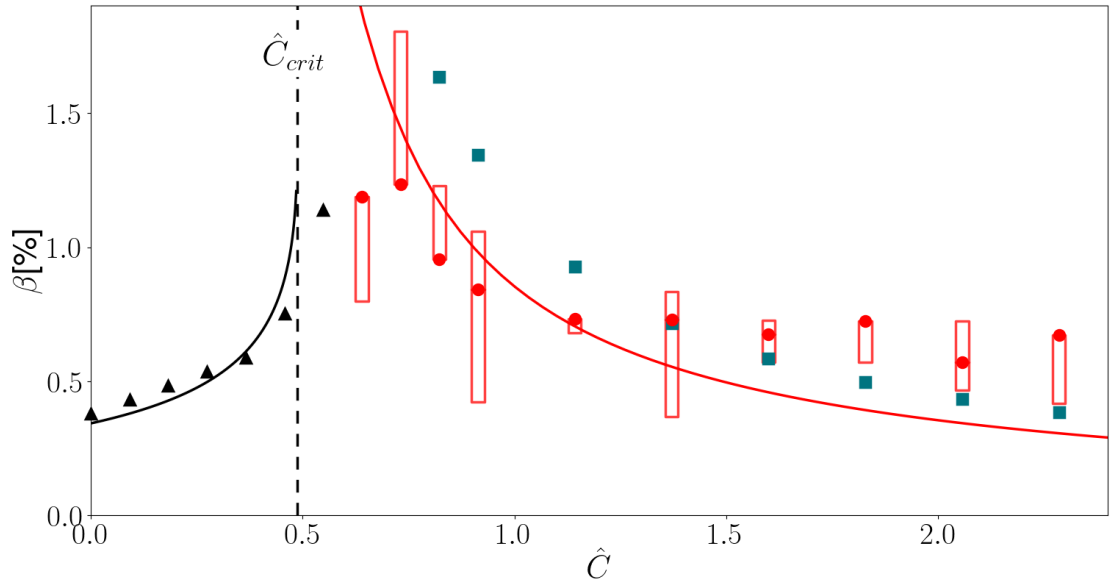


Figure 5.9: Equilibrium  $\beta$ -limit as a function of  $\hat{C}$ . Black: ideal equilibrium  $\beta$ -limit. Triangles:  $\beta_{ideal}^{lim}$ , as obtained from SPEC. Solid black line: analytical prediction for  $\beta_{ideal}^{lim}$  from Eq.(5.14). The dashed vertical line indicates the analytical value of  $\hat{C}_{crit}$  from Eq.(5.15). Red: chaotic equilibrium  $\beta$ -limit. Dots indicate the values obtained from SPEC for  $B_{r,crit}/B = 10^{-5}$ , and the rectangular boxes showing the range obtained from SPEC for  $B_{r,crit}/B \in [10^{-6}, 10^{-4}]$ . Solid red line: analytical prediction obtained by solving from Equation (5.18). Blue squares: SPEC values for which  $t_a = 2t_v$ .



indeed not known if the solution exists and additional analysis would be required, for example with convergence studies as proposed by Qu et al. (2021). Below the equilibrium  $\beta$ -limit, however, only small islands are present. The interfaces are not perturbed by neighbouring, large magnetic islands, and it is likely that the volume interfaces are magnetic surfaces. Since we are only interested in computing the equilibrium  $\beta$ -limit, it is sufficient to calculate equilibria *below or equal to* the equilibrium  $\beta$ -limit; larger  $\beta$  equilibria are irrelevant, and thus the question of existence of interfaces is eluded. In practice, we observe that large magnetic islands and chaotic field lines get close to the volume interfaces only for equilibria with  $\beta$  sufficiently large, giving strong confidence into the results presented in this chapter. Nevertheless, convergence studies have been performed, and results presented in this chapter have been shown to be independent of the numerical resolution.

The second possibility is that the pressure jump on an interface is too large and a solution to the force-balance equation (2.75) does not exist (McGann et al., 2010). This is a possible explanation for when SPEC does not find an interface geometry that satisfies the force balance equation. However, in our calculations, SPEC finds magnetic geometries that do satisfy force balance. This means that the pressure jump across the interfaces is small enough and a solution exists. To summarize this discussion, we can trust SPEC solutions for all  $\beta$  smaller or around the equilibrium  $\beta$ -limit, which is sufficient for the study presented in this chapter.

To evaluate the chaotic equilibrium limit numerically, the volume of chaos ( $V_{chaos}$ ) introduced in section 4.2 can be exploited. The chaotic equilibrium  $\beta$ -limit could then be defined as the  $\beta$  above which  $V_{chaos} > 0$ . The volume of chaos, however, while very useful as a measure of the amount of chaotic field lines, does not provide enough information about whether or not the radial transport is enhanced by the destruction of magnetic surfaces. In addition, the volume of chaos is sensitive to the numerical resolution of the equilibrium — the larger the number of Fourier modes, the greater the number of potential resonances in the equilibrium. Due to overlap between small islands chains generated by high order rationals, chaos may emerge at smaller  $\beta$  as the Fourier resolution is increased. For example, in Figure 5.10 the volume of chaos is plotted as a function of  $\beta$  for two different Fourier resolutions,  $M = N = 6$  and  $M = N = 10$  (blue lines). We see that with this diagnostic, the measured chaotic equilibrium  $\beta$ -limit would drop from  $\sim 1.5\%$  to  $\sim 1\%$  if it were defined as the  $\beta$  above which  $V_{chaos} > 0$ . However, in the  $M = N = 10$  scan, some of the chaotic field lines are formed by high order rationals and their associated smaller islands are expected to participate weakly to the radial transport, and could potentially be ignored.

Instead, we define the equilibrium  $\beta$  limit as the  $\beta$  above which the volume of effective parallel diffusion,  $V_{PD}$ , is greater than zero (see section 4.3). To evaluate this critical  $\beta$ , we use the fraction of effective parallel diffusion  $f_{PD}$  as a proxy function. With this definition, only resonances with large radial magnetic field component matter (we

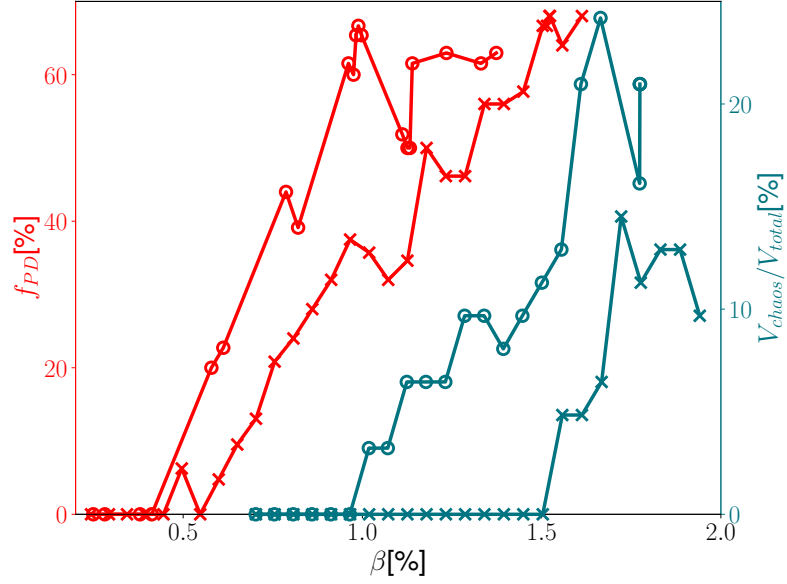


Figure 5.10:  $V_{chaos}/V_{total}$  (blue), and  $f_{PD}$  evaluated for  $B_{r,crit}/B = 10^{-5}$  (red) versus plasma averaged  $\beta$ , for  $M = N = 6$  (crosses) and  $M = N = 10$  (circles).

recall that the radial direction is the direction perpendicular to isotherms); increasing the Fourier resolution of the equilibrium only introduces resonances with small radial magnetic field components, and thus does not impact the value of  $f_{PD}$  — see for example the comparison between two  $\beta$ -scans with resolution  $M = N = 6$  and  $M = N = 10$  in Figure 5.10 (red curves). The critical  $\beta$  at which  $f_{PD}$  becomes larger than zero is quite insensitive to the Fourier resolution. In that sense, this new diagnostic is more robust than the diagnostic based on the volume of chaos.

Note that this does not define an equilibrium  $\beta$ -limit from an experimental point of view — the metric  $f_{PD}$  is positive as soon as one resonance satisfies Eq.(4.12), which would, in practice, only flatten the temperature and density profiles locally. It is certainly possible to increase the plasma averaged  $\beta$  further by increasing the input power. Our metric  $f_{PD}$  however informs us that the effect of field line topology starts to become important and has to be taken into account in transport calculations for  $\beta > \beta_{lim}^{chaos}$ . One could imagine to combine the volume of chaos given by Eq.(4.10) with the criterion given by Eq.(4.12), and only consider resonances that span a sufficiently large volume *and* that contribute significantly to the radial transport. This idea will not be explored in this chapter, and is left for future studies.

The chaotic equilibrium  $\beta$ -limit obtained using the metric  $f_{PD}$  defined in Eq.(4.15) is plotted in Figure (5.9) with red rectangles, spanning the range of  $\beta_{lim}^{chaos}$  obtained when varying  $B_{r,crit}/B$  from  $10^{-6}$  to  $10^{-4}$ . We remind here that this range of values

was obtained by considering typical temperature and densities that cover most regimes in stellarators (see section 4.3). The value of  $\beta_{lim}^{chaos}$  obtained for  $B_{r,crit}/B = 10^{-5}$  is shown with red dots. We observe that the largest  $\beta$ -limit occurs at  $\hat{C} \approx 0.75$ . A small, but non-zero bootstrap current thus *increases* the equilibrium  $\beta$ -limit with respect to a classical stellarator without any net toroidal current ( $\hat{C} = 0$ ), and is thus beneficial. An analytical model that explain the results will be derived in section 5.2.2.

In practice, the metric  $f_{PD}$  is greater than zero when relatively small islands in comparison to the plasma minor radius emerge (using  $B_{r,crit}/B = 10^{-5}$ ). Thus, as long as the SPEC volumes are large enough to allow these islands to grow, the number of volumes does not affect the metric evaluation. In addition, given a sufficiently large number of volumes, the pressure profile is well resolved by the stepped-pressure approximation and thus the equilibrium does not depend strongly on the number of volumes. In summary, the number of volumes has to be large enough to resolve well the pressure profile, but small enough to allow islands to grow — this is how it has been decided to use seven plasma volumes (and one vacuum region).

### 5.2.2 Analytical prediction for the equilibrium $\beta$ -limits

We now derive an analytical model that predicts both the ideal and chaotic equilibrium  $\beta$ -limits. We make use of high- $\beta$  stellarator (HBS) expansion theories derived by Wakatani (1998) and Freidberg (2014) to describe how the rotational transform at the plasma edge  $t_a$  evolves with  $\beta$ , taking into account the effect of the bootstrap current as well. Once a formula for  $t_a(\beta)$  has been derived, we can find whether an ideal  $\beta$ -limit is reached by solving  $t_a(\beta) = 0$ . When no solution is possible, a chaotic  $\beta$ -limit may also be estimated by assuming that the edge iota is modified by order one with respect to the vacuum rotational transform,  $t_a(\beta) - t_a(0) \sim t_a(0)$ , at which point it is likely that many resonances exist.

Assuming that (i)  $\epsilon \ll 1$ ,  $\delta = |\mathbf{B}_p|/B_\phi \sim \epsilon^{3/4}$  with  $\mathbf{B}_p$  the poloidal magnetic field,  $\beta \sim \epsilon$  and  $N_{fp} \sim \epsilon^{-1/2}$ , that (ii) magnetic surfaces are circular, and (iii) considering Solov'ev profiles for the pressure  $dp/d\psi_p = \text{const}$ , and the surface averaged toroidal current density  $\langle j_\phi \rangle = \text{const}$ , one can derive (Wakatani, 1998; Freidberg, 2014) an analytical model for the edge rotational transform,

$$t_a = (t_I + t_v)\sqrt{1 - \nu^2} \quad (5.9)$$

$$\text{with } t_I = \frac{R_0}{2\psi_a} \mu_0 I_\phi(\beta) \quad (5.10)$$

$$\text{and } \nu = \frac{\beta}{\epsilon_a(t_I + t_v)^2}, \quad (5.11)$$

where  $I_\phi$  is the net toroidal current enclosed by the plasma and  $t_v$  is the edge rotational transform in vacuum.



The bootstrap current model we employed in our equilibrium calculations (Eq.(5.6)) implies a linear relation between the net toroidal current in the system and the plasma  $\beta$ , thus

$$\iota_I = \sigma\beta, \quad (5.12)$$

where  $\sigma$  is a proportionality constant. It can be related to  $C$  by integrating Eq.(5.7) to compute  $I_\phi$  in Eq.(5.11), leading to

$$\sigma = \frac{2}{5} \frac{1}{\pi \epsilon_a^{3/2} \iota_v} \hat{C}. \quad (5.13)$$

Combining Eqs.(5.9)-(5.13), analytical expressions of the edge rotational transform as a function of  $\beta$  for different values of  $\hat{C}$  can be obtained. Figure 5.8 compares the analytical curves to results obtained with SPEC. We observe reasonable agreement especially at low  $\beta$ . As  $\beta$  increases however, Eq.(5.9) consistently underestimates the actual value of the rotational transform found by SPEC. Thus, even though the equilibrium constructed in section 5.2 does not exactly satisfy the assumptions used to derive Eq.(5.9), the assumptions are reasonable enough to use this analytical model to understand our numerical results. Equation (5.9) provides indeed an analytical (non-linear) relation for  $\iota_a(\beta)$  which can be used to predict both the ideal and chaotic  $\beta$ -limits, as described in the following subsections.

### Ideal equilibrium $\beta$ -limit

The solution to the relation  $\iota_a(\beta_{lim}^{ideal}) = 0$  is given by

$$\beta_{lim}^{ideal} = \frac{1}{\epsilon_a \sigma^2} \left[ \frac{1}{2} - \iota_v \epsilon_a \sigma - \sqrt{1 - 4\iota_v \epsilon_a \sigma} \right], \quad (5.14)$$

which is real for  $\sigma < (4\iota_v \epsilon_a)^{-1}$ , or

$$\hat{C} \leq \frac{5}{8} \frac{\psi_a}{\epsilon_a^{3/2} R_0^2 B_0} \equiv \hat{C}_{crit}. \quad (5.15)$$

Note the limit

$$\lim_{\sigma \rightarrow 0} \beta_{lim}^{ideal} = \epsilon_a \iota_v^2, \quad (5.16)$$

retrieving the result from Freidberg (2014) and Loizu et al. (2017) for a zero-net-current stellarator ( $\hat{C} = 0$ ).

The curve  $\beta_{lim}^{ideal}(\hat{C})$  is plotted in Figure 5.9 with a black line. We observe that as  $\hat{C}$  increases, the ideal equilibrium  $\beta$ -limit increases. Comparison with data points measured from SPEC equilibria (red triangles) shows good agreement, especially for weaker bootstrap current ( $\hat{C} < 0.5$ ). The analytical value of  $\hat{C}_{crit} \approx 0.48$ , obtained from

Eq.(5.15), is reasonably close to the one obtained with SPEC, namely  $\hat{C}_{crit} \approx 0.59$  (thus smaller by about 18%).

### Chaotic equilibrium $\beta$ -limit

For larger values of  $\hat{C}$ , *i.e.*  $\hat{C} > \hat{C}_{crit}$ , the equilibrium  $\beta$ -limit is due to the emergence of chaos and its effectiveness in increasing the transport, thus estimating the chaotic equilibrium  $\beta$ -limit with Eq.(5.9) is not trivial - it is not known, *a priori*, which resonance will participate to the radial transport first. However it is reasonable to assume that when the bootstrap current modifies the edge rotational transform by order one with respect to  $t_v$ , *i.e.*

$$\Delta t_a \equiv t_a - t_v = t_v, \quad (5.17)$$

magnetic islands and chaos are expected to appear. The values of  $\beta$  computed with SPEC at which the condition Eq.(5.17) is satisfied are plotted with blue squares in Figure 5.9. We observe good agreement with the chaotic equilibrium  $\beta$ -limit (red dots) for  $\hat{C} > 1$ .

We can also directly solve equation (5.17) using equation (5.9). We obtain a fourth order polynomial equation for  $\beta$ ,

$$\beta^4 + 4\frac{t_v}{\sigma}\beta^3 + \left(2\frac{t_v^2}{\sigma^2} - \frac{1}{\epsilon_a^2\sigma^4}\right)\beta^2 - 4\frac{t_v^3}{\sigma^3}\beta - 3\left(\frac{t_v}{\sigma}\right)^4 = 0. \quad (5.18)$$

The real, positive root of Eq.(5.18) is plotted with an orange line in Figure 5.9. Direct comparison with the numerical data (blue squares) shows that Eq.(5.18) consistently underestimates the values of  $\beta$  that satisfy Eq.(5.17); this is a direct consequence of the underestimate of  $t_a$  by the analytical model (Figure 5.8). The general dependence on  $\hat{C}$  is however recovered, capturing the chaotic equilibrium  $\beta$ -limit trend (red dots in Figure 5.9) observed numerically for  $\hat{C}_{crit} < \hat{C} < 1.5$ . We remark that there are no free parameters in this analytical model. For  $\hat{C} > 1.5$ , the analytical model (5.18) underestimates greatly the chaotic equilibrium  $\beta$ -limit obtained with SPEC. This region is however less relevant for experiments, as it corresponds to bootstrap currents much larger than what is found in tokamaks, which is usually not sought in stellarators.

### 5.2.3 Dependence of the equilibrium $\beta$ -limit on design parameters

The edge rotational transform in vacuum is approximately equal to the rotational transform on axis (low shear configuration), and can be estimated by a zeroth order near axis expansion (Helander, 2014; Loizu et al., 2017),

$$t_v^{axis} \approx t_v = \frac{N_{fp}}{2} \frac{(r_{max} - r_{min})^2}{r_{max}^2 + r_{min}^2}. \quad (5.19)$$

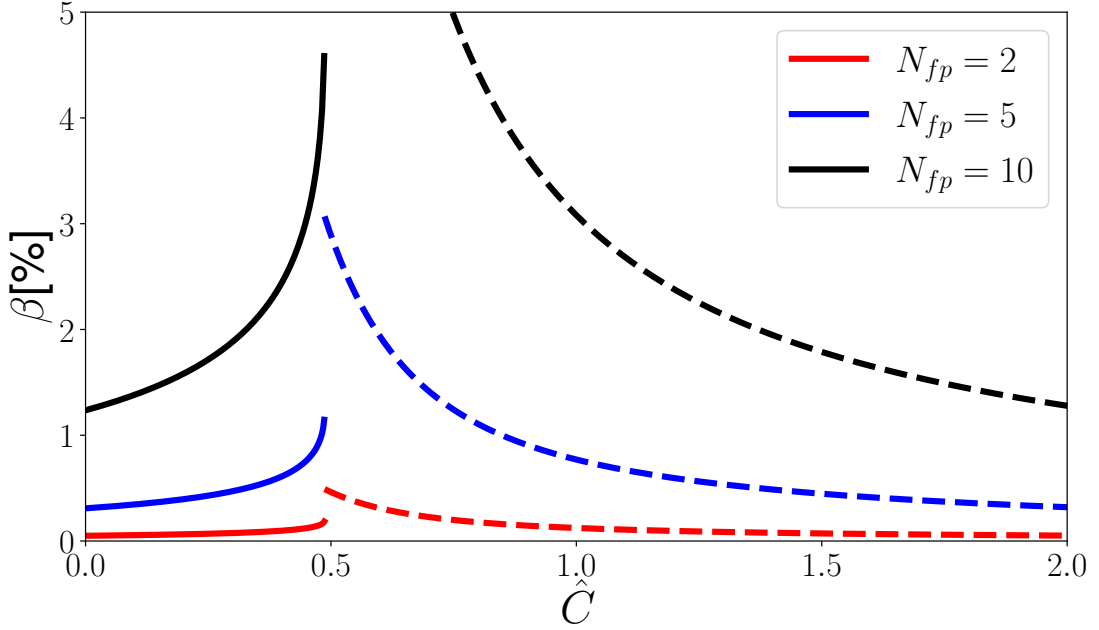


Figure 5.11: Analytical predictions of the equilibrium  $\beta$ -limit for different numbers of field period  $N_{fp}$ . Full lines: ideal limit ( $t_a = 0$ ) as predicted by Eq.(5.14), dashed lines: chaos limit ( $t_a = 2t_v$ ) as predicted by Eq.(5.18)

For low values of  $\hat{C}$ , the ideal equilibrium  $\beta$ -limit grows quadratically with the vacuum rotational transform (see equation (5.16)). For example, increasing the number of field periods increases  $t_v$ , thus also the equilibrium  $\beta$ -limit, as shown in Figure 5.11. These results were corroborated by a limited amount of SPEC calculations with  $N_{fp} = 2$  and  $N_{fp} = 10$  (data not shown). More generally, any mechanism that increases the rotational transform in vacuum will increase the ideal and chaotic equilibrium  $\beta$ -limits. An increase in rotational transform can be achieved by either increasing the number of field periods, increasing the ellipse eccentricity (*i.e.* increasing the harmonic  $R_{11} = Z_{11}$ ) or adding some torsion to the magnetic axis. Magnetic axis torsion can however have an impact on the computed equilibrium, and additional studies would be required to see if it affects the conclusions of this chapter.

Equation (5.15) gives  $\hat{C}_{crit} \approx 0.48$ , *i.e.* the equilibrium  $\beta$ -limit is maximized for a bootstrap current that has half the strength of the bootstrap current in an equivalent circular tokamak. Interestingly, if we approximate the total toroidal flux in the plasma as  $\psi_a \approx \pi a^2 B_0$ , we get  $\hat{C}_{crit} = 5\pi\sqrt{\epsilon_a}/8$ , which only depends on the inverse aspect ratio.

In this section, we have constructed a free-boundary equilibrium in a rotating ellipse geometry, and included a simple analytical model for the bootstrap current in SPEC. We have identified two equilibrium  $\beta$ -limits, namely the ideal  $\beta$ -limit and the chaotic  $\beta$ -limit, and computed their dependencies on the bootstrap current strength. Finally,

we applied the HBS expansion to model analytically our results. The idea to work in a classical stellarator geometry was motivated by two reasons: (i) in a simplified geometry, analytical work is more tractable, and it is possible to keep an analytical understanding of the results, and (ii) SPEC is not robust enough to compute scans in strongly shaped stellarators (see the discussion in section 3.3), especially when multiple plasma volumes are considered. In the same spirit as (i), the study presented here used a simple bootstrap current model to keep the analytical work tractable. In the next sections, we relax these limitations, and present scans in temperature and densities in a quasi-axisymmetric (QA) geometry, with self-consistent bootstrap current calculations.

### 5.3 Quasi-axisymmetric configuration

We consider here a QA stellarator, with two field periods ( $N_{fp} = 2$ ), that is determined by the geometry of one magnetic surface in vacuum, which we denote  $\Gamma_{QA}$ , obtained by Nies et al. (2022). QA stellarators are a particular type of stellarator where the magnetic field is three-dimensional, but its modulus is independent toroidal angle expressed in Boozer coordinates. On an magnetic surface, we define the QA metric,

$$f_{QA} = \sqrt{\sum_m \sum_{n \neq 0} \left( \frac{B_{b,mn}}{B_{b,00}} \right)^2}, \quad (5.20)$$

where  $B_{b,mn}$  are the Fourier modes of the modulus of  $\mathbf{B}$  in Boozer coordinates. For a perfectly QA field,  $B_{b,mn} = 0$  for all  $n \neq 0$ , and therefore  $f_{QA} = 0$ . The configuration we study here is a large aspect ratio configuration with an inverse aspect ratio at the plasma edge of  $\epsilon_a = 1/30$ , and vacuum rotational transform at the plasma edge  $-t_a = 0.11$  (see Figure 5.12).

We first evaluate the vacuum magnetic field by evaluating a single plasma volume, free-boundary SPEC equilibrium. We set the computational boundary to  $\Gamma_{CB} = \Gamma_{QA}$ , and we assume that there exist coils that generates a vacuum magnetic field such that  $\mathbf{B}^c \cdot \mathbf{n} = 0$  on  $\Gamma_{QA}$ , with  $\mathbf{n}$  a normal vector to  $\Gamma_{QA}$ . We assume that the total current flowing in the torus hole is 5.1MA, and set the plasma enclosed toroidal flux to  $3.5 \cdot 10^{-3} \text{Tm}^2$ . The Poincaré section of the vacuum field at three different poloidal planes is shown on Figure 5.13. We observe that the plasma and the surrounding vacuum are filled with magnetic surfaces. To evaluate the QA metric  $f_{QA}$  on the plasma boundary, we couple the SPEC code to the *booz\_xform* python package (Landreman, 2022). This package can evaluate the booz angles  $(\theta_b, \phi_b)$  and the Fourier harmonics of the modulus of  $\mathbf{B}$ , *i.e.*  $B_{b,mn}$ , on a magnetic surface, provided the surface geometry and the magnetic field on the magnetic surface. As the magnetic field is in general discontinuous across SPEC's interfaces, and in particular across the plasma boundary, the Fourier harmonics  $B_{b,mn}$  will be different on each side of the interfaces, and so does the metric  $f_{QA}$ . The

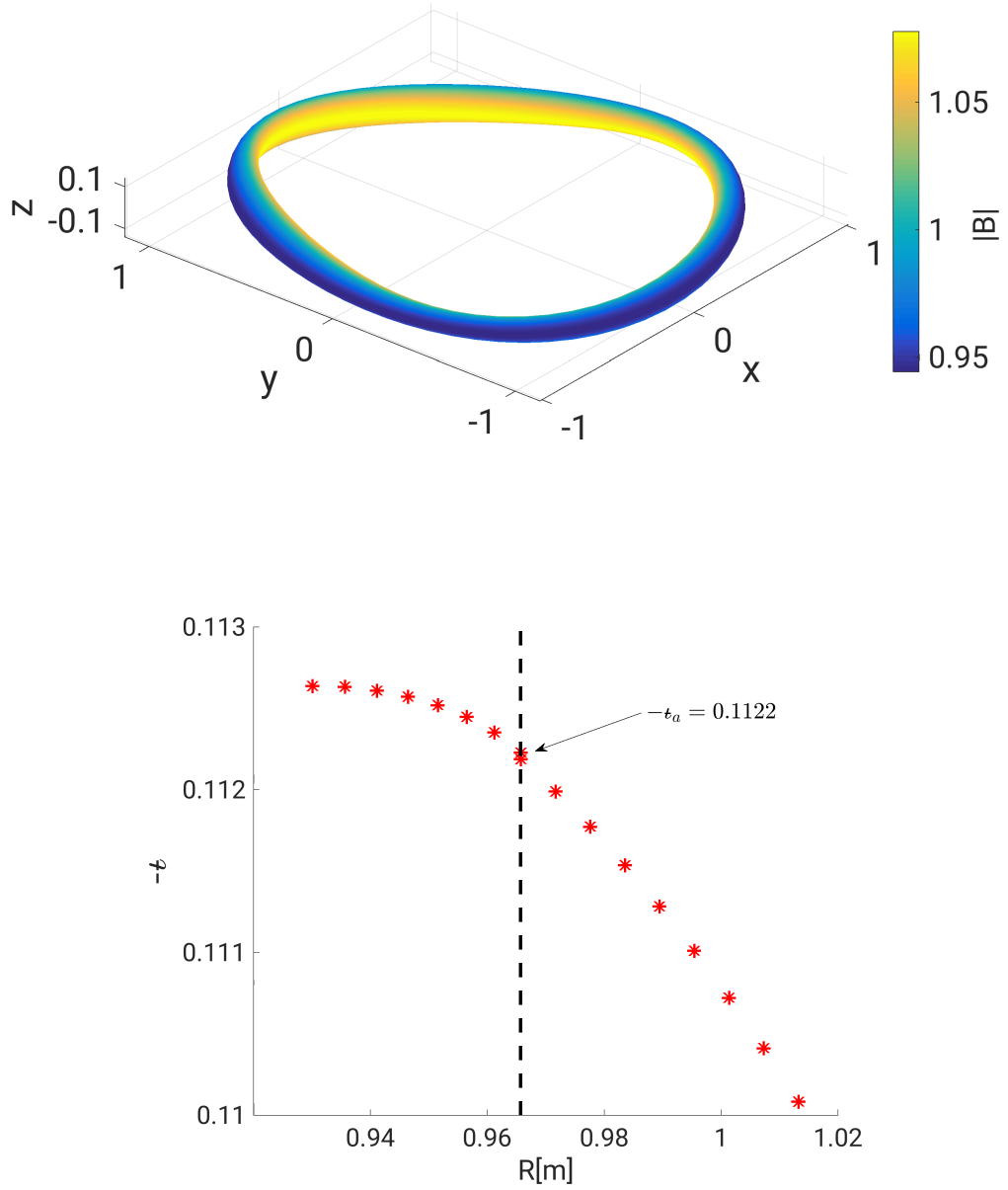


Figure 5.12: QA configuration. Top: 3D shape, colors indicate the magnetic field strength on the computational boundary in vacuum. Bottom: rotational transform profile in vacuum obtained with SPEC (red stars). Here the rotational transform is negative because of the poloidal angle definition in SPEC (see Figure 3.1). The position of the plasma boundary is indicated by a black dashed vertical line.

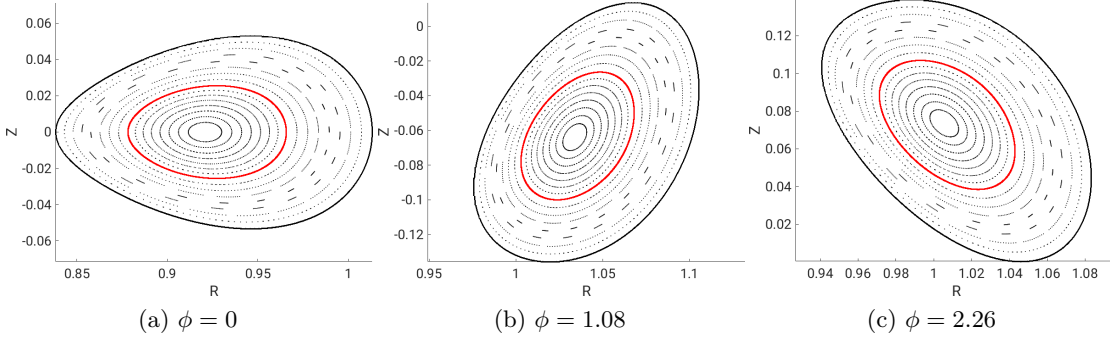


Figure 5.13: Poincaré section of the vacuum field for the QA configuration, at three different toroidal sections. The red surface is the plasma boundary in SPEC, the outermost black surface is the computational boundary in SPEC, which coincides with the boundary provided to describe this QA configuration.

Fourier spectrum of the magnetic field strength in Boozer coordinates on the inner and outer side of the plasma boundary of the QA configuration in vacuum is shown in Figure 5.14. We observe that the symmetry breaking harmonics  $B_{b,mn}$ , with  $n \neq 0$ , are of the order of 0.013% of the  $B_{00}$  harmonic at the plasma boundary. Evaluating the metric  $f_{QA}$ , we obtain  $f_{QA} = 1.6 \cdot 10^{-4}$  and  $f_{QA} = 2.6 \cdot 10^{-3}$  on the inner and outer side of the plasma boundary, respectively. Note that configurations with  $f_{QA}$  orders of magnitude lower than the configuration shown here can be obtained (Landreman and Paul, 2022). Before discussing how the self-consistent bootstrap current can be calculated in a SPEC equilibrium, we first look at the equilibrium  $\beta$ -limit when there is no plasma current.

### 5.3.1 Equilibrium $\beta$ -limit in a current-free QA stellarator

We evaluate the equilibrium  $\beta$ -limit when the net toroidal current is set to zero for all values of  $\beta$ . We use the current constraint to compute SPEC equilibria while maintaining the net toroidal current to zero both in the plasma volume and at the plasma boundary,  $I_{\phi,1}^v = I_{\phi,1}^s = 0$ . The plasma  $\beta$  is controlled by the pressure  $p_1$  in the plasma volume.

We evaluate 28 free-boundary equilibria, from  $\beta = 0\%$  to  $\beta = 0.036\%$ , and plot the rotational transform evaluated at the plasma edge, as a function of  $\beta$ , on Figure 5.15. We observe a similar behavior as in the case of a rotating ellipse (see the black stars on Figure 5.8) — the rotational transform at the plasma edge decreases with increasing  $\beta$ , until reaching  $\iota_a = 0$ , where the ideal equilibrium  $\beta$ -limit is hit. On Figure 5.15, we show the analytical curve obtained with the HBS theory, Eq.(5.9). While the HBS theory is derived assuming a classical stellarator geometry, we remark that it qualitatively retrieves the dependence of  $\iota_a$  on  $\beta$  in the case of the QA configuration. Furthermore, in the case of the classical stellarator, the HBS theory underestimates the ideal equilibrium  $\beta$ -limit, while in the case of the QA configuration, it overestimates it. Indeed, from the analytical

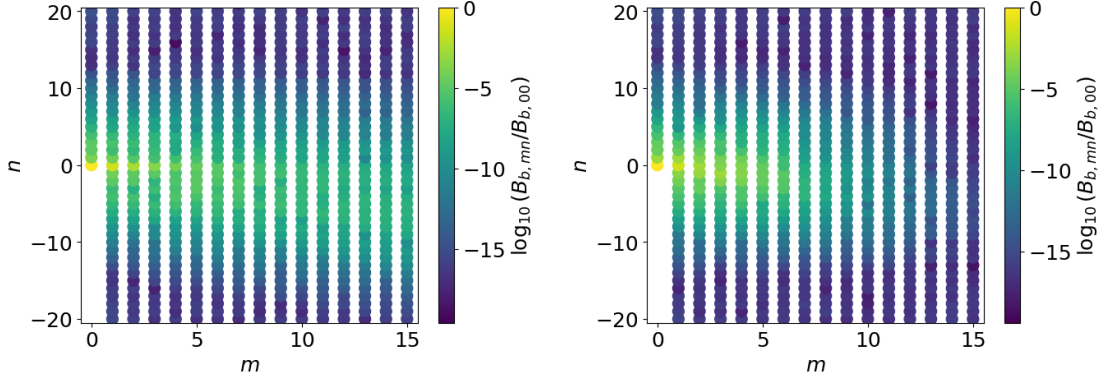


Figure 5.14: Fourier harmonics of the modulus of  $\mathbf{B}$  on the plasma boundary, using Boozer coordinates, as evaluated by the `booz_xform` python package coupled to the SPEC code. Left: inner side of the plasma boundary, and right: outer side of the plasma boundary.

predictions of the ideal equilibrium  $\beta$ -limit in a current-free stellarator, *i.e.* Eq.(5.16), we get

$$\beta_{lim}^{ideal} = \epsilon_a t_v^2 = 0.04\%, \quad (5.21)$$

which is larger than the value obtained with SPEC,  $\beta_{lim}^{ideal} = 0.03\%$  (see Figure 5.15). We conclude that the additional shaping in the QA configuration is, for the case presented here, detrimental to the equilibrium  $\beta$ -limit. In particular, this shows that the ideal equilibrium  $\beta$ -limit depends on the plasma geometry, and thus could potentially be optimized to larger values by modifying the plasma shape, while keeping the rotational transform at the plasma edge constant. In chapter 6, we will discuss how the chaotic equilibrium  $\beta$ -limit can be increased by optimizing different sets of degrees of freedom.

In this section, the equilibrium  $\beta$ -limit of the QA configuration was obtained when the net toroidal current in the plasma was set to zero. In the next section, we include the effect of the bootstrap current by evaluating the self-consistent bootstrap current for a wide range of density and temperature values.

### 5.3.2 Self-consistent bootstrap current and equilibrium $\beta$ -limit

We now describe how a free-boundary SPEC equilibrium in the QA geometry can be evaluated with self-consistent bootstrap current. We use the bootstrap current formulas derived by Redl et al. (2021), and apply the isomorphism between tokamaks and QS stellarators (Boozer, 1983), to describe the bootstrap current in QS stellarators, and, in particular, in QA stellarators (Landreman et al., 2022). The formula by Redl et al.,

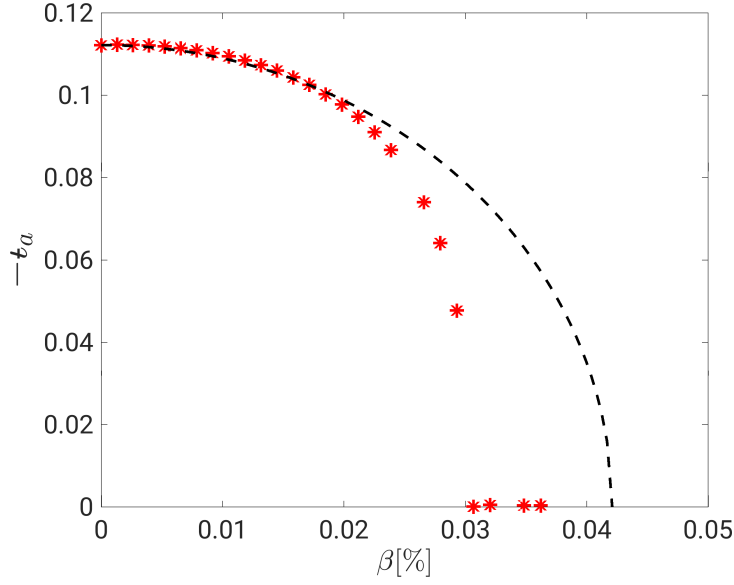


Figure 5.15: Rotational transform at the plasma edge of a current-free QA stellarator. Red stars: rotational transform as evaluated by SPEC. Black, dashed line: analytical prediction, given by Eq.(5.9).

modified for QA stellarators, provides the bootstrap current on a magnetic surface as

$$\langle \mathbf{J} \cdot \mathbf{B} \rangle^{\text{Redl}} = -\frac{G}{t} \left( \mathcal{L}_{31} \left[ n_e T_e \frac{d \ln n_e}{d \psi_t} + n_i T_i \frac{d \ln n_i}{d \psi_t} \right] + p_e (\mathcal{L}_{31} + \mathcal{L}_{32}) \frac{d \ln T_e}{d \psi_t} + p_i (\mathcal{L}_{31} + \mathcal{L}_{34} \alpha) \frac{d \ln T_i}{d \psi_t} \right). \quad (5.22)$$

Here,  $G(\psi_t)$  is the total poloidal current flowing around the magnetic surface,  $\mathcal{L}_{ij}$  and  $\alpha$  are coefficients that depend on the magnetic surface geometry, on the magnetic field evaluated at the magnetic surface and expressed with Boozer coordinates, and on the effective collisionalities of electrons and ions (see the appendix in Landreman et al. (2022) for more details). With stepped-density and stepped-temperature profiles, Eq.(5.22) evaluated at a SPEC interface  $\mathcal{I}_l$  reduces to

$$\langle \mathbf{J} \cdot \mathbf{B} \rangle_{l,\pm}^{\text{Redl}} = -\frac{G_l^\pm}{t_l^\pm} \left( \mathcal{L}_{31,l}^\pm \left[ T_{e,l}^\pm [[n_e]]_l + T_{i,l}^\pm [[n_i]]_l \right] + n_{e,l}^\pm (\mathcal{L}_{31,l}^\pm + \mathcal{L}_{32,l}^\pm) [[T_e]]_l + n_{i,l}^\pm (\mathcal{L}_{31,l}^\pm + \mathcal{L}_{34,l}^\pm \alpha_l^\pm) [[T_i]]_l \right) \delta(\psi_t - \psi_{t,l}), \quad (5.23)$$

where here the  $l$  subscript indicates a quantity evaluated at the interface  $\mathcal{I}_l$ , and the  $\pm$  refers to the inner ( $-$ ) and outer ( $+$ ) side of the interface.

As expected, the bootstrap current, as it is a pressure-driven current, is a delta-function localized at the interface. The bootstrap current on each side of the interface  $\mathcal{I}_l$  can thus be evaluated for any SPEC equilibrium, if the densities and temperature



profiles are provided. Similarly, the flux surface averaged parallel current density can be evaluated from a SPEC equilibrium by using Eq.(2.79). Assuming that magnetic surfaces exist, we work with the  $(\psi_t, \theta, \phi)$  coordinate system and obtain

$$\langle \mathbf{J} \cdot \mathbf{B} \rangle_{l,\pm}^{\text{SPEC}} = \frac{1}{V'(\psi_{t,l})} \iint \frac{dS}{|\nabla\psi_t|} \left\{ (\hat{\mathbf{n}} \times [[\mathbf{B}]]_l) \cdot \mathbf{B}_l^\pm \delta(\mathbf{x} - \mathbf{x}_l) \right\} \quad (5.24)$$

$$= \frac{1}{V'(\psi_{t,l})} \iint d\theta d\phi \left\{ \left( [[B_\theta]]_l B_{l,\phi}^\pm - [[B_\phi]]_l B_{l,\theta}^\pm \right) \delta(\psi_t - \psi_{t,l}) \right\}. \quad (5.25)$$

We can thus evaluate the bootstrap current averaged on each side of the interface  $\mathcal{I}_l$ , with  $\langle \mathbf{J} \cdot \mathbf{B} \rangle_l^{\text{Redl}} = (\langle \mathbf{J} \cdot \mathbf{B} \rangle_{l,+}^{\text{Redl}} + \langle \mathbf{J} \cdot \mathbf{B} \rangle_{l,-}^{\text{Redl}})/2$ , and the flux surface averaged parallel current in a SPEC equilibrium, averaged on each side of the interface  $\mathcal{I}_l$ , with  $\langle \mathbf{J} \cdot \mathbf{B} \rangle_l^{\text{SPEC}} = (\langle \mathbf{J} \cdot \mathbf{B} \rangle_{l,+}^{\text{SPEC}} + \langle \mathbf{J} \cdot \mathbf{B} \rangle_{l,-}^{\text{SPEC}})/2$ .

The difference between the bootstrap current evaluated by the Redl et al. formula, and the flux surface averaged parallel current evaluated from a SPEC equilibrium, can be minimized by optimizing SPEC input profiles, for example the net toroidal current at the interfaces,  $\{I_{\phi,l}^s\}$ . For a single plasma volume free-boundary SPEC equilibrium, we construct a target function

$$f_{\text{bootstrap}} = \left( \langle \mathbf{J} \cdot \mathbf{B} \rangle_l^{\text{Redl}} - \langle \mathbf{J} \cdot \mathbf{B} \rangle_l^{\text{SPEC}} \right)^2, \quad (5.26)$$

with  $l = 1$ . By iterating on SPEC's input profiles, an optimizer can then minimize the target function  $f_{\text{bootstrap}}$ . When  $f_{\text{bootstrap}} = 0$ , a SPEC equilibrium with self-consistent bootstrap current is found. Typically, this requires about 30 free-boundary SPEC computations.

We now consider the vacuum QA configuration constructed in section 5.3.1, and compute free-boundary SPEC equilibria with self-consistent bootstrap current for a large range of temperature and densities,  $n \in [10^{18}, 10^{19}] \text{m}^{-3}$  and  $T \in [50, 500] \text{eV}$ . We consider a single plasma volume and a vacuum region, even though the same procedure could be applied to multi-volume equilibria. Here the pressure gradient is thus uniquely supported by the plasma boundary. We assume quasi-neutrality,  $n_i = n_e = n$  in Eq.(5.23), and set the ion temperature to be one tenth of the electron temperature,  $T_i = T_e/10$ . This choice is somewhat arbitrary; the motivation here is to describe a plasma where electrons are the ones absorbing the external heating power (*e.g.* ECRH), and are not confined long enough to thermalize with the ions. We consider stepped-density and stepped-temperature profiles, where the density and temperature in the plasma are constant, and are zero in the vacuum region. The pressure in the plasma is thus given by  $p = n(T_i + T_e)/2$ . We constrain the net toroidal current in the plasma volume to be zero,  $I_{\phi,1}^v = 0$ , and constraint the net toroidal current at the plasma boundary to be a self-consistent bootstrap current, that we evaluate by iterating on SPEC, using the net toroidal current at the interface,  $I_{\phi,1}^s$ , as a degree of freedom, until  $f_{\text{bootstrap}}$  is minimized. We use the SIMSOPT python framework for stellarator optimization (Landreman et al.,

2021a), which has been recently coupled to SPEC, to drive the optimization. This optimization is run for each pair of values  $(n, T_e)$ .

The Poincaré section of the magnetic field at  $\phi = 0$ , for three different pairs of  $(n, T)$  is shown on Figure 5.16. We observe that, increasing either the density or the temperature leads to the opening of a central  $(m, n) = (1, 0)$  island, which is characteristic of the ideal equilibrium  $\beta$ -limit. Additional figures of merit are presented on Figures 5.17-5.18. As expected,  $\beta$  increases as the density or temperature increases — see Figure 5.17a. For large values of densities or temperature, SPEC is not able to find the equilibrium, and the force scalar, shown on Figure 5.17b, goes from  $10^{-13}$  in vacuum to  $10^{-7}$  for the largest considered densities and temperatures. The QA metric is not affected by the increase in pressure, as it stays close to  $10^{-6}$  for all densities and temperatures. The Redl formulas can thus be applied for all considered densities and temperatures. On Figure 5.18a, we show the net bootstrap current at the plasma boundary. It shows interesting features, with combinations of densities and temperature leading to negative or positive bootstrap current. This is surprising: in QA configurations, we expect the bootstrap current to increase the amount of rotational transform; as the rotational transform is negative here, we thus expect the bootstrap current to be negative. This apparent contradiction with the results would require careful investigations of the implementation, which is unfortunately not possible in the time frame of this thesis.

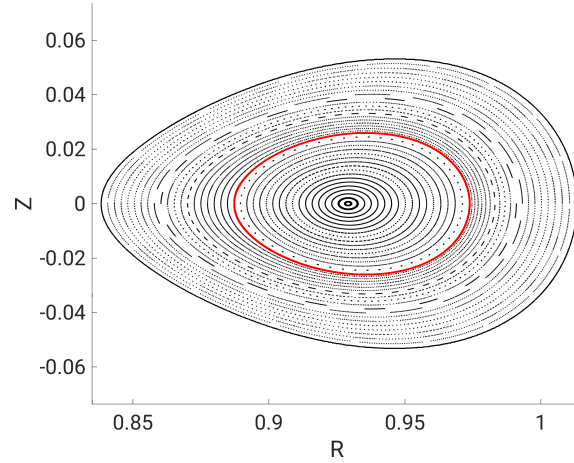
The value of  $\hat{C}$  is a useful metric for comparison with the analytical theory we developed in section 5.2.2. At the plasma boundary,  $\psi_{t,l} = \psi_a$  and Eq.(5.6) reduces to  $I_{\phi,l}^s = -C[[p]]_l$ . In the SPEC calculations, only one plasma volume was considered, thus  $[[p]]_l = -p_0$ . We thus obtain

$$\hat{C} = \frac{C}{C_0} = \frac{I_{\phi,l}^s}{p_0} \frac{t_v B_0}{\sqrt{\epsilon_a} R_0}, \quad (5.27)$$

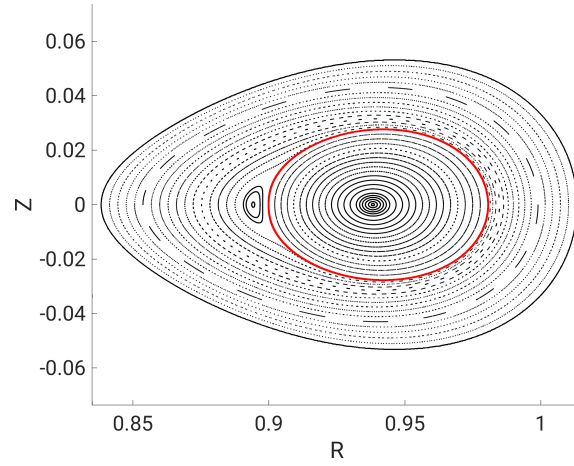
where  $C_0$  is defined in Eq.(5.8). Here  $\epsilon_a = r_{eff}/R_0$  is the inverse aspect ration of the plasma boundary; the effective minor radius,  $r_{eff}$ , is evaluated such that a circular tokamak with the same major radius would have the same plasma volume,

$$r_{eff} = \sqrt{\frac{V_P}{2\pi^2 R_0}}, \quad (5.28)$$

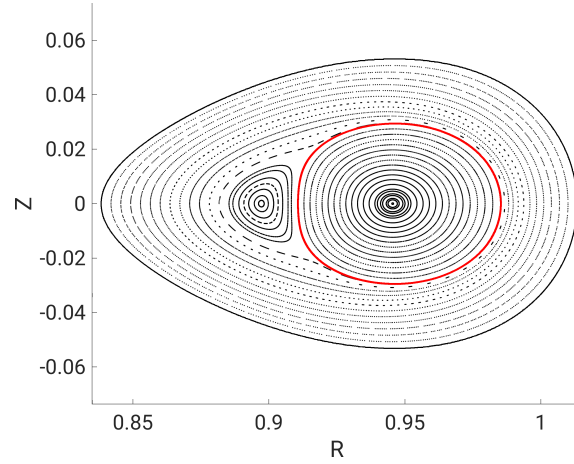
with  $V_P$  the volume enclosed by the plasma boundary. The value of  $\hat{C}$  is shown in Figure 5.18b, where purple and orange colors indicate values larger and smaller than the critical value  $\hat{C}_{crit} = 5\sqrt{\epsilon_a}/8$ , respectively. Interestingly, for low densities and large temperatures, we expect to observe a chaotic equilibrium  $\beta$ -limit, as  $\hat{C} > \hat{C}_{crit}$ , while the ideal equilibrium  $\beta$ -limit is expected to be observed for smaller temperatures and larger densities. This contradicts our numerical results, as the ideal equilibrium  $\beta$ -limit was found for any choice of density. Nevertheless, the theoretical predictions made in section 5.2.2 still apply for a large range of densities and temperatures.



(a)  $n = 3 \cdot 10^{18} \text{m}^{-3}$ ,  $T = 165 \text{eV}$



(b)  $n = 3 \cdot 10^{18} \text{m}^{-3}$ ,  $T = 275 \text{eV}$



(c)  $n = 7 \cdot 10^{18} \text{m}^{-3}$ ,  $T = 165 \text{eV}$

Figure 5.16: Poincaré section of the magnetic field, obtained with SPEC, in the QA configuration with self-consistent bootstrap current, for different values of density and temperature.

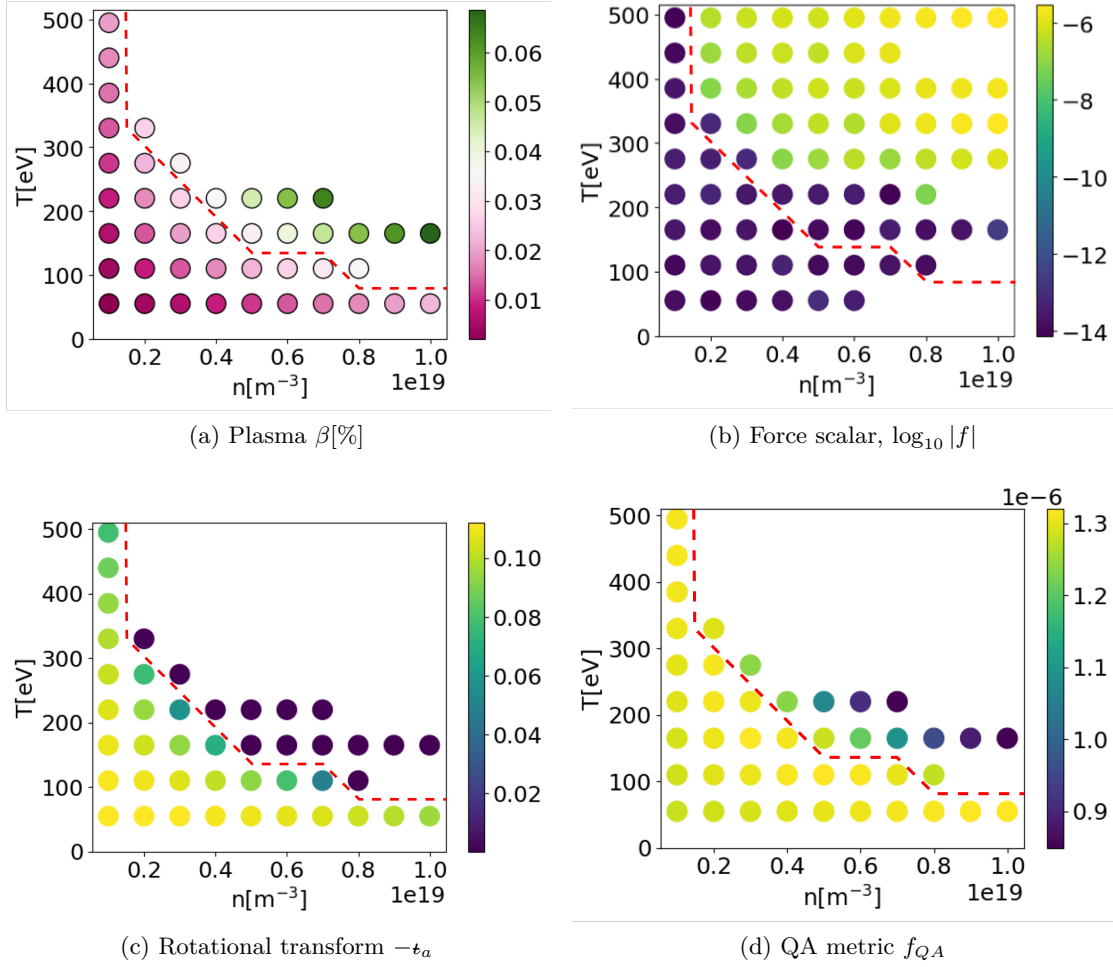


Figure 5.17: Scan in density and temperature in a QA stellarator. Top left: plasma averaged  $\beta$ . Pink and green colors indicate  $\beta$ -values smaller and larger than the equilibrium  $\beta$ -limit found in the current-free case, respectively. Top right: Force scalar  $|f|$ . Bottom left: rotational transform at the plasma edge. Bottom right: QA metric, as defined by Eq.(5.20). The red dashed line shows the ideal equilibrium  $\beta$ -limit. Data is shown if  $|f| \leq 10^{-12}$ .

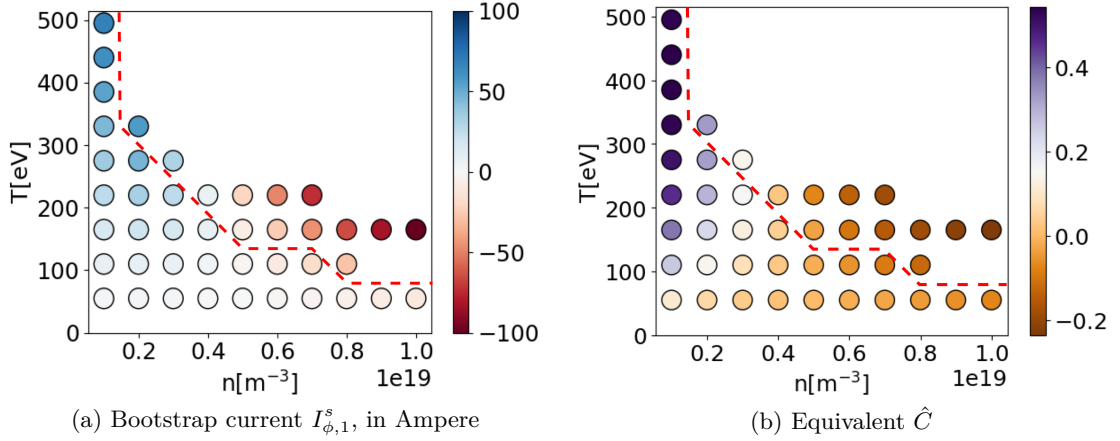


Figure 5.18: Left: net bootstrap current at the plasma boundary. Red and blue colors indicate negative and positive values respectively. Right:  $\hat{C}$ , evaluated with Eq.(5.27). Purple colors indicate  $\hat{C} > \hat{C}_{crit}$ , while orange colors indicate  $\hat{C} < \hat{C}_{crit}$ . The red dashed line shows the ideal equilibrium  $\beta$ -limit. Data is shown if  $|f| \leq 10^{-12}$ .

We plot the rotational transform at the plasma edge as a function of density and temperature in Figure 5.17c. As density or temperature increases (*i.e.* as pressure increases), the rotational transform at the plasma edge increases until reaching zero — this is again the ideal  $\beta$ -limit identified already in the case of a rotating ellipse with small bootstrap current (see section 5.2.1), or in the current-free QA configuration (see section 5.3.1). The ideal equilibrium  $\beta$ -limit is of the same order as in the case of the current-free QA configuration,  $\beta_{lim}^{ideal} \sim 0.03\%$ . For some choice of density and temperature however, the bootstrap current is positive, and reduces the amount of rotational transform, which lowers the equilibrium  $\beta$ -limit, as opposed to what has been observed in the case of the classical stellarator.

## 5.4 Summary

This chapter introduced the concept of bootstrap current and presented studies of the equilibrium  $\beta$ -limits in a classical stellarator and in a QA stellarator. As discussed in section 2.1.3, externally driven currents and bootstrap currents are the main sources of net toroidal current in a magnetic fusion reactor, and in particular in stellarators. It is crucial to include their contribution when computing magnetic equilibria, either with an analytical model or with self-consistent bootstrap current calculations.

In the case of the classical stellarator, a simple analytical bootstrap current model was developed. In this model, the bootstrap current amplitude was controlled by a parameter  $\hat{C}$ . The SPEC code was used to perform a large number of free-boundary stellarator equilibrium calculations including bootstrap current that allowed us to completely

characterize classical stellarators in terms of their equilibrium  $\beta$ -limit. For configurations with low bootstrap current ( $\hat{C} < \hat{C}_{crit}$ ), an ideal equilibrium  $\beta$ -limit was identified, where a central  $(m, n) = (1, 0)$  island appears. Stronger bootstrap current ( $\hat{C} > \hat{C}_{crit}$ ) prevents this central island opening. Instead, a chaotic equilibrium  $\beta$ -limit is reached, where the radial heat transport generated by pressure-induced magnetic islands and magnetic field line chaos competes with turbulence. An analytical model, based on the HBS expansion, showed good agreement with the ideal equilibrium  $\beta$ -limit obtained numerically for weak bootstrap current. The general trend for the chaotic equilibrium  $\beta$ -limit could also be obtained analytically for stronger bootstrap current, up to  $\hat{C} \sim 1.5$ . Analytical insights provided ways to predict the effect of design parameters on the equilibrium  $\beta$ -limit; for example, the ideal  $\beta$ -limit was shown to increase with  $\hat{C}$ , while the chaotic equilibrium  $\beta$ -limit decreases with  $\hat{C}$ , thereby showing a peak equilibrium  $\beta$ -limit around  $\hat{C}_{crit}$ . Interestingly, we found that the critical value of  $\hat{C}_{crit}$  depends only on the inverse aspect ratio, under reasonable assumptions.

We then studied the case of a large aspect ratio QA configuration with small vacuum rotational transform,  $\iota_v \approx 0.1$ . Constraining the net toroidal current to be zero, we observed a similar behavior as in the case of the rotating ellipse and an ideal equilibrium  $\beta$ -limit was found. Despite being derived assuming a classical stellarator geometry, the HBS theory showed good agreement with the results obtained with SPEC in the current-free QA stellarator. In addition, we showed that the shaping of the plasma lowered the ideal equilibrium  $\beta$ -limit in this particular QA geometry, meaning that the equilibrium  $\beta$ -limit depends on the plasma geometry. This is of particular importance for stellarator optimization, since it means that the equilibrium  $\beta$ -limit can be increased by modifying the plasma shape, as it will be discussed in chapter 6.

We then included the effects of the bootstrap current by considering wide ranges of temperature and densities, and evaluating free-boundary magnetic equilibria with self-consistent bootstrap current for each pair of temperature and density. To evaluate the self-consistent bootstrap current, SPEC was coupled to the `booz_xform` code, that computes the Boozer coordinates on each of SPEC volume's interface. The net toroidal current at each of SPEC interface was then optimized such that it was consistent with the bootstrap current evaluated using the formulas proposed by Redl et al. (2021). As a consequence of the small vacuum rotational transform, and as predicted by the analytical model developed in the case of the classical stellarator, the equilibrium  $\beta$ -limit in this configuration was again found to be the ideal equilibrium  $\beta$ -limit.

In the QA study presented here, the pressure profile could only be approximated by a single step; adding more interfaces, as in the classical stellarator study, was not possible due to SPEC robustness issues (see section 3.3). The shape of the pressure profile has however a strong impact on the equilibrium and on the bootstrap current. It is thus important to revisit the study in the QA geometry once SPEC robustness issues are resolved. Furthermore, the configuration studied here features a particularly small

rotational transform in vacuum,  $\iota = 0.1$ , meaning that the ideal equilibrium  $\beta$ -limit is quickly reached, and no chaotic equilibrium  $\beta$ -limit was observed. Other configurations with larger rotational transform should be investigated using the same methodology. This remark also extends to other kind of QS stellarators, for example QH stellarators, where the self-consistent bootstrap current can be evaluated using the same method as presented in this chapter. It is also important to note that the coupling between SPEC, the booz\_xform code, and the computation of the self-consistent bootstrap current with the Redl et al. (2021) formula were not rigorously verified. Further studies should first verify the correct implementation of this coupling, for example by benchmarking the calculated bootstrap current with the results of other codes, such as the SFINCS code (Landreman et al., 2014).

To improve the equilibrium  $\beta$ -limit of stellarators, optimization of different parameters can be performed. For example, Landreman et al. (2021b) recently performed optimization for good magnetic surfaces at the same time as QS in vacuum. In the next chapter, we will discuss how good magnetic surfaces can be recovered in finite  $\beta$ , finite current equilibria by modifying either the plasma boundary, the coils, or by injecting a toroidal current in the plasma. Applying the same recipe to a sequence of equilibria with increasing  $\beta$ , we will discuss the possibility of optimizing a stellarator configuration for larger equilibrium  $\beta$ -limit.





## 6 Optimization for nested magnetic surfaces

In toroidal geometries, 3D MHD equilibria are, in general, a mix of nested magnetic surfaces, magnetic islands and magnetic field line chaos (Helander, 2014; Hanson and Cary, 1984; Cary and Hanson, 1986) — see the discussion in section 1.5. In the plasma core, the latter two topologies are usually detrimental to confinement, *i.e.* the radial transport of particles and energy is much greater than in regions of nested magnetic surfaces. In addition to other desirable properties, a common target of stellarator optimization is thus to increase the volume occupied by magnetic surfaces (Hudson et al., 2002). Note that this is not necessarily the case at the edge of the plasma; for example, magnetic islands can be desirable at the plasma edge to direct particle and energy fluxes towards divertor plates — instances of these so-called island divertors have been used on W7-AS (Hirsch et al., 2008), and are currently used on W7-X (Pedersen et al., 2018). An ergodic edge region consisting mostly of magnetic field line chaos has also been conceived — an example being the LHD stellarator (Ohyabu et al., 1994).

In addition, most physics codes developed by the stellarator community are based on the assumption of nested magnetic surfaces — for example neoclassical codes such as SFINCS (Landreman et al., 2014), and DKES (Hirshman et al., 1986b; van Rij and Hirshman, 1989), or gyrokinetic turbulence codes such as GENE(3D) (Maurer et al., 2020), and XGC (Chang and Ku, 2008; Chang et al., 2009; Nührenberg, 1999), or MHD stability codes such as CAS3D (Schwab, 1993; Nührenberg, 1996, 1999), and TERPSICHORE (Anderson et al., 1990). These codes thus require, for example, a VMEC equilibrium as input. In a recent publication, Landreman et al. (2021b) showed that by optimizing the plasma boundary geometry, SPEC can be used in combination with VMEC to obtain self-consistent vacuum configurations where both codes are in agreement, ensuring good magnetic surfaces in the region of interest. This allows then to trust any auxiliary codes that assume nested magnetic surfaces in this configuration, and to safely optimize for other metrics.

In this chapter, we extend the work by Landreman et al. (2021b) by showing that finite- $\beta$  SPEC equilibria with non-zero net toroidal currents can also be optimized to reduce the volume occupied by magnetic islands and field line chaos in a reasonable amount of time. Additionally, we explore the use of parameter spaces other than the plasma boundary geometry that could be of interest. Indeed, by using new capabilities of the SPEC code, we show that the volume of magnetic surfaces in a stellarator can be maximized by optimizing the injected toroidal current profile, or the coil configuration — two experimentally relevant "knobs" (Geiger et al., 2015). For example, ECCD, or coil currents, are used in W7-X to control the rotational transform at the plasma edge (Geiger et al., 2010). For the optimization, we follow Landreman et al. (2021b) and use the SIMSOPT framework (Landreman et al., 2021a), which in particular can construct an objective function based on Greene's residues (Greene, 1979) of some selected rational surfaces (see section 4.1).

This chapter is adapted from the following publication: A. Baillod *et. al.*, Stellarator optimization for nested magnetic surfaces at finite  $\beta$  and toroidal current, *Physics of Plasmas* **29**, 042505 (2022), published under the license CC BY 4.0.

### 6.1 Method

We consider the optimization of a finite- $\beta$ , finite current equilibrium in a classical stellarator geometry (rotating ellipse) calculated with SPEC (see chapter 3), which presents regions of magnetic islands and magnetic field line chaos. This model of a classical stellarator was chosen for simplicity, as few Fourier modes are required to describe the equilibrium. However, the optimization procedure presented here does not depend on the specific choice of geometry. A strongly shaped stellarator, such as W7-X, could also in principle be optimized with the presented approach.

We construct a free-boundary equilibrium, similar to but different from those studied in chapter 5.2, which will be the initial state for the optimizations presented in this chapter. We choose the computational boundary  $\Gamma_{CB}$  to be a rotating ellipse (see Figure 5.3),

$$R^{CB}(\theta, \phi) = R_{00}^{CB} + R_{10}^{CB} \cos \theta + R_{11}^{CB} \cos(\theta - N_{fp}\phi), \quad (6.1)$$

$$Z^{CB}(\theta, \phi) = Z_{10}^{CB} \sin \theta + Z_{11}^{CB} \sin(\theta - N_{fp}\phi), \quad (6.2)$$

where  $R_{00}^{CB} = 10\text{m}$ ,  $R_{10}^{CB} = -Z_{10} = 1\text{m}$ ,  $R_{11}^{CB} = Z_{11} = 0.25\text{m}$ , and with  $N_{fp} = 5$ . We impose a pressure profile linear in toroidal flux  $\psi_t$ , that we approximate with seven steps, *i.e.* we consider  $N_{vol} = 7$  plasma volumes, and one vacuum region surrounding the plasma. We scale the pressure profile such that  $\beta = 1.5\%$ . We assume no externally induced currents by setting the total toroidal current flowing in each volume to zero,  $\{I_{\phi,l}^v\}_{l=\{1,\dots,N_{vol}\}} = 0$ , and we assume that the plasma generates a bootstrap-like toroidal

current proportional to the pressure jump at the interface  $I_{\phi,l}^s \propto [[p]]_l$  (see Figure 6.4), which sums up to a net toroidal current enclosed by the plasma of 29.5kA. Finally, we suppose the existence of coils, with a total current of 17.1MA, such that  $\mathbf{B} \cdot \mathbf{n} = 0$  on  $\Gamma_{CB}$ , with  $\mathbf{B} = \mathbf{B}^c + \mathbf{B}^p$  and  $\mathbf{B}^p$  is the magnetic field produced by the plasma currents in the initial equilibrium. The condition  $\mathbf{B} \cdot \mathbf{n} = 0$  is only valid for the specified  $\Gamma_{CB}$ ,  $\beta$  and profiles. Note that the existence of a feasible coil system that generates such a field is not covered in this chapter — only their normal projection on the computational boundary is specified here. Other codes, such as the FOCUS code (Zhu et al., 2018), can be used to obtain such coils.

We will refer to this equilibrium as the *initial free-boundary equilibrium*; its associated magnetic topology is shown via its Poincaré section and rotational transform, plotted on the top panel of Figure 6.1 and on Figure 6.2, respectively. The discontinuities observed in the rotational transform profile are due to SPEC’s stepped-pressure equilibrium model — since the magnetic field is generally discontinuous across the interfaces, and so is the rotational transform.

Free-boundary equilibria can be emulated by a fixed-boundary calculation by setting the toroidal current and the pressure in the last volume to zero,  $I_{\phi,N_{vol}}^v = 0$  and  $p_{N_{vol}} = 0$ . This corresponds to an equilibrium where a perfectly conducting wall  $\Gamma_w$ , parameterized by  $R^w(\theta, \phi)$  and  $Z^w(\theta, \phi)$ , is located at the last interface,  $l = N_{vol}$ , and the plasma boundary  $\Gamma_{PB}$  is the interface  $l = N_{vol} - 1$ , which is allowed to move. The exact same equilibrium as the initial free-boundary equilibrium can thus be generated with fixed-boundary conditions if we set  $\Gamma_w = \Gamma_{CB}$ , given by Eqs.(6.1)-(6.2). The difference is, however, that for any value of  $\beta$  and choice of profiles  $\{I_{\phi,l}^v\}$ ,  $\{I_{\phi,l}^s\}$ , the condition  $\mathbf{B} \cdot \mathbf{n} = 0$  remains valid (perfectly conducting wall). In addition, the toroidal flux in the vacuum region,  $\Delta\psi_{t,V}$ , has to be carefully chosen to be the same as in the free-boundary calculation. We will refer to this equilibrium as the *perfectly conducting wall equilibrium*. Note that the free-boundary equilibrium has effectively no conducting wall (no wall limit).

We now consider different degrees of freedom depending on the type of initial equilibrium. For the free-boundary equilibrium, we write the contribution from the coils to the normal magnetic field on the computational boundary as a double Fourier series,

$$\mathbf{B}^c \cdot \mathbf{n} = \sum_{m=0}^{M_{pol}} \sum_{n=-N_{tor}}^{N_{tor}} V_{mn} \sin(m\theta - nN_{fp}\phi). \quad (6.3)$$

We choose then a selected set of the Fourier harmonics  $V_{mn}$  as parameter space, which emulate an optimization of the coil geometry and coil currents, as would be done in a single-step stellarator optimization (Hudson et al., 2002; Henneberg et al., 2021b). Indeed, assuming that a coil system exists that generates any considered  $V_{mn}$ , optimizing the coils would be equivalent to optimizing the  $V_{mn}$  harmonics.

For the perfectly conducting wall equilibrium, we consider two different parameter spaces. The first is the current flowing in the plasma volumes,  $\{I_{\phi,l}^v\}_{l=\{1,\dots,N_{vol}\}}$ , which is the externally induced net toroidal plasma current (see section 2.3.1). This parameter space is relevant for example for scenario design, where one could desire to heal magnetic islands and chaos for a given plasma geometry and coil system. The second parameter space is the geometry of the wall expressed as Fourier series,

$$R^w(\theta, \phi) = \sum_{m=0}^{M_{pol}} \sum_{n=-N_{tor}}^{N_{tor}} R_{mn}^w \cos(m\theta - nN_{fp}\phi) \quad (6.4)$$

$$Z^w(\theta, \phi) = \sum_{m=0}^{M_{pol}} \sum_{n=-N_{tor}}^{N_{tor}} Z_{mn}^w \sin(m\theta - nN_{fp}\phi). \quad (6.5)$$

The degrees of freedom are then a selected set of Fourier harmonics  $\{R_{mn}^w, Z_{mn}^w\}$ .

The objective functions for each optimization are based on Greene's residues (Greene, 1979), described in section 4.1. We remind here that the Greene's residue  $R$  is a quantity that can be computed for any periodic orbit, with  $R = 0$  when the island width is zero,  $0 < R < 1$  for an O-point, and  $R > 1$  or  $R < 0$  for an X-point. The objective function is

$$f(\mathbf{x}) = \sum_i R_i^2(\mathbf{x}), \quad (6.6)$$

where  $R_i$  is the residue for a field line on the  $i^{th}$  targeted island chain, and  $\mathbf{x}$  are the considered degrees of freedom. The downside of this approach is that each resonant field line has to be selected by hand before starting the optimization. If a new resonance becomes excited during the optimization, it will not be included in the objective function. From the initial equilibrium, *i.e.* the top panel of Figure 6.1, we can identify a set of resonant rational surfaces and their associated residue, listed in Table 6.1. We use the SIMSOPT python framework to drive the optimization, which is based on the default *scipy.optimize* (Virtanen et al., 2020) python algorithm for non-linear least squares optimization.

## 6.2 Quasi-free-boundary optimization

We start by optimizing the initial free-boundary equilibrium. Residues with indices 1-3 in Table 6.1 are used to build the objective function according to Eq.(6.6). These residues correspond to the islands and subsequent chaos present in the vacuum region, just outside the plasma edge. This choice is somewhat arbitrary and is mainly due to the fact that this particular equilibrium presents most of the chaos in that region. Indeed, the core confinement of particles and heat may not be directly affected by the topology of field lines in the vacuum region, but it is in general important to control the presence of magnetic islands or field line chaos in this region for the stellarator heat exhaust system.

## 6.2 Quasi-free-boundary optimization

Index $i$	Volume $l$	Toroidal mode $nN_{fp}$	Poloidal mode $m$	$\epsilon$	Initial $R_i$
1	8	5	9	0.55	0.08
2	8	5	8	0.63	-0.22
3	8	5	7	0.71	0.30
4	5	5	6	0.83	0.26
5	5	5	5	1.00	-0.77
6	4	5	5	1.00	0.05
7	3	5	6	0.83	-0.34
8	3	5	5	1.00	0.82
9	3	5	4	1.25	-0.32

Table 6.1: Identified resonant surfaces and their rotational transform  $\epsilon$  from the initial equilibrium.

The parameter space is a selected set of Fourier modes  $\{V_{mn}\}$ ,  $(m, n) = \{(6, n)\}$ , with  $n = \{-3, \dots, 3\}$ . In principle, more residues listed in Table 6.1 could be targeted if more  $\{V_{mn}\}$  modes were used as degrees of freedom. This is however computationally expensive and was not done for this proof-of-principle calculation. Here, the optimizer required  $\sim 10^3$  CPU-hours, and performed 165 free-boundary SPEC calculations.

The Poincaré section of the optimized equilibrium is plotted on the middle panel of Figure 6.1. As expected,  $\Gamma_{CB}$  is no longer a magnetic surface since  $\mathbf{B}^c$  has been changed relative to the unoptimized equilibrium shown on the top panel of Figure 6.1. The difference between the magnetic field generated by the coils pre- and post-optimization is of the order of 1% of the total magnetic field, *i.e.*  $\delta B/B \sim 1\%$ . We observe that the targeted island chains are no longer visible. The rotational transform profile of the optimized equilibrium is plotted on Figure 6.2. We observe that the rotational transform profile after optimization is of the same order as before the optimization — it still crosses the same rationals, but these rationals do not generate noticeable islands anymore! This optimization clearly demonstrates that the parameter space  $\{V_{mn}\}$  is suitable for stellarator optimization.

New resonances however appeared close to the computational boundary  $\Gamma_{CB}$ , in particular one with mode number  $(m, n) = (10, 5)$ . The residue associated with this resonance was not included in the objective function, which explains why the optimizer was able to converge to this state. One approach to reduce the size of the  $(m, n) = (10, 5)$  island chain is to add the square of its associated residue to the objective function, and continue the optimization from the previous optimized state. The optimizer is then able to reduce the  $(m, n) = (10, 5)$  island size — see the bottom panel of Figure 6.1. This "stepped" optimization process, in which the objective function has to be modified multiple times, is avoidable if a global diagnostic to measure the extent of magnetic islands and chaos is used instead of a local diagnostic such as the Greene's residues. For example, one could consider using the volume of chaos introduced in section 4.1, the

fraction of effective parallel diffusion introduced in section 4.3, or the volume of effective parallel diffusion discussed by Paul et al. (2022). These measures, constructed with a Heaviside function, are however not smooth, and would require the implementation of alternative optimization algorithms (Mongeau, 2009).

### 6.3 Perfectly conducting wall optimization

We now look at two different optimizations of the perfectly conducting wall equilibrium. In the first one, we only target the residues in the vacuum region, *i.e.* residues with indices 1-3 of Table 6.1, and the parameter space is the profile of current flowing in the plasma volumes  $\{I_{\phi,l}^v\}_{l=\{1,\dots,7\}}$ . When more residues listed in Table 6.1 are included in the objective function, the optimizer is not able to lower the objective function sufficiently to observe an effect on the island width. This might be because not enough degrees of freedom were provided. Increasing the number of volumes  $N_{vol}$  in SPEC, consequently increasing the number of degrees of freedom  $\{I_{\phi,l}^v\}_{l=\{1,\dots,N_{vol}\}}$ , is however not a guaranteed solution, since it adds additional topological constraints on the magnetic field and some island chains might remain undetected. The optimization of the injected current profile  $\{I_{\phi,l}^v\}_{l=\{1,\dots,7\}}$  could however be combined with other parameters, for example the coil optimization with degrees of freedom  $\{V_{mn}\}$ , to target more residues. Note that this optimization could also be achieved in the initial free-boundary equilibrium, but the perfectly conducting wall equilibrium was considered here for simplicity.

In the second optimization, all residues listed in Table 6.1 are included in the objective function and the geometry of the perfectly conducting wall  $\Gamma_w$  is optimized. The selected degrees of freedom are the modes  $R_{mn}^w$  and  $Z_{mn}^w$  with  $(m,n) = (1,1), (1,2), (2,1)$ . Low order Fourier modes are chosen for their capacity to penetrate deeper in the plasma (Helander, 2014). In principle, higher order Fourier modes could be used, however the required deviation from the initial state might need to be large to minimize the objective function and thus the optimum state difficult to find for the optimizer. Note that the poloidal angle defined by the Fourier representation of the perfectly conducting wall  $\Gamma_w$  is generally not a straight-field line angle. Which Fourier mode  $R_{mn}^w$  and  $Z_{mn}^w$  affects the targeted rationals is thus a non-trivial question — in general, the residue associated to the  $n/m$  rational might not be affected by the modes  $\{R_{mn}^w, Z_{mn}^w\}$ !

Figure 6.3 shows the result of the optimization of  $\{I_{\phi,l}^v\}_{l=\{1,\dots,7\}}$  (middle panel) and the optimization of  $\Gamma_w$  (bottom panel). Comparing both Poincaré plots with the initial equilibrium (top), we observe that the targeted residues have indeed been minimized - the islands are now much smaller, and are no longer visible in some cases. The rotational transform profiles are plotted on Figure 6.2 and the total enclosed toroidal current on Figure 6.4. Again, the rotational transform profiles are of the same order as for the unoptimized case. Regarding the optimized current profile, the total injected current is  $\Delta I_\phi = -5.2\text{kA}$ , less than 20% of the initial total enclosed toroidal current. Interestingly,

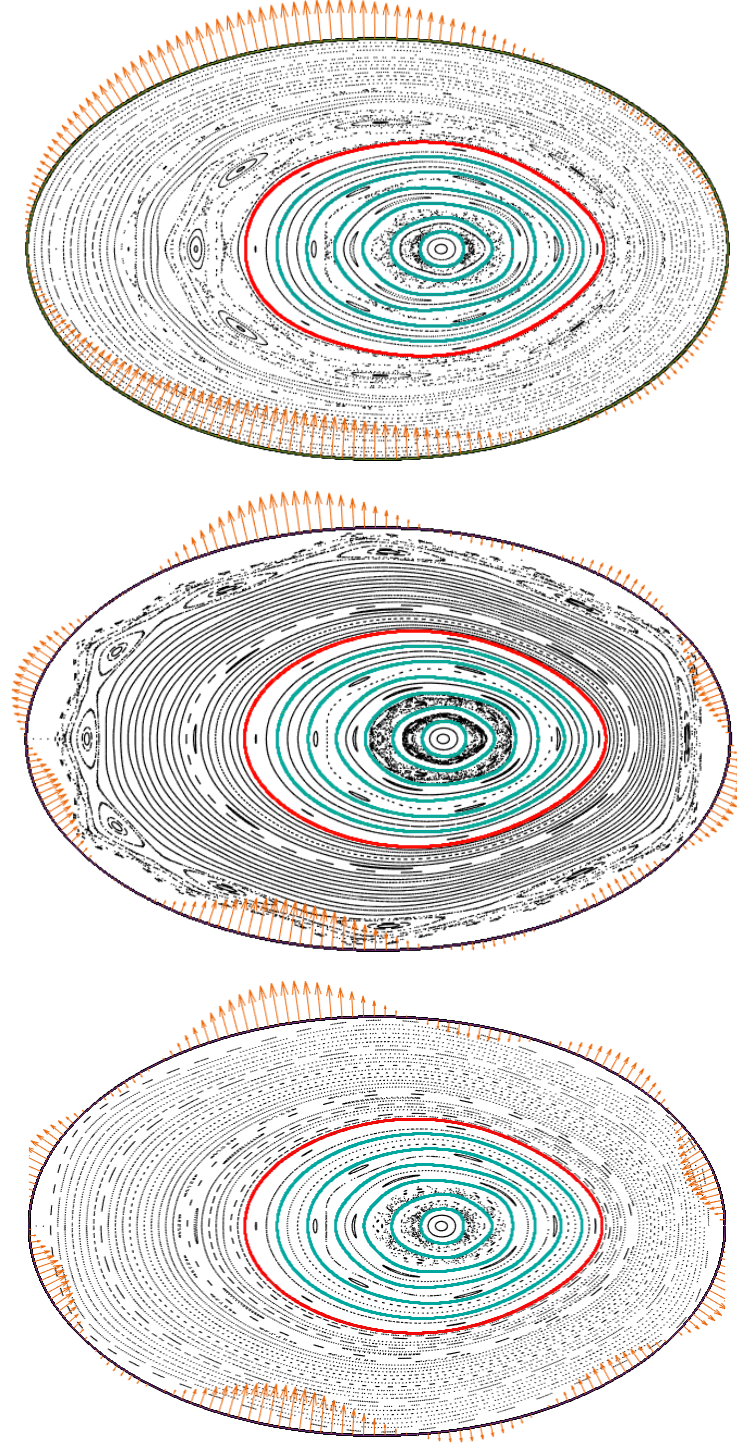


Figure 6.1: Poincaré section of the initial and optimized equilibria. Top: Initial free-boundary equilibrium. Middle: first optimization of  $\{V_{mn}\}$ , targeting residues with index 1-3 in table 6.1. Bottom: second optimization of  $\{V_{mn}\}$ , where the residue associated to the resonance  $(m, n) = (10, 5)$  is included in the target function. In blue: inner interfaces. In red: plasma boundary. In bold black: computational boundary. Orange arrows:  $\mathbf{B}^c \cdot \mathbf{n}$  on the computational boundary

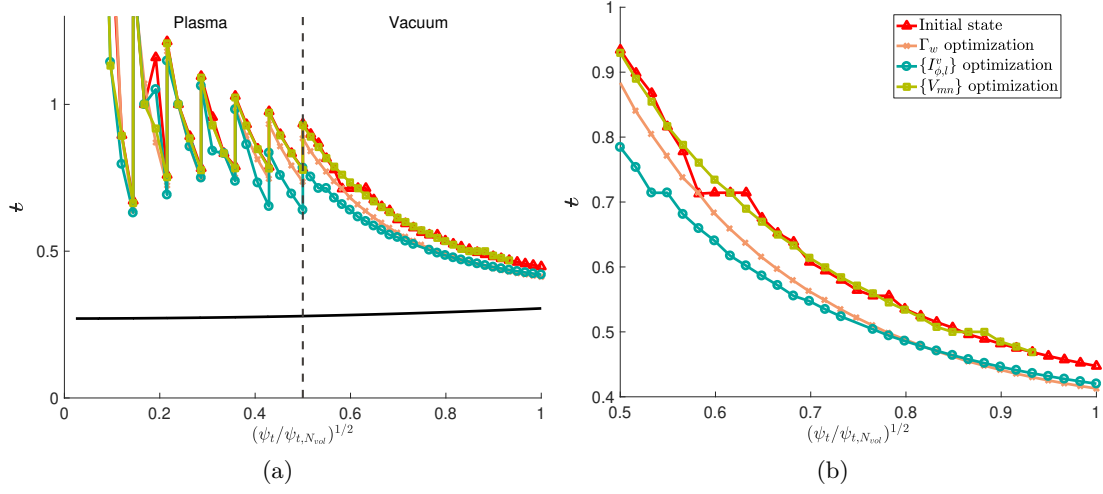


Figure 6.2: Rotational transform as a function of the square-root of the normalized toroidal flux. Left: Full profile. Right: zoom on vacuum region. Black, dashed line: position of the plasma boundary. Black, full line: vacuum profile. The toroidal flux  $\psi_t$  in volume  $l$  is defined via interpolation between  $\psi_{t,l-1}$  and  $\psi_{t,l}$ .

the optimizer found an equilibrium close to the initial state, and did not converge to the obvious global minimum, where a large toroidal current would be injected in the volumes to lift the rotational transform profile in order to push all the targeted rationals out of the plasma. Similarly, for the optimization of  $\Gamma_w$ , a trivial solution would be the axisymmetric solution, with  $R_{mn}^w = Z_{mn}^w = 0$  for  $n \neq 0$ . Again, since a local optimizer is being used, the optimum found is a local optimum close to the initial state, and not the global optimum.

## 6.4 Convergence and computation time

The normalized value of the objective function as a function of the number of iterations is plotted for each optimization in Figure 6.5. The optimization of  $\Gamma_w$  (orange crosses) cannot be compared with the other two, since it uses a different objective function. We see that the optimization of  $\{I_{\phi,l}^v\}_{l=\{1,\dots,7\}}$  (blue circles) saturates at a larger value than the optimization of  $\{V_{mn}\}$  (green squares), despite optimizing the same objective function (the same residues were selected). Intuitively, this can be understood by noticing that the number Fourier harmonics of the magnetic field that are affected by the plasma current is smaller than those that can be affected by the  $\{V_{mn}\}$ . In that sense, the space of possible perturbations of the magnetic field for influencing the islands is more constrained in the  $\{I_{\phi,l}^v\}_{l=\{1,\dots,7\}}$  optimization.



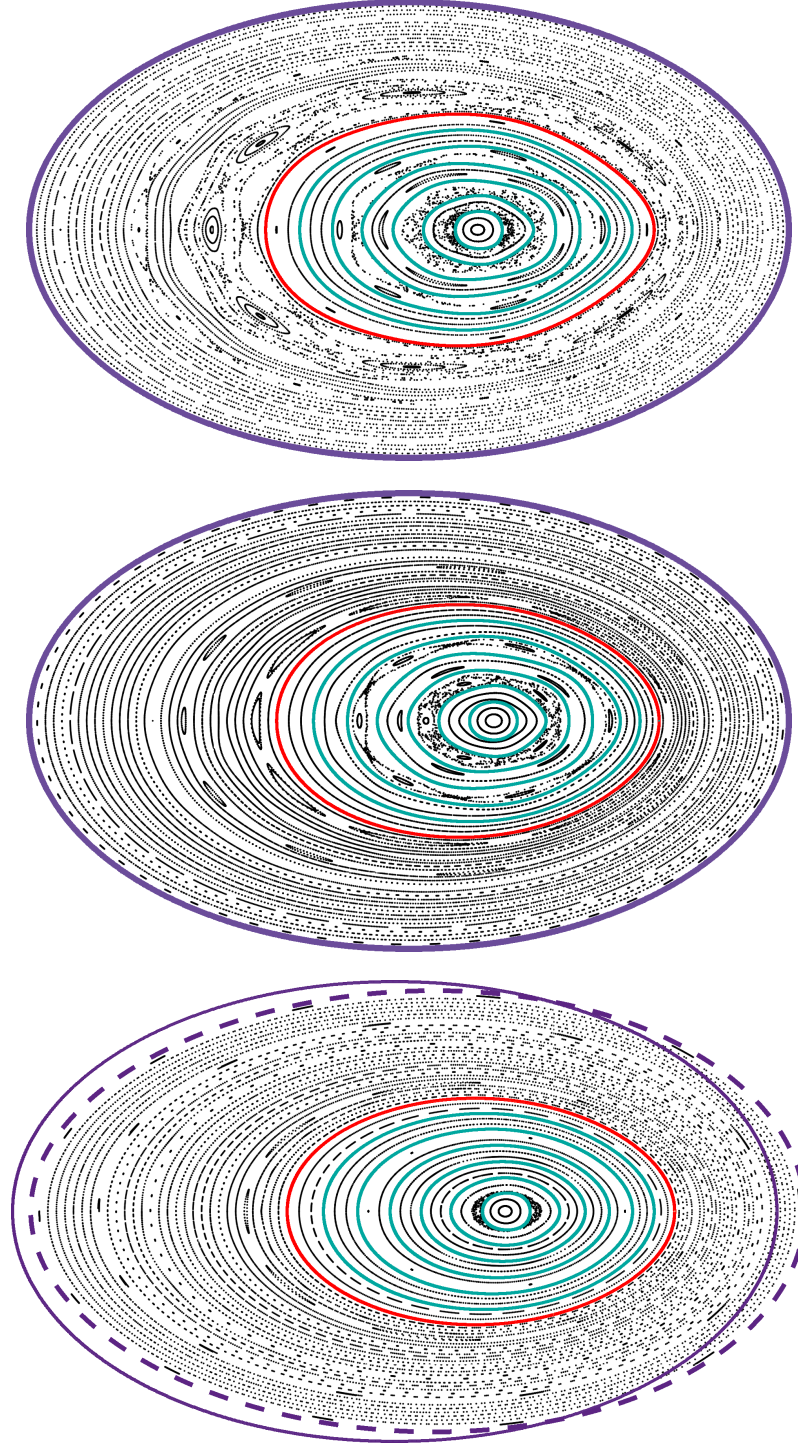


Figure 6.3: Poincaré section of the initial and optimized equilibria. Top: Initial perfectly conducting wall equilibrium. In purple: perfectly conducting wall. In red: plasma boundary. In blue: inner plasma interfaces. Middle: optimization of  $\{I_{\phi,l}^v\}_{l=\{1,\dots,7\}}$ . Bottom: optimization of  $\Gamma_w$ . In purple (dashed): optimized  $\Gamma_w$ .

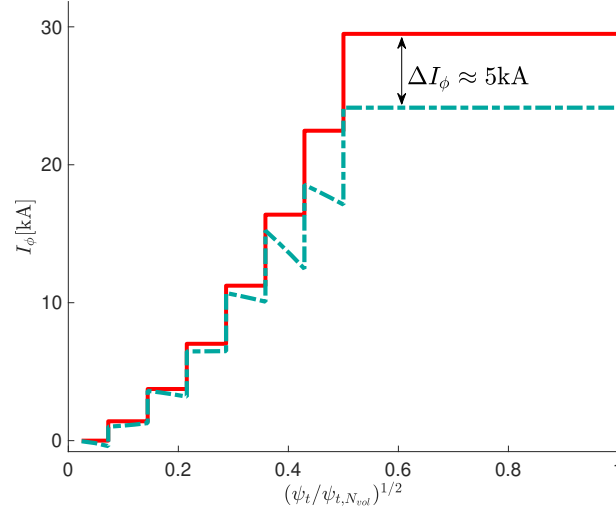


Figure 6.4: Total enclosed toroidal current as a function of the square-root of the normalized toroidal flux. In red: initial equilibrium and in blue:  $\{I_{\phi,l}^v\}_{l=\{1,\dots,7\}}$  optimized equilibrium. Other optimized equilibria have the same toroidal current profile as the initial equilibrium, and are thus not plotted.

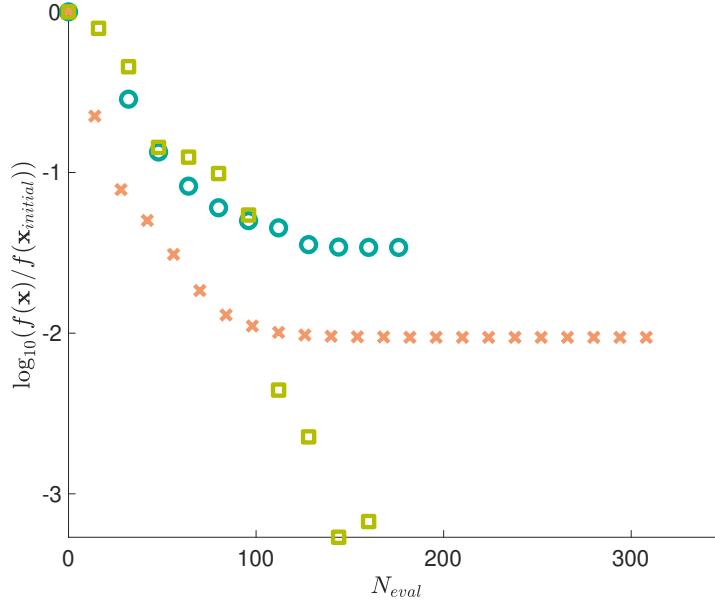


Figure 6.5: Logarithmic plot of the normalized objective function as a function of the number of SPEC calculations. Orange crosses: optimization of  $\Gamma_w$ . Blue circles: optimization of  $\{I_{\phi,l}^v\}_{l=\{1,\dots,7\}}$ . Green squares: optimization of  $\{V_{mn}\}$ .

The optimization was run in parallel on  $2k + 1$  cores of Intel Broadwell processors at 2.6GHz, where  $k$  is the number of degrees of freedom of the optimization. Each core computed a different SPEC equilibrium when evaluating the finite difference estimate of the objective function gradient. The  $\{V_{mn}\}$  optimization required 165 equilibrium calculations, the  $\{I_{\phi,l}^v\}_{l=\{1,\dots,7\}}$  optimization 187 and the  $\Gamma_w$  optimization 309. The total CPU time for execution was respectively  $\sim 41$  days,  $\sim 10$  days and  $\sim 21$  days for a total wall-clock time of respectively  $\sim 65$ h,  $\sim 17$ h and  $\sim 39$ h. As expected, the optimizations of the perfectly conducting wall equilibrium were faster, as fixed-boundary calculations are faster than free-boundary ones.

Note that the presented optimizations did not take advantage of the full parallelization of SPEC — only a single core computed each SPEC equilibrium, while SIMSOPT allows the user to use  $M \leq N_{vol}$  CPUs on  $N \leq 2k + 1$  SPEC instances, which would speedup the computation greatly. Nevertheless, our calculations show that the total time required to perform a SPEC optimization is small enough to be considered in more advanced stellarator optimizations.

## 6.5 Optimization of the equilibrium $\beta$ -limit

In the previous sections, we showed that it is possible to reduce the number of islands and amount of chaos in a *given* finite- $\beta$  equilibrium. We propose here to optimize a *sequence* of equilibria at different values of  $\beta$  to increase a stellarator equilibrium  $\beta$ -limit. In this section, we define the equilibrium  $\beta$ -limit using the volume of chaos defined in section 4.2, and we consider that the equilibrium  $\beta$ -limit has been crossed if  $V_{chaos} > 0$ . We study the case of a rotating ellipse with bootstrap current, described in section 5.2, with  $\hat{C} = 1.37$ . Without any external driven currents,  $I_{\phi,l}^v = 0 \forall l$ , the equilibrium  $\beta$ -limit is  $\beta_{chaos}^{lim} = 1.12\%$  (see the blue curve on Figure 6.6b).

We select a sequence of equilibria, namely at  $\beta = 1.09\%$ ,  $1.16\%$ ,  $1.22\%$ ,  $1.32\%$ , and optimize the net toroidal current in each volume,  $I_{\phi,l}^v$ , to minimize a target function constructed with the Greene's residues of the largest islands in each equilibrium. To improve the convergence of the optimizer, the optimal volume current profile found for one equilibrium is used as an initial guess for the optimization of the next equilibrium in the sequence. The initial and optimized equilibria Poincaré sections are plotted on Figure 6.7. While some islands are still present in some optimized equilibria, their width has been sufficiently reduced to remove chaotic field lines from the equilibrium. Further optimization, to further reduce the islands width, could be achieved by considering additional degrees of freedom, for example a set of  $\{V_{mn}\}$  harmonics. The optimized net toroidal current profiles are shown in Figure 6.6a, and the volume of chaos of the optimized equilibria are shown with red stars in Figure 6.6b. The optimized sequence of equilibria has  $V_{chaos} = 0$  up till  $\beta = 1.24\%$ , effectively increasing the equilibrium  $\beta$ -limit from the unoptimized sequence of equilibria by  $\sim 12\%$ .

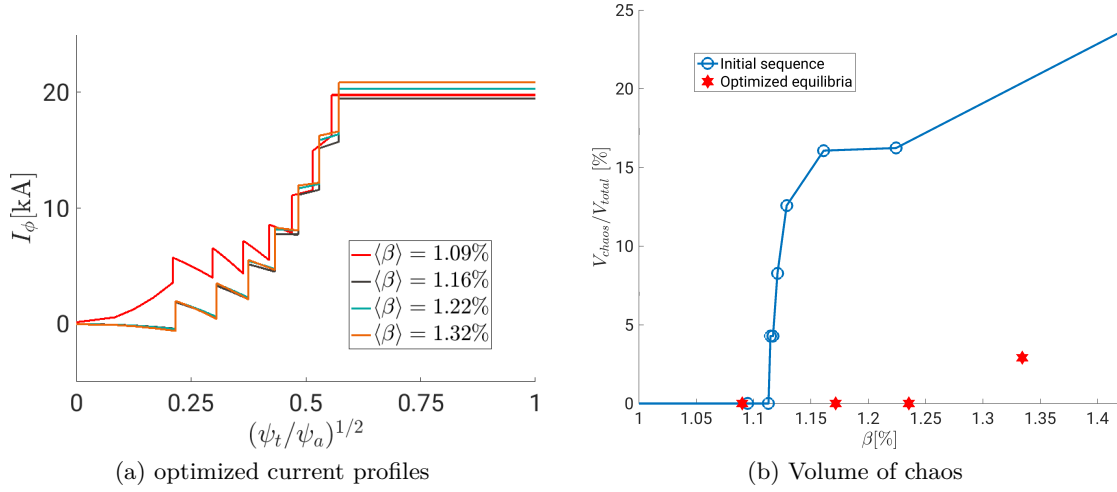


Figure 6.6: Optimization of a sequence of rotating ellipses equilibria for good magnetic surfaces. Left: net toroidal current profile. Right: Volume of chaos as a function of  $\beta$ .

Previous studies already showed the possibility of eliminating islands in high pressure equilibria — see for example the work by Hudson et al. (2002), where the volume occupied by magnetic surfaces, as evaluated by the PIES code, was increased in the W7-AS stellarator. In this section, we showed that similar results could be obtained using the SPEC code, in a fast and simple way. Indeed, as discussed in section 6.4, a single free-boundary optimization takes  $\sim 3$  days to run, though this computation time could probably be an order of magnitude smaller if the full parallelization of the SPEC code was taken advantage of. While our calculations were done in a classical stellarator geometry, the procedure can easily be applied to more complex geometries such as the W7-AS configuration, provided that SPEC numerical issues are mitigated (see chapter 3.3). Of course, more complex geometries would require to increase the Fourier resolution in SPEC (see section 3.1.3), which would require more computational power.

## 6.6 Summary

In this chapter, we showed the first fixed- and free-boundary, multi-volume, finite  $\beta$  SPEC equilibrium optimizations of a classical stellarator using the SIMSOPT framework. The objective function was constructed from the Greene’s residues of selected rational surfaces. Different parameter spaces were considered: either the boundary of a perfectly conducting wall surrounding the plasma, or the enclosed toroidal current profile, or the vacuum field produced by the coils were optimized. Furthermore, we presented how the same approach could be used to optimize the equilibrium  $\beta$ -limit of a stellarator. We considered a sequence of equilibria at different  $\beta$ , and showed that the critical  $\beta$  at which field line chaos emerges could be increased by optimizing the net toroidal current profile in the plasma.

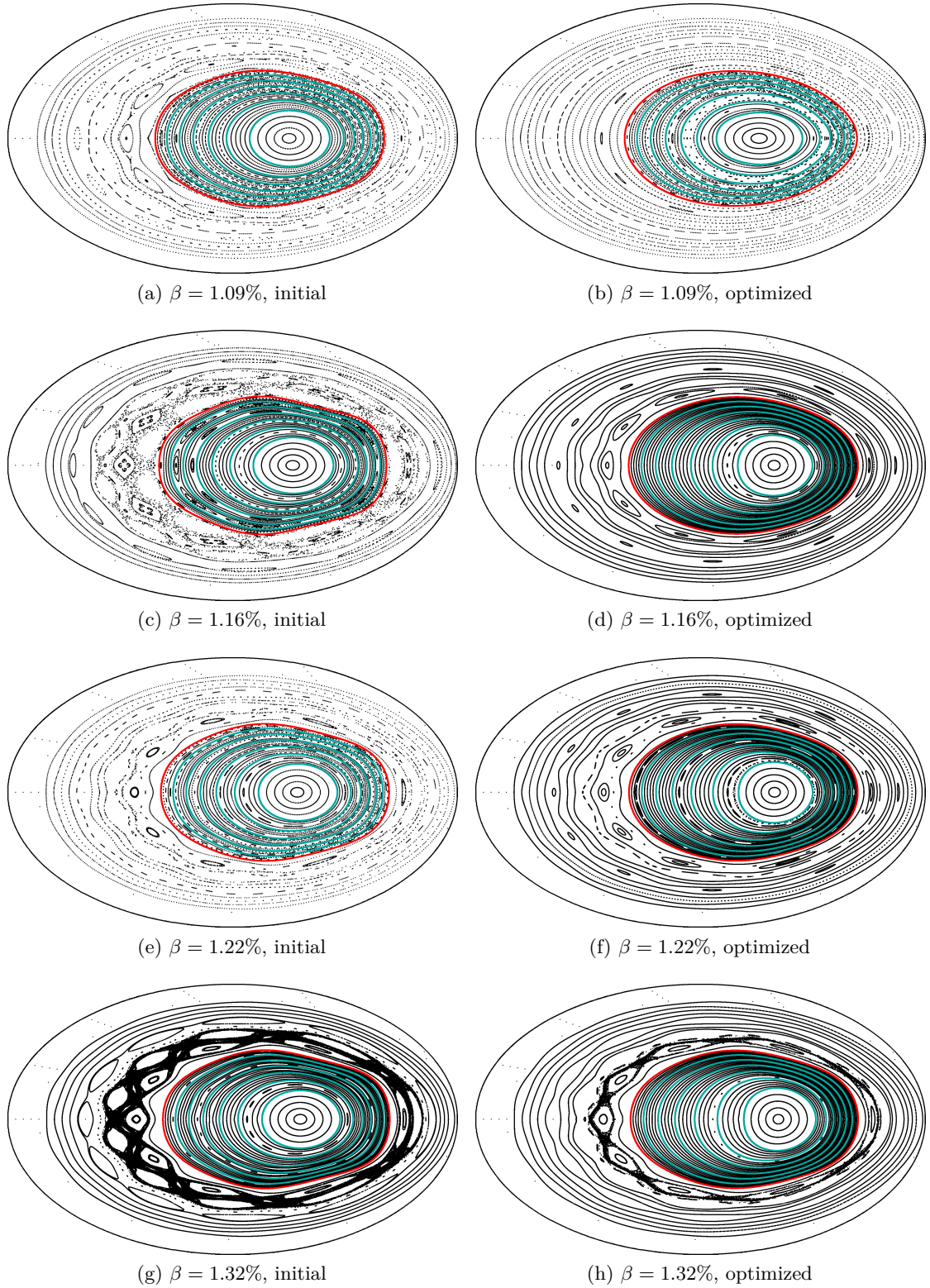


Figure 6.7: Poincaré section of the optimized sequence of equilibria. Left: unoptimized equilibria, right: optimized equilibria.

In all optimizations, it was possible to reduce the objective function significantly, which in turn translated to a reduction of the targeted magnetic island width. In the case of the current profile optimization, the volume occupied by magnetic islands and chaotic field lines was considerably reduced in the vacuum region surrounding the plasma. While not important for plasma confinement, the control of the magnetic field topology in the vacuum region is of paramount importance for divertor design and operation. In the case of the perfectly conducting wall optimization, the volume occupied by magnetic surfaces was increased both in the vacuum region and in the plasma volume. In the case of the optimization of the vacuum field produced by the coils, the islands present in the initial unoptimized equilibrium were reduced in size, but additional rationals and island chains emerged, since their associated residues were not included in the objective function.

Different measures of the magnetic field integrability are currently being considered to overcome the shortcomings of Greene’s residues. Indeed, as observed in the coil optimization, Greene’s residue is a local measure, which requires input from the user — any rational surface emerging during the optimization remains undetected. Ideally, a global measure is thus required. The volume occupied by chaotic field lines, the fraction of effective parallel diffusion, or the volume of effective parallel diffusion, all introduced in chapter 4, are potential candidates.

In the work by Landreman et al. (2021b), it was shown that SPEC could be coupled to VMEC in order to achieve an optimization in a vacuum, where both QS and nested magnetic surfaces could be obtained. The obvious next step is then to perform a combined SPEC-VMC finite- $\beta$  optimization for good magnetic surfaces as well as other metrics, such as QS. This will require significant deviation from a classical stellarator geometry, as opposed to what was presented in this chapter, and the computational cost of the optimization will be greater due to the increased complexity of the problem. While this task does not require extensive development of the optimization tool SIMSOPT, a number of convergence issues in SPEC arising in strongly shaped geometries have to be solved (see section 3.3).

## 7 Conclusion and outlooks

In this thesis, significant advances were made in the computation of 3-dimensional (3D) magnetohydrodynamic (MHD) equilibria, and the understanding of the non-linear relation between pressure and magnetic field line topologies. For the first time, large parameter scans of stellarator equilibria were performed, allowing a deeper understanding of the equilibrium  $\beta$ -limit in a stellarator. In addition, analytical models for the equilibrium  $\beta$ -limits were proposed, and were shown to capture the main parameter dependencies exposed by the numerical scans. First-of-its-kind optimization of the equilibrium  $\beta$ -limit in a stellarator was presented, where it was clearly shown that slight adjustments in the net toroidal current profile, *e.g.* by means of electron cyclotron current drive (ECCD) injection, can be enough to recover good magnetic surfaces at finite  $\beta$ , and therefore increase the equilibrium  $\beta$ -limit of the configuration. Similarly, we showed that a small modification in the vacuum magnetic field, typically produced by external coils, can also heal a configuration with islands and chaos.

In chapter 2, the ideal MHD model was presented. In particular, the potential emergence of diverging Pfirsch-Schlüter currents when considering 3D MHD equilibria with magnetic surfaces was discussed. The multi-region relaxed magnetohydrodynamic (MRxMHD) equilibrium model, which provides weak solutions to the ideal MHD equilibrium equations, was presented. An MRxMHD equilibrium is characterized by a finite number of nested toroidal volumes with constant pressure, separated by magnetic surfaces that support pressure discontinuities. Between the interfaces, magnetic field lines can form magnetic islands and magnetic field line chaos in a finite volume, allowing MRxMHD equilibria to describe magnetic equilibria with pressure gradient, magnetic islands, and magnetic field line chaos. The different kinds of currents in this model were introduced, namely the volume currents, which represent all externally driven currents, and the surface currents, which represent all pressure-induced currents, such as diamagnetic, Pfirsch-Schlüter, and bootstrap currents.



Chapter 3 then introduced the stepped-pressure equilibrium code (SPEC) code, which solves the MRxMHD equilibrium equations in stellarator geometries. In particular, the details of how the net toroidal current profile can be constrained in SPEC were described, including a rigorous verification of its implementation. In an attempt to solve SPEC robustness issues in strongly shaped stellarator geometries, the implementation of an alternative representation of the volume interfaces, called the Henneberg representation, was described. While encouraging, the results seem to indicate that the numerical fragility of SPEC remains even when there is no angle freedom in the interface geometry. Indeed, SPEC could not find the solution to the MRxMHD equilibrium equations in some simple geometries when using the Henneberg representation. Unfortunately, this was the opposite of what was expected and hoped for.

In chapter 4, different metrics to characterize the degree of degradation of magnetic surfaces in a given MHD equilibrium were described. First, the Greene's residue, which is a local measurement of the field line orbit, was discussed. The volume of chaos was then introduced as a first attempt to define a global measure of the existence of good magnetic surfaces. This metric measures the amount of plasma occupied by chaotic magnetic field lines by calculating the fractal dimension of the field lines. Finally, in order to augment the metric to include the effect of the breaking of surfaces on heat transport, the fraction of effective parallel diffusion was defined. This metric is non-zero if there is at least one island in the plasma such that its effect on the radial heat transport dominates the turbulent transport.

Equipped with these metrics, chapter 5 presented the calculation of the equilibrium  $\beta$ -limit in a classical stellarator, and a quasi-axisymmetric (QA) configuration with self-consistent bootstrap current, and showed its dependency on the bootstrap current strength by evaluating free-boundary SPEC equilibria for a large range of pressures. Two types of equilibrium  $\beta$ -limit were identified depending on the strength of the bootstrap current: for configurations with low bootstrap current, an ideal equilibrium  $\beta$ -limit was found, above which a separatrix formed at the plasma edge and  $\epsilon_a \rightarrow 0$ , while for configurations with high bootstrap current, a chaotic equilibrium  $\beta$ -limit was identified, above which chaotic field lines emerged. In particular, it was shown that in a classical stellarator, a small but non-zero bootstrap current could be beneficial in increasing the stellarator equilibrium  $\beta$ -limit. An analytical model, based on the high beta stellarator (HBS) expansion, was proposed and showed good agreement with the numerical results. In the case of the QA configuration, the additional shaping of the plasma was shown to impact negatively the equilibrium  $\beta$ -limit, as compared to a classical stellarator.

Chapter 6 looked into the possibility to optimize the equilibrium  $\beta$ -limit of stellarators. Using the SIMSOPT code, it was shown that good magnetic surfaces could be retrieved by either (i) modifying the coils, or (ii) injecting an externally driven current such as ECCD, or (iii) changing the plasma shape. A sequence of classical stellarator equilibria were then optimized, ultimately increasing the configuration equilibrium  $\beta$ -limit.



## 7.1 Outlook

The studies presented in this thesis were limited by the robustness issues of SPEC. Currently, it is difficult to compute strongly shaped, multi-volume SPEC equilibria, thereby preventing, for example, equilibrium  $\beta$ -limit studies in Wendelstein 7-X (W7-X) with realistic pressure profiles. The SPEC code needs to be improved to allow these more advanced studies. There are numerous ideas that could potentially improve SPEC robustness; unfortunately these could not be tested in the time frame of this thesis. Such ideas were discussed in the conclusion of chapter 3.

If SPEC numerical robustness is improved, its model could be benchmarked against 3D resistive MHD codes, such as M3D-C1 (Park et al., 1999; Reiman et al., 2015), or JOREK (Huysmans and Czarny, 2007; Czarny and Huysmans, 2008; Hoelzl et al., 2021). Validation of SPEC model against experimental data would also become possible. The study of the equilibrium  $\beta$ -limit could be one research direction for such validation. One could for example attempt to evaluate the equilibrium  $\beta$ -limit in the Wendelstein 7-AS (W7-AS) stellarator, and validate the obtained results with PIES calculations (Reiman et al., 2007). Similar studies could then be performed in W7-X geometry, potentially finding configurations with larger equilibrium  $\beta$ -limit that could be validated by experimental data. Furthermore, understanding further the equilibrium  $\beta$ -limit and its dependencies on design parameters could provide valuable information for experiments and for stellarator optimization and design. With SPEC robustness issues solved, it would become possible to fully exploit SPEC for stellarator optimization. In a similar spirit to what has been done by Landreman et al. (2021b), both SPEC and VMEC could be combined in optimization loops in order to perform multi-objective stellarator optimization. Of particular interest would be to study the competition between different targets, for example the quality of good magnetic surfaces and quasi-symmetry (QS) at finite  $\beta$ . Furthermore, a topic that has not been addressed in this thesis is the robustness of magnetic field line topologies to perturbations in the plasma parameters. This could be studied using the SPEC code, and the stochastic optimization algorithm implemented in the SIMSOPT python framework (Giuliani et al., 2022; Wechsung et al., 2022).

On a broader picture, stellarators are today developing extremely fast. Stellarator optimization tools can now leverage the full power of the most advanced supercomputers in the world to find configurations that are getting better every day. It might be only a matter of years before a realistic configuration where a fusion triple product that satisfies the Lawson criterion is found. While there are still numerous engineering challenges, such as manufacturing high-temperature superconductors, designing plasma-facing components that support the extreme heat fluxes, and dealing with the intense neutron flux generated by the fusion reaction, the stellarator concept is closer than ever to a nuclear fusion power plant. It is not unimaginable that, in the future, a stellarator power plant will deliver electricity produced by nuclear fusion reactions on the grid.



# A Appendices

## A.1 Boozer coordinates

In this appendix, we follow Helander (2014) to derive a transformation from general toroidal coordinates  $(p, \theta, \phi)$ , where  $p$  is the pressure, and  $(\theta, \phi)$  are general poloidal and toroidal angles, to Boozer coordinates  $(\psi_t, \theta_b, \phi_b)$ , where  $\psi_t$  is the toroidal flux and  $(\theta_b, \phi_b)$  are the poloidal and toroidal Boozer angles. We start by considering the force balance equation of ideal MHD, Eq.(2.10), which implies that  $\mathbf{B} \cdot \nabla p = 0$ . Assuming that the pressure is monotonically decreasing from the plasma core to the edge, the magnetic field can be written as

$$\mathbf{B} = B_1(p, \theta, \phi) \nabla p \times \nabla \theta + B_2(p, \theta, \phi) \nabla \phi \times \nabla p. \quad (\text{A.1})$$

We derive

$$\nabla \cdot [B_1 \nabla p \times \nabla \theta] = \frac{\partial B_1}{\partial \phi} \nabla \phi \cdot (\nabla p \times \nabla \theta) \quad (\text{A.2})$$

$$\nabla \cdot [B_2 \nabla \phi \times \nabla p] = \frac{\partial B_2}{\partial \phi} \nabla \phi \cdot (\nabla p \times \nabla \theta), \quad (\text{A.3})$$

which, according to the equation  $\nabla \cdot \mathbf{B} = 0$ , imply

$$\left( \frac{\partial B_1}{\partial \phi} + \frac{\partial B_2}{\partial \theta} \right) \nabla p \cdot (\nabla \theta \times \nabla \phi) = 0. \quad (\text{A.4})$$

As we assume our coordinates to not be degenerate, *i.e.* the inverse jacobian never cancels,  $\nabla p \cdot (\nabla \theta \times \nabla \phi) = 1/\sqrt{g} \neq 0$ , we deduce  $\partial B_1/\partial \phi + \partial B_2/\partial \theta = 0$ . Integrating over

## Appendix A. Appendices

---

a poloidal loop, and using the  $2\pi$  periodicity of  $\mathbf{B}$  over  $\theta$ , we get that

$$\frac{\partial}{\partial \phi} \int_0^{2\pi} B_1 d\theta = 0 \quad \forall \{p, \phi\} \quad (\text{A.5})$$

$$\text{Thus} \quad \int_0^{2\pi} B_1 d\theta = g(p) \quad (\text{A.6})$$

$$\text{and} \quad B_1 = \frac{\partial f}{\partial \theta} + \frac{g(p)}{2\pi}. \quad (\text{A.7})$$

with  $f = f(p, \theta, \phi)$  and  $g = g(p)$  two functions. Similarly, we get for  $B_2$ ,

$$B_2 = -\frac{\partial f}{\partial \phi} + \frac{h(p)}{2\pi}, \quad (\text{A.8})$$

with  $h = h(p)$  another function. Defining  $\psi'_t(p) = g(p)/2\pi$ ,  $\psi'_p(p) = h(p)/2\pi$  and  $\lambda = f(p, \theta, \phi)/\psi'_t(p)$ , we get

$$\mathbf{B} = \left(1 + \frac{\partial \lambda}{\partial \theta}\right) \psi'_t(p) \nabla p \times \nabla \theta + \left(\psi'_p(p) - \psi'_t(p) \frac{\partial \lambda}{\partial \phi}\right) \nabla \phi \times \nabla p. \quad (\text{A.9})$$

We define now the *straight field line coordinates*  $(\psi_t, \theta_s, \phi)$ , with

$$\theta_s = \theta + \lambda. \quad (\text{A.10})$$

With these coordinates, the magnetic field can be written as

$$\mathbf{B} = \nabla \psi_t \times \nabla \theta_s + \nabla \phi \times \nabla \psi_p. \quad (\text{A.11})$$

It can be easily verified that the functions  $\psi_t(p)$  and  $\psi_p(p)$  are the toroidal and poloidal fluxes respectively. Note that while here we assumed that the pressure,  $p$ , could be used as a radial coordinate, the equation (A.11) is completely general, as it has been shown in section 1.5. The straight field line coordinates have the property that magnetic field lines are straight when plotted in the  $(\theta_s, \phi)$  plane — indeed, the rotational transform is

$$t = \frac{\mathbf{B} \cdot \nabla \theta_s}{\mathbf{B} \cdot \nabla \phi} = \frac{(\nabla \phi \times \nabla \psi_p) \cdot \nabla \theta_s}{(\nabla \psi_t \times \nabla \theta_s) \cdot \nabla \phi} = \frac{d\psi_p}{d\psi_t}, \quad (\text{A.12})$$

which is independent of the poloidal and toroidal angles, *i.e.* the field lines are straight in the  $(\theta_s, \phi)$  plane (see Figure 2.1).

Equation (A.11) is the covariant representation of the magnetic field in straight field line coordinates. Starting from the charge conservation equation  $\nabla \cdot \mathbf{J} = 0$  and  $\nabla \times \mathbf{B} = \mathbf{J}$ , one can derive a contravariant representation. First, we notice that the force balance equation (2.10) implies that  $\mathbf{J} \cdot \nabla p = 0$ . Using the same reasoning as for the magnetic field, we can write

$$\mathbf{J} = J_1 \nabla \psi_t \times \nabla \theta_s + J_2 \nabla \phi \times \nabla \psi_t. \quad (\text{A.13})$$

Charge conservation implies

$$J_1(\psi_t, \theta_s, \phi) = I'(\psi_t) - \frac{\partial K}{\partial \theta_s} \quad (\text{A.14})$$

$$J_2(\psi_t, \theta_s, \phi) = -G'(\psi_t) + \frac{\partial K}{\partial \phi}, \quad (\text{A.15})$$

with  $I = I(\psi_t)$  and  $G = G(\psi_t)$  two functions that depend only on the toroidal flux and  $K = K(\psi_t, \theta_s, \phi)$  another function that depends on the position. Now, we notice that the curl of  $I\nabla\theta_s + G\nabla\phi + K\nabla\psi_t$  gives

$$\nabla \times (I\nabla\theta_s + G\nabla\phi + K\nabla\psi_t) = \left(I' - \frac{\partial K}{\partial \theta_s}\right) \nabla\psi_t \times \nabla\theta_s + \left(-G' + \frac{\partial K}{\partial \phi}\right) \nabla\psi_t \times \nabla\phi. \quad (\text{A.16})$$

We can thus identify

$$\mathbf{B} = I\nabla\theta_s + G\nabla\phi + K\nabla\psi_t + \nabla H, \quad (\text{A.17})$$

where  $H = H(\psi_t, \theta_s, \phi)$  is an integration constant. Equation (A.17) is the contravariant representation of the magnetic field in straight field line coordinates. Note that  $I$  can easily be identified as the total toroidal current enclosed by the magnetic surface labelled by  $\psi_t$  and  $G$  as the total poloidal current flowing around the magnetic surface labelled by  $\psi_t$ .

In the straight field line coordinates derived above, the toroidal angle  $\phi$  is still completely general — a straight field line poloidal angle  $\theta_s$  exist for any choice of toroidal angle  $\phi$ . There is however a specific choice of toroidal angle  $\phi_b$ , called the Boozer angle, for which  $H = 0$ . To derive it, we define a function  $\omega = \omega(\psi_t, \theta_s, \phi)$  and the transformation

$$\theta_b = \theta_s - \epsilon\omega \quad (\text{A.18})$$

$$\phi_b = \phi - \omega. \quad (\text{A.19})$$

Note that

$$\mathbf{B} = \nabla\psi_t \times \nabla\theta_s + \nabla\phi \times \nabla\psi_p \quad (\text{A.20})$$

$$= \nabla\psi_t \times \nabla(\theta_b + \epsilon\omega) + \nabla(\phi_b + \omega) \times \nabla\psi_p \quad (\text{A.21})$$

$$= \nabla\psi_t \times \nabla\theta_b + \nabla\phi_b \times \nabla\psi_p + \underbrace{\frac{d\psi_p}{d\psi_t} \nabla\psi_t \times \nabla\omega - \nabla\psi_p \times \nabla\omega}_{=0} \quad (\text{A.22})$$

$$= \nabla\psi_t \times \nabla\theta_b + \nabla\phi_b \times \nabla\psi_p, \quad (\text{A.23})$$

## Appendix A. Appendices

---

*i.e.* the angles  $(\theta_b, \phi_b)$  are also straight field line angles. Similarly,

$$\mathbf{B} = I\nabla(\theta_b + \iota\omega) + G\nabla(\phi_b + \omega) + K\nabla\psi_t + \nabla H \quad (\text{A.24})$$

$$= I\nabla\theta_b + G\nabla\phi_b + \left[ K - \omega \left( \iota \frac{dI}{d\psi_t} + \frac{dG}{d\psi_t} \right) \right] \nabla\psi_t + \nabla [H + (I\iota + G)\omega] \quad (\text{A.25})$$

$$= I\nabla\theta_b + G\nabla\phi_b + K_b\nabla\psi_t + \nabla H_b, \quad (\text{A.26})$$

where

$$K_b = K - \omega \left( \iota \frac{dI}{d\psi_t} + \frac{dG}{d\psi_t} \right) \quad (\text{A.27})$$

$$H_b = H + (\iota I + G)\omega. \quad (\text{A.28})$$

Thus, choosing the function  $\omega$  to be

$$\omega = -\frac{H}{\iota I + G}, \quad (\text{A.29})$$

we get the Boozer coordinates, where  $H_b = 0$ . The coordinate jacobian,  $\sqrt{g_b}$ , can be obtained by evaluating  $B^2$ ; taking the product between the covariant (Eq.(A.23)) and contravariant (Eq.(A.26)) representations of  $\mathbf{B}$ , we obtain

$$B^2 = (\nabla\psi_t \times \nabla\theta_b + \nabla\phi_b \times \nabla\psi_p) \cdot (I\nabla\theta_b + G\nabla\phi_b + K_b\nabla\psi_t) \quad (\text{A.30})$$

$$= \frac{G}{\sqrt{g_b}} + \frac{\iota I}{\sqrt{g_b}}, \quad (\text{A.31})$$

which leads to

$$\sqrt{g_b} = \frac{G + \iota I}{B^2}. \quad (\text{A.32})$$

## A.2 Toroidal coordinates

We derive in this appendix the metric and jacobian analytical relations in toroidal coordinates  $(s, \theta, \phi)$ . The position vector is given by

$$\mathbf{x} = R(s, \theta, \phi)\mathbf{e}_R + Z(s, \theta, \phi)\mathbf{e}_Z, \quad (\text{A.33})$$

with  $\mathbf{e}_R$ ,  $\mathbf{e}_\phi$ , and  $\mathbf{e}_Z$  the usual unitary basis vector in cylindrical geometry (see Figure 3.1). The covariant basis vectors are given by  $\mathbf{e}_\alpha = \partial\mathbf{x}/\partial\alpha$ ,

$$\mathbf{e}_s = R_s\mathbf{e}_R + Z_s\mathbf{e}_Z \quad (\text{A.34})$$

$$\mathbf{e}_\theta = R_\theta\mathbf{e}_R + Z_\theta\mathbf{e}_Z \quad (\text{A.35})$$

$$\mathbf{e}_\phi = R_\phi\mathbf{e}_R + R\mathbf{e}_\phi + Z_\phi\mathbf{e}_Z, \quad (\text{A.36})$$

where the subscripts denote partial derivatives. The jacobian is then obtained by taking the triple product between the covariant basis vectors,

$$\sqrt{g} = \mathbf{e}_s \cdot (\mathbf{e}_\theta \times \mathbf{e}_\phi) \quad (\text{A.37})$$

$$= \mathbf{e}_s \cdot (-RR_\theta\mathbf{e}_R + (R_\theta Z_\phi - R_\phi Z_\theta)\mathbf{e}_\phi + RR_\theta\mathbf{e}_Z) \quad (\text{A.38})$$

$$= R(R_\theta Z_s - R_s Z_\theta). \quad (\text{A.39})$$

The contravariant basis is obtained by taking the cross-product of the covariant basis and normalizing by the jacobian,

$$\nabla s = \frac{1}{\sqrt{g}}\mathbf{e}_\theta \times \mathbf{e}_\phi \quad (\text{A.40})$$

$$= \frac{-RR_\theta\mathbf{e}_R + (R_\theta Z_\phi - R_\phi Z_\theta)\mathbf{e}_\phi + RR_\theta\mathbf{e}_Z}{\sqrt{g}}, \quad (\text{A.41})$$

and similarly

$$\nabla\theta = \frac{RZ_s\mathbf{e}_R + (R_s Z_\phi - R_\phi Z_s)\mathbf{e}_\phi - RR_s\mathbf{e}_Z}{\sqrt{g}} \quad (\text{A.42})$$

$$\nabla\phi = \frac{1}{\sqrt{g}}(R_\theta Z_s - R_s Z_\theta)\mathbf{e}_\phi = \frac{\mathbf{e}_\phi}{R}. \quad (\text{A.43})$$

Finally, the metric elements  $g_{ij}$  are

$$\mathbf{g} = \begin{pmatrix} R_s^2 + Z_s^2 & R_s R_\theta + Z_s Z_\theta & R_s R_\phi + Z_s Z_\phi \\ R_s R_\theta + Z_s Z_\theta & R_\theta^2 + Z_\theta^2 & R_\theta R_\phi + Z_\theta Z_\phi \\ R_s R_\phi + Z_s Z_\phi & R_\theta R_\phi + Z_\theta Z_\phi & R_\phi^2 + R^2 + Z_\phi^2 \end{pmatrix}. \quad (\text{A.44})$$

### A.3 SPEC spectral condensation

The standard representation given in Eqs.(3.6)-(3.7) to represent an interface  $\mathcal{I}_l$  depends on the choice of poloidal angle  $\theta$ . In SPEC, a so-called *spectral condensation* (Hirshman et al., 1986a) is implemented to select the poloidal angle (Hudson et al., 2012a). The idea is to minimize the number of Fourier harmonics required to represent a surface, *i.e.* minimize

$$M_l = \frac{1}{2} \sum_{m=0}^{M_{pol}} \sum_{n=-N_{tor}}^{N_{tor}} m^\lambda ((R_{mn}^l)^2 + (Z_{mn}^l)^2), \quad (\text{A.45})$$

by only considering variations tangential to the surface,  $\delta R = R_\theta \delta u$  and  $\delta Z = Z_\theta \delta u$ , where the  $X_i$  designates a derivative of  $X$  with respect to  $i$ ,  $\delta u$  is arbitrary, and  $\lambda$  is a user input. In SPEC, an additional target is included in the minimization, called the *spectral length* — its role is to ensure smooth transition between the angles used to represent two neighboring interfaces (S. R. Hudson, *SPECtacular meeting*, April 2021). It is expressed for volume  $\mathcal{V}_l$  as

$$L_l = \oint \oint \sum_{i=1}^{N_s} \sqrt{[R_l(\theta, \phi) - R_{l-1}(\theta, \phi)]^2 + [Z_l(\theta, \phi) - Z_{l-1}(\theta, \phi)]^2} d\theta d\phi, \quad (\text{A.46})$$

where  $N_s$  is the number of radial grid points  $s_i$ . The target to minimize on each interface  $\mathcal{I}_l$  is then a linear combination of the spectral width and spectral length, Eqs.(A.45)-(A.46),

$$W_l^{sc} = \sum_{l=1}^{N_{vol}-1} \alpha_l M_l + \beta_l L_l \quad (\text{A.47})$$

where  $(\alpha_l, \beta_l)$  are user supplied weights. Variations of  $W_l^{sc}$  with respect to the interface geometry, where only tangential variations are allowed,  $\delta R = R_\theta \delta u$  and  $\delta Z = Z_\theta \delta u$ , can be written under the form

$$\delta W_l^{sc} = \oint \oint Y_l(\theta, \phi) \delta u d\theta d\phi, \quad (\text{A.48})$$

meaning that the minimum of  $W_l^{sc}$  is found for

$$Y_l = \sum_{m=0}^{M_{pol}} \sum_{n=-N_{tor}}^{N_{tor}} Y_{lmn} \sin(m\theta - nN_{fp}\phi) = 0. \quad (\text{A.49})$$



## A.4 Derivation of the Beltrami linear system

Consider the Beltrami equation (2.74). It is a linear relation between the vector potential Fourier-Chebyshev harmonics  $A_{ikmn}$  (see section 3.1). We derive in this appendix how the Beltrami equation can be casted, in each SPEC volume, into a linear system

$$(\mathbf{G} - \mu\mathbf{D}) \mathbf{a} = \mathbf{C}. \quad (\text{A.50})$$

We work with SPEC's coordinates  $(s, \theta, \phi)$ . First, we define the vector potential gauge such that

$$A_s = 0 \quad (\text{A.51})$$

$$A_\theta(-1, \theta, \phi) = 0 \quad (\text{A.52})$$

$$A_\phi(-1, 0, \phi) = 0. \quad (\text{A.53})$$

Second, we enforce the boundary conditions at the volume's boundary,  $\mathbf{B} \cdot \nabla s = 0$  at  $s = -1$ . We find that  $\sqrt{g}B^s = \partial_\theta A_\phi - \partial_\phi A_\theta = 0$ , which, using Eq.(A.52)-(A.53), reduces to

$$A_\phi(-1, \theta, \phi) = 0. \quad (\text{A.54})$$

At  $s = 1$ , if the outer boundary is a magnetic surface, we have also  $\mathbf{B} \cdot \nabla s = 0$ , which reduces to

$$\partial_\theta A_\phi - \partial_\phi A_\theta = 0. \quad (\text{A.55})$$

As derived in section 2.4.3, the Beltrami equation (2.74) minimizes the energy functional  $F$ , defined in equation (2.120). Additional constraints to the Taylor state can be included by using the Lagrange multiplier method. Here, we construct an energy functional whose minimum corresponds to a Taylor state, where  $\mathbf{B} \cdot \nabla s = 0$  on the volume's boundary, where the vector potential gauge, Eq.(A.51)-(A.52), is satisfied and where the toroidal and poloidal fluxes are  $\Delta\psi_{t,l}$  and  $\Delta\psi_{p,l}$  respectively. We thus write

$$F_l = \int_{\mathcal{V}_l} \left( \frac{p}{\gamma - 1} + \frac{B^2}{2\mu_0} \right) dv \quad \text{The MHD energy functional} \quad (\text{A.56})$$

$$- \frac{\mu_l}{\mu_0} (K - K_l) \quad \text{The helicity constraint} \quad (\text{A.57})$$

$$+ b_l \int_{S[\phi=\text{const}]} \mathbf{B} \cdot d\mathbf{S} - \Delta\psi_{t,l} \quad \text{The toroidal flux constraint} \quad (\text{A.58})$$

$$+ c_l \int_{S[\theta=\text{const}]} \mathbf{B} \cdot d\mathbf{S} - \Delta\psi_{p,l} \quad \text{The poloidal flux constraint} \quad (\text{A.59})$$

$$+ \sum_{m=0}^{M_{pol}} \sum_{n=-N_{tor}}^{N_{tor}} d_{lmn} \sum_{k=0}^{L_{rad}} A_{l\theta kmn} T_{km}(-1) \quad \text{Vector potential gauge} \quad (\text{A.60})$$

$$+ \sum_{m=0}^{M_{pol}} \sum_{n=-N_{tor}}^{N_{tor}} e_{lmn} \sum_{k=0}^{L_{rad}} A_{l\phi kmn} T_{km}(-1) \quad \text{Internal boundary condition} \quad (\text{A.61})$$

$$+ \sum_{m=0}^{M_{pol}} \sum_{n=-N_{tor}}^{N_{tor}} f_{lmn} \sum_{k=0}^{L_{rad}} (-m A_{l\theta kmn} - n A_{l\phi kmn}) T_{km}(1), \quad \text{External boundary condition} \quad (\text{A.62})$$

where we assumed stellarator symmetry, and the  $\{b_l, c_l, d_{lmn}, e_{lmn}, f_{lmn}\}$  are Lagrange multipliers. We now pack all the Fourier harmonics of the vector potential,  $\{A_{likmn}\}$ , and the Lagrange multipliers,  $\{b_l, c_l, d_{lmn}, e_{lmn}, f_{lmn}\}$ , in a single array of unknowns  $\mathbf{a}$ . Note that here  $\mu_l$  is known, as it is assumed to be an input to the Beltrami solver. We now seek to minimize  $F_l$  under variations of  $\mathbf{a}$ , *i.e.* find the unknowns  $\mathbf{a}$  such that  $\partial F_l / \partial \mathbf{a} = 0$ . Remark that Eqs.(A.56)-(A.62) have at most a quadratic dependence on the unknown  $\mathbf{a}$ . The equations  $\partial F_l / \partial \mathbf{a} = 0$  can thus be written as a linear system. For example, we take the derivative of  $F_l$  with respect to  $A_{l\theta kmn}$ . We first use Eq.(3.12)-(3.14), and write the derivatives of the contravariant magnetic field,

$$\sqrt{g} \frac{\partial \mathbf{B}}{\partial A_{l\theta kmn}} = -n T_{km}(s) \sin(m\theta - n N_{fp} \phi) \mathbf{e}_s + T'_{km}(s) \cos(m\theta - n N_{fp} \phi) \mathbf{e}_\phi. \quad (\text{A.63})$$

The derivative of the MHD energy functional thus becomes

$$\begin{aligned} \frac{\partial}{\partial A_{l\theta kmn}} \int_{\mathcal{V}_l} \left( \frac{p}{\gamma - 1} + \frac{B^2}{2\mu_0} \right) dv = \\ \int_{\mathcal{V}_l} \frac{\mathbf{B}}{\mu_0 \sqrt{g}} \cdot (-nT_{km}(s) \sin(m\theta - nN_{fp}\phi) \mathbf{e}_s + T'_{km}(s) \cos(m\theta - nN_{fp}\phi) \mathbf{e}_\phi) dv. \end{aligned} \quad (\text{A.64})$$

Similarly, the derivative of the helicity constraint, Eq.(A.57), can be written as

$$\begin{aligned} \frac{\mu_l}{\mu_0} \frac{\partial}{\partial A_{l\theta kmn}} (K - K_l) &= \frac{\mu_l}{\mu_0} \frac{\partial}{\partial A_{l\theta kmn}} \int_{\mathcal{V}_l} \mathbf{A} \cdot \mathbf{B} dv \\ &= \frac{\mu_l}{\mu_0} \int_{\mathcal{V}_l} [T_{km}(s) \nabla \theta \cdot \mathbf{B} + A_\phi T'_{km}(s)] \cos(m\theta - nN_{fp}\phi). \end{aligned} \quad (\text{A.65})$$

The derivative of the toroidal and poloidal flux constraints, Eqs.(A.58)-(A.59), can easily be obtained by considering Eqs.(3.15)-(3.16),

$$b_l \frac{\partial}{\partial A_{l\theta kmn}} \int_{S[\phi=\text{const}]} \mathbf{B} \cdot d\mathbf{S} - \Delta\psi_{t,l} = 2\pi b_l \frac{\partial}{\partial A_{l\theta kmn}} A_{l\theta k00} [T_{k0}(1) - T_{k0}(-1)] \quad (\text{A.66})$$

$$= 2\pi b_l [T_{k0}(1) - T_{k0}(-1)] \delta_{m0} \delta_{n0} \quad (\text{A.67})$$

$$c_l \frac{\partial}{\partial A_{l\theta kmn}} \int_{S[\theta=\text{const}]} \mathbf{B} \cdot d\mathbf{S} - \Delta\psi_{p,l} = -2\pi c_l \frac{\partial}{\partial A_{l\theta kmn}} A_{l\phi k00} [T_{k0}(1) - T_{k0}(-1)] \quad (\text{A.68})$$

$$= 0. \quad (\text{A.69})$$

The derivatives of Eqs.(A.60)-(A.62) with respect to  $A_{l\theta kmn}$  provide

$$\frac{\partial}{\partial A_{l\theta kmn}} \sum_{m=0}^{M_{pol}} \sum_{n=-N_{tor}}^{N_{tor}} d_{lmn} \sum_{k=0}^{L_{rad}} A_{l\theta kmn} T_{km}(-1) = d_{lmn} T_{km}(-1) \quad (\text{A.70})$$

$$\frac{\partial}{\partial A_{l\theta kmn}} \sum_{m=0}^{M_{pol}} \sum_{n=-N_{tor}}^{N_{tor}} e_{lmn} \sum_{k=0}^{L_{rad}} A_{l\phi kmn} T_{km}(-1) = 0 \quad (\text{A.71})$$

$$\begin{aligned} \frac{\partial}{\partial A_{l\theta kmn}} \sum_{m=0}^{M_{pol}} \sum_{n=-N_{tor}}^{N_{tor}} f_{lmn} \sum_{k=0}^{L_{rad}} (-mA_{l\theta kmn} - nA_{l\phi kmn}) T_{km}(1) = -mf_{lmn} T_{km}(1). \end{aligned} \quad (\text{A.72})$$

## Appendix A. Appendices

---

Collecting the derivative of each term, we finally obtain

$$\frac{\partial F_l}{\partial A_{l\theta kmn}} = \int_{\mathcal{V}_l} \frac{\mathbf{B}}{\mu_0 \sqrt{g}} \cdot (-n T_{km}(s) \sin(m\theta - n N_{fp} \phi) \mathbf{e}_s + T'_{km}(s) \cos(m\theta - n N_{fp} \phi) \mathbf{e}_\phi) \quad (\text{A.73})$$

$$+ \frac{\mu_l}{\mu_0} \int_{\mathcal{V}_l} [T_{km}(s) \nabla \theta \cdot \mathbf{B} + A_\phi T'_{km}(s)] \cos(m\theta - n N_{fp} \phi) \quad (\text{A.74})$$

$$+ 2\pi b_l [T_{k0}(1) - T_{k0}(-1)] \delta_{m0} \delta_{n0} \quad (\text{A.75})$$

$$+ d_{lmn} T_{km}(-1) - m f_{lmn} T_{km}(1) = 0, \quad (\text{A.76})$$

which provides a first set of equations. Note that the products  $\mathbf{B} \cdot \mathbf{e}_i$  can be written easily expressed as a linear combination of the  $A_{likmn}$  harmonics. For example, we find

$$\mathbf{B}_l \cdot \mathbf{e}_s = \frac{g_{gg}}{\sqrt{g}} \sum_{k=0}^{L_{rad}} \sum_{m=0}^{M_{pol}} \sum_{n=-N_{tor}}^{N_{tor}} -(m A_{l\phi kmn} + n A_{l\theta kmn}) T_{km}(s) \sin(m\theta - n N_{fp} \phi) \quad (\text{A.77})$$

$$+ \frac{g_{s\theta}}{\sqrt{g}} \sum_{k=0}^{L_{rad}} \sum_{m=0}^{M_{pol}} \sum_{n=-N_{tor}}^{N_{tor}} -A_{l\phi kmn} T'_{km}(s) \cos(m\theta - n N_{fp} \phi) \quad (\text{A.78})$$

$$+ \frac{g_{s\phi}}{\sqrt{g}} \sum_{k=0}^{L_{rad}} \sum_{m=0}^{M_{pol}} \sum_{n=-N_{tor}}^{N_{tor}} A_{l\theta kmn} T'_{km}(s) \cos(m\theta - n N_{fp} \phi), \quad (\text{A.79})$$

where the metric elements  $g_{ij}$  are derived in appendix A.2. Similarly, the derivatives of  $F_l$  with respect to  $A_{l\phi kmn}$ , and with respect to the Lagrange multipliers  $\{a_l, b_l, c_{lmn}, d_{lmn}, e_{lmn}\}$  can be derived. The linear system (A.50) is then constructed by writing

$$\frac{\partial F_l}{\partial \mathbf{a}} = 0. \quad (\text{A.80})$$

## A.5 Linear relation between surface currents and poloidal fluxes

In this appendix we show the linear relation between the surface currents (2.77) and the poloidal fluxes in an MRxMHD equilibrium. We rewrite here Eq.(2.77) for convenience,

$$\mu_0 I_{l,\phi}^s = 2\pi \left[ \left[ \tilde{B}_\theta \right] \right]_l. \quad (\text{A.81})$$

We use general coordinates notation, with  $u^i \equiv \{s, \theta, \phi\}$ ,  $\{\nabla s, \nabla \theta, \nabla \phi\}$  the contravariant basis, and  $\mathbf{e}_i \equiv \{\mathbf{e}_s, \mathbf{e}_\theta, \mathbf{e}_\phi\}$  the covariant basis. This derivation is local to a volume and we drop the subscript  $l$  everywhere for simplicity.

We first show that the surface currents depend linearly on the vector potential degrees of freedom  $\mathbf{a}$ . The contravariant components of the magnetic field are obtained from  $\nabla \times \mathbf{A} = \mathbf{B}$ ,

$$B^k = \frac{\epsilon^{ijk}}{\sqrt{g}} \frac{\partial A_j}{\partial u^i}, \quad (\text{A.82})$$

where  $\epsilon^{ijk}$  is the Levi-Civita tensor,  $\sqrt{g}$  is the jacobian, and the Einstein summation convention has been used. The covariant component of the magnetic field can then easily be expressed by  $B_\theta = g_{k\theta} B^k$ . The  $m = n = 0$  Fourier mode of  $B_\theta$  is then

$$\tilde{B}_\theta = \frac{1}{S} \int_0^{2\pi} \int_0^{2\pi} g_{k\theta} \epsilon^{ijk} \frac{\partial A_j}{\partial u^i} dS, \quad (\text{A.83})$$

with  $S$  the total area of the flux surface, which depends only on geometrical quantities. Derivatives of  $A_j$  are

$$\frac{\partial A_j}{\partial s} = \sum_{m=0}^{M_{pol}} \sum_{n=-N_{tor}}^{N_{tor}} \sum_{k=0}^{L_{rad}} A_{jkmn} T'_k(s) \cos(m\theta - nN_p\phi) \quad (\text{A.84})$$

$$\frac{\partial A_j}{\partial \theta} = \sum_{m=0}^{M_{pol}} \sum_{n=-N_{tor}}^{N_{tor}} \sum_{k=0}^{L_{rad}} -mA_{jkmn} T_k(s) \sin(m\theta - nN_p\phi) \quad (\text{A.85})$$

$$\frac{\partial A_j}{\partial \phi} = \sum_{m=0}^{M_{pol}} \sum_{n=-N_{tor}}^{N_{tor}} \sum_{k=0}^{L_{rad}} nN_p A_{jkmn} T_k(s) \sin(m\theta - nN_p\phi), \quad (\text{A.86})$$

where the prime denotes the derivative with respect to the main argument. Equations (A.83) and (A.84)-(A.86) combined show the linear dependence of  $\tilde{B}_\theta$  on  $\mathbf{a}$ . Finally, the Beltrami equation (3.18) provides a linear relation between  $\mathbf{a}$  and  $\{\Delta\psi_p, \Delta\psi_t, \mu\}$ , as shown in appendix A.4. All relations being linear, this shows that the surface currents depend linearly on the poloidal and toroidal magnetic fluxes.

## A.6 Free-boundary SPEC equilibrium computation with prescribed toroidal current profile

In this appendix, the main differences between a fixed- and free-boundary calculation with the new developed current constraint are outlined. The linear system (3.28) has to be rewritten by extending the arrays  $\boldsymbol{\psi}$  and  $\mathbf{I}$  with two new pairs of scalars: the poloidal and toroidal flux enclosed by the vacuum region,  $(\Delta\psi_{p,V}, \Delta\psi_{t,V})$ , and the net toroidal current at the plasma boundary and the total current flowing through the torus hole,  $(I_{N_{vol}}^s, I_{coil})$ , namely  $\boldsymbol{\psi} \equiv (\Delta\psi_{p,2}, \dots, \Delta\psi_{p,N_{vol}}, \Delta\psi_{p,V}, \Delta\psi_{t,V})^t$  and  $\mathbf{I} \equiv (I_1^s, \dots, I_{N_{vol}}^s, I_{coil})^t$ . Then,

$$\mathbf{M}_{Fr}(\bar{\boldsymbol{\psi}} - \boldsymbol{\psi}) = \bar{\mathbf{I}} - \mathbf{I}, \quad (\text{A.87})$$

with the matrix  $\mathbf{M}_{Fr}$ ,

$$\mathbf{M}_{Fr} = \frac{2\pi}{\mu_0} \begin{bmatrix} \frac{\partial \tilde{B}_{\theta,2}^-}{\partial \Delta\psi_{p,2}} & 0 & \dots & \dots & \dots & 0 \\ \frac{\partial \tilde{B}_{\theta,2}^+}{\partial \Delta\psi_{p,2}} & \frac{\partial \tilde{B}_{\theta,3}^-}{\partial \Delta\psi_{p,3}} & 0 & \dots & \dots & 0 \\ \vdots & \ddots & \ddots & \ddots & \ddots & 0 \\ 0 & 0 & -\frac{\partial \tilde{B}_{\theta,N_{vol}-1}^+}{\partial \Delta\psi_{p,N_{vol}-1}} & \frac{\partial \tilde{B}_{\theta,N_{vol}}^-}{\partial \Delta\psi_{p,N_{vol}}} & 0 & 0 \\ \vdots & \dots & 0 & -\frac{\partial \tilde{B}_{\theta,N_{vol}}^+}{\partial \Delta\psi_{p,N_{vol}}} & \frac{\partial \tilde{B}_{\theta,V}^-}{\partial \Delta\psi_{p,V}} & \frac{\partial \tilde{B}_{\theta,V}^-}{\partial \Delta\psi_{t,V}} \\ 0 & \dots & \dots & 0 & \frac{\partial \tilde{B}_{\phi,V}^-}{\partial \Delta\psi_{p,V}} & \frac{\partial \tilde{B}_{\phi,V}^-}{\partial \Delta\psi_{t,V}} \end{bmatrix}, \quad (\text{A.88})$$

with  $\tilde{B}_{\phi,V}^-$  the  $m = n = 0$  Fourier mode of the covariant toroidal magnetic field on the plasma boundary outer side. Regarding Eq.(3.32), no changes are needed in the plasma volumes. In the vacuum region, however, the toroidal flux is not an input and an additional term is needed,

$$A_{V,i} = \overline{A_{V,i}} - \frac{\partial A_{V,i}}{\partial \Delta\psi_{p,V}} (\overline{\Delta\psi_{p,V}} - \Delta\psi_{p,V}) - \frac{\partial A_{V,i}}{\partial \Delta\psi_{t,V}} (\overline{\Delta\psi_{t,V}} - \Delta\psi_{t,V}), \quad (\text{A.89})$$

where the subscript  $V$  denotes the vacuum region.

Regarding the force gradient, the derivative of the toroidal flux with respect to the geometry is non-zero in the vacuum region. This means that

$$\frac{d\tilde{B}_{\theta,V}^-}{dx_i} = \frac{\partial \tilde{B}_{\theta,V}^-}{\partial x_i} + \frac{\partial \tilde{B}_{\theta,V}^-}{\partial \Delta\psi_{t,V}} \frac{d\Delta\psi_{t,V}}{dx_i} + \frac{\partial \tilde{B}_{\theta,V}^-}{\partial \Delta\psi_{p,V}} \frac{d\Delta\psi_{p,V}}{dx_i}, \quad (\text{A.90})$$

## A.6 Free-boundary SPEC equilibrium computation with prescribed toroidal current profile

---

An additional equation is required for  $\frac{d\Delta\psi_{t,V}}{dx_i}$ , and is provided by

$$\frac{dI_{coil}}{dx_i} = \frac{2\pi}{\mu_0} \left( \frac{\partial \tilde{B}_{V,\phi}^+}{\partial x_i} + \frac{\partial \tilde{B}_{V,\phi}^+}{\partial \Delta\psi_{p,V}} \frac{\partial \Delta\psi_{p,V}}{\partial x_i} + \frac{\partial \tilde{B}_{V,\phi}^+}{\partial \Delta\psi_{t,V}} \frac{\partial \Delta\psi_{t,V}}{\partial x_i} \right) = 0, \quad (\text{A.91})$$

leading to

$$\mathbf{M}_{Fr} \cdot \frac{d}{dx_i} \boldsymbol{\psi} = \frac{2\pi}{\mu_0} \begin{bmatrix} \frac{\partial \tilde{B}_{\theta,1}^+}{\partial x_i} - \frac{\partial \tilde{B}_{\theta,2}^-}{\partial x_i} \\ \vdots \\ \frac{\partial \tilde{B}_{\theta,N_{vol}}^+}{\partial x_i} - \frac{\partial \tilde{B}_{\theta,V}^-}{\partial x_i} \\ - \frac{\partial \tilde{B}_{\phi,V}^-}{\partial x_i} \end{bmatrix} \quad (\text{A.92})$$

## A.7 Analytical derivation of SPEC force gradient in an axisymmetric cylinder

The solution to the Beltrami equation (2.74) in the  $l^{\text{th}}$  volume of an axisymmetric cylinder is (see section 2.2.2)

$$\mathbf{B}_l = [c_{l,1}rJ_1(\mu_l r) + c_{l,2}rY_1(\mu_l r)] \nabla\theta + [c_{l,1}J_0(\mu_l r) + c_{l,2}Y_0(\mu_l r)] \nabla\phi, \quad (\text{A.93})$$

where the usual  $(r, \theta, \phi)$  cylindrical coordinate system has been used,  $J_i$  and  $Y_i$  are the Bessel functions of the  $i^{\text{th}}$  order of the first and second kind, respectively, and  $c_{l,1}$ ,  $c_{l,2}$  are integration constants. Here  $\nabla\theta$  and  $\nabla\phi$  are the contravariant basis vectors.

In addition, since  $B_\theta$  must vanish at the origin, we have that  $c_{1,2} = 0$ . Indeed, the asymptotic expansion of  $Y_1(x)$  close to  $x = 0$  gives (Abramowitz and Stegun, 1965)

$$\lim_{r \rightarrow 0} c_{1,2}rY_1(\mu_1 r) \sim \lim_{r \rightarrow 0} -c_{1,2}r \frac{2}{\pi r} = -\frac{2c_{1,2}}{\pi}, \quad (\text{A.94})$$

which is only zero if  $c_{1,2} = 0$ .

We consider now the case of a screw pinch with three inner volumes,  $N_{\text{vol}} = 3$ . The assumed constrained profiles are the toroidal flux  $\{\Delta\psi_{t,l}\}_{l=1,2,3}$ , the volume current  $\{I_{l,\phi}^v\}_{l=1,2,3}$  and the surface current  $\{I_{l,\phi}^s\}_{l=1,2}$ . The constraint on the toroidal flux is

$$\Delta\psi_{t,l} = \iint_{S_{l,\phi}} \mathbf{B} \cdot \nabla\phi \sqrt{g} dr d\theta \quad (\text{A.95})$$

$$= \int_{R_{l-1}}^{R_l} dr \int_0^{2\pi} d\theta [c_{l,1}J_0(\mu_l r)r + c_{l,2}Y_0(\mu_l r)r] \quad (\text{A.96})$$

$$\equiv 2\pi c_{l,1}\bar{J}_l + 2\pi c_{l,2}\bar{Y}_l, \quad (\text{A.97})$$

where  $\sqrt{g} = r$  is the jacobian and  $S_{l,\phi}$  is a constant- $\phi$  surface in volume  $l$ . The Bessel function integrals have been renamed as  $\bar{J}_l$  and  $\bar{Y}_l$ , and  $R_l$  is the radius of the  $l^{\text{th}}$  interface. The constraints on the currents lead to

$$\mu_0 I_{l,\phi}^v = \frac{\mu_l}{\mu_0} \Delta\psi_{t,l} \quad (\text{A.98})$$

$$\mu_0 I_{l,\phi}^s = 2\pi R_l [c_{l+1,1}J_1(\mu_{l+1}R_l) - c_{l,1}J_1(\mu_l R_l) + c_{l+1,2}Y_1(\mu_{l+1}R_l) - c_{l,2}Y_1(\mu_l R_l)], \quad (\text{A.99})$$



## A.7 Analytical derivation of SPEC force gradient in an axisymmetric cylinder

Solving for  $\{c_{l,1}, c_{l,2}\}$  is equivalent to solving the linear system

$$\begin{bmatrix} \bar{J}_1 & 0 & 0 & 0 & 0 \\ 0 & \bar{J}_2 & \bar{Y}_2 & 0 & 0 \\ 0 & 0 & 0 & \bar{J}_3 & \bar{Y}_3 \\ -J_{111} & J_{121} & Y_{121} & 0 & 0 \\ 0 & -J_{122} & -Y_{122} & J_{132} & Y_{132} \end{bmatrix} \begin{bmatrix} c_{1,1} \\ c_{2,1} \\ c_{2,2} \\ c_{3,1} \\ c_{3,2} \end{bmatrix} = \begin{bmatrix} \Delta\psi_{t,1}/2\pi \\ \Delta\psi_{t,2}/2\pi \\ \Delta\psi_{t,3}/2\pi \\ \mu_0 I_{\phi,1}^s/2\pi R_1 \\ \mu_0 I_{\phi,2}^s/2\pi R_2 \end{bmatrix}, \quad (\text{A.100})$$

with  $J_{ijk} = J_i(\mu_j R_k)$  and  $Y_{ijk} = Y_i(\mu_j R_k)$ . Derivatives of the force  $F_l = [(B_{l+1}(R_l))^2 - (B_l(R_l))^2]/2$  can also be expressed analytically, leading to

$$\frac{\partial F_l}{\partial R_j} = \frac{1}{2} \frac{\partial (B_{l+1}(R_l))^2}{\partial R_j} - \frac{1}{2} \frac{\partial (B_l(R_l))^2}{\partial R_j}, \quad (\text{A.101})$$

with  $l, j \in \{1, 2\}$ . Consider, *e.g.*, the derivative of  $B_l(R_k)$ ,  $k = \{l-1, l\}$ ,

$$[B_l(R_k)]^2 = [c_{l,1}J_{1lk} + c_{l,2}Y_{1lk}]^2 + [c_{l,1}J_{0lk} + c_{l,2}Y_{0lk}]^2 \quad (\text{A.102})$$

$$B_l \frac{\partial B_l}{\partial R_k} = (c_{l,1}J_{1lk} + c_{l,2}Y_{1lk})(c'_{l,1}J_{1lk} + c_{l,1}\mu_l J'_{1lk} + c'_{l,2}Y_{1lk} + c_{l,2}\mu_l Y'_{1lk}) \quad (\text{A.103})$$

$$+ (c_{l,1}J_{0lk} + c_{l,2}Y_{0lk})(c'_{l,0}J_{0lk} + c_{l,2}\mu_l J'_{0lk} + c'_{l,2}Y_{0lk} + c_{l,2}\mu_l Y'_{0lk}) \quad (\text{A.104})$$

where the prime denotes a derivative with respect to the function argument. Finally, all derivatives must be taken at constant  $\psi_{t,l}$ ,  $I_l^{vol}$  and  $I_{\phi,l}^s$ . In particular, the coefficients  $\frac{dc_{l,i}}{dR_k}$  are obtained from derivatives of Eq.(A.100) with respect to  $R_k$ .



# Acknowledgements

The successful completion of this thesis would not have been possible without the unwavering support, encouragement, and guidance from a multitude of individuals who have played a crucial role in my academic journey.

I would like to give a special thanks to my supervisors, Jon and Joaquim. Joaquim, I was honored to be your first Ph.D. student, and I am grateful for the ample time you dedicated to me. Your open-door policy, invaluable guidance, and insightful discussions on physics have shaped me into the researcher I am today. I will forever be grateful for your impact and think of you every time I prepare a presentation, especially when choosing a slide title. Jon, I cannot express enough gratitude for your support and insightful suggestions that have improved my work. I also apologize — or should I say, apologise — for my English, and I promise to adopt British spelling for any future writing endeavors.

I would also like to extend my appreciation to the Swiss Plasma Center direction, Ambrogio, Paolo, and Yves, for providing me with the opportunity to pursue my research. I am also thankful for the administrative support from Edith and Roxane.

A heartfelt thank you to the SPEcTacular team — Stuart, Joaquim, Zhisong, Arunav, Jonathan, Chris, Caoxiang, and Erol — for your technical expertise and emotional support in navigating the intricacies of the SPEC code.

To my friends and colleagues at the Swiss Plasma Center, including Antoine H., Arnas, Louis, Baptiste, Simon, Jean, Margot, my office mates Mike and Erol, Guillaume, Claudia, Antonio, Moahan, Renat, Kyungtak and many others, I thank you for your friendship and stimulating discussions during coffee and lunch breaks. A special shoutout to Louis, who went above and beyond in teaching me how to compile codes on various computers and clusters. Your technical prowess is nothing short of magical.

## Acknowledgements

---

To my wife, Mélanie, I cannot thank you enough for being my rock and constant source of inspiration. Your support and encouragement have been a driving force behind my academic achievements. I am grateful for our wine-filled discussions on obscure physics theories and am looking forward to facing new challenges together. I am sure our life "across the pond" will be as enjoyable as it was these past four years, though with potentially lesser wine quality.

To my parents, Madeleine and Olivier, your constant support and encouragement to pursue my interests have been instrumental in shaping me into the person I am today. Since I was a kid, you fed my never-ending interest for everything — I truly admire you for that, it must have been quite exhausting to answer to my endless questions! I will forever be grateful for your love and support. To my brother, Nicolas, I thank you for your encouragements.

To my friends - Etienne, Cyril, Gaétan, Alexis, Yohan, William, Félix, David, André, and my cousin Jérémie - thank you for your constant support and for keeping me sane throughout this journey. I cannot stress how important it was to have social interactions outside the academic bubble. Thank you.

Finally, I would like to thank everyone who has played a role in my academic journey, no matter how small. Your contributions have not gone unnoticed, and I am grateful for your support.

*Lausanne, April 4, 2023*

A. B.

# Bibliography

- M. Abramowitz and I. A. Stegun, editors. *Handbook of mathematical functions*. Dover Books on Mathematics. Dover Publications, Mineola, NY, June 1965.
- K. Aleynikova, S. Hudson, P. Helander, A. Kumar, J. Geiger, M. Hirsch, J. Loizu, C. Nührenberg, K. Rahbarnia, Z. Qu, Y. Gao, H. Thomsen, Y. Turkin, M. Zanini, and T. W7-X Team. Model for current drive induced crash cycles in W7-X. *Nuclear Fusion*, 61(12):126040, Dec. 2021. ISSN 0029-5515. doi: 10.1088/1741-4326/ac2ab9.
- H. Alfvén. Existence of electromagnetic-hydrodynamic waves. *Nature*, 150(3805):405–406, Oct. 1942.
- R. P. Allan, P. A. Arias, S. Berger, J. G. Canadell, C. Cassou, D. Chen, A. Cherchi, S. L. Connors, E. Coppola, F. A. Cruz, A. Diongue-Niang, F. J. Doblas-Reyes, H. Douville, F. Driouech, T. L. Edwards, F. Engelbrecht, V. Eyring, E. Fischer, G. M. Flato, P. Forster, B. Fox-Kemper, J. S. Fuglestedt, J. C. Fyfe, N. P. Gillett, M. I. Gomis, S. K. Gulev, J. M. Gutiérrez, R. Hamdi, J. Harold, M. Hauser, E. Hawkins, H. T. Hewitt, T. G. Johansen, C. Jones, R. G. Jones, D. S. Kaufman, Z. Klimont, R. E. Kopp, C. Koven, G. Krinner, J.-Y. Lee, I. Lorenzoni, J. Marotzke, V. Masson-Delmotte, T. K. Maycock, M. Meinshausen, P. M. S. Monteiro, A. Morelli, V. Naik, D. Notz, F. Otto, M. D. Palmer, I. Pinto, A. Pirani, G.-K. Plattner, K. Raghavan, R. Ranasinghe, J. Rogelj, M. Rojas, A. C. Ruane, J.-B. Sallée, B. H. Samset, S. I. Seneviratne, J. Sillmann, A. A. Sörensson, T. S. Stephenson, T. Storelvmo, S. Szopa, P. W. Thorne, B. Trewin, R. Vautard, C. Vera, N. Yassaa, S. Zaehle, P. Zhai, X. Zhang, and K. Zickfeld. *Summary for policymakers*, pages 3–32. Cambridge University Press, 2021. doi: 10.1017/9781009157896.001.
- D. V. Anderson, W. A. Cooper, R. Gruber, S. Merazzi, and U. Schwenn. Terpsichore: A three-dimensional ideal magnetohydrodynamic stability program. In J. T. Devreese and P. E. Van Camp, editors, *Scientific Computing on Supercomputers II*, pages 159–174. Springer US, Boston, MA, 1990. doi: 10.1007/978-1-4613-0659-7\_8.
- H. Arbez. Minimization of chaos volume in classical stellarator. Internship, Swiss Plasma Center, SPC, Dec. 2021.

## Bibliography

---

- V. I. Arnold and B. A. Khesin. *Topological Properties of Magnetic and Vorticity Fields*, pages 127–205. Springer International Publishing, Cham, 2021. ISBN 978-3-030-74278-2. doi: 10.1007/978-3-030-74278-2\_3.
- I. P. Bagolin and F. V. Comim. Human Development Index (HDI) and its family of indexes: An evolving critical review. *Revista de Economia*, 34(2):7–28, 2008.
- G. W. Bailey, M. R. Gilbert, and O. Vilkhivskaya. Waste classification assessment of nuclear steels for fusion power applications. *EPJ Web Conf.*, 247:18003, 2021a.
- G. W. Bailey, O. V. Vilkhivskaya, and M. R. Gilbert. Waste expectations of fusion steels under current waste repository criteria. *Nucl. Fusion*, 61(3):036010, Mar. 2021b.
- A. Baillod, J. Loizu, Z. Qu, A. Kumar, and J. Graves. Computation of multi-region, relaxed magnetohydrodynamic equilibria with prescribed toroidal current profile. *Journal of Plasma Physics*, 87(4):905870403, Aug. 2021. ISSN 0022-3778. doi: 10.1017/S0022377821000520.
- A. Baillod, J. Loizu, Z. Qu, H. P. Arbez, and J. P. Graves. Equilibrium  $\beta$ -limits dependence on bootstrap current in classical stellarators. <https://doi.org/10.48550/arXiv.2211.12948>, 2022.
- C. D. Beidler, H. M. Smith, A. Alonso, T. Andreeva, J. Baldzuhn, M. N. A. Beurskens, M. Borchardt, S. A. Bozhnikov, K. J. Brunner, H. Damm, M. Drevlak, O. P. Ford, G. Fuchert, J. Geiger, P. Helander, U. Hergenbahn, M. Hirsch, U. Höfel, Y. O. Kazakov, R. Kleiber, M. Krychowiak, S. Kwak, A. Langenberg, H. P. Laqua, U. Neuner, N. A. Pablant, E. Pasch, A. Pavone, T. S. Pedersen, K. Rahbarnia, J. Schilling, E. R. Scott, T. Stange, J. Svensson, H. Thomsen, Y. Turkin, F. Warmer, R. C. Wolf, and D. Zhang. Demonstration of reduced neoclassical energy transport in Wendelstein 7-X. *Nature*, 596(7871):221–226, Aug. 2021. ISSN 1476-4687. doi: 10.1038/s41586-021-03687-w.
- M. A. Berger. Introduction to magnetic helicity. *Plasma Physics and Controlled Fusion*, 41(12B):B167–B175, Dec. 1999. ISSN 0741-3335, 1361-6587. doi: 10.1088/0741-3335/41/12B/312.
- O. Betancourt. BETAS, a spectral code for three-dimensional magnetohydrodynamic equilibrium and nonlinear stability calculations. *Communications on Pure and Applied Mathematics*, 41(5):551–568, July 1988. ISSN 00103640. doi: 10.1002/cpa.3160410504.
- A. Bhattacharjee, T. Hayashi, C. C. Hegna, N. Nakajima, and T. Sato. Theory of pressure-induced islands and self-healing in three-dimensional toroidal magnetohydrodynamic equilibria. *Physics of Plasmas*, 2(3):883–888, 1995. ISSN 1070664X. doi: 10.1063/1.871369.
- M. Biggeri and V. Mauro. Towards a more ‘Sustainable’ Human Development Index: Integrating the environment and freedom. *Ecological Indicators*, 91:220–231, Aug. 2018. ISSN 1470-160X. doi: 10.1016/j.ecolind.2018.03.045.

- B. Bishop. National Ignition Facility achieves fusion ignition | Lawrence Livermore National Laboratory. <https://www.llnl.gov/news/national-ignition-facility-achieves-fusion-ignition>, 12 2022.
- A. H. Boozer. Transport and isomorphic equilibria. *The Physics of Fluids*, 26(2):496–499, Feb. 1983. ISSN 0031-9171. doi: 10.1063/1.864166.
- A. H. Boozer and H. J. Gardner. The bootstrap current in stellarators. *Physics of Fluids B*, 2(10):2408–2421, 1990. ISSN 08998221. doi: 10.1063/1.859506.
- BP. BP Statistical Review of World Energy 2020, 2020.
- S. I. Braginskii. Transport Processes in a Plasma. *Reviews of Plasma Physics*, 1:205, 1965.
- O. P. Bruno and P. Laurence. Existence of three-dimensional toroidal MHD equilibria with nonconstant pressure. *Communications on Pure and Applied Mathematics*, 49(7): 717–764, July 1996. ISSN 00103640.
- A. Carlton-Jones, E. J. Paul, and W. Dorland. Computing the shape gradient of stellarator coil complexity with respect to the plasma boundary. *Journal of Plasma Physics*, 87(2): 905870222, Apr. 2021. ISSN 0022-3778, 1469-7807. doi: 10.1017/S0022377821000386.
- J. R. Cary and J. D. Hanson. Stochasticity reduction. *Physics of Fluids*, 29(8):2464, 1986. ISSN 00319171. doi: 10.1063/1.865539.
- J. R. Cary and M. Kotschenreuther. Pressure induced islands in three-dimensional toroidal plasma. *Physics of Fluids*, 28(5):1392–1401, 1985. ISSN 10706631. doi: 10.1063/1.864973.
- C. S. Chang and S. Ku. Spontaneous rotation sources in a quiescent tokamak edge plasma. *Phys. Plasmas*, 15(6):062510, June 2008.
- C. S. Chang, S. Ku, P. H. Diamond, Z. Lin, S. Parker, T. S. Hahm, and N. Samatova. Compressed ion temperature gradient turbulence in diverted tokamak edge. *Phys. Plasmas*, 16(5):056108, May 2009.
- B. V. Chirikov. A universal instability of many-dimensional oscillator systems. *Physics Reports*, 52(5):263–379, 1979. ISSN 03701573. doi: 10.1016/0370-1573(79)90023-1.
- M. Coronado and H. Wobig. On the definition of Pfirsch–Schlüter and bootstrap currents in toroidal systems. *Physics of Fluids B: Plasma Physics*, 4(5):1294–1300, May 1992. ISSN 0899-8221. doi: 10.1063/1.860085.
- O. Czarny and G. Huysmans. Bézier surfaces and finite elements for MHD simulations. *J. Comput. Phys.*, 227(16):7423–7445, Aug. 2008.

- J. Degraeve, F. Felici, J. Buchli, M. Neunert, B. Tracey, F. Carpanese, T. Ewalds, R. Hafner, A. Abdolmaleki, D. de las Casas, C. Donner, L. Fritz, C. Galperti, A. Huber, J. Keeling, M. Tsimpoukelli, J. Kay, A. Merle, J.-M. Moret, S. Noury, F. Pesamosca, D. Pfau, O. Sauter, C. Sommariva, S. Coda, B. Duval, A. Fasoli, P. Kohli, K. Kavukcuoglu, D. Hassabis, and M. Riedmiller. Magnetic control of tokamak plasmas through deep reinforcement learning. *Nature*, 602(7897):414–419, Feb. 2022. ISSN 1476-4687. doi: 10.1038/s41586-021-04301-9.
- G. R. Dennis, S. R. Hudson, D. Terranova, P. Franz, R. L. Dewar, and M. J. Hole. Minimally constrained model of self-organized helical states in reversed-field pinches. *Physical Review Letters*, 111(5):055003, 2013. ISSN 00319007. doi: 10.1103/PhysRevLett.111.055003.
- G. R. Dennis, S. R. Hudson, R. L. Dewar, and M. J. Hole. Multi-region relaxed magnetohydrodynamics with anisotropy and flow. *Physics of Plasmas*, 21(7):072512, 2014. ISSN 10897674. doi: 10.1063/1.4890847.
- K. Dervis and J. Klugman. Measuring human progress: the contribution of the Human Development Index and related indices. *Revue d'économie politique*, 121(1):73–92, 2011. ISSN 0373-2630. doi: 10.3917/redp.211.0073.
- R. Dewar and S. Hudson. Stellarator symmetry. *Physica D: Nonlinear Phenomena*, 112(1-2):275–280, Jan. 1998. ISSN 01672789. doi: 10.1016/S0167-2789(97)00216-9.
- R. L. Dewar, S. R. Hudson, and P. F. Price. Almost invariant manifolds for divergence-free fields. *Physics Letters A*, 194(1):49–56, Oct. 1994. ISSN 0375-9601. doi: 10.1016/0375-9601(94)00707-V.
- R. L. Dewar, Z. Yoshida, A. Bhattacharjee, and S. R. Hudson. Variational formulation of relaxed and multi-region relaxed magnetohydrodynamics. *Journal of Plasma Physics*, 81(6):515810604, 2015. ISSN 14697807. doi: 10.1017/S0022377815001336.
- P. H. Diamond, C. J. McDevitt, Ö. D. Gürçan, T. S. Hahm, W. X. Wang, E. S. Yoon, I. Holod, Z. Lin, V. Naulin, and R. Singh. Physics of non-diffusive turbulent transport of momentum and the origins of spontaneous rotation in tokamaks. *Nuclear Fusion*, 49(4):045002, Mar. 2009. ISSN 0029-5515. doi: 10.1088/0029-5515/49/4/045002.
- A. Dinklage, E. Ascasíbar, C. D. Beidler, R. Brakel, J. Geiger, J. H. Harris, A. Kus, S. Murakami, S. Okamura, R. Preuss, F. Sano, U. Stroth, Y. Suzuki, J. Talmadge, V. Tribaldos, K. Y. Watanabe, A. Weller, H. Yamada, and M. Yokoyama. Assessment of Global Stellarator Confinement: Status of the International Stellarator Confinement Database. *Fusion Science and Technology*, 51(1):1–7, Jan. 2007. ISSN 1536-1055, 1943-7641. doi: 10.13182/FST07-A1281.
- M. Drevlak, D. Monticello, and A. Reiman. PIES free boundary stellarator equilibria with improved initial conditions. *Nuclear Fusion*, 45(7):731–740, 2005. ISSN 00295515. doi: 10.1088/0029-5515/45/7/022.



- M. Drevlak, C. Beidler, J. Geiger, P. Helander, and Y. Turkin. Optimisation of stellarator equilibria with ROSE. *Nuclear Fusion*, 59(1):016010, Jan. 2019. ISSN 0029-5515. doi: 10.1088/1741-4326/aaed50.
- D. W. Dudt and E. Kolemen. DESC: A stellarator equilibrium solver. *Physics of Plasmas*, 27(10):102513, Oct. 2020. ISSN 1070-664X. doi: 10.1063/5.0020743.
- K. Dungan, G. Butler, F. Livens, and L. Warren. Uranium from seawater - Infinite resource or improbable aspiration? | Elsevier Enhanced Reader. *Progress in Nuclear Energy*, 99:81–85, 2017. doi: 10.1016/j.pnucene.2017.04.016.
- J. M. Faustin, W. A. Cooper, J. P. Graves, D. Pfefferlé, and J. Geiger. Fast particle loss channels in Wendelstein 7-X. *Nucl. Fusion*, 56(9):092006, Sept. 2016a.
- J. M. Faustin, W. A. Cooper, J. P. Graves, D. Pfefferlé, and J. Geiger. ICRH induced particle losses in Wendelstein 7-X. *Plasma Phys. Control. Fusion*, 58(7):074004, July 2016b.
- B. Fornberg. Generation of Finite Difference Formulas on Arbitrarily Spaced Grids. *Mathematics of Computation*, 51(184):699–706, 1988. ISSN 00255718. doi: 10.2307/2008770.
- J. P. Freidberg. Single-particle motion in a plasma – guiding center theory. In *Plasma Physics and Fusion Energy*, pages 139–182. Cambridge University Press, Cambridge, 2007. doi: 10.1017/CBO9780511755705.010.
- J. P. Freidberg. *Ideal MHD*. Cambridge University Press, Cambridge, 2014. ISBN 978-0-511-79504-6. doi: 10.1017/CBO9780511795046.
- J. Geiger, C. D. Beidler, M. Drevlak, H. Maaßberg, C. Nührenberg, Y. Suzuki, and Y. Turkin. Effects of Net Currents on the Magnetic Configuration of W7-X. *Contributions to Plasma Physics*, 50(8):770–774, 2010. ISSN 08631042. doi: 10.1002/ctpp.200900028.
- J. Geiger, C. D. Beidler, Y. Feng, H. Maaßberg, N. B. Marushchenko, and Y. Turkin. Physics in the magnetic configuration space of W7-X. *Plasma Physics and Controlled Fusion*, 57(1):014004, Jan. 2015. ISSN 0741-3335. doi: 10.1088/0741-3335/57/1/014004.
- E. Gibney. Nuclear-fusion reactor smashes energy record. *Nature*, 602(7897):371–371, Feb. 2022. doi: 10.1038/d41586-022-00391-1.
- M. R. Gilbert, T. Eade, C. Bachmann, U. Fischer, and N. P. Taylor. Activation, decay heat, and waste classification studies of the european DEMO concept. *Nucl. Fusion*, 57(4):046015, Apr. 2017.
- M. R. Gilbert, T. Eade, T. Rey, R. Vale, C. Bachmann, U. Fischer, and N. P. Taylor. Waste implications from minor impurities in european DEMO materials. *Nucl. Fusion*, 59(7):076015, July 2019.

## Bibliography

---

- A. Giuliani, F. Wechsung, A. Cerfon, G. Stadler, and M. Landreman. Single-stage gradient-based stellarator coil design: Optimization for near-axis quasi-symmetry. *Journal of Computational Physics*, 459:111147, June 2022. ISSN 0021-9991. doi: 10.1016/j.jcp.2022.111147.
- S. M. Gonzalez de Vicente, N. A. Smith, L. El-Guebaly, S. Ciattaglia, L. Di Pace, M. Gilbert, R. Mandoki, S. Rosanvallon, Y. Someya, K. Tobita, and D. Torcy. Overview on the management of radioactive waste from fusion facilities: ITER, demonstration machines and power plants. *Nucl. Fusion*, 62(8):085001, Aug. 2022.
- A. Goodman, K. C. Mata, S. A. Henneberg, R. Jorge, M. Landreman, G. Plunk, H. Smith, R. Mackenbach, and P. Helander. Constructing precisely quasi-isodynamic magnetic fields. <https://arxiv.org/abs/2211.09829>, 2022.
- H. Grad. Toroidal containment of a plasma. *The Physics of Fluids*, 10(1):137–154, 1967. ISSN 10706631. doi: 10.1063/1.1761965.
- H. Grad and H. Rubin. Hydromagnetic equilibria and force-free fields. *Journal of Nuclear Energy (1954)*, 7(3-4):284–285, Sept. 1958. ISSN 08913919. doi: 10.1016/0891-3919(58)90139-6.
- J. M. Greene. Two-Dimensional Measure-Preserving Mappings. *Journal of Mathematical Physics*, 9(5):760–768, May 1968. ISSN 0022-2488. doi: 10.1063/1.1664639.
- J. M. Greene. A method for determining a stochastic transition. *Journal of Mathematical Physics*, 20(6):1183–1201, June 1979. ISSN 0022-2488. doi: 10.1063/1.524170.
- H. S. Greenside, A. H. Reiman, and A. Salas. Convergence properties of a nonvariational 3D MHD equilibrium code. *Journal of Computational Physics*, 81(1):102–136, Mar. 1989. ISSN 0021-9991. doi: 10.1016/0021-9991(89)90066-1.
- G. Grieger, H. Renner, and H. Wobig. Wendelstein stellarators. *Nuclear Fusion*, 25(9):1231–1242, 1985. ISSN 17414326. doi: 10.1088/0029-5515/25/9/040.
- J. D. Hanson. The virtual-casing principle and Helmholtz’s theorem. *Plasma Physics and Controlled Fusion*, 57(11), 2015. ISSN 13616587. doi: 10.1088/0741-3335/57/11/115006.
- J. D. Hanson and J. R. Cary. Elimination of stochasticity in stellarators. *Physics of Fluids*, 27(4):767, 1984. ISSN 00319171. doi: 10.1063/1.864692.
- J. D. Hanson, S. P. Hirshman, S. F. Knowlton, L. L. Lao, E. A. Lazarus, and J. M. Shields. V3FIT: A code for three-dimensional equilibrium reconstruction. *Nuclear Fusion*, 49(7):075031, 2009. ISSN 00295515. doi: 10.1088/0029-5515/49/7/075031.
- K. Harafuji, T. Hayashi, and T. Sato. Computational study of three-dimensional magnetohydrodynamic equilibria in toroidal helical systems. *Journal of Computational Physics*, 81(1):169–192, 1989. ISSN 10902716. doi: 10.1016/0021-9991(89)90069-7.

- W. W. Heidbrink and T. H. Dang. Magnetic helicity is conserved at a tokamak sawtooth crash. *Plasma Physics and Controlled Fusion*, 42(12), 2000. ISSN 07413335. doi: 10.1088/0741-3335/42/12/101.
- P. Helander. Theory of plasma confinement in non-axisymmetric magnetic fields. *Reports on Progress in Physics*, 77(8):087001, July 2014. ISSN 0034-4885. doi: 10.1088/0034-4885/77/8/087001.
- P. Helander and D. J. Sigmar. *Collisional Transport in Magnetized Plasmas*. Cambridge University Press, Cambridge ; New York, Jan. 2002. ISBN 978-0-521-80798-2.
- P. Helander and A. N. Simakov. Intrinsic Ambipolarity and Rotation in Stellarators. *Physical Review Letters*, 101(14):145003, Sept. 2008. doi: 10.1103/PhysRevLett.101.145003.
- P. Helander, J. Geiger, and H. Maaßberg. On the bootstrap current in stellarators and tokamaks. *Physics of Plasmas*, 18(9), 2011. ISSN 1070664X. doi: 10.1063/1.3633940.
- P. Helander, M. Drevlak, M. Zarnstorff, and S. C. Cowley. Stellarators with permanent magnets. *Physical Review Letters*, 124(9):95001, 2019. ISSN 1079-7114. doi: 10.1103/PhysRevLett.124.095001.
- S. A. Henneberg, M. Drevlak, C. Nührenberg, C. Beidler, Y. Turkin, J. Loizu, and P. Helander. Properties of a new quasi-axisymmetric configuration. *Nuclear Fusion*, 59(2):026014, Feb. 2019. ISSN 0029-5515. doi: 10.1088/1741-4326/aaf604.
- S. A. Henneberg, P. Helander, and M. Drevlak. Representing the boundary of stellarator plasmas. *Journal of Plasma Physics*, 87(5):905870503, Oct. 2021a. ISSN 0022-3778. doi: 10.1017/S0022377821000891.
- S. A. Henneberg, S. R. Hudson, D. Pfefferlé, and P. Helander. Combined plasma-coil optimization algorithms. *Journal of Plasma Physics*, 87(2):905870226, 2021b. ISSN 0022-3778. doi: 10.1017/S0022377821000271.
- M. Hirsch, J. Baldzuhn, C. Beidler, R. Brakel, R. Burhenn, A. Dinklage, H. Ehmler, M. Endler, V. Erckmann, Y. Feng, J. Geiger, L. Giannone, G. Grieger, P. Grigull, H. J. Hartfuß, D. Hartmann, R. Jaenicke, R. König, H. P. Laqua, H. Maaßberg, K. McCormick, F. Sardei, E. Speth, U. Stroth, F. Wagner, A. Weller, A. Werner, H. Wobig, and S. Zoletnik. Major results from the stellarator Wendelstein 7-AS. *Plasma Physics and Controlled Fusion*, 50(5):053001, May 2008. ISSN 07413335. doi: 10.1088/0741-3335/50/5/053001.
- S. Hirshman, W. van RIJ, and P. Merkel. Three-dimensional free boundary calculations using a spectral Green’s function method. *Computer Physics Communications*, 43(1): 143–155, Dec. 1986a. ISSN 00104655. doi: 10.1016/0010-4655(86)90058-5.

## Bibliography

---

- S. P. Hirshman. Steepest-descent moment method for three-dimensional magnetohydrodynamic equilibria. *Physics of Fluids*, 26(12):3553, 1983. ISSN 00319171. doi: 10.1063/1.864116.
- S. P. Hirshman and J. Breslau. Explicit spectrally optimized Fourier series for nested magnetic surfaces. *Physics of Plasmas*, 5(7):2664–2675, July 1998. ISSN 1070-664X, 1089-7674. doi: 10.1063/1.872954.
- S. P. Hirshman and H. K. Meier. Optimized Fourier representations for three-dimensional magnetic surfaces. *The Physics of Fluids*, 28(1387):6, 1985. doi: 10.1063/1.864972.
- S. P. Hirshman and H. Weitzner. A convergent spectral representation for three-dimensional inverse magnetohydrodynamic equilibria. *Physics of Fluids*, 28(4):1207, 1985. ISSN 00319171. doi: 10.1063/1.864998.
- S. P. Hirshman, K. C. Shaing, W. I. van Rij, C. O. Beasley, and E. C. Crume. Plasma transport coefficients for nonsymmetric toroidal confinement systems. *The Physics of Fluids*, 29(9):2951–2959, 1986b. doi: 10.1063/1.865495.
- S. P. Hirshman, R. Sanchez, and C. R. Cook. SIESTA: A scalable iterative equilibrium solver for toroidal applications. *Physics of Plasmas*, 18(6):062504, June 2011. ISSN 1070-664X. doi: 10.1063/1.3597155.
- M. Hoelzl, G. T. A. Huijsmans, S. J. P. Pamela, M. Bécoulet, E. Nardon, F. J. Artola, B. Nkonga, C. V. Atanasiu, V. Bandaru, A. Bhole, D. Bonfiglio, A. Cathey, O. Czarny, A. Dvornova, T. Fehér, A. Fil, E. Franck, S. Futatani, M. Gruca, H. Guillard, J. W. Haverkort, I. Holod, D. Hu, S. K. Kim, S. Q. Korving, L. Kos, I. Krebs, L. Kripner, G. Latu, F. Liu, P. Merkel, D. Meshcheriakov, V. Mitterauer, S. Mochalskyy, J. A. Morales, R. Nies, N. Nikulsin, F. Orain, J. Pratt, R. Ramasamy, P. Ramet, C. Reux, K. Särkimäki, N. Schwarz, P. Singh Verma, S. F. Smith, C. Sommariva, E. Strumberger, D. C. van Vugt, M. Verbeek, E. Westerhof, F. Wieschollek, and J. Zielinski. The JOREK non-linear extended MHD code and applications to large-scale instabilities and their control in magnetically confined fusion plasmas. *Nucl. Fusion*, 61(6):065001, June 2021.
- M. J. Hole, S. R. Hudson, and R. L. Dewar. Stepped pressure profile equilibria in cylindrical plasmas via partial Taylor relaxation. *Journal of Plasma Physics*, 72(6):1167–1171, 2006. ISSN 00223778. doi: 10.1017/S0022377806005861.
- Y.-M. Huang, S. R. Hudson, J. Loizu, Y. Zhou, and A. Bhattacharjee. Numerical study of  $\delta$ -function current sheets arising from resonant magnetic perturbations. *Physics of Plasmas*, 29(3):032513, Mar. 2022. doi: 10.1063/5.0067898.
- Y.-m. Huang, S. R. Hudson, J. Loizu, Y. Zhou, and A. Bhattacharjee. Structure of pressure-gradient-driven current singularity in ideal magnetohydrodynamic equilibrium. (in press), 2023.

- S. R. Hudson and J. Breslau. Temperature contours and ghost surfaces for chaotic magnetic fields. *Physical Review Letters*, 100(9):1–4, 2008. ISSN 00319007. doi: 10.1103/PhysRevLett.100.095001.
- S. R. Hudson and R. L. Dewar. Almost-invariant surfaces for magnetic field-line flows. *Journal of Plasma Physics*, 56(2):361–382, Oct. 1996. ISSN 1469-7807, 0022-3778. doi: 10.1017/S0022377800019309.
- S. R. Hudson and R. L. Dewar. Construction of an integrable field close to any non-integrable toroidal magnetic field. *Physics Letters A*, 247(3):246–251, Oct. 1998. ISSN 0375-9601. doi: 10.1016/S0375-9601(98)00558-1.
- S. R. Hudson and R. L. Dewar. Are ghost surfaces quadratic-flux-minimizing? *Physics Letters A*, 373(48):4409–4415, Dec. 2009. ISSN 0375-9601. doi: 10.1016/j.physleta.2009.10.005.
- S. R. Hudson and B. F. Kraus. Three-dimensional magnetohydrodynamic equilibria with continuous magnetic fields. *Journal of Plasma Physics*, 83(4):715830403, 2017. ISSN 0022-3778. doi: 10.1017/s0022377817000538.
- S. R. Hudson and N. Nakajima. Pressure, chaotic magnetic fields, and magnetohydrodynamic equilibria. *Physics of Plasmas*, 17(5):052511, May 2010. ISSN 1070664X. doi: 10.1063/1.3431090.
- S. R. Hudson, D. A. Monticello, A. H. Reiman, A. H. Boozer, D. J. Strickler, S. P. Hirshman, and M. C. Zarnstorff. Eliminating Islands in High-Pressure Free-Boundary Stellarator Magnetohydrodynamic Equilibrium Solutions. *Physical Review Letters*, 89(27):275003, Dec. 2002. ISSN 0031-9007. doi: 10.1103/PhysRevLett.89.275003.
- S. R. Hudson, R. L. Dewar, G. Dennis, M. J. Hole, M. McGann, G. von Nessi, and S. Lazerson. Computation of multi-region relaxed magnetohydrodynamic equilibria. *Physics of Plasmas*, 19(11):112502, Nov. 2012a. ISSN 1070-664X. doi: 10.1063/1.4765691.
- S. R. Hudson, R. L. Dewar, M. J. Hole, and M. McGann. Non-axisymmetric, multi-region relaxed magnetohydrodynamic equilibrium solutions. *Plasma Physics and Controlled Fusion*, 54:014005, 2012b. doi: 10.1088/0741-3335/54/1/014005.
- S. R. Hudson, J. Loizu, C. Zhu, Z. S. Qu, C. Nührenberg, S. Lazerson, C. B. Smiet, and M. J. Hole. Free-boundary MRxMHD equilibrium calculations using the stepped-pressure equilibrium code. *Plasma Physics and Controlled Fusion*, 62(8):084002, Aug. 2020. ISSN 0741-3335. doi: 10.1088/1361-6587/ab9a61.
- G. T. A. Huysmans and O. Czarny. MHD stability in x-point geometry: simulation of ELMs. *Nucl. Fusion*, 47(7):659–666, July 2007.

- T. Klinger, T. Andreeva, S. Bozhenkov, C. Brandt, R. Burhenn, B. Buttenschön, G. Fuchert, B. Geiger, O. Grulke, H. Laqua, N. Pablant, K. Rahbarnia, T. Stange, A. von Stechow, N. Tamura, H. Thomsen, Y. Turkin, T. Wegner, I. Abramovic, S. Äkäslompolo, J. Alcuson, P. Aleynikov, K. Aleynikova, A. Ali, A. Alonso, G. Anda, E. Ascasibar, J. Bähner, S. Baek, M. Balden, J. Baldzuhn, M. Banduch, T. Barbui, W. Behr, C. Beidler, A. Benndorf, C. Biedermann, W. Biel, B. Blackwell, E. Blanco, M. Blatzheim, S. Ballinger, T. Bluhm, D. Böckenhoff, B. Böswirth, L.-G. Böttger, M. Borchardt, V. Borsuk, J. Boscary, H.-S. Bosch, M. Beurskens, R. Brakel, H. Brand, T. Bräuer, H. Braune, S. Brezinsek, K.-J. Brunner, R. Bussiahn, V. Bykov, J. Cai, I. Calvo, B. Cannas, A. Cappa, A. Carls, D. Carralero, L. Carraro, B. Carvalho, F. Castejon, A. Charl, N. Chaudhary, D. Chauvin, F. Chernyshev, M. Cianciosa, R. Citarella, G. Claps, J. Coenen, M. Cole, M. Cole, F. Cordella, G. Cseh, A. Czarnecka, K. Czerski, M. Czerwinski, G. Czymek, A. da Molin, A. da Silva, H. Damm, A. de la Pena, S. Degenkolbe, C. Dhard, M. Dibon, A. Dinklage, T. Dittmar, M. Drevlak, P. Drewelow, P. Drews, F. Durodie, E. Edlund, P. van Eeten, F. Effenberg, G. Ehrke, S. Elgeti, M. Endler, D. Ennis, H. Esteban, T. Estrada, J. Fellingner, Y. Feng, E. Flom, H. Fernandes, W. Fietz, W. Figacz, J. Fontdecaba, O. Ford, T. Fornal, H. Frerichs, A. Freund, T. Funaba, A. Galkowski, G. Gantenbein, Y. Gao, J. García Regaña, D. Gates, J. Geiger, V. Giannella, A. Gogoleva, B. Goncalves, A. Gorlaev, D. Gradic, M. Grahl, J. Green, H. Greuner, A. Grosman, H. Grote, M. Gruca, C. Guerard, P. Hacker, X. Han, J. Harris, D. Hartmann, D. Hathiramani, B. Hein, B. Heinemann, P. Helander, S. A. Henneberg, M. Henkel, J. Hernandez Sanchez, C. Hidalgo, M. Hirsch, K. Hollfeld, U. Höfel, A. Hölting, D. Höschen, M. Houry, J. Howard, X. Huang, Z. Huang, M. Hubeny, M. Huber, H. Hunger, K. Ida, T. Ilkei, S. Illy, B. Israeli, S. Jablonski, M. Jakubowski, J. Jelonnek, H. Jenzsch, T. Jesche, M. Jia, P. Jungmanns, J. Kacmarczyk, J.-P. Kallmeyer, U. Kamionka, H. Kasahara, W. Kasperek, Y. Kazakov, N. Kenmochi, C. Killer, A. Kirschner, R. Kleiber, J. Knauer, M. Knaup, A. Knieps, T. Kobarg, G. Kocsis, F. Köchl, Y. Kolesnichenko, A. Könies, R. König, P. Kornejew, J.-P. Koschinsky, F. Köster, M. Krämer, R. Krampitz, A. Krämer-Flecken, N. Krawczyk, T. Kremeyer, J. Krom, M. Krychowiak, I. Ksiazek, M. Kubkowska, G. Kühner, T. Kurki-Suonio, P. Kurz, S. Kwak, M. Landreman, P. Lang, R. Lang, A. Langenberg, S. Langish, H. Laqua, R. Laube, S. Lazerson, C. Lechte, M. Lennartz, W. Leonhardt, C. Li, C. Li, Y. Li, Y. Liang, C. Linsmeier, S. Liu, J.-F. Lobsien, D. Loesser, J. Loizu Cisquilla, J. Lore, A. Lorenz, M. Losert, A. Lücke, A. Lumsdaine, V. Lutsenko, H. Maaßberg, O. Marchuk, J. Matthew, S. Marsen, M. Marushchenko, S. Masuzaki, D. Maurer, M. Mayer, K. McCarthy, P. McNeely, A. Meier, D. Mellein, B. Mendelevitch, P. Mertens, D. Mikkelsen, A. Mishchenko, B. Missal, J. Mittelstaedt, T. Mizuuchi, A. Mollen, V. Moncada, T. Mönnich, T. Morisaki, D. Moseev, S. Murakami, G. Náfrádi, M. Nagel, D. Naujoks, H. Neilson, R. Neu, O. Neubauer, U. Neuner, T. Ngo, D. Nicolai, S. Nielsen, H. Niemann, T. Nishizawa, R. Nocentini, C. Nührenberg, J. Nührenberg, S. Obermayer, G. Offermanns, K. Ogawa, J. Ölmanns, J. Ongena, J. Oosterbeek, G. Orozco, M. Otte, L. Pacios Rodriguez, N. Panadero,

- N. Panadero Alvarez, D. Papenfuß, S. Paqay, E. Pasch, A. Pavone, E. Pawelec, T. Pedersen, G. Pelka, V. Perseo, B. Peterson, D. Pilopp, S. Pingel, F. Pisano, B. Plaum, G. Plunk, P. Pölöskei, M. Porkolab, J. Proll, M.-E. Puiatti, A. Puig Sitjes, F. Purps, M. Rack, S. Récssei, A. Reiman, F. Reimold, D. Reiter, F. Remppel, S. Renard, R. Riedl, J. Riemann, K. Risse, V. Rohde, H. Röhlinger, M. Romé, D. Rondeshagen, P. Rong, B. Roth, L. Rudischhauser, K. Rummel, T. Rummel, A. Runov, N. Rust, L. Ryc, S. Ryosuke, R. Sakamoto, M. Salewski, A. Samartsev, E. Sanchez, F. Sano, S. Satake, J. Schacht, G. Satheeswaran, F. Schauer, T. Scherer, J. Schilling, A. Schlaich, G. Schlisio, F. Schluck, K.-H. Schlüter, J. Schmitt, H. Schmitz, O. Schmitz, S. Schmuck, M. Schneider, W. Schneider, P. Scholz, R. Schrittwieser, M. Schröder, T. Schröder, R. Schroeder, H. Schumacher, B. Schweer, E. Scott, S. Sereda, B. Shanahan, M. Sibia, P. Sinha, S. Sipliä, C. Slaby, M. Slecza, H. Smith, W. Spiess, D. Spong, A. Spring, R. Stadler, M. Stejner, L. Stephey, U. Stridde, C. Suzuki, J. Svensson, V. Szabó, T. Szabolcs, T. Szepesi, Z. Szökefalvi-Nagy, A. Tancetti, J. Terry, J. Thomas, M. Thumm, J. Traverso, P. Traverso, J. Tretter, H. Trimino Mora, H. Tsuchiya, T. Tsujimura, S. Tulipán, B. Unterberg, I. Vakulchyk, S. Valet, L. Vano, B. van Milligen, A. van Vuuren, L. Vela, J.-L. Velasco, M. Vergote, M. Vervier, N. Vianello, H. Viebke, R. Vilbrandt, A. Vorköper, S. Wadle, F. Wagner, E. Wang, N. Wang, Z. Wang, F. Warmer, T. Wauters, L. Wegener, J. Weggen, Y. Wei, G. Weir, J. Wendorf, U. Wenzel, A. Werner, A. White, B. Wiegel, F. Wilde, T. Windisch, M. Winkler, A. Winter, V. Winters, S. Wolf, R. Wolf, A. Wright, G. Wurden, P. Xanthopoulos, H. Yamada, I. Yamada, R. Yasuhara, M. Yokoyama, M. Zanini, M. Zarnstorff, A. Zeitler, D. Zhang, H. Zhang, J. Zhu, M. Zilker, A. Zocco, S. Zoletnik, and M. Zuin. Overview of first Wendelstein 7-X high-performance operation. *Nuclear Fusion*, 59(11):112004, Nov. 2019. ISSN 0029-5515, 1741-4326. doi: 10.1088/1741-4326/ab03a7.
- M. D. Kruskal and R. M. Kulsrud. Equilibrium of a Magnetically Confined Plasma in a Toroid. *The Physics of Fluids*, 1(4):265–274, July 1958. ISSN 0031-9171. doi: 10.1063/1.1705884.
- A. Kumar, Z. Qu, M. J. Hole, A. M. Wright, J. Loizu, S. R. Hudson, A. Baillod, R. L. Dewar, and N. M. Ferraro. Computation of linear MHD instabilities with the multi-region relaxed MHD energy principle. *Plasma Physics and Controlled Fusion*, 63(4), 2021. ISSN 13616587. doi: 10.1088/1361-6587/abdbd0.
- A. Kumar, C. Nührenberg, Z. Qu, M. J. Hole, J. Doak, R. L. Dewar, S. R. Hudson, J. Loizu, K. Aleynikova, A. Baillod, and H. Hezaveh. Nature of ideal MHD instabilities as described by multi-region relaxed MHD. *Plasma Physics and Controlled Fusion*, 64(6), 2022. ISSN 13616587. doi: 10.1088/1361-6587/ac53ee.
- M. Landreman. Booz\_xform documentation. [https://hiddensymmetries.github.io/booz\\_xform/](https://hiddensymmetries.github.io/booz_xform/), 2022.
- M. Landreman and E. Paul. Magnetic Fields with Precise Quasisymmetry for Plasma

## Bibliography

---

- Confinement. *Physical Review Letters*, 128(3):35001, 2022. ISSN 10797114. doi: 10.1103/PhysRevLett.128.035001.
- M. Landreman, H. M. Smith, A. Mollén, and P. Helander. Comparison of particle trajectories and collision operators for collisional transport in nonaxisymmetric plasmas. *Physics of Plasmas*, 21(4):042503, Apr. 2014. ISSN 1070-664X. doi: 10.1063/1.4870077.
- M. Landreman, B. Medasani, F. Wechsung, A. Giuliani, R. Jorge, and C. Zhu. SIMSOPT: A flexible framework for stellarator optimization. *Journal of Open Source Software*, 6(65):3525, 2021a. ISSN 2475-9066. doi: 10.21105/joss.03525.
- M. Landreman, B. Medasani, and C. Zhu. Stellarator optimization for good magnetic surfaces at the same time as quasisymmetry. *Physics of Plasmas*, 28(9):092505, June 2021b. ISSN 1070-664X. doi: 10.1063/5.0061665.
- M. Landreman, S. Buller, and M. Drevlak. Optimization of quasi-symmetric stellarators with self-consistent bootstrap current and energetic particle confinement. *Physics of Plasmas*, 29(8):082501, Aug. 2022. ISSN 1070-664X, 1089-7674. doi: 10.1063/5.0098166.
- L. L. Lao, H. S. John, R. D. Stambaugh, A. G. Kellman, and W. Pfeiffer. Reconstruction of current profile parameters and plasma shapes in tokamaks. *Nuclear Fusion*, 25(11):1611–1622, 1985. ISSN 17414326. doi: 10.1088/0029-5515/25/11/007.
- J. D. Lawson. Some Criteria for a Power Producing Thermonuclear Reactor. *Proceedings of the Physical Society. Section B*, 70(1):6–10, Jan. 1957. ISSN 0370-1301. doi: 10.1088/0370-1301/70/1/303.
- S. A. Lazerson. The virtual-casing principle for 3D toroidal systems. *Plasma Physics and Controlled Fusion*, 54(12), 2012. ISSN 07413335. doi: 10.1088/0741-3335/54/12/122002.
- S. Li, H. Jiang, Z. Ren, and C. Xu. Optimal Tracking for a Divergent-Type Parabolic PDE System in Current Profile Control. *Abstract and Applied Analysis*, 2014:e940965, June 2014. ISSN 1085-3375. doi: 10.1155/2014/940965.
- A. J. Lichtenberg and M. A. Lieberman. *Regular and chaotic dynamics*. Applied Mathematical Sciences. Springer, New York, NY, 2 edition, Mar. 2013.
- J. Loizu and S. R. Hudson. Multi-region relaxed magnetohydrodynamic stability of a current sheet. *Physics of Plasmas*, 26(3):030702, 2019. ISSN 10897674. doi: 10.1063/1.5091765.
- J. Loizu, S. Hudson, A. Bhattacharjee, and P. Helander. Magnetic islands and singular currents at rational surfaces in three-dimensional magnetohydrodynamic equilibria. *Physics of Plasmas*, 22(2):022501, Feb. 2015a. ISSN 1070-664X. doi: 10.1063/1.4906888.
- J. Loizu, S. R. Hudson, A. Bhattacharjee, S. Lazerson, and P. Helander. Existence of three-dimensional ideal-magnetohydrodynamic equilibria with current sheets. *Physics of Plasmas*, 22(9):090704, Sept. 2015b. ISSN 1070-664X. doi: 10.1063/1.4931094.



- J. Loizu, S. R. Hudson, and C. Nührenberg. Verification of the SPEC code in stellarator geometries. *Physics of Plasmas*, 23(11):112505, Nov. 2016. doi: 10.1063/1.4967709.
- J. Loizu, S. R. Hudson, C. Nührenberg, J. Geiger, and P. Helander. Equilibrium  $\beta$ -limits in classical stellarators. *Journal of Plasma Physics*, 83(6):715830601, 2017. doi: 10.1017/S0022377817000861.
- J. Loizu, Y.-M. Huang, S. R. Hudson, A. Baillod, A. Kumar, and Z. S. Qu. Direct prediction of nonlinear tearing mode saturation using a variational principle. *Physics of Plasmas*, 27(7):070701, July 2020. ISSN 1070-664X. doi: 10.1063/5.0009110.
- M. Maurer, A. Bañón Navarro, T. Dannert, M. Restelli, F. Hindenlang, T. Görler, D. Told, D. Jarema, G. Merlo, and F. Jenko. GENE-3D: A global gyrokinetic turbulence code for stellarators. *Journal of Computational Physics*, 420:109694, Nov. 2020. ISSN 0021-9991. doi: 10.1016/j.jcp.2020.109694.
- M. McGann, S. R. Hudson, R. L. Dewar, and G. Von Nessi. Hamilton-Jacobi theory for continuation of magnetic field across a toroidal surface supporting a plasma pressure discontinuity. *Physics Letters, Section A: General, Atomic and Solid State Physics*, 374(33):3308–3314, 2010. ISSN 03759601. doi: 10.1016/j.physleta.2010.06.014.
- M. McGillivray and H. White. Measuring development? The UNDP’s human development index. *Journal of International Development*, 5(2):183–192, Mar. 1993. ISSN 09541748, 10991328. doi: 10.1002/jid.3380050210.
- K. M. McGuire, H. Adler, P. Alling, C. Ancher, H. Anderson, J. L. Anderson, J. W. Anderson, V. Arunasalam, G. Ascione, D. Ashcroft, C. W. Barnes, G. Barnes, S. Batha, G. Bateman, M. Beer, M. G. Bell, R. Bell, M. Bitter, W. Blanchard, N. L. Bretz, C. Brunkhorst, R. Budny, C. E. Bush, R. Camp, M. Caorlin, H. Carnevale, S. Cauffman, Z. Chang, C. S. Chang, C. Z. Cheng, J. Chrzanowski, J. Collins, G. Coward, M. Cropper, D. S. Darrow, R. Daugert, J. DeLooper, R. Dendy, W. Dorland, L. Dudek, H. Duong, R. Durst, P. C. Efthimion, D. Ernst, H. Evenson, N. Fisch, R. Fisher, R. J. Fonck, E. Fredd, E. Fredrickson, N. Fromm, G. Y. Fu, T. Fujita, H. P. Furth, V. Garzotto, C. Gentile, J. Gilbert, J. Gioia, N. Gorelenkov, B. Grek, L. R. Grisham, G. Hammett, G. R. Hanson, R. J. Hawryluk, W. Heidbrink, H. W. Herrmann, K. W. Hill, J. Hosea, H. Hsuan, M. Hughes, R. Hulse, A. Janos, D. L. Jassby, F. C. Jobes, D. W. Johnson, L. C. Johnson, M. Kalish, J. Kamperschroer, J. Kesner, H. Kugel, G. Labik, N. T. Lam, P. H. LaMarche, E. Lawson, B. LeBlanc, J. Levine, F. M. Levinton, D. Loesser, D. Long, M. J. Loughlin, J. Machuzak, R. Majeski, D. K. Mansfield, E. S. Marmar, R. Marsala, A. Martin, G. Martin, E. Mazzucato, M. Mauel, M. P. McCarthy, J. McChesney, B. McCormack, D. C. McCune, G. McKee, D. M. Meade, S. S. Medley, D. R. Mikkelsen, S. V. Mirnov, D. Mueller, M. Murakami, J. A. Murphy, A. Nagy, G. A. Navratil, R. Nazikian, R. Newman, M. Norris, T. O’Connor, M. Oldaker, J. Ongena, M. Osakabe, D. K. Owens, H. Park, W. Park, P. Parks, S. F. Paul, G. Pearson, E. Perry, R. Persing, M. Petrov, C. K. Phillips, M. Phillips,

## Bibliography

---

- S. Pitcher, R. Pysher, A. L. Qualls, S. Raftopoulos, S. Ramakrishnan, A. Ramsey, D. A. Rasmussen, M. H. Redi, G. Renda, G. Rewoldt, D. Roberts, J. Rogers, R. Rossmassler, A. L. Roquemore, E. Ruskov, S. A. Sabbagh, M. Sasao, G. Schilling, J. Schivell, G. L. Schmidt, R. Scillia, S. D. Scott, I. Semenov, T. Senko, S. Sesnic, R. Sissingh, C. H. Skinner, J. Snipes, J. Stencel, J. Stevens, T. Stevenson, B. C. Stratton, J. D. Strachan, W. Stodiek, J. Swanson, E. Synakowski, H. Takahashi, W. Tang, G. Taylor, J. Terry, M. E. Thompson, W. Tighe, J. R. Timberlake, K. Tobita, H. H. Towner, M. Tuszewski, A. von Halle, C. Vannoy, M. Viola, S. von Goeler, D. Voorhees, R. T. Walters, R. Wester, R. White, R. Wieland, J. B. Wilgen, M. Williams, J. R. Wilson, J. Winston, K. Wright, K. L. Wong, P. Woskov, G. A. Wurden, M. Yamada, S. Yoshikawa, K. M. Young, M. C. Zarnstorff, V. Zaverreev, and S. J. Zweben. Review of deuterium–tritium results from the tokamak fusion test reactor. *Physics of Plasmas*, 2(6):2176–2188, June 1995. doi: 10.1063/1.871303.
- J. R. McNally. The ignition parameter  $Tn\tau$  and the energy multiplication factor  $k$  for fusing plasmas. *Nuclear Fusion*, 17(6):1273–1281, Dec. 1977. ISSN 0029-5515, 1741-4326. doi: 10.1088/0029-5515/17/6/014.
- J. D. Meiss. Symplectic maps, variational principles, and transport. *Reviews of Modern Physics*, 64(3):795–848, 1992.
- C. Mercier. Equilibrium and stability of a toroidal magnetohydrodynamic system in the neighbourhood of a magnetic axis. *Nuclear Fusion*, 4(3):213, Sept. 1964. ISSN 0029-5515. doi: 10.1088/0029-5515/4/3/008.
- H. K. Moffatt. The degree of knottedness of tangled vortex lines. *Journal of Fluid Mechanics*, 35(1):117–129, Jan. 1969. ISSN 0022-1120, 1469-7645. doi: 10.1017/S0022112069000991.
- M. Mongeau. *Discontinuous optimization*, pages 739–744. Springer US, Boston, MA, 2009. ISBN 978-0-387-74759-0. doi: 10.1007/978-0-387-74759-0\_130.
- R. Nies, E. J. Paul, S. R. Hudson, and A. Bhattacharjee. Adjoint methods for quasi-symmetry of vacuum fields on a surface. *Journal of Plasma Physics*, 88(1), 2022. ISSN 14697807. doi: 10.1017/S0022377821001264.
- C. Nührenberg. Global ideal magnetohydrodynamic stability analysis for the configurational space of Wendelstein 7–X. *Phys. Plasmas*, 3(6):2401–2410, June 1996.
- C. Nührenberg. Compressional ideal magnetohydrodynamics: Unstable global modes, stable spectra, and Alfvén eigenmodes in Wendelstein 7–X-type equilibria. *Phys. Plasmas*, 6(1):137–147, Jan. 1999.
- J. Nührenberg and R. Zille. Quasi-helically symmetric toroidal stellarators. *Physics Letters A*, 129(2):113–117, May 1988. ISSN 0375-9601. doi: 10.1016/0375-9601(88)90080-1.

- N. Ohyabu, T. Watanabe, H. Ji, H. Akao, T. Ono, T. Kawamura, K. Yamazaki, K. Akaishi, N. Inoue, A. Komori, Y. Kubota, N. Noda, A. Sagara, H. Suzuki, O. Motojima, M. Fujiwara, and A. Iiyoshi. The Large Helical Device (LHD) helical divertor. *Nuclear Fusion*, 34(3):387, Mar. 1994. ISSN 0029-5515. doi: 10.1088/0029-5515/34/3/I07.
- M. O’Neil and A. J. Cerfon. An integral equation-based numerical solver for Taylor states in toroidal geometries. *Journal of Computational Physics*, 359:263–282, 2018. ISSN 10902716. doi: 10.1016/j.jcp.2018.01.004.
- R. Orbach. Future of the Princeton Plasma Physics Laboratory (PPPL), May 2008.
- J. Parisi and J. Ball. *The Future Of Fusion Energy*. World Scientific Publishing Europe, London, England, 2019. ISBN 978-1-78634-749-7.
- W. Park, E. V. Belova, G. Y. Fu, X. Z. Tang, H. R. Strauss, and L. E. Sugiyama. Plasma simulation studies using multilevel physics models. *Physics of Plasmas*, 6(5):1796–1803, May 1999. doi: 10.1063/1.873437.
- E. J. Paul, S. R. Hudson, and P. Helander. Heat conduction in an irregular magnetic field. Part 2. Heat transport as a measure of the effective non-integrable volume. *Journal of Plasma Physics*, 88(1):905880107, Feb. 2022. ISSN 0022-3778, 1469-7807. doi: 10.1017/S0022377821001306.
- T. S. Pedersen, M. Otte, S. Lazerson, P. Helander, S. Bozhnikov, C. Biedermann, T. Klinger, R. C. Wolf, and H.-S. Bosch. Confirmation of the topology of the Wendelstein 7-X magnetic field to better than 1:100,000. *Nature Communications*, 7(1):13493, Nov. 2016. ISSN 2041-1723. doi: 10.1038/ncomms13493.
- T. S. Pedersen, R. König, M. Krychowiak, M. Jakubowski, J. Baldzuhn, S. Bozhnikov, G. Fuchert, A. Langenberg, H. Niemann, D. Zhang, K. Rahbarnia, H.-S. Bosch, Y. Kazakov, S. Brezinsek, Y. Gao, N. Pablant, and t. W.-X. Team. First results from divertor operation in Wendelstein 7-X. *Plasma Physics and Controlled Fusion*, 61(1): 014035, Nov. 2018. ISSN 0741-3335. doi: 10.1088/1361-6587/aaec25.
- H. Peraza-Rodriguez, J. M. Reynolds-Barredo, R. Sanchez, J. Geiger, V. Tribaldos, S. P. Hirshman, and M. Cianciosa. Extension of the SIESTA MHD equilibrium code to free-plasma-boundary problems. *Physics of Plasmas*, 24(8):082516, 2017. ISSN 10897674. doi: 10.1063/1.4986447.
- M. J. D. Powell. A hybrid method for nonlinear equations. In P. Rabinowitz, editor, *Numerical methods for nonlinear algebraic equations*, chapter 7, pages 87–114. Harwood Academic, Amsterdam, Netherlands, Nov. 1971.
- T. Qian, M. Zarnstorff, D. Bishop, A. Chamblis, A. Dominguez, C. Pagano, D. Patch, and C. Zhu. Simpler optimized stellarators using permanent magnets. *Nuclear Fusion*, 62(8):084001, Aug. 2022. ISSN 0029-5515, 1741-4326. doi: 10.1088/1741-4326/ac6c99.

## Bibliography

---

- Z. S. Qu, D. Pfefferlé, S. R. Hudson, A. Baillod, A. Kumar, R. L. Dewar, and M. J. Hole. Coordinate parametrization and spectral method optimisation for Beltrami field solver in stellarator geometry. *Plasma Physics and Controlled Fusion*, 62(12):124004, Oct. 2020. ISSN 0741-3335. doi: 10.1088/1361-6587/abc08e.
- Z. S. Qu, S. R. Hudson, R. L. Dewar, J. Loizu, and M. J. Hole. On the non-existence of stepped-pressure equilibria far from symmetry. *Plasma Physics and Controlled Fusion*, 63(12), 2021. ISSN 13616587. doi: 10.1088/1361-6587/ac2afc.
- A. B. Rechester and M. N. Rosenbluth. Electron Heat Transport in a Tokamak with Destroyed Magnetic Surfaces. *Physical Review Letters*, 40(1):38–41, Jan. 1978. ISSN 0031-9007. doi: 10.1103/PhysRevLett.40.38.
- A. Redl, C. Angioni, E. Belli, and O. Sauter. A new set of analytical formulae for the computation of the bootstrap current and the neoclassical conductivity in tokamaks. *Physics of Plasmas*, 28(2), 2021. ISSN 10897674. doi: 10.1063/5.0012664.
- A. Reiman and H. Greenside. Calculation of three-dimensional MHD equilibria with islands and stochastic regions. *Computer Physics Communications*, 43(1):157–167, Dec. 1986. ISSN 00104655. doi: 10.1016/0010-4655(86)90059-7.
- A. Reiman, M. Zarnstorff, D. Monticello, A. Weller, J. Geiger, and t. W.-A. Team. Pressure-induced breaking of equilibrium flux surfaces in the W7AS stellarator. *Nuclear Fusion*, 47(7):572–578, July 2007. ISSN 0029-5515. doi: 10.1088/0029-5515/47/7/008.
- A. Reiman, N. Ferraro, A. Turnbull, J. Park, A. Cerfon, T. Evans, M. Lanctot, E. Lazarus, Y. Liu, G. McFadden, D. Monticello, and Y. Suzuki. Tokamak plasma high field side response to an  $n = 3$  magnetic perturbation: a comparison of 3d equilibrium solutions from seven different codes. *Nuclear Fusion*, 55(6):063026, May 2015. doi: 10.1088/0029-5515/55/6/063026.
- H. Ritchie. Which sources does our global energy come from? How much is low-carbon? <https://ourworldindata.org/sources-global-energy>, Nov. 2021. Last consulted in January 2023.
- H. Ritchie. How does the land use of different electricity sources compare? <https://ourworldindata.org/land-use-per-energy-source>, June 2022. Last consulted in January 2023.
- E. Rodríguez, P. Helander, and A. Bhattacharjee. Necessary and sufficient conditions for quasisymmetry. *Physics of Plasmas*, 27(6):062501, June 2020. ISSN 1070-664X. doi: 10.1063/5.0008551.
- O. Sauter, C. Angioni, and Y. R. Lin-Liu. Neoclassical conductivity and bootstrap current formulas for general axisymmetric equilibria and arbitrary collisionality regime. *Physics of Plasmas*, 6(7):2834–2839, July 1999. ISSN 1070-664X. doi: 10.1063/1.873240.

- C. Schwab. Ideal magnetohydrodynamics: Global mode analysis of three-dimensional plasma configurations. *Phys. Fluids*, 5(9):3195–3206, Sept. 1993.
- V. D. Shafranov. Plasma Equilibrium in a Magnetic Field. *Reviews of Plasma Physics*, 2:103, Jan. 1966.
- A. N. Simakov and P. Helander. Plasma rotation in a quasi-symmetric stellarator. *Plasma Physics and Controlled Fusion*, 53(2):024005, Jan. 2011. ISSN 0741-3335. doi: 10.1088/0741-3335/53/2/024005.
- D. A. Spong. Generation and damping of neoclassical plasma flows in stellarators. *Physics of Plasmas*, 12(5):056114, May 2005. ISSN 1070-664X. doi: 10.1063/1.1887172.
- D. J. Strickler, S. P. Hirshman, D. A. Spong, M. J. Cole, J. F. Lyon, B. E. Nelson, D. E. Williamson, and A. S. Ware. Development of a robust quasi-poloidal compact stellarator. *Fusion Science and Technology*, 45(1):15–26, 2004. ISSN 15361055. doi: 10.13182/FST04-A421.
- S. Suckewer, H. P. Eubank, R. J. Goldston, E. Hinnov, and N. R. Sauthoff. Toroidal Plasma Rotation in the Princeton Large Torus Induced by Neutral-Beam Injection. *Physical Review Letters*, 43(3):207–210, July 1979. doi: 10.1103/PhysRevLett.43.207.
- Y. Suzuki, N. Nakajima, K. Watanabe, Y. Nakamura, and T. Hayashi. Development and application of HINT2 to helical system plasmas. *Nuclear Fusion*, 46(11):L19–L24, 2006. ISSN 00295515. doi: 10.1088/0029-5515/46/11/L01.
- Y. Suzuki, K. Y. Watanabe, and S. Sakakibara. Theoretical studies of equilibrium beta limit in LHD plasmas. *Physics of Plasmas*, 27(10):102502, Oct. 2020. ISSN 1070-664X, 1089-7674. doi: 10.1063/5.0015106.
- J. B. Taylor. Relaxation of toroidal plasma and generation of reverse magnetic fields. *Physical Review Letters*, 33(19):1139–1141, 1974. ISSN 00319007. doi: 10.1103/PhysRevLett.33.1139.
- J. B. Taylor. Relaxation and magnetic reconnection in plasmas. *Reviews of Modern Physics*, 58(3):741–763, 1986. ISSN 00346861. doi: 10.1103/RevModPhys.58.741.
- M. Taylor. A High Performance Spectral Code for Nonlinear MHD Stability. *Journal of Computational Physics*, 110(2):407–418, Feb. 1994. ISSN 00219991. doi: 10.1006/jcph.1994.1035.
- T. S. Taylor. Physics of advanced tokamaks. *Plasma Phys. Control. Fusion*, 39(12B):B47–B73, Dec. 1997.
- UNDP. Human development report 1990. *UNDP (United Nations Development Programme)*, 1990.

## Bibliography

---

- W. I. van Rij and S. P. Hirshman. Variational bounds for transport coefficients in three-dimensional toroidal plasmas. *Physics of Fluids B: Plasma Physics*, 1(3):563–569, Mar. 1989. ISSN 0899-8221. doi: 10.1063/1.859116.
- J. L. Velasco, I. Calvo, S. Mulas, E. Sánchez, F. I. Parra, Á. Cappa, and the W7-X Team. A model for the fast evaluation of prompt losses of energetic ions in stellarators. *Nucl. Fusion*, 61(11):116059, Nov. 2021.
- P. Virtanen, R. Gommers, T. E. Oliphant, M. Haberland, T. Reddy, D. Cournapeau, E. Burovski, P. Peterson, W. Weckesser, J. Bright, S. J. van der Walt, M. Brett, J. Wilson, K. J. Millman, N. Mayorov, A. R. Nelson, E. Jones, R. Kern, E. Larson, C. J. Carey, I. Polat, Y. Feng, E. W. Moore, J. VanderPlas, D. Laxalde, J. Perktold, R. Cimrman, I. Henriksen, E. A. Quintero, C. R. Harris, A. M. Archibald, A. H. Ribeiro, F. Pedregosa, P. van Mulbregt, A. Vijaykumar, A. P. Bardelli, A. Rothberg, A. Hilboll, A. Kloeckner, A. Scopatz, A. Lee, A. Rokem, C. N. Woods, C. Fulton, C. Masson, C. Häggström, C. Fitzgerald, D. A. Nicholson, D. R. Hagen, D. V. Pasechnik, E. Olivetti, E. Martin, E. Wieser, F. Silva, F. Lenders, F. Wilhelm, G. Young, G. A. Price, G. L. Ingold, G. E. Allen, G. R. Lee, H. Audren, I. Probst, J. P. Dietrich, J. Silterra, J. T. Webber, J. Slavič, J. Nothman, J. Buchner, J. Kulick, J. L. Schönberger, J. V. de Miranda Cardoso, J. Reimer, J. Harrington, J. L. C. Rodríguez, J. Nunez-Iglesias, J. Kuczynski, K. Tritz, M. Thoma, M. Newville, M. Kümmerer, M. Bolingbroke, M. Tartre, M. Pak, N. J. Smith, N. Nowaczyk, N. Shebanov, O. Pavlyk, P. A. Brodtkorb, P. Lee, R. T. McGibbon, R. Feldbauer, S. Lewis, S. Tygier, S. Sievert, S. Vigna, S. Peterson, S. More, T. Pudlik, T. Oshima, T. J. Pingel, T. P. Robitaille, T. Spura, T. R. Jones, T. Cera, T. Leslie, T. Zito, T. Krauss, U. Upadhyay, Y. O. Halchenko, and Y. Vázquez-Baeza. SciPy 1.0: Fundamental algorithms for scientific computing in Python. *Nature Methods*, 17(3):261–272, 2020. ISSN 15487105. doi: 10.1038/s41592-019-0686-2.
- M. Wakatani. *Stellarator and Heliotron Devices*. Number 95 in International Series of Monographs on Physics. Oxford University Press, 1998. ISBN 978-0-19-507831-2.
- F. Wechsung, A. Giuliani, M. Landreman, A. Cerfon, and G. Stadler. Single-stage gradient-based stellarator coil design: Stochastic optimization. *Nuclear Fusion*, 62(7):076034, May 2022. ISSN 0029-5515. doi: 10.1088/1741-4326/ac45f3.
- H. Weitzner. Ideal magnetohydrodynamic equilibrium in a non-symmetric topological torus. *Physics of Plasmas*, 21(2):022515, Feb. 2014. ISSN 1070-664X. doi: 10.1063/1.4867184.
- J. Wesson. *Tokamaks*. International Series of Monographs on Physics. Oxford University Press, London, England, 4 edition, May 2011.
- L. Woltjer. A theorem on force-free magnetic fields. *Proceedings of the National Academy of Sciences*, 44(6):489–491, 1958. doi: 10.1073/pnas.44.6.489.

- World Nuclear Association. Uranium Supplies: Supply of Uranium - World Nuclear Association. <https://world-nuclear.org/information-library/nuclear-fuel-cycle/uranium-resources/supply-of-uranium.aspx>, Dec. 2022. Last consulted in January 2023.
- World Nuclear Association. Nuclear Power in France. <https://world-nuclear.org/information-library/country-profiles/countries-a-f/france.aspx>, 2023.
- A. Wright, P. Kim, N. Ferraro, and S. Hudson. Modelling the nonlinear plasma response to externally applied three-dimensional fields with the Stepped Pressure Equilibrium Code. *Journal of Plasma Physics*, 88(5):905880508, Oct. 2022. ISSN 0022-3778, 1469-7807. doi: 10.1017/S0022377822000927.
- P. Xanthopoulos, H. E. Mynick, P. Helander, Y. Turkin, G. G. Plunk, F. Jenko, T. Görler, D. Told, T. Bird, and J. H. E. Proll. Controlling Turbulence in Present and Future Stellarators. *Physical Review Letters*, 113(15):155001, Oct. 2014. ISSN 0031-9007, 1079-7114. doi: 10.1103/PhysRevLett.113.155001.
- X. Zhao, H. Yang, Y. Wang, and Z. Sha. Review on the electrochemical extraction of lithium from seawater/brine. *Journal of Electroanalytical Chemistry*, 850:113389, Oct. 2019. ISSN 1572-6657. doi: 10.1016/j.jelechem.2019.113389.
- C. Zhu, S. R. Hudson, Y. Song, and Y. Wan. New method to design stellarator coils without the winding surface. *Nuclear Fusion*, 58(1):016008, Nov. 2017. ISSN 0029-5515. doi: 10.1088/1741-4326/aa8e0a.
- C. Zhu, S. R. Hudson, S. A. Lazerson, Y. Song, and Y. Wan. Hessian matrix approach for determining error field sensitivity to coil deviations. *Plasma Physics and Controlled Fusion*, 60(5), 2018. ISSN 13616587. doi: 10.1088/1361-6587/aab6cb.
- C. Zhu, K. Hammond, A. Rutkowski, K. Corrigan, D. Bishop, A. Brooks, P. Dugan, R. Ellis, L. Perkins, Y. Zhai, A. Chambliss, D. Gates, D. Steward, C. Miller, B. Lown, and R. Mercurio. PM4Stell: A prototype permanent magnet stellarator structure. *Physics of Plasmas*, 29(11):112501, Nov. 2022. ISSN 1070-664X, 1089-7674. doi: 10.1063/5.0102754.





# Antoine Baillod

*Ph.D. in physics*

27/10/1995

Nationality: Swiss

+41 79 481 72 22

antoine.baillod@outlook.com

Ch. du Boisy 30, 1004 Lausanne, VD

www.linkedin.com/in/antoinebaillod



## Career Objective

Finishing my Ph.D. in computational plasma physics by the end of March 2023, I am looking for a new exciting postdoctoral position, where I could continue to expand my knowledge in stellarator physics, and participate in bringing the international community one step closer to commercial fusion energy.

## Work Experience

- 2018–(2023) **Swiss Plasma Center, Lausanne, Switzerland**, Ph.D. in plasma physics.
- **Development (FORTRAN, MATLAB)**: Implementation and verification of new capabilities in the Stepped Pressure Equilibrium Code (SPEC) [1].
  - **Modeling, analysis**: Development of new field line topology measurement. Study of the pressure limit in a stellarator [2].
  - **Optimisation (PYTHON)**: Coupling of SPEC with simsopt, a framework stellarator optimisation. Application to stellarator magnetic field topology [3].
  - **Team work, multi tasking**: Participation to international research [4-9]. Master students project management.
  - **Communication**: Presentations at international conferences. Tour guide for visits of the Swiss Plasma Center.
  - **Pedagogy**: Exercise session teaching to Bachelor student.
- 2018 **Culham Centre for Fusion Energy, Culham, United Kingdom**, Master thesis.
- **Development (PYTHON)**: Improvements of a Bayesian statistical code for data analysis.
- 2017–2018 **Radiophysics department, Centre Hospitalier Universitaire Vaudois (CHUV), Lausanne, Switzerland**, Stage.
- **Problem solving skills**: Design of a measurement system for x-rays sources of the Cyberknife apparatus.
  - **Quick learning**: Employment of a *Treatment Planning System (TPS)* to evaluate the effective dose deposited in patients [10].

## Education

- 2016–2018 **Master in applied physics**, *École Polytechnique Fédérale de Lausanne (EPFL)*, Lausanne, Switzerland.
- 2015–2016 **Student exchange program**, *Kungliga Tekniska Högskolan (KTH)*, Stockholm, Sweden.
- 2013–2016 **Bachelor in physics**, *École Polytechnique Fédérale de Lausanne (EPFL)*, Lausanne, Switzerland.
- 2010–2013 **Federal maturity**, *Gymnase Auguste Piccard*, Lausanne, Switzerland.
- **Award**: Best results in physics

## Other experiences

- Polyphys Association for Ph.D. students in physics at EPFL.**
- Vice-president (2022) — event organisation
  - Treasurer (2021) — bank account management

---

## Skills

**Coding** PYTHON, FORTRAN, MATLAB, Bash, C++,  $\LaTeX$   
**Tools** MPI, OpenMP, SLURM, Git, Zoom, Microsoft Office  
**Codes** SPEC, simsopt, VMEC, FOCUS, DESCUR, booz\_xform  
**Soft skills** Autonomous, organised, rigorous, critical thinking, empathy, sociable, communication

---

## Langues

**French** Mother tongue  
**English** C1-C2  
**German** B1

---

## Personal interests

**Hobbies** Outdoor sports, board games, chess, exploration, cooking

---

## References - on request

# Appendices

## Conferences contribution

- 07.2022 **Contributed talk**, *New Angle Representation Implemented in SPEC*, Simons Collaboration on Hidden Symmetries and Fusion Energy Workshop, Greifswald, Germany.
- 07.2022 **Contributed Talk**, *Shearless Quasi-Symmetry*, Simons Collaboration on Hidden Symmetries and Fusion Energy Workshop, Greifswald, Germany.
- 06.2022 **Invited Talk**, *Stellarator optimization for nested magnetic surfaces at finite beta and toroidal current*, International Stellarator and Heliotron Workshop (ISHW), Warsaw, Poland.
- 03.2022 **Poster**, *Optimization of the equilibrium  $\beta$ -limit in a classical stellarator with bootstrap current*, Simons Collaboration on Hidden Symmetries and Fusion Energy Meeting, New York, USA.
- 10.2021 **Contributed talk**, *Pressure effects on the topology of magnetic fields in stellarators*, European Fusion Theory Conference (EFTC), Remote.
- 08.2021 **Contributed talk**, *Pressure effects on the topology of magnetic fields in stellarators*, Sherwood Fusion Theory Conference, Remote.
- 10.2020 **Poster**, *Bootstrap current effect on classical stellarator beta limit*, Varenna Fusion Theory conference, Remote.
- 08.2019 **Poster**, *Toroidal current effects on 3D magnetic equilibria*, Joint Annual Meeting of SPS and ÖPG, Zürich, Switzerland.
- 03.2019 **Poster**, *Constraining the toroidal current profile in SPEC equilibria*, Simons Collaboration on Hidden Symmetries and Fusion Energy Meeting, New York, USA.

## Publications

### First author

- [1] **Computation of multi-region, relaxed magnetohydrodynamic equilibria with prescribed toroidal current profile**, A. Baillod et. al., Journal of Plasma Physics **87** (4), 2021.
- [2] **Equilibrium  $\beta$ -limits dependence on bootstrap currents in classical stellarators**, A. Baillod et. al., arXiv:2211.12948.
- [3] **Stellarator optimization for nested magnetic surfaces at finite  $\beta$  and toroidal current**, A. Baillod et. al., Physics of Plasmas **29** (4), 2021.

### Co-author

- [4] **Experimental confirmation of efficient island divertor operation and successful neoclassical transport optimization in Wendelstein 7-X**, T. S. Pedersen et al., Nuclear Fusion **64** (4), 2022.
- [5] **Nature of ideal MHD instabilities as described by multi-region relaxed MHD**, A. Kumar et al., Plasma Physics and Controlled Fusion **64** (6), 2022.
- [6] **Computation of linear MHD instabilities with the multi-region relaxed MHD energy principle**, A. Kumar et al., Plasma Physics and Controlled Fusion **63** (4), 2021.
- [7] **Coordinate parameterisation and spectral method optimisation for Beltrami field solver in stellarator geometry**, Z. Qu et al., Plasma Physics and Controlled Fusion **62** (12), 2020.
- [8] **Direct prediction of nonlinear tearing mode saturation using a variational principle**, J. Loizu et al., Physics of Plasmas **27** (7), 2020.
- [9] **Analysis of wall-embedded Langmuir probe signals in different conditions on the Tokamak à Configuration Variable**, O. Février et al., Review of Scientific Instruments **18**, 2018.
- [10] **Dose indicator for CyberKnife image-guided radiation therapy**, R. Moeckli, et. al., Medical Physics **47** (5), 2020.